AirEco

Final Report

AE3200: Design Synthesis Exercise

Group 1

Delft University of Technology

TU Delft

This page has been intentionally left blank

AirEco

Final Report

by

Group 1

Student Name	Student Number
Lars Dijkstra	4860403
Daan Dieben	4856678
Yvar Vliex	4820169
Loreto Bordas Díaz	4778219
Farouk Khalil	4771478
Katarina Grubbe Hildebrandt	4784995
Luigi Pescio	4837142
Rahiq Ullah	4841867
Guillaume van Dijk	4672968
Thomas van Rens	4867548

Version: 1.1

Instructor: Dr. ir. R.C. Alderliesten
Coaches: Dr. B.F. Santos & Mr. D. Giannopoulos
Institution: Delft University of Technology
Place: Faculty of Aerospace Engineering, Delft
Project Duration: April, 2021 - July, 2021

TU Delft

Preface

This report was written as part of the Design Synthesis Exercise, a 10 week project in which groups of 10 members create a design to obtain their bachelor's degree at the Faculty of Aerospace Engineering. AirEco's task is to design and develop a revolutionary and sustainable solution for the future of long-range commercial aviation.

This report deals with the final design, in which a long-range commercial (150-250 passengers) aircraft with a propulsion system based on renewable energy principles is proposed.

The document is structured as follows. Firstly, Chapter 2 and Chapter 3 present the functional and market analysis of the aircraft. The latter will be followed by a financial analysis, in Chapter 15. The numerous design justifications are elaborated upon in Chapter 5-13. The reliability, availability, maintainability and safety of the design is addressed in Chapter 14. Readers with a particular interest in the outcome and continuation of the Design Synthesis Exercise are referred to Chapter 16 and Chapter 18, respectively. Lastly, the various system integration diagrams, as for example hardware and data handling diagram, are presented in Chapter 17.

With this, we would also like to express our gratitude to dr. ir. R.C. Alderliesten, the principal tutor, as well as the coaches, dr.ir. B.F. Lopes dos Santos and D. Giannopoulos MSc., for their help, feedback and guidance during the project. Furthermore, we would also like to thank the TA's, the support staff, all people we approached from the various departments of the Faculty of Aerospace Engineering and Loris Gilner from Universal Hydrogen[1] for their time and support.

Group 1
Delft, June 2021

[1] https://www.hydrogen.aero/

Executive Overview

AirEco was tasked with designing a commercial aircraft (150-250 pax) with a range of 5000 [km] and a propulsion system based on renewable energy principles. Furthermore, the team was challenged to seek out revolutionary solutions in order to significantly improve the sustainability of the aircraft compared to its direct competitors.

AirEco proposes an adaptable solution. The concept is an aircraft that is able to enter into service by 2035 as a hybrid configuration, running on both biofuel and hydrogen. By 2050, when the green production of hydrogen is expected to be more prominent, the aircraft will undergo minor modifications and continue as a full hydrogen configuration.

At the core of this adaptable concept lies a revolutionary propulsion system combined with the use of non-integral hydrogen tanks which ensure that operational requirements are met. The power and propulsion system is housed in a conventional tube-and-wing configuration, which employs a T-tail to ensure longitudinal stability and control. Furthermore, cutting-edge technologies like AeroShark are used to improve the sustainability of the design even further than it was with the novel propulsion system alone. The aircraft can carry 150 passengers, and has a range of 5623 [km] for the 100% hydrogen and 8192 [km] for the hybrid configuration.

To evaluate sustainability it is important to define it as the sum of three pillars; social, economical and environmental. Social sustainability is achieved by means of various noise reduction techniques reducing noise levels for both passengers and people outside of the aircraft. A new hydrogen propulsion system will decrease emissions. While, a sharkskin like riblet film that is applied to 70% of the aircraft reduces will reduce drag by 2 to 3%. The use of non-integral tanks will improve turn-around times considerably, lowering them from 2 hours to possibly under 1 hour with parallel refueling. Additionally, waste is reduced. According to Universal Hydrogen, with convectional refueling 10% of hydrogen is lost. With this method no hydrogen is lost. Lastly, non-integral tanks are easier to inspect, lowering maintenance costs. The adaptability of aircraft ensures prolonged sales for AirEco and greater flexibility to airlines. Airlines may reach airports where the hydrogen infrastructure is lacking, widening their routes. Lastly, the selected material for the wing and fuselage, aluminium alloys, are more sustainable and cheaper.

A preliminary profitability analysis was performed. An upper and lower bound on costs was determined, including or not including the commonality effect achieved through a partnership with Boeing. The upper bound on cost is $157 millions, yielding an ROI of -1.6%. However, when benefiting from the economies of scale of Boeing the total cost of AirEco is $108 millions, resulting in a return on investment (ROI) of 43.6%.

Apart from all the features that make the design itself more sustainable, AirEco believes that their concept could also play a key role in facilitating and accelerating commercial aviation's transition to hydrogen powered flight. If this is to be the case then it would actually be the fulfillment of this role that will contribute the most to a more sustainable future.

For the continuation of the project, some of the most important recommendations are investigating the flashback effect for propulsion, the hydrogen infrastructure and production for hydrogen tanks and finally essentially conducting more detailed structural analyses for structures.

Contents

Nomenclature

Constants

κ_{air}	Ratio of specific heat for air	[-]
κ_{gas}	Ratio of specific heat for gas	[-]
$C_{p_{\text{air}}}$	Air Specific heat at constant pressure	[J/kgK]
$C_{p_{\text{gas}}}$	Gas Specific heat at constant pressure	[J/kgK]
g	Gravitational constant	9.80665 [m/s^2]
K_t	Stress concentration factor	[-]
S_ult	Ultimate tensile stress	[MPa]
N	Number of fatigue cycles	[-]
R	Gas Constant	[J/kgK]

Latin Symbols

ΔL_{c-jet}	Additive term to account for secondary jet	[dB]
$\Delta L_{dir/spec}$	Combined term for spectral shape and directivity	[dB]
$\dot{m}_{\text{biofuel}}$	Biofuel mass flow rate	[kg/s]
$\dot{m}_{\text{bypass}}$	Bypass air mass flow rate	[kg/s]
$\dot{m}_{\text{core}}$	Core air mass flow rate	[kg/s]
$\dot{m}_{\text{hydrogen}}$	Hydrogen fuel mass flow rate	[kg/s]
$\dot{m}_{\text{total}}$	Air mass flow rate	[kg/s]
F_{Core}	Core thrust	[N]
F_{Fan}	Fan thrust	[N]
F_{Total}	Engine total thrust	[kN]
A_{m}	Enclosed area	[mm^2]
b	Wing span	[m]
b_N	Distance between nose landing gear and aft center of gravity	[m]
c	Chord length	[m]
$C1$	Taper ratio correction factor	[$-$]
c_a	Aileron chord length	[m]
c_j	Specific fuel consumption	[g/KNs]
C_D	Aircraft drag coefficient	[$-$]
C_d	Airfoil drag coefficient	[$-$]
$C_{L,\alpha}$	Wing lift gradient	[rad]
$C_{L,des}$	Aircraft design lift coefficient	[$-$]
$C_{l,des}$	Airfoil design lift coefficient	[$-$]
$C_{l_{\delta a}}$	Rolling moment coefficient	[$-$]
$C_{L_{\text{max}}}$	Maximum lift coefficient	[-]
C_{l_P}	Roll damping coefficient	[-]
C_L	Aircraft lift coefficient	[$-$]
C_l	Airfoil lift coefficient	[$-$]
c_r	Root chord	[m]
c_t	Tip chord	[m]
D	Drag	[N]
d	Distance between nose landing gear and main landing gear	[m]
d	Distance to observer	[m]
D_g	Drag due to landing gear	[N]
D_{fan}	Fan diameter	[m]
E	Young's modulus	[MPa]
e	Oswald efficiency factor	[$-$]
f	Frequency	[Hz]
G	Shear modulus	[MPa]
H	Gust gradient distance	[m]
h_0	Sea level altitude	[m]
H_E	Engine height	[m]
h_{cruise}	Cruise altitude	[m]
I	Moment of inertia	[mm^4]
k	Airfoil efficiency factor	[$-$]
K_c	Flat plate buckling coefficient	[-]
$L_{spec}(Str)$	Spectral shape function	[dB]
L_{loiter}	Loiter time	[min]
$L_{bbn,ex}$	Exhaust broadband noise contribution	[dB]
$L_{bbn,in}$	Inlet broadband noise contribution	[dB]
$L_{ctn,in}$	Inlet combination-tone noise contribution	[dB]
L_{dir}	Emission directivity correlation	[dB]
$L_{dtn,ex}$	Exhaust discrete-tone noise contribution	[dB]
$L_{dtn,in}$	Inlet discrete-tone noise contribution	[dB]
$L_{fan,ex}$	Fan exhaust noise level	[dB]
$L_{fan,in}$	Fan inlet noise level	[dB]
L_{jet}	Jet noise level	[dB]
$L_{norm/spec}(Str)$	Normalised reference level as a function of Strouhal number	[dB]
L_{norm}	Normalised reference level	[dB]
L_{vel}	Velocity dependence noise level	[dB]
$L_{dir/spec}(Str)$	Directivity and spectral shape function noise effects	[dB]
L_{geo}	Geometry dependent adjustment factor	[dB]
$L_{norm/vel/geo}$	Reference noise level	[dB]
LD	Lift to drag ratio	[-]
M	Mach number	[-]

M^*	Critical Mach number	[−]
M_{dd}	Drag divergence Mach number	[−]
M_{ff}	Product of all fuel fractions	[-]
n	Load factor	[-]
n_{max}	Maximum load factor	[-]
P	Steady state roll rate	[rad/s]
P_0	Sea level pressure	[pa]
q	Dynamic pressure	[Pa]
q_s	Shear flow	[N/mm]
Re	Reynolds number	[−]
S	Wing surface area	[m^2]
S'	Increased wing surface area with flaps extended	[m^2]
S_x	Shear force in X-direction	[N]
S_z	Shear force in Z-direction	[N]
S_{wet}	Wetted area	[m^2]
S_{wf}	Flapped surface area	[m^2]
Str	Strouhal number	[-]
T	Thrust	[N]
t/c	Thickness to chord ratio of ratio	[−]
T_0	Sea level temperature	[K]
T_{ref}	Thrust due to thrust reversers	[N
U_{ds}	Gust design velocity	[m/s]
U_{ref}	Reference gust velocity	[m/s]
V_x	Shear force in X-direction	[N]
V_z	Shear force in Z-direction	[N]
V_{cruise}	Cruise velocity	[m/s
$V_{\text{D,min}}$	Speed at minimum drag	[m/s]
V_{max}	Maximum velocity	[m/s]
V_{min}	Minimum velocity	[m/s]
V_{opt}	Optimal velocity for max. range	[m/s]
V_{TO}	Take-off speed	[m/s]
V_{lof}	Lift-off velocity	[m/s]
V_{min}	Minimum speed	[m/s]
W	Weight	[N]
$W_4/W5$	Cruise fuel fraction	[-]
$W_6/W7$	Loiter fuel fraction	[-]
W_f	Fuel weight	[kg]
Y_E	Lateral distance to engine	[m]
Y_{LG}	Lateral location of landing gear	[m]
y_{MAC}	Spanwise location of MAC	[m]
Z_{cg}	Height of center of gravity with respect to the ground	[m]

Greek Symbols

α	Angle between nose landing gear and main landing gear	[°]
α	Angle of attack	[°]
α^*	Directivity angle	[°]
α^*	Polar noise emission angle	[○]
β^*	Lateral emission angle	[°]
β^*	Longitudinal noise emission angle	[○]
δ_a	Aileron deflection	[rad]
η_{cc}	Combuster efficiency	[-]
η_{fan}	Fan isentropic efficiency	[-]
η_{HPC}	high pressure compressor isentropic efficiency	[-]
η_{HPT}	high pressure turbine isentropic efficiency	[-]
η_{inlet}	Intake isentropic efficiency	[-]
η_{LPC}	Low pressure compressor isentropic efficiency	[-]
η_{LPT}	Low pressure turbine isentropic efficiency	[-]
η_{mech}	High and low speed shaft mechanical efficiency	[-]
η_{nozzle}	Nozzle efficiency	[-]
γ	Climb angle	[○]
λ	Taper ratio	[−]
λ	Time constant	[s]
$\Lambda_{c/2}$	Half chord sweep angle	[°]
Λ_{hinge_line}	Sweep angle at the hinge line	[°]
$\mu_{\text{brakes on}}$	Fiction coefficient between ground and landing gear at landing	[-]
$\mu_{rolling}$	Friction coefficient between ground and landing gear at take-off	[-]
ω	Radial frequency of the response	[rad/s]
Φ_I	Clearance angle	[°]
Π_{CC}	Combuster pressure ratio	[-]
Π_{fan}	Fan pressure ratio	[-]
Π_{HPC}	High pressure compressor	[-]
Π_{LPC}	Low pressure compressor ratio	[-]
ρ_0	Sea level density	[kg/m^3]
σ	Stress	[MPa]
σ_{amp}	Stress amplitude	[MPa]
σ_{cr}	Critical buckling stress	[MPa]
τ	Aileron effectiveness	[rad^{-1}]
τ	Shear stress	[N/mm^2]

Abbreviations

CH_4	Methane	[-]
CO_2	Carbon dioxide	[-]
CO_2e	CO_2 equivalent	[-]
H_2	Hydrogen	[-]
LHV_{bio}	Biofuel calorific value	[MJ/kg]
LHV	Hydrogen calorific value	[MJ/kg]
N_2O	Nitrous oxide	[-]
a/c	Aircraft	[-]
BPR	Bypass Ratio	[-]
c.g.	Center of gravity	[-]

CAGR	Compound Annual Growth Rate	[-]
CER	Cost-estimating relation	[-]
CLC	Combined load case	[-]
DOC	Direct operating cost	[$/flight]
ECS	Environment Control System	[-]
FBD	Free body diagram	[-]
GHG	Greenhouse gasses	[-]
GWP	Global Warming potential	[-]
HEPA	High-Efficiency Particulate Arrestors	[-]
HLDs	High Lift Devices	[-]
HSR	High Speed Rail	[-]
ICAO	International Civil Aviation Organisation	[-]
IFE	In-Flight Entertainment	[-]
LE	Leading Edge	[-]
LH2	Liquid hydrogen	[-]
LPT	Low Pressure Turbine	[-]
MAC	Mean aerodynamic chord	$[m]$
MLG	Main landing gear	[-]
MTOW	Maximum Take-Off Weight	
n.p.	Neutral point	[-]
NLG	Nose landing gear	[-]
RMSE	Root mean squared error	[-]
ROC	Rate of Climb	[m/s]
ROI	Return On Investment	[$]
RPK	revenue per kilometer	$[-]$
S.M.	Stability Margin	[-]
SMR	Steam methane reforming process	[-]
SWOT	Strengths, Weaknesses, Opportunities and Threats	[-]
TE	Trailing Edge	[-]
ULC	Unit load case	[-]

1. Introduction

Ever since the Industrial Revolution, the emission of green house gasses has been affecting our planet at an ever increasing pace. Over the past decades, the commercial aviation industry has heavily contributed to this fact and now it finds itself at a crossroads. While most industries are taking radical steps towards a more sustainable future, the aviation industry is lacking a response to the outcry for sustainability that is omnipresent in today's world. The leaders of the industry keep coming up with evolutionary solutions while it is clear that a revolution in sustainability is necessary.

Over the past years, the term 'sustainability' has developed to be a buzzword that has been misused in all types of industries. It is therefore important to define sustainability as the sum of three pillars: social, economical and environmental. Another important phenomenon to introduce is that of proportionality bias. Proportionality bias is the principle that people are inclined to believe that a big and outspoken consequences must have a disruptive cause or origin and vice versa.

Many prominent parties in the aviation industry have proposed futuristic concepts and exotic configurations. These solutions certainly look revolutionary, but do they actually offer radical improvements in terms of sustainability? Due to proportionality bias most people would believe that this is the case, but is this belief justified? These were some of the questions the AirEco team set out to answer.

This report is the final report in a series that documents the design of a commercial aircraft (150-250 pax) with a range of 5000 kilometers and a propulsion system based on renewable energy principles. The AirEco team was challenged to propose a solution that would be a revolution in terms of sustainability, surpassing all current evolutionary solutions by a great margin. The previous reports contain the conceptual design phase which converged to a conventional wing-and-tube design, powered by a hybrid mix of both hydrogen and biofuel. The aim of this report is to present the detailed design process together with the final design and provide the context in which the aircraft will enter into service in 2035.

The report is structured to start with a functional and market analysis in Chapter 2 and 3 respectively. Chapter 4 focuses on sustainability while Chapter 5 through 13 present the technical details of the aircraft. Chapter 14 is concerned with RAMS and Chapter 15 performs a financial analysis. The final design is presented in Chapter 16 and the integration of its systems is elaborated on in Chapter 17. Future developments are addressed in 18. Finally, Chapter 19 presents the conclusion and Chapter 20 contains some recommendations for future design phases.

2. Functional Analysis

A functional analysis was made in order to have a complete overview of all the functions performed by AirEco. The analysis included a functional breakdown structure (FBS) and a functional flow diagram (FFD). These diagrams show six different phases of the aircraft: design, production, distribution, operation, maintenance and end-of-life. The FBS and FFD are covered in Section 2.1 and Section 2.2 respectively.

2.1. Functional Breakdown structure

As is shown in Figure 2.1, the FBS represents AirEco's six main different functions. Levels are presented hierarchically and the different levels are represented with different colors as shown in the legend. The top level, blue is divided into into six functions. The six functions are colored with green, and every sub-level has different color purple, yellow and white in order of level.

2.2. Functional Flow Diagram

The FFD in Figure 2.2 is derived from the FBS and it presents the aircraft functions in a chronological order. Validation and verification in the design process are demonstrated in iteration loops. Loops for the aircraft operations do also exist where approval for take-off by air-traffic control is needed. The same numbering in the FBS is used in the FFD.

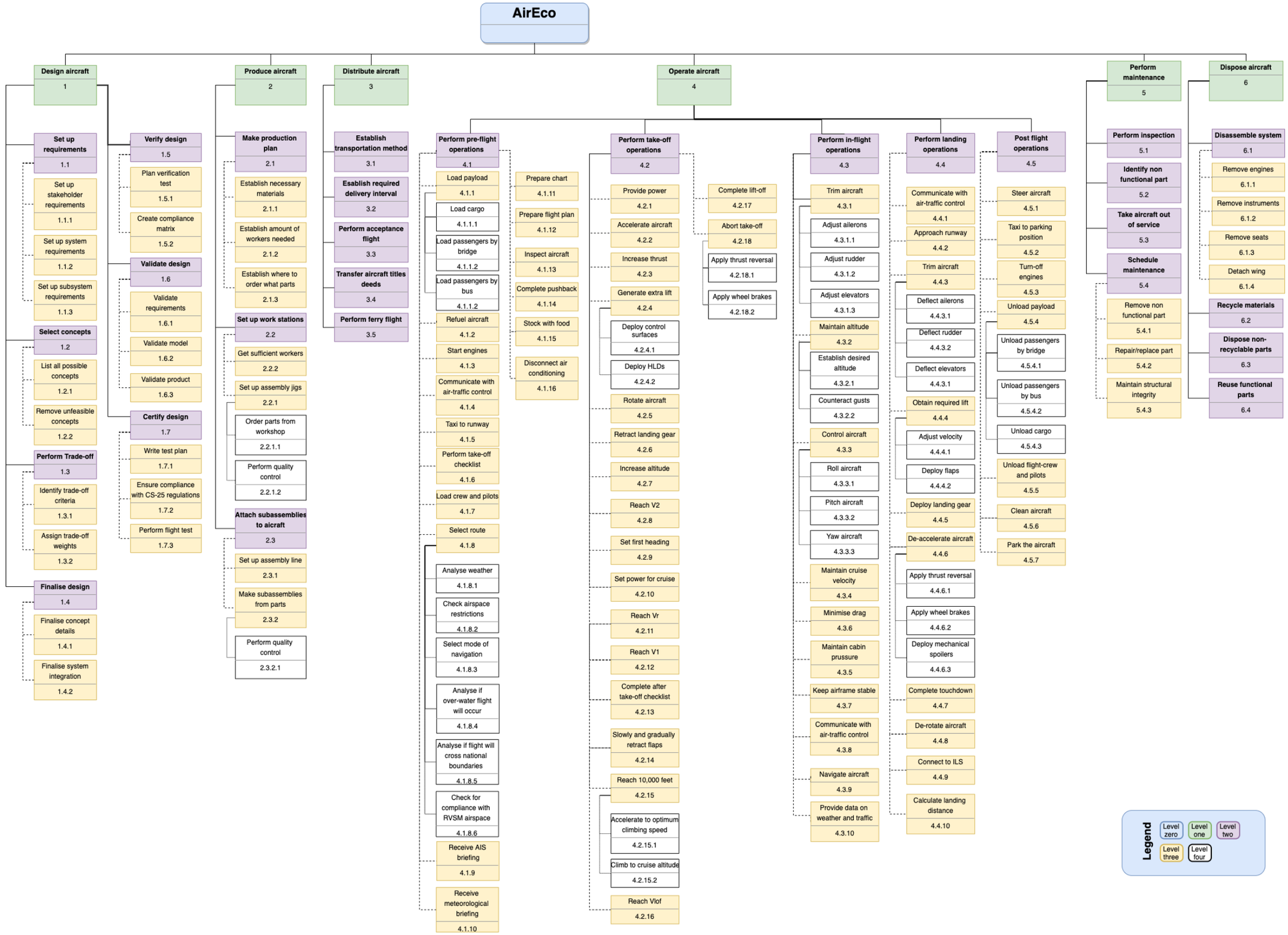

Figure 2.1: Functional breakdown structure.

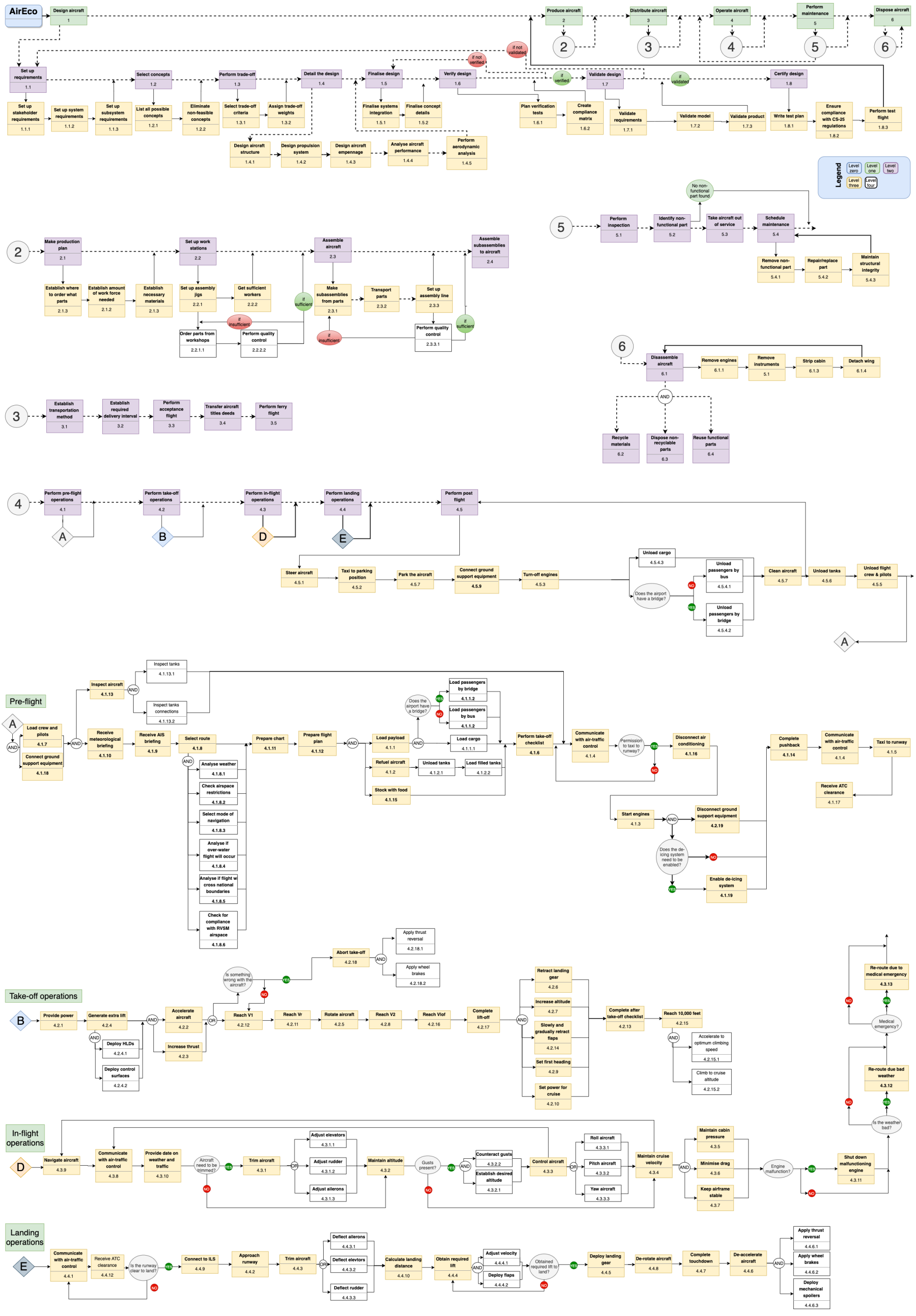

Figure 2.2: Functional flow diagram

3. Market Analysis

The aim of this chapter is to give an overview of the market AirEco is trying to enter, as well as provide some context for the entry strategy AirEco will employ. The market analysis starts with the identification of the stakeholders and their respective needs in Section 3.1. Next, Section 3.2 presents a general market outlook while Section 3.3 analyses the competitive landscape. Section 3.4 provides a SWOT analysis and Section 3.5 explains AirEco's position. Lastly, Section 3.6 elaborates on the entry strategy AirEco will employ.

3.1. Stakeholder Identification

The first step in performing the market analysis is identifying the stakeholders and ranking them by importance, which was already touched upon in the Baseline report [1]. The result is summarised in Table 3.1. The table shows the various stakeholders, their ranks and their needs. From these needs, requirements are generated to which (non)compliance will be shown in Section 16.5. The rank of a stakeholder shows the power and influence the stakeholder has on the aircraft programme, ranking from 1 to 5. In rank 1, the airlines, airports and partners and investment companies are located. The airlines are the likely customers of the aircraft and are arguably the most important stakeholder. However, the revolutionary concept as presented in this report is infeasible without adaptation from the airport perspective, and funds from partners and investment companies. Therefore, airports, partners and investment companies are also located in rank 1. The ranking of the rest of stakeholders will not be explained in greater detail as it was already touched upon in the Baseline report [1].

Table 3.1: Ranked stakeholder needs for requirements generation [1].

Rank	Stakeholder	Needs
1.	Airlines	• Range of 5000 km • Transport 150 - 250 passengers • Propulsion based on renewable energy • Production cost of maximum 120% of the A321XLR • Passenger comfort at low cost • Low operations costs • High revenue • Less noise than conventional aircraft • Reliable • Operational efficiency shall not be compromised by energy source
	Airports	• Comply with noise and emission policies • Meet passenger travel demands (such as turnaround time) • Usable with minor change to existing infrastructure • Safe ground operations • Usable with current landing and take-off paths
	Partners & Investment Companies	• Return on investment • Being part of sustainability movement for PR reasons
2.	Contractors and subcontractors	• Ensure safety of manufacturers • Make use of existing manufacturing techniques
	Workers and employees	• Fair pay • Safe working environment
3.	Governments	• Safe aircraft • Compliance to noise and emission policies • Sustainable movement
4.	Passengers	• Comfort and sufficient cabin space • Sufficient cargo space • Safe and reliable aircraft • Sustainability
	Cargo industry	• Move cargo in a safe and reliable way • Easy on- and off loading of cargo
5.	Local residents	• Minimize noise pollution • Minimize emissions

3.2. Market Outlook

In 2018, the total commercial aircraft market was valued at 191 billion [USD] and was predicted to grow at a compound annual growth rate (CAGR) of 2.9%[1]. In 2020, the industry was heavily struck by the COVID-19 pandemic, almost halving the market's valuation to 99 billion [USD][2]. Despite this recent development, the market is expected to recover within the next three years and continue its rapid growth at 8.9% CAGR[2].

Based on the range and passenger requirements defined in the Baseline report [1], AirEco's design will fall into the 'single aisle' segment. Figure 3.1 and 3.2 show that both Airbus and Boeing expect around 75% of the new deliveries over the next 20 years to be within this segment. From this, AirEco can conclude that it is targeting a large portion of the total market with its design.

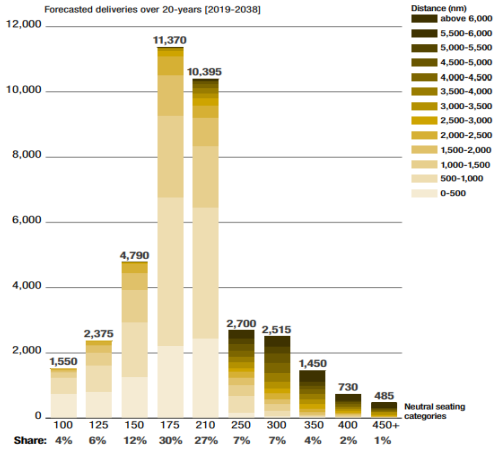

Figure 3.1: Airbus' deliveries forecast from 2019 to 2038 [2].

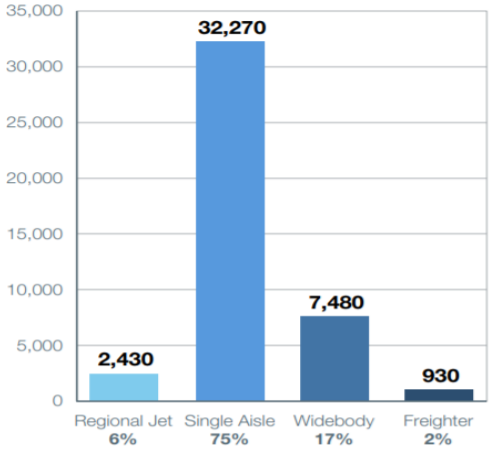

Figure 3.2: Boeing's deliveries forecast from 2020 to 2039 [3].

3.3. Competitor and Substitute Analysis

Before entering into a new market, it is important to understand what the competitive landscape looks like and what substitutes might threaten development of the total market in the future. The commercial aircraft market is characterised by a duopoly, where Boeing and Airbus together occupy almost 90% of the total market for narrow- and wide-body aircraft[2]. A handful of other competitors are also active in the market. These include smaller manufacturers like Embraer, Comac and Irkut[3]. Table 3.2 presents the most direct competitors to AirEco's design, in terms of passenger and range capacities.

The most notable substitutes that threaten the short-haul aviation market as a whole are train-like means of transportation such as the Maglev train[4], the High Speed Rail (HSR)[5] and the Hyperloop concept[6]. With the added benefits of being able to stop at a station right in (or under) a city centre, minimal turnaround times and a rapid boarding process, these high speed

[1] https://www.researchandmarkets.com/reports/4583619/the-global-commercial-aircraft-market-2018-2028

[2] https://www.reportlinker.com/p06089434/Global-Commercial-Aircraft-Market-By-Aircraft-Type-By-Engine-Type-By-Application-By-End-Use-and-By-Region-Competition-Forecast-Opportunities.html?utm_source=GNW

[3] https://www.flightglobal.com/insight fromflightglobal flight fleet forecasts single aisle outlook 2016 2035/121497.article

[4] https://www.jrailpass.com/blog/maglev-bullet-train

[5] https://www.eesi.org/papers/view/fact-sheet-high-speed-rail-development-worldwide

[6] https://www.zdnet.com/article/what-is-hyperloop-everything-you-need-to-know-about-the-future-of-transport/

Table 3.2: Direct competitors in the same market segment as AirEco's design [4].

Manufacturer	Aircraft type	Catalogue price [USD]	Passengers (1 class)	Cruise Mach	Aircraft ordered
Airbus	A220-300	91.5 million[5]	160[8]	0.78[8]	540[4]
	A319neo	101.5 million[5]	160[8]	0.78[8]	72[4]
	A320neo	110.6 million[5]	189[8]	0.78[8]	3852[4]
	A321neo	129.5 million[5]	244[8]	0.78[8]	3448[4]
	A321XLR	142 million[1]	NDA	0.78[8]	
Boeing	737-MAX7	99.7 million[6]	153[3]	0.785[8]	222[7]
	737-MAX8	121.6 million[6]	178[3]	0.785[8]	2135[7]
	737-MAX9	128.9 million[6]	193[3]	0.785[8]	234[7]
	737-MAX10	134.9 million[6]	204[3]	0.785[8]	483[7]
	Unknown MAX orders	NA	NA	NA	1490[7]
Comac	C919	50 million[9]	168[2]	0.785 (est)[8]	NDA

[1] https://www.iairgroup.com/en/newsroom/press-releases/newsroom-listing/2019/airbus-a321xlr-for-aer-lingus-and-iberia
[2] https://web.archive.org/web/20170616174300/http://www.aspireaviation.com/2011/04/19/comac-c919-threat-overblown/
[3] http://www.boeing.com/commercial/737max/#/design-highlights/
[4] https://www.airbus.com/content/dam/corporate-topics/publications/o&d/ODs-March-2021-Airbus-Commercial-Aircraft.xlsx
[5] https://www.airbus.com/content/dam/corporate-topics/publications/backgrounders/Airbus-Commercial-Aircraft-list-prices-2018.pdf
[6] https://www.statista.com/statistics/273941/prices-of-boeing-aircraft-by-type/
[7] https://www.boeing.com/commercial/#/orders-deliveries
[8] https://customer.janes.com/JAWADevelopmentProduction/Reference
[9] https://www.cnet.com/features/chinas-aviation-future-rests-with-the-comac-c919-aircraft/

trains may very well substitute short-haul flights in the nearby future. For oversea and intercontinental travel however, this remains to be seen as aircraft maintain the advantage of not needing infrastructure along the entirety of the route. Furthermore, due to their relatively low average speed with respect to aircraft, it is expected that the substitutes will not be competitive on the medium haul (1500-4000 [km][7]) and long haul (>4000 [km][7]), which requires aircraft that are able to fly such distances.

3.4. Strengths, Weaknesses, Opportunities and Threats (SWOT)

Table 3.3 presents a SWOT analysis of AirEco in the commercial aircraft market. As can be observed, there are plenty of strengths and opportunities which make entering this market an interesting proposition. The weaknesses and threats, however, are also significant and should therefore be addressed with great care.

3.5. AirEco's Position

Now that the competitors in the market are known and a SWOT analysis has been performed, it is time to consider AirEco's position within the aviation market. As mentioned in Section 3.3, the commercial aircraft market is highly consolidated. As discussed in the Baseline report [1], independent entry of such a consolidated market with high barriers to entry would not lead to a profitable business plan. This is because the market share that can be obtained is relatively low. For this reason, the case is considered where AirEco partners with one of the major players and obtains its market share through them.

Airbus has already announced their solution for hydrogen powered flight by 2035 with their ZEROe project[8]. However, Boeing is a bit more skeptical of full hydrogen aviation[9] by that time. Boeing's focus is on sustainable fuels as they do not believe aircraft will be able to

[7] https://web.archive.org/web/20170221110344/https://www.eurocontrol.int/sites/default/files/content/documents/official-documents/facts-and-figures/coda-reports/study-impact-global-economic-crisis-2011.pdf
[8] https://www.airbus.com/innovation/zero-emission/hydrogen/zeroe.html
[9] https://simpleflying.com/boeing-no-hydrogen-aircraft/

Table 3.3: SWOT analysis of AirEco's design in the aviation market.

	Helpful	Harmful
Internal origin	**Strengths:** • First of its kind. • Proposing a revolutionary solution in terms of sustainability. • AirEco's positioning as a sustainability specialist. • Possible government incentives for opting for a sustainable option. • Adaptability of the aircraft concept.	**Weaknesses:** • Higher operational costs. • Higher up-front cost. • Developments costs are higher due to immature technology. • Feasibility not yet proven. • Requires additional crew training and updated manuals.
External origin	**Opportunities:** • Global outcry for sustainability. • Fast growing air travel. • Regulators involved at an early stage of the development which adds to the credibility of the design. • Growth of short haul routes. • Large demand for aircraft of a comparable size in the next 20 years. • Chosen sustainable fuel source is uncorrelated to oil price fluctuations.	**Threats:** • Passengers may fear flying with such a such a novel propulsion system. • Potential lack of infrastructure for the chosen propulsion system. • Highly consolidated market. • The rise of train-like substitutes. • Low cost carriers might not be interested due to the higher up front and additional operational costs this sustainable concept brings.

fly on only hydrogen in 2035[9]. For this reason, AirEco's adaptability concept (introduced in Section 3.6) could prove to be the perfect solution helping Boeing transition to full hydrogen aircraft by 2050.

3.6. Entry Strategy

AirEco is aiming to have its concept enter into service by 2035. Because of the expected rate of green hydrogen production and the level of infrastructure by that time, it was discussed in the Midterm report [5] that a hybrid configuration (running on biofuel and hydrogen) would be desirable. Also in terms of market entry, these feasibility concerns rule out a full hydrogen aircraft in 2035, as, most likely, there will be no market for it. In terms of sustainability, however, further analysis (provided in Chapter 5) showed that a full hydrogen configuration is in fact more sustainable. For this reason the adaptability concept was brought into life.

The adaptability concept entails an aircraft that enters into service by 2035 as a hybrid configuration, running on both biofuel and hydrogen. By 2050, when the feasibility concerns have been addressed, the infrastructure is more advanced and the production of green hydrogen has increased sufficiently [6], the aircraft will be able to switch over to a full hydrogen configuration, requiring only minor modifications to the engines. This poses a logistical challenge due to the revolutionary way of refuelling the aircraft, which should also be accounted for in the development of the concept. However, it is expected that new companies will arise that will take care of the logistical aspect, i.e. the refuelling and transfer of the tanks between the hydrogen plant and aircraft.

With the adaptability concept, AirEco aims to facilitate and accelerate commercial aviation's transition to hydrogen powered flight as well as provide a solution that can adapt and even become more sustainable over time. The technical details of the adaptability concept will be explained in the following chapters.

4. Revolution to Achieve Sustainability

The mission need statement of this project is to design an aircraft that ensures sustainable air travel. This is inherently tied to the core of AirEco's adaptable design, which allows airlines to fly on two types of renewable energy sources, which is set to revolutionise the aviation industry. While people tend to believe that a radical change is needed to allow for revolution, AirEco achieves revolution through a series of less obvious, but still very much effective, changes. These changes are part of every phase of the mission life cycle, as discussed in Section 4.1, and affect the three pillars of sustainability. Revolution regarding environmental, economical and social sustainability are discussed in Section 4.2, Section 4.3 and Section 4.4 respectively. The overall sustainability assessment of the AirEco aircraft is shown in Section 4.5.

4.1. Sustainability Approach

AirEco's approach to sustainability covers all phases of the mission. This section shortly describes the practices that are taken to ensure sustainability in the design, materials extraction and manufacturing, operations and end-of-life phase.

Design

The largest contribution to sustainability in the design is the adaptable design based on either full hydrogen propulsion or a hydrogen-biofuel mix. Not only does this affect environmental sustainability due to a reduction of emissions and the use of renewable energy sources, but the adaptability offers economical benefits for airlines as well. Apart from that several smaller design choices that affect one or more pillars of sustainability are made, which are discussed in the following sections.

Material Extraction and Manufacturing

As already discussed in the Midterm Report [5], care will be taken to ensure the sustainable extraction of raw materials. This covers all three pillars of sustainability: avoidance of resource depletion from an environmental standpoint, fair prizing from an economic standpoint and avoidance of human rights violation from a social standpoint. Regarding production, the lean manufacturing principle[1] is used to minimise waste and maximise value of the product. Additionally, harmful manufacturing processes (such as processes that work with hazardous fumes or toxic materials) are avoided as much as possible. If there is no other option, suitable protection for workers will be provided.

Operations

The operation phase is governed by the design choices. Emissions are greatly reduced as compared to current aircraft due to the use of biofuel and hydrogen. Several noise reduction technologies are used to comply with regulations and improve social sustainability, these are described in Section 4.4.1, Section 4.4.2 and Section 4.4.3. From an airline perspective, the usage of removable hydrogen tanks (which is discussed in more detail in Chapter 10) improves turnaround time and requires less changes to airport infrastructure. These tanks also allow for easier maintenance as compared to integral hydrogen tanks [7].

End of life

Sustainability in the end of life phase focuses on the economic and environmental pillar. From both standpoints it is beneficial to re-use and recycle as many parts of the aircraft as possible.

[1] https://www.leanproduction.com/

Certain parts such as the engines and the APU can be stripped from the aircraft and re-used for other aircraft or sold. By dismantling the aircraft, parts can be sold to other industries for re-use or material can be recycled. One way of doing this is by selling the decommissioned aircraft to a company that takes care of the disassembling and recycling, such as Aircraft En of Life Solutions [2].

4.2. Environmental Sustainability

Environmental sustainability focuses on preserving planet Earth and conserving natural resources. Two main parts of this for the AirEco aircraft are reducing fuel consumption, mostly done by reducing drag, and reducing emissions. Section 4.2.1 describes the usage of so called 'sharkskin' technology, which aims to reduce the overall drag of the AirEco aircraft. Section 4.2.2 deals with gas emissions and how they contribute to the greenhouse effect.

4.2.1. Sharkskin

A promising way to reduce drag and therefore fuel consumption is the usage of so called sharkskin (or riblets). These are small grooves that can be added to the surface and that are aligned with the flow direction to reduce skin friction drag in turbulent flow due to the generation of counteracting vortices [8]. For airfoils, a drag reduction between 3 - 8 % is achieved based on windtunnel testing, depending on the shape and orientation [8, 9]. From Figure 4.1 and Figure 4.2 it can be concluded that blade type riblets are the most effective in reducing drag. The different riblet geometries are shown in Figure 4.3, Figure 4.4 and Figure 4.5.

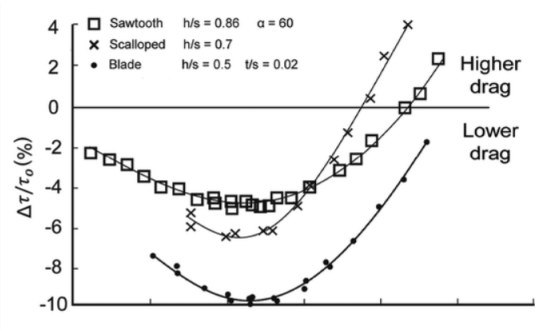

Figure 4.1: Drag reduction effect of different riblets on an airfoil. Drag reduction is presented as negative Δτ/τo (%) values [10].

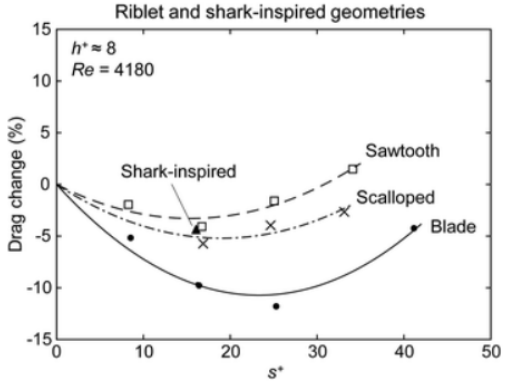

Figure 4.2: Airfoil drag change due to different riblet types [11].

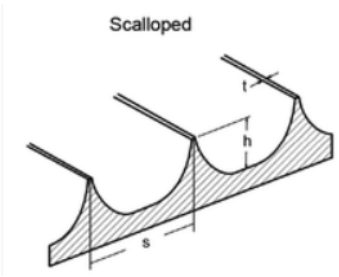

Figure 4.3: Scalloped riblets [8].

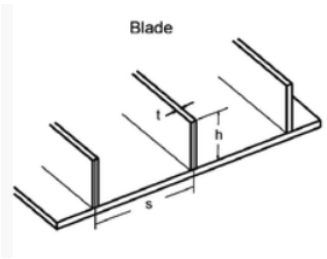

Figure 4.4: Blade riblets [8].

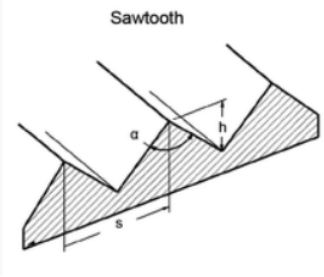

Figure 4.5: Sawtooth riblets [8].

[2] https://aels.nl/

The drag reduction of the entire aircraft is less than that of the airfoil, and is highly influenced by the area covered by riblets. As can be seen in Figure 4.6, the highest drag reduction can be achieved when both the wings and the fuselage are covered, and the drag reduction depends on the angle of attack. About 70 % of the surface area of the aircraft can be covered (as can be seen in Figure 4.7), this excludes for example the windows and the leading edge of the wing and horizontal tail as this interferes with the de-icing system, as well as the riblets not being effective in laminar flow. With this coverage, a total aircraft drag reduction (and with that a fuel consumption reduction) of 2-3% is likely possible for transonic swept wing aircraft [8, 12, 13] over the entire flight.

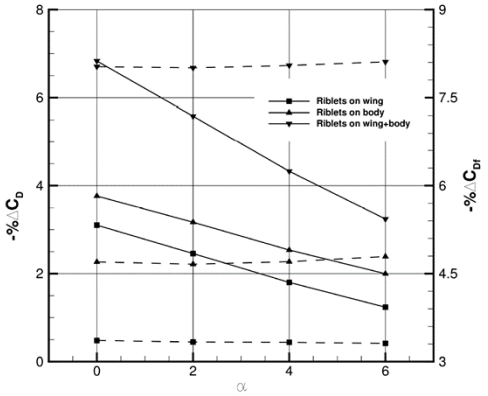

Figure 4.6: Drag reduction effect of riblets [8].

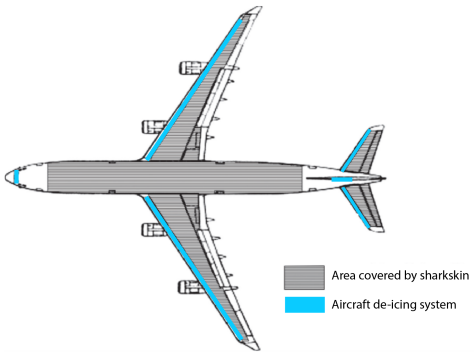

Figure 4.7: Riblet coverage of the AirEco aircraft (adapted from [12]).

Several manufacturing options for this sharkskin technology are being developed, but the most promising is the AeroSHARK technology from Lufthansa Technik[3]. This is an adhesive film that can simply be applied to the surface of the aircraft, which also covers the social sustainability pillar regarding safety and ease of manufacturing. It is resistant against temperature, corrosion and UV. With a weight of 180 [g/m^2] the added weight (approximately 294.8 [kg]) is compensated by the drag reduction. The additional drag due to the added weight of the sharkskin is 0.157%, which is compensated by the expected drag reduction of 2 - 3 %.

Chapter 15 estimates that the fuel cost of the AirEco aircraft ($20269) is around 68% of the direct operating cost for the full hydrogen version ($20269 per flight) and 86% for the hybrid version ($60248 per flight). A reduction of fuel consumption of 2-3% therefore has a substantial influence on the direct operating cost, saving between $400 and $600 per flight for the full hydrogen version and $1200 and $1800 per flight for the hybrid version. No real values for the price and manufacturing of the sharkskin are found, for now an initial estimation of 0.2% of the total manufacturing costs of the aircraft is taken [14], which is equal to $311440.8. With these costs the return on investment of the sharkskin fits within the 1-2 year window as estimated by Lufthansa[3]. The relative minor decision of equipping the aircraft with sharkskin has a significant contribution towards the revolution AirEco is trying to achieve.

4.2.2. Gas Emissions

In order for the aircraft to be more sustainable, emissions need to be decreased, specifically, greenhouse gasses (GHG) . They are the main cause of global warming, which is a massive

[3] https://www.lufthansa-technik.com/aeroshark

issue in today's world. Liquid hydrogen and biofuel were chosen as a way to decrease such emissions. However, to understand the effect of using different fuels, the emissions need to be examined in more detail. Not only should emissions during flight be considered, but also those that occur due to the production of those fuels.

There are four main GHG: Carbon dioxide (CO_2) , methane (CH_4) , nitrous oxide (N_2O) , and fluorinated gases[4]. However, only CO_2 and CH_4 will be emitted from the combustion of the fuels, as will be seen in Section 13.8. Production of biofuel also causes nitrous oxide [15]. These three GHG have different Global Warming Potentials (GWP) , which is a measure of how much a gas warms Earth. CO_2 has a GWP of 1, while CH_4 has a GWP between 28 and 36 and N_2O has GWP between 265 and 298[5], meaning that CH_4 is much worse for the planet than CO_2, but N_2O has an even more detrimental effect on global warming.

During combustion of hydrogen in air, no CH_4 emissions occur as there are no carbon atoms to react with the hydrogen. This also means that no CO_2 products are created. This is very sustainable in relation to today's jet-A fuel, which releases both types of emissions when combusted. However, burning biofuel with hydrogen produces CH_4 since biofuel contains carbon atoms, which will react with the hydrogen atoms in the biofuel itself or with the additional hydrogen atoms provided by the liquid hydrogen. Moreover, CO_2 products are also created when biofuel is added in the fuel mixture because its carbon will react with the oxygen in the air. However, this is much less compared to current aircraft on jet-A fuel. This is partly due to the fact the hydrogen also reacts the oxygen in the air, limiting the oxygen left to react with the carbon atoms in the biofuel. For 20% hydrogen and 80% biofuel, approximately 68488 [kgCO_2e] of GHG are emitted. The method to find this value is explained in Section 13.8. For an aircraft only burning kerosene, it was found that for narrow-body aircraft such as the A321 the average CO_2 intensity is 90 [g] per revenue passenger kilometer [RPK][6]. Note that this does not account for any methane. If comparing it to the range of the hybrid aircraft, as seen in Section 13.2, the CO_2 emissions would be equal to 110592 [kg].

On the other hand, the production of liquid hydrogen may release CO_2 into the air, depending on the type of production method used. Only green hydrogen, where liquid hydrogen is made by splitting water atoms by using a process called electrolysis, does not cause CO_2 emissions. This production method is, however, less common than the steam methane reforming process (SMR) , which releases a lot of CO_2. Over 95% of today's hydrogen is produced in this way. The SMR method is estimated to emit approximately 9.3 [kg] of CO_2 per [kg] of hydrogen produced[7]. It should be noted that green hydrogen will most likely become more common in the future, but by 2030, only approximately 3.4% of the world's hydrogen production will use this method[8][9]. Hence, using liquid hydrogen as a fuel will still cause a lot of GHG emissions. Specifically, 147478 [kgCO_2e] are emitted from producing LH_2 when using 100% hydrogen. If, however, during the lifetime of AirEco's aircraft, the world's green liquid hydrogen production becomes more prominent and the aircraft can fly on only green LH_2, then no GHG are emitted.

[4] https://www.epa.gov/ghgemissions/overview-greenhouse-gases

[5] https://www.epa.gov/ghgemissions/understanding-global-warming-potentials

[6] https://theicct.org/sites/default/files/publications/CO2-commercial-aviation-oct2020.pdf

[7] https://www.forbes.com/sites/rrapier/2020/06/06/estimating-the-carbon-footprint-of-hydrogen-production/?sh=4a40e5a324bd

[8] https://www.environmentalleader.com/2021/01/study-says-global-green-hydrogen-production-to-skyrocket-57-to-2030/

[9] https://renewablesnow.com/news/hydrogen-production-to-surge-by-2030-as-more-countries-embrace-it-720430/

The production of biofuel also causes GHG to be emitted into Earth's atmosphere. It is assumed that the biofuel used on the AirEco aircraft will be biokerosene. One of the ways to create biokerosene is by using the camelina plant [16]. When producing biokerosene from camelina, 47 [gCO_2e/MJ] is emitted. This is the figure for the whole production chain and includes CO_2, CH_4 and N_2O [17]. For the hybrid fuel mixture, the fuel weight is equal to 36976.8 [kg] and biofuel has a specific energy of 43 [MJ/kg] [18]. This results in 26824.4 [$kgCO_2e$] being emitted from biofuel production. Adding the emissions from liquid hydrogen production for the hybrid mixture results in a total emission of 56314 [$kgCO_2e$].

As a comparison, 87.5 [gCO_2e/MJ] is emitted from using jet fuel produced from fossil fuels [17]. No calculations have been made as to how much fuel weight is required for a fully conventional aircraft. However, it is expected to be higher than the fuel weight for the hybrid fuel mixture. With kerosene having a specific energy of 46.2 [MJ/kg][10], the production of kerosene for one flight would result in more than 149478.7 [$kgCO_2e$]. This is higher than the GHG emissions from the production of biofufuels for the two different fuel fractions.

Hence using both a mixture of liquid hydrogen and biofuel or liquid hydrogen alone clearly reduces GHG emissions. Not only in terms of combustion, but also in terms of production of the fuels.

4.3. Economical Sustainability

Environmental sustainability comes at a price, nonetheless, it must be achieved for a project to be fully sustainable and achieve its environmental goals. Therefore, AirEco aims at achieving economical sustainability, through a revolutionary refueling infrastructure, through a highly flexible aircraft, and through the the fuel source itself.

4.3.1. Revolutionary Refueling Process

To achieve economical sustainability, AirEco had to revolutionise refueling. Currently kerosene refueling is rapid and risk-free. However, hydrogen refueling takes significantly longer, increasing turn around time by roughly 5-10% [19]. Additionally, hydrogen refueling when implemented like kerosene refueling requires substantial change to airport infrastructure. Lastly, hydrogen is highly flammable, therefore any spill could be catastrophic, such as the Hindenburg disaster[11]. Therefore a new solution is introduced, one that is economically sustainable for airports and airlines, and that can ensure higher safety.

Various solutions have been identified to address the problems of hydrogen refueling. Some are presented in a study of hydrogen integration at airport [20]. The most conventional solution involves using trucks. However, this is not a viable solution for large airports like Amsterdam Schiphol Airport where on ground vehicle traffic is an issue, and only works in small city airports. Alternatives suggest using pipeline refueling. For example, one concept uses a modified passenger boarding bridge with a hydrogen pipeline to refuel an aircraft with integral tanks, as shown in the left of Figure 4.8. Another solution uses a modified truck to refuel the aircraft through the tail from an underground pipeline system, as shown in the right of Figure 4.8. Although safer, these two cryogenic hydrant refueling concepts, are cost-technically infeasible, as they require a complete modernisation of airports' infrastructure. Furthermore, turn around time is still extensive, unless refueling in parallel with passenger boarding becomes a possibility, which is at the expense of safety.

[10] https://neutrium.net/properties/specific-energy-and-energy-density-of-fuels/
[11] https://www.airships.net/hindenburg/disaster/

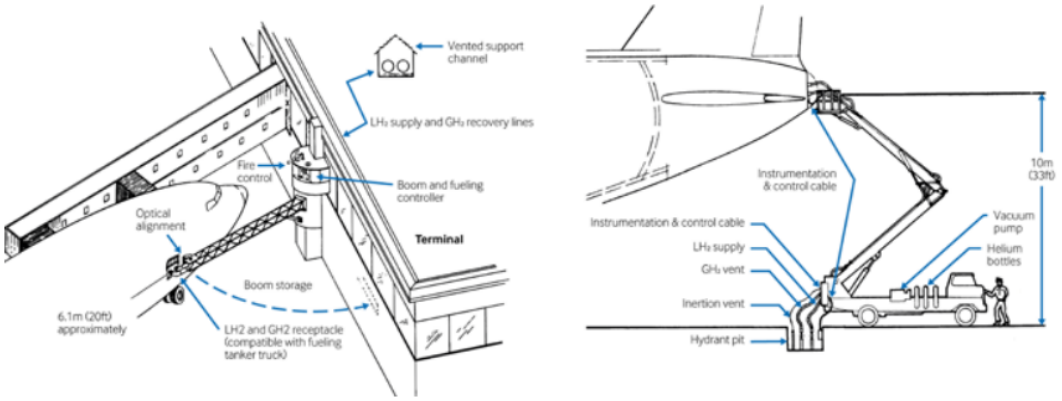

Figure 4.8: Two refueling solutions that utilise hydrogen pipelines [20].

As all these solutions are problematic and fail to be economically sustainable, AirEco revolutionised hydrogen aircraft refueling through its solution. Inspiration was taken from Universal Hydrogen's concept to obtain this solution [12]. AirEco's aircraft will utilise non-integral tanks, which are refueled at an external location and then loaded on the aircraft. This solution is visualised through Figure 4.9. This concept has multiple advantages, such as its compatibility with current airport infrastructure and ground support vehicles. Furthermore, according to Universal Hydrogen, safety is improved, as there are less chances of fuel spilling and thus also less chances of fires. This makes a push towards parallel refueling, and therefore towards reduced turn around times, a large benefit for airlines. Reduced turn around time means lower crew and CAPEX costs [19]. Advantages extend also to maintenance and waste reduction. Maintenance and inspection of integral tanks is deemed to be arduous, due to limited access to the tanks. However, non-integral tanks can be more easily inspected, as they can be taken off the aircraft. Regarding waste, with conventional hydrogen refueling at the airport, significant hydrogen is lost, up to 10% according to Universal Hydrogen. However, non-integral tanks would be refueled at hydrogen refueling stations where the leaked gas can be recaptured, thus reducing waste and costs.

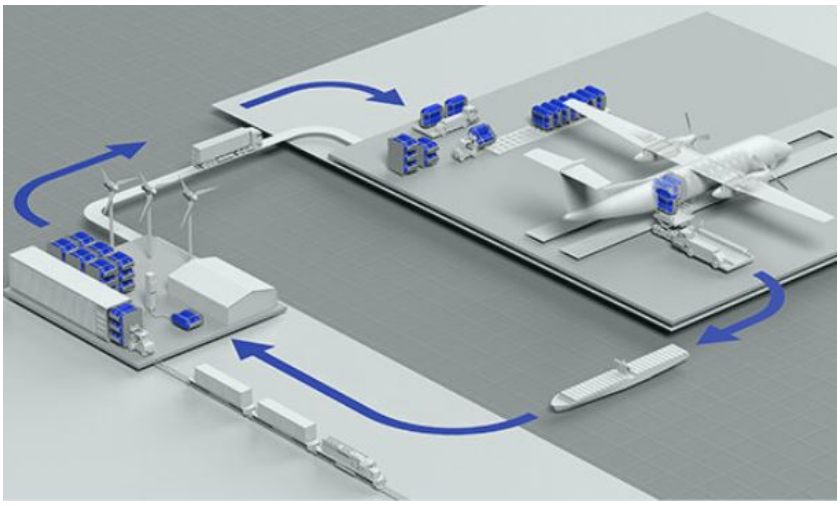

Figure 4.9: Non-integral tank solution proposed by Universal Hydrogen and very similar to the one implemented by AirEco [13]

[12] `https://www.hydrogen.aero/`

There are various other advantages related to this solution regarding fatigue loading of the tanks, but these are explained later. Furthermore, the whole infrastructure and logistics behind this refueling solution is also provided later in Chapter 10. Overall, AirEco's revolutionary refueling solution will ensure that the aircraft is economically sustainable for airlines and airports by improving safety, reducing waste, decreasing turn around time, and bringing minimal to no change to airports infrastructure.

4.3.2. Flexibility in the Energy Source

Airlines seek aircraft which are flexible and can be easily reconfigured depending on the mission. This drives economical sustainability. Therefore, AirEco set a goal to develop an aircraft that can be flown on two types of fuels: a hybrid mixture of biofuel and hydrogen, or 100% hydrogen. The development, as well as the feasibility of this concept, are explained later. For now, focus is put on showing how this revolutionary concept drives economical sustainability.

An aircraft that can fly on two different fuels is flexible, and thus economically sustainable for an airline. According to Dr. Langella, Assistant Professor at TU Delft, engines that can burn both biofuel and hydrogen simultaneously and separately will be very likely by 2035 [21]. With minor modifications, the engine can be converted from hybrid to fully hydrogen. With AirEco's solution, airliners are not required to purchase new aircraft once production of (green) hydrogen ramps up. This provides airlines with ample flexibility for the upcoming energy transition. For example, airlines can keep part of their fleet in the hybrid configuration, allowing them to always fly to remote locations where the required hydrogen infrastructure is unavailable. This innovation widens the possibilities for airliners to operate at more airports than they initially could have with an aircraft powered solely by hydrogen. Additionally, airlines can adapt their fuel decision based on fuel price, significantly reducing profits volatility. All this serves to make AirEco more economically feasible for airlines.

This innovation does not only bring economical sustainability to airlines, but also to AirEco. In 2035, as explained in Chapter 3, a fully hydrogen powered aircraft will not be sustainable as hydrogen prices would be too high due to limited supply, and green-hydrogen production to low to support all the demand. However, a full biofuel configuration is also not a sensible option, as in the long run hydrogen prices are expected to decrease. By 2050 the price of hydrogen will be lower than that of biofuel [19]. Therefore, an aircraft that can fly on both biofuel and hydrogen simultaneously or separately is an aircraft which adapts to the needs of the market, and one that will guarantee prolonged sales. Thus, the aircraft is economically sustainable for AirEco.

4.4. Social Sustainability

The main aspect that is considered regarding social sustainability is aircraft noise. Aircraft noise can have negative effects on the health of local residents, such as sleep disturbance, cardiovascular disease and mental health problems [22]. It is also in the airline's best interest to minimise aircraft noise to comply with current and future regulations. Aircraft noise can be divided in engine noise and airframe noise. For both of these noise reduction technologies are discussed below. It must be noted that the values for reduction given in this section are based on numerical simulations and acoustic testing found in literature. The exact effect of these modifications to the total aircraft noise cannot be given, however at this stage of the design these values are deemed to be accurate enough to take them into account in the engine noise calculation as done in Section 13.7. An additional part of noise that is considered is cabin noise as it can cause passenger and crew discomfort, and should therefore be minimised.

4.4.1. Engine Noise Reduction

Engine noise is caused by two factors: the mixture of exit flow with air and the rotating parts of the engine. One of the main trends in reducing engine noise is the increase of the bypass ratio (BPR). The addition of a layer of fast moving cold air reduces the friction between the hot exhaust and the cold air, which reduces engine noise. Current engines can achieve a cruise bypass ratio of 10 - 12, which will be even larger at the time of AirEco's entry into service [23].

A way to reduce engine noise is the usage of an acoustic liner, which is a sandwich panel that is applied to the inside of the nacelle to dampen engine noise. Several options for this exist, but using zero splice liner such as on the A380 (shown in Figure 4.10) is the chosen option for the AirEco aircraft. By using this a reduction in engine noise of 3 - 5 [dB] can be achieved without any significant weight or drag penalty [24].

A further way to reduce engine noise without any significant weight or drag penalty is the addition of noise reducing chevrons [25]. By adding triangular wedges to the nozzle of the nacelle and the inner core engine (as shown in Figure 4.11), a reduction in effective perceived noise level (EPNL) of 2 - 3 [EPNdB] can be achieved [26]. The effective perceived noise level is defined as the relative noise level of a single aircraft pass-by. This not only takes into account the noise level but also the duration, and it puts extra emphasis on the produced tones in the broadband noise.

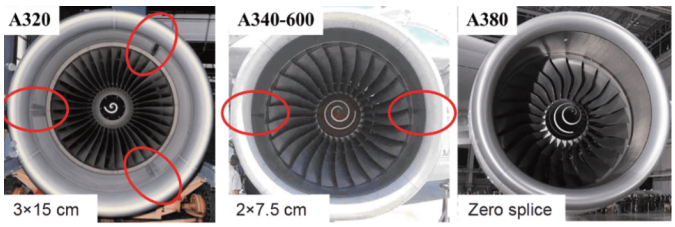

Figure 4.10: Different type of acoustic liners [27].

Figure 4.11: Nacelle with Chevrons [14]

A last thing to investigate regarding engine noise is the difference in produced engine noise when flying on (bio)kerosene, full hydrogen or on a mix between the two fuels, given that the combustion pressure and temperature differ depending on the fuel that is used. According to [28], a reduction in engine combustion noise is achieved when increasing the amount of hydrogen in a mixture of hydrogen and diesel, however nothing is said here about (bio)kerosene or full hydrogen combustion. Furthermore, Funke states that hydrogen combustion creates a lower average noise level, but a higher sound pressure in the frequencies that are critical for human hearing [29]. This leads to the impression that hydrogen combustion is louder, and thus it would be more harmful for local residents. However, this is contradicted by [30] and [31] which state that the engine noise decreases with an increase of hydrogen in a fuel mix. Evidently, more research into this topic is needed to be able to state whether hydrogen combustion is quieter than (bio)kerosene, and what the psychoacoustic effects of both are. It should also be noted that engine noise is the dominant factor for flyover noise only, which means that for take-off and landing the fuel type does not actually influence the sound level of the aircraft that is being heard by local residents.

[14] https://www.nasa.gov/topics/aeronautics/features/bridges_chevron_events.html

4.4.2. Airframe Noise Reduction

Aiframe noise is the noise that is created by the aircraft itself (without its propulsion system), and is caused by air flowing around and over the aircraft. Major contributors to this are the high lift devices and the landing gear.

One of the most dominant parts in generating airframe noise during take-off and landing is the vertical airflow around the edge of deployed flaps. Altering this flow can lead to a reduction in airframe noise, but care has to be taken that any modifications to the flaps will not have any detrimental effects on the performance of the flaps. Windtunnel experiments have shown the effectiveness of flap fences, as shown in Figure 4.12, which can reduce the airframe noise during take-off and landing by up to 3 - 5 [dB] [32]. Furthermore, [33] shows that a drag decrease of up to 1% can be achieved in take-off and climb, however this is based on numerical simulations and wind tunnel tests of a wing model, so the exact effect on a full scale aircraft still has to be analysed. Adding these tip fences leads to additional weight and cost, however this is deemed acceptable based on the sustainability goal.

A second dominant component in approach noise is the landing gear, which accounts for around 30% of the airframe noise during landing [23]. This noise is caused by the interaction of the airflow with the landing gear, which due to its aerodynamic unfriendly shape creates a lot of noise. Research has been done to reduce this phenomena by adding a full fairing to the landing gear but this adds weight and leads to issues with retracting and storing the landing gear. Partial fairings would solve this problem, but the deflection of the airflow towards other components of the landing gear still generates a lot of noise [34].

To deal with this, the TIMPAN project [35] designed a conceptual landing gear that reduces noise without any structural and weight penalties. This is done by adding porous fairings for the brakes and the main struts as can be seen in Figure 4.13, as well as covering up the side stay of the landing gear as seen in Figure 4.14. Results of the study have shown a reduction of landing gear noise of 7 [EPNdB]. The TIMPAN fairing will be added to main landing gear, the wing landing gear and the nose landing gear.

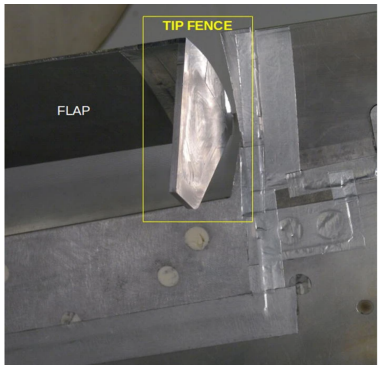

Figure 4.12: Flap fence on outboard flap in windtunnel setup [32].

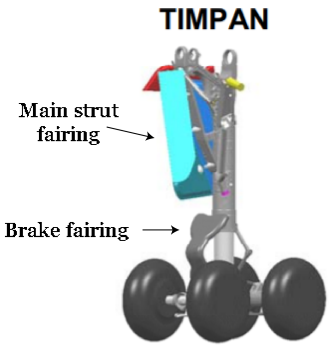

Figure 4.13: TIMPAN landing gear concept [35].

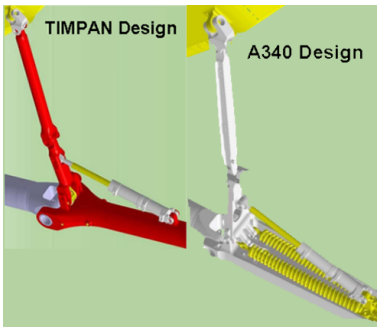

Figure 4.14: Comparison of the TIMPAN side stay [35].

4.4.3. Cabin Noise Reduction

During flight, passengers are subjected to the noise of the aircraft. The material of the fuselage itself provides some transmission loss, however, the noise levels are still quite high. The average has been found to be between 80 and 85 [dB] [36], where 85 [dB] is right on the

limit where harmful noise occurs[15]. Therefore, to keep the comfort and the health of AirEco's passengers in mind, sound absorption material will be used inside the fuselage. The material chosen is tea leaf fibre waste material, which is made from tea leaves. This also tackles another pillar of sustainability, namely environmental, as it is made from waste.

The tea leaf fibre has been shown to have quite good sound absorption coefficient for larger thicknesses of the material. For a thickness of 30 [mm], the sound absorption coefficient range is better compared to smaller thicknesses. Hence, it was chosen to use the tea leaf fibre waste material with a 30 [mm] thickness. This has a sound absorption coefficient range between 0.12 to 0.7 between the frequencies 500 [Hz] and 6300 [Hz]. The overall range of the sound absorption coefficient as a function of frequency can be seen in Figure 4.15. The 30 [mm] variant has a specific weight of 27.5 [kg/m^3]. This means that covering the diameter of the cabin with this material, would only add an additional 341.7 [kg] to the operational empty weight [37]. The sound absorption material should also fit in the fuselage with there being 0.37 [m] between the inner and outer diameter. It should also be noted that the tea leaf fibre waste material is also low cost [37] and hence, it will have a low impact on the cost of the aircraft. Moreover, tea leaves are being investigated as a flame retardant[16]. This suggests that tea leaf fibre waste material is most likely not a flammable material.

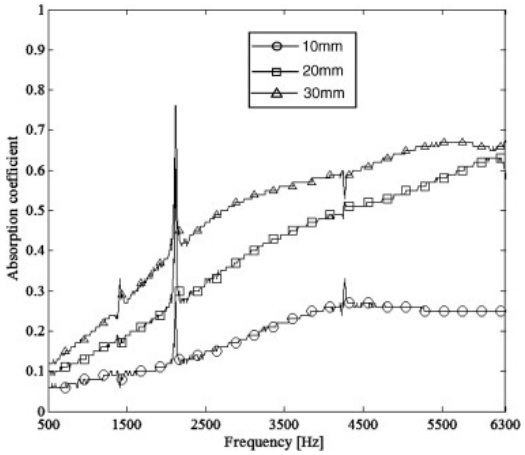

Figure 4.15: Sound absorption coefficient of tea leaf fibre waste material as a function of frequency for different thicknesses of the material [37].

4.4.4. Improved Passenger Comfort

AirEco provides improved passenger comfort through a modern cabin environment. AirEco's cabin is substantially wider that those of competitors, and even of some wide body aircraft. For example, the 777 has a cabin width of 5.87 [m], while AirEco has a cabin width of 6.36 [m], but both have the same seating arraignment (3-4-3 in economy class). Therefore, passenger comfort is superior. The extra cabin width also ensures wider aisles, which facilitate cabin crew, and some of the widest seats in the business. Overall, passenger comfort is superior than that offered by competitors and even than that of long range jets.

Passenger on board AirEco will also enjoy new level of on-board connectivity. All aircraft will be equipped with internet capabilities, enabling passengers to use the mobile devices to send and receive SMS and e-mails, as well as make and receive phone calls. All seats can also be equipped with In-Flight Entertainment (IFE) systems, offering each passenger

[15] https://www.healthlinkbc.ca/health-topics/tf4173

[16] https://letsgetsciencey.com/tea-leaves-fire/

individual screens. Although some airlines already provide these services, AirEco has the goal to make this standard on all aircraft. The latest IFE will also enable passengers to connect their electronic devices to the screen, either through a USB cable or Bluetooth, and utilise that instead of the service provided by the airline. This technology already exists in cars, such as Apple CarPlay and Android Auto, thus implementing it into IFE will not be difficult. The problem of implementing this technology does not stand in the interference of flight-critical services, as Bluetooth device are used today in aircraft during cruise[17], but rather in the fact that airlines often use their IFE as a promotion medium.

The aircraft will make use of satellite connectivity, rather than the more conventionally used air-to-ground connectivity, ensuring a better and faster Wi-Fi connection. For satellite connectivity, one has the option between the cheaper Ku-bands or the faster Ka-bands. As prices are expected to decrease, the Ka-bands are selected, which should also provided a longer life to the product [18]. The aircraft will be reached by an antenna placed in the empennage, while the modem and power supply will be placed in the avionics bay.

Passenger safety on AirEco's aircraft is of first importance, and even more so now in these difficult times. Each aircraft will be equipped with an air filtration system that will ensure the highest level of air quality. AirEco will make use of Airbus Environment Control System (ECS), which uses High-Efficiency Particulate Arrestors (HEPA) filters, to purify the cabin air [19]. These HEPA filters will eliminate 99.9% of particles from recirculated air. The systems renews the air every two to three minutes by constantly expelling 'used' air and exchanging it with fresh air from outside. The result is a cabin with very clean and virus-free air.

4.5. Sustainability assessment

To assess the sustainability of the AirEco aircraft, several aspects that cover all three pillars of sustainability are compared with values from the A321. The comparison is presented in the plot of Figure 4.16. The scoring for the plot is done as follows: the A321 is taken as a baseline and receives a score of 1 for each criteria. The AirEco aircraft (both the 100 % and the hybrid propulsion version) score is then obtained by scaling this with the ratio of the values for each criteria (for example if the production costs are 1.5 times larger for the AirEco, it receives a scored of $1.5 \cdot 1 = 1.5$).

Environmental Sustainability

The two aspect of environmental sustainability that are considered are recycling and emissions. Regarding recycling, the AirEco is expected to perform equal to the A321 due to the AireEco's wings and fuselage being made out of aluminium which can easily be recycled.

A comparison of the greenhouse gas emissions is given in Table 4.1. A distinction is made between the emissions during production (discussed in Section 4.2.2) and in-flight emissions (discussed in Section 13.8), this is to clearly show the effect of hydrogen production in a non-green way. Flying full hydrogen produces no CO_2 equivalent emissions, the produced water vapour is not included here since it has much less contribution to the greenhouse effect as it only stays in the atmosphere for a few days[20].

[17] https://www.britishairways.com/cms/global/pdfs/handheld-devices-used-onboard_Dec14.pdf

[18] https://www.aviationpros.com/engines-components/aircraft-airframe-accessories/cabin-communications/article/21147075/the-wide-world-of-wifi

[19] https://www.airbus.com/aircraft/passenger-aircraft/cabin-comfort.html

[20] https://www.rolandberger.com/en/Insights/Publications/Hydrogen-A-future-fuel-for-aviation.html

Table 4.1: Emission comparison between the A321 and the AirEco aircraft.

	AirEco Hybrid	AirEco Full Hydrogen	A321
Flight emissions [kg CO_2e]	68488	0	110592
Production emissions [kg CO_2e]	56314	147478	149478

Economical Sustainability

The economical sustainability pillar consists of the development & production costs and the direct operating costs. The detailed calculations for these are given in Section 15.2 and Section 15.3. A summary of the values is given in Table 4.2. Note that these values are given in millions, and are calculated per flight. For the development % operating cost the average of the AirEco aircraft the average of the upper and lower bound is taken.

Table 4.2: Cost comparison between the A321 and the AirEco aircraft.

	AirEco Hybrid	AirEco Full Hydrogen	A321
Development & Production Cost	133.05	133.05	89.2
Direct Operating Cost	29705	69684	28494

Social Sustainability

For social sustainability, the noise aspect is considered which is split into cabin, flyover, approach and lateral. A comparison of the values for the AirEco aircraft (calculated in Section 13.7) and the values from the A321 found in literature is given in Table 4.3.

Table 4.3: Comparison of the noise levels between the A321 and the AirEco aircraft.

	AirEco Hybrid	AirEco Full Hydrogen	A321
Flyover noise [dB]	95.46	95.46	91.9
Lateral noise [dB]	93.51	93.51	100.7
Approach noise [dB]	95.6	95.6	100.7

In Figure 4.16 it can be seen that the AirEco aircraft has a better noise performance (regardless of fuel type) and produces much less emissions, especially for the full hydrogen version. This version also has comparable operational costs to the A321. Development & production cost is the only area where the A321 vastly outperforms the AirEco aircraft.

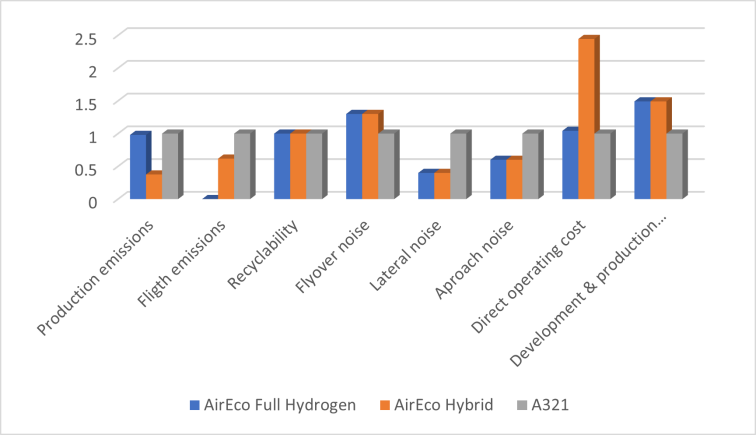

Figure 4.16: Sustainability assessment of the AirEco aircraft as compared to the A321.

5. Initial Sizing

This chapter focuses on the initial sizing of the aircraft. First, a sensitivity analysis is performed to determine the optimal fuel fraction in Section 5.1. Then the iteration process is explained in Section 5.2, and lastly the fuselage layout is provided in Section 5.3.

5.1. Hybrid Fuel Fraction Sensitivity

A sensitivity analysis is performed to verify what the effect of different hybrid fuel fractions on sustainability is. The objective of this sensitivity analysis is to retrieve a fuel fraction for the hybrid configuration that is optimal for all three pillars of sustainability. To quantify each pillar of sustainability, a set of specific aspects that can be easily related and affect a specific pillar are evaluated at various fuel fractions. For example, to address economic sustainability, fuel costs are calculated for a range of fuel fractions.

The environmental pillar of sustainability is quantified through emissions and fuel volume. Emissions include CO_2 and methane. Furthermore, not only operating emissions are considered, but also emissions generated during the production of the fuel. A more detailed description of how the emissions were calculated is given later, in Chapter 13. Fuel volume is also considered to affect the environmental pillar, as a larger fuel volume leads to a larger required tank space, and thus more drag. Figure 5.1 shows the sensitivity of emissions and fuel volume with the hydrogen fuel fraction. As visible from the plot, aircraft with higher hydrogen fractions will perform better with respect to environmental sustainability. Note that the ambiguous decrease in emissions at a fuel fraction of roughly 0.75 is caused by the fact that there are not enough carbon atoms from biofuel that can act with the hydrogen atoms according to the molar ratio, leading to a decrease in methane (CH_4). This is because the carbon atoms do not only form bonds with hydrogen but also with oxygen in the air, which decreases the available carbon atoms. Furthermore, the hydrogen atoms in the liquid hydrogen also react with oxygen. Hence, as the elements forming methane are being used for other chemical reactions and as the ratio between the molecules falls below the required molar ratio to form CH_4, the amount of methane drastically decreases at a fuel fraction of 0.75.

The economics pillar is addressed through fuel costs, maintenance costs, manufacturing costs, and fuel mass. Fuel costs are determined using fuel prices per kilogram, while maintenance and manufacturing costs are determined using regression models that use the aircraft's features as inputs. These models are corrected to account for the use of hydrogen. More detail regarding these cost models and their derivation are provided in Chapter 15. The variations of the economic sustainability aspects with the hydrogen fuel fraction are shown in Figure 5.2. Similar to environmental sustainability, it is more economically sustainable to have a high hydrogen fuel fraction, mostly driven by lower fuel costs due to lower fuel mass required.

Lastly, the social pillar of sustainability is accounted for by considering noise variation. Only airframe noise is considered, as engine noise did not vary with the fuel fraction. Again, more details regarding noise calculations provided in Chapter 13. The variation of the airframe noise with the hydrogen fuel fraction is shown in Figure 5.3. From a social sustainability standpoint, low and high hydrogen fractions fair best.

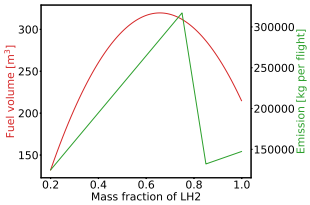

Figure 5.1: Variation of emissions and fuel volume with hydrogen mass fraction.

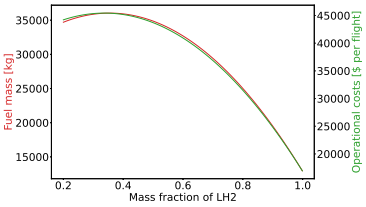

Figure 5.2: Variation of operational cost per flight and fuel mass with the hydrogen mass fraction.

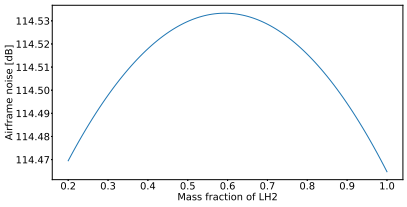

Figure 5.3: Variation of the airframe noise with the hydrogen fuel mass.

Achieving sustainability does not mean excelling in one of the pillars, but rather attaining a balance between all three pillars. Therefore, one must find a global optimum. This optimum does not necessarily minimise all parameters that build up each pillar, but finds a balance where the combination of all aspects is minimised, hence achieving sustainability. The global optimum is performed by superimposing the three pillars of sustainability, by multiplying the aspects that constitute them. The found optimisation parameter, whose variation with the hydrogen fuel ratio is shown in Figure 5.4, has to be minimal for sustainability as a whole to be optimal. With regards to sustainability as a whole, low and high hydrogen fuel fractions yield the best results. This can be explained. When hydrogen increases, the size and MTOW of the aircraft both increase to accommodate for the larger required tank space. However, at a certain point (in this case at a LH_2 mass fraction of 0.6) increasing hydrogen decreases the size and MTOW, as less fuel is required due to hydrogen's higher energy density.

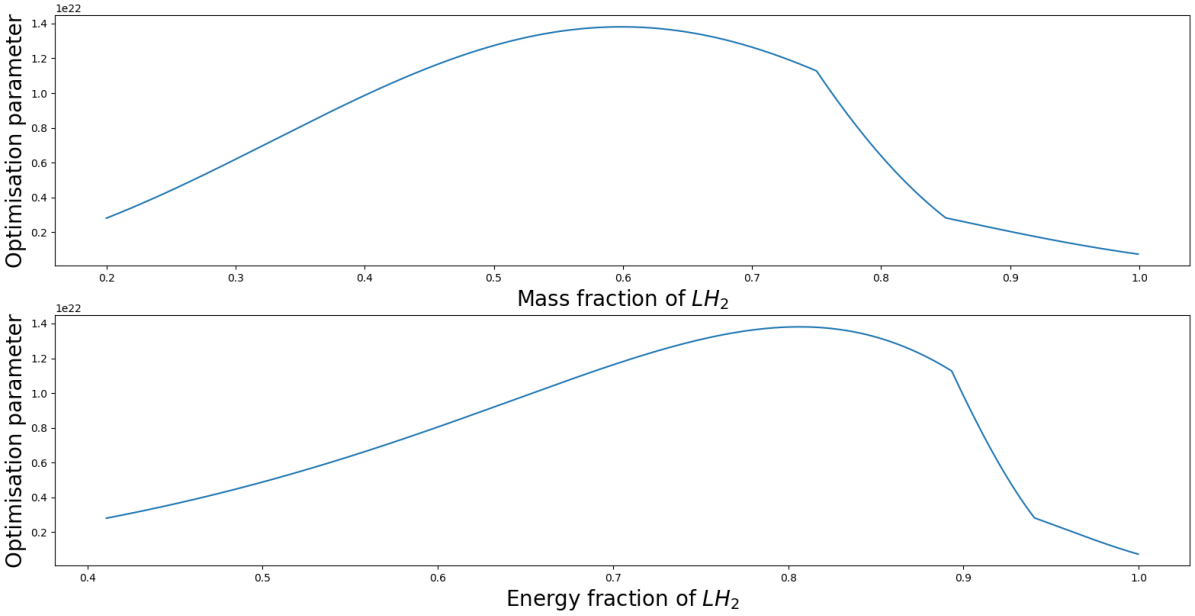

Figure 5.4: Variation of the optimisation parameter with the mass fraction and energy fraction of LH_2.

As stated previously, the goal is to have AirEco fly on two fuel sources: first a hybrid mixture of biofuel and hydrogen, and later 100% hydrogen. Using what is found in in this section, the hybrid configuration will comprise of 20% hydrogen and 80% biofuel when looking at mass. Not only is this ratio optimal for sustainability, but also with its lower hydrogen fraction it gives time for the industry to transition to fully hydrogen, without going for a sudden transition.

5.2. Design Iterations

The design of the AirEco aircraft is an iterative process which considers all subsystems. While a more detailed subsystem description is given in their respective chapter, this section deals with the overall iterative process. The starting point of the iteration is the class I weight estimation, for which the assumptions and method were given in the Midterm Report [5]. With these results, the wing and thrust loading diagrams were created, from which the initial wing sizing was done. These were inputs for the class II weight estimation, again described in more detail in the Midterm Report [5]. This then again serves as an input to the class I weight estimation. The iteration then runs until convergence is achieved, as can be seen in Figure 5.5.

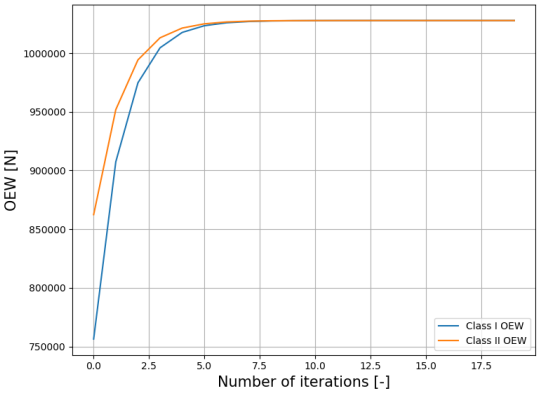

Figure 5.5: Convergence of the design iterations of the AirEco aircraft.

5.3. Fuselage Layout

The fuselage is broken up into multiple sections: the cockpit at the front, followed by the cabin and fuel bay, and lastly the tail cone. AirEco has a fuselage length of 52.54 [m], comparable with the Boeing 757-300[1] and the Boeing 767-300 [2], and a fuselage diameter of 6.73 [m], comparable with the new Boeing 777X[3] and the Boeing 747-8[4]. The large fuselage diameter is chosen to ensure more space for the hydrogen tanks, and hence shorten the length of the aircraft, which otherwise would not fit in the A321 stand. Furthermore, the wide configuration ensures extra comfort and space for the passengers.

The passengers are seated into a 17.5 [m] long and 6.3 [m] wide cabin, in a 10 seats abreast configuration. This is a twin aisle 3-4-3 seating configuration, with 15 rows to accommodate the 150 passengers on board. The double aisle layout will ensure faster boarding times than that of competitors. The cabin is equipped with three lavatories, which is the same as the A320, and two galleys, and it can be accessed from four type-A doors. For emergency evacuation two additional over the wing exists of type-III can be used, for a total passenger certification of 255 passengers. The two extra exits over the wing are required to prevent congestion at the mid-cabin type-A doors. Lastly, for the comfort of the passengers and cruise the cabin and cockpit are pressurised for an altitude of 2500 [m].

Below the cabin there is a cargo hold that can be accessed through a door placed on the right of the aircraft. The cargo hold can store many types of unit load devices (ULD). Up to 12 LD-3 containers can fit in the cargo hold. These are the most commonly used ULDs in Airbus and Boeing wide body aircraft, and are 1.5 x 1.6 x 2 [m] (width x height x depth)[5]. Alternatively, 6 LD-8 containers can be used instead[6]. A schematic of the fuselage cross section over the cabin is shown in Figure 5.6, showing the 3-4-3 seating arrangement and two LD-3 containers.

[1] http://www.flugzeuginfo.net/acdata_php/acdata_7573_en.php
[2] https://www.airlines-inform.com/commercial-aircraft/boeing-767-300.html
[3] https://modernairliners.com/boeing-777/boeing-777-specs/
[4] https://modernairliners.com/boeing-747-8/boeing-747-8i-and-8f-specs/
[5] https://www.searates.com/reference/ld3/
[6] https://incodocs.com/blog/unit-load-device-uld-air-container-specifications/

The hydrogen tanks are loaded in two fuel bays, one on the lower deck and one on the upper deck. The upper fuel bay extends from the cabin, after the bulkhead, for 20.2 [m] and partially into the tail cone. The smaller lower fuel bay begins after the fuselage landing gear compartment, and extends for 12.1 [m]. Both are not pressurised, and each is accessed by a cargo-type door on the side of the aircraft. The two doors are situated on opposite sides of the aircraft, to ensure simultaneous loading of the lower and upper fuel bays. A top and and side view of the fuselage are shown in Figure 5.7 and Figure 5.8 respectively, while a technical drawing of the fuselage is provided in Figure 5.9.

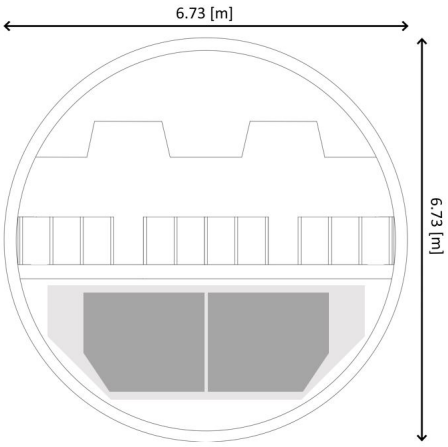

Figure 5.6: Technical drawing of the fuselage cross section.

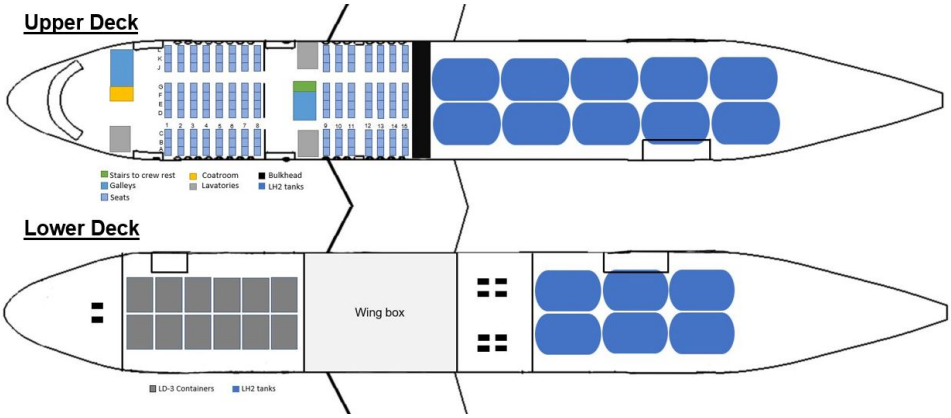

Figure 5.7: Cabin layout of AirEco's aircraft.

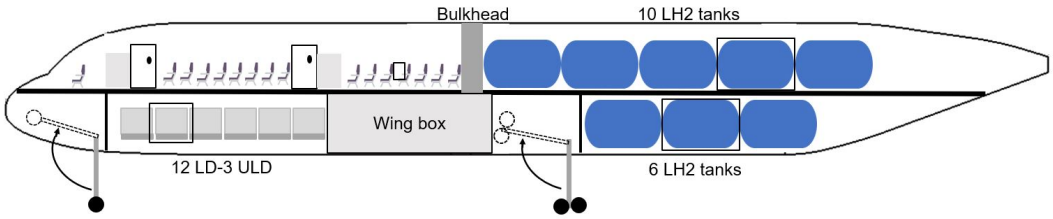

Figure 5.8: Side profile of AirEco's aircraft.

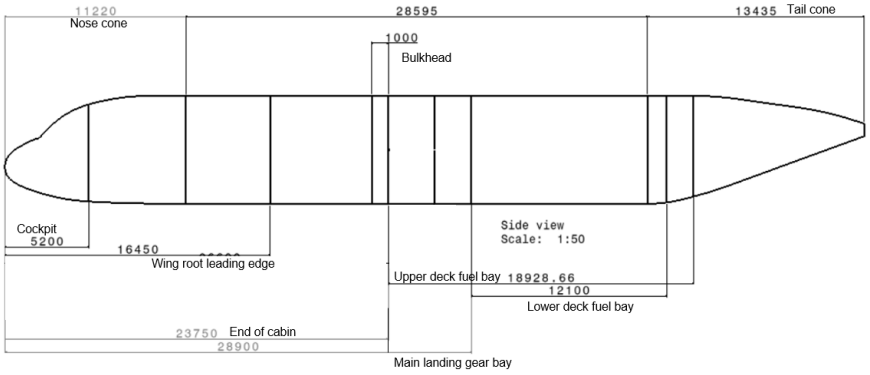

Figure 5.9: Technical drawing of the fuselage with all relevant dimensions expressed in [mm].

6. Aerodynamics

This section describes the aerodynamic performance of AirEco's aircraft. First the airfoil for the wing, the horizontal tail and the vertical tail is selected in Section 6.1. With that, the wing planform is designed in Section 6.2. Several options for winglets are explored in Section 6.3. With all of these components designed, and keeping in mind the effect of the sharkskin as described in Section 4.2.1, the aerodynamic performance is analysed in Section 6.4. The calculations in this chapter are verified and validated in Section 6.5, after which a sensitivity analysis is performed in Section 6.6.

6.1. Airfoil Selection

The first step in the aerodynamic analysis is the selection of the airfoil of the wing. At this stage in the design, an existing airfoil is chosen, as designing an airfoil is costly and requires a lot of testing. From the cruise Mach number of 0.78, it follows that a supercritical airfoil is needed to delay shock waves over the surface. This Mach number also has an influence on how thick the airfoil can be, given by the relation in Equation 6.1.

$$(t/c)\left(\cos\Lambda_{c/2}\right)^2 = \left(\cos\Lambda_{c/2}\right)^3\left(M^\star - M_{dd}\cos\Lambda_{c/2}\right) - 0.115\cdot C_{L,des}^{1.5} \quad (6.1) \qquad C_{L,des} = \frac{1.1\cdot MTOW}{q\cdot S} \quad (6.2)$$

A second important part in selecting an airfoil is the design lift coefficient. The design lift coefficient of the aircraft is calculated using Equation 6.2 and is equal to 0.617. It can then be converted to the airfoil design lift coefficient using the sweep angle of the wing. It is calculated to be 0.628. Care is taken to select an airfoil with a lift coefficient close to the design lift coefficient, as at this lift coefficient the airfoil produces the least drag. In addition, a high maximum lift coefficient and a high stall angle are preferred. The trade-off for the airfoil selection is shown in Table 6.1. The best performing airfoil for each parameter is marked in green. The chosen airfoil for the wing is the NACA-SC(2)0612, with its additional benefit of being designed for a C_l of 0.6, meaning its drag is nearly minimised for our cruise condition. The profile is shown in Figure 6.2.

Table 6.1: Airfoil trade-off table. Note that the preferred value of the parameter is indicated in brackets behind each parameter.

	NPL 9510	SC(2)-0610	SC(2)-0612	SC(2)-0712	Boeing 737 Outboard	Boeing HSNLF
t/c (high)	0.11	0.1	0.12	0.12	0.1	0.108
L/D max(high)	58	70	78	85	95	95
C_L at L/D max (close to cruise C_L)	0.7	0.55	0.55	0.5	0.6	0.45
C_L max (high)	1.4	1.25	1.7	1.7	0.6	0.45
C_D min (low)	0.08	0.08	0.08	0.08	0.08	0.05
C_L at C_D min (close to cruise C_L)	0.25	0.48	0.3	0.25	0.18	0.25
C_L at zero AOA (close to cruise C_L)	0.25	0.5	0.5	0.45	0.18	0.2
Stall Angle (high)	12	11	17	17	17	11
$C_m$at zero AOA (close to 0)	-0.085	-0.1	-0.11	-0.12	-0.02	-0.02
$C_{l,des}$ in drag bucket (Yes)	No	No	Yes	Yes	Yes	No

The airfoil for the horizontal and vertical tail also needs to be chosen. Both of them must be able to provide lift in both the 'positive' and the 'negative' direction (to allow for stability and controllability), which is why a symmetrical airfoil is chosen [38]. Additionally, an airfoil with a large range of angle of attacks, a high stall angle and a high lift curve slope is preferred. Therefore, the NACA 0012 airfoil is chosen and is shown in Figure 6.1.

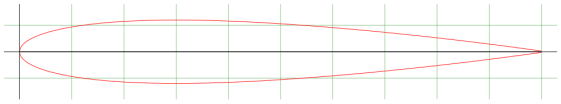

Figure 6.1: NACA 0012 airfoil (data taken from Airfoil Tools[a]).

[a] http://airfoiltools.com/search/index

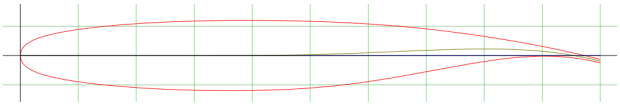

Figure 6.2: NASA-SC(2)0612 airfoil (data taken from Airfoil Tools[a]).

[a] http://airfoiltools.com/search/index

6.2. Final Wing Planform

The values of the final wing planform are given in Table 6.2. The values are obtained with an iterative process, starting with the initial wing sizing as described in the Midterm Report [5]. The values of the aspect ratio, quarter chord sweep and Oswald efficiency factor are estimated based on literature and historical trends from Raymer [39] and Roskam [40]. The assumption of a trapezoidal wing is still upheld, as the addition of a yehudi was not needed to store the landing gear. The aspect ratio has been changed from 8 to 9 as compared to the earlier design that was presented in the Midterm Report to make the wings more slender in order to reduce the induced drag and fuel consumption. An aspect ratio of 9 still meets the requirement on stand size (**AE-OPER-01**) and is also more in line with comparable aircraft such as the A320 and the A321[1].

Table 6.2: Final wing planform parameters.

Parameter	Symbol	Value	Unit	Parameter	Symbol	Value	Unit
Wing area	S	244.23	m^2	Dihedral angle	Γ	7	°
Wing span	b	48.60	m	Root chord	c_r	8.23	m
Aspect ratio	A	9	-	Tip chord	c_t	2.57	m
Oswald efficiency factor	e	0.85	-	Taper Ratio	λ	0.31	-
Leading edge sweep angle	Λ_{LE}	27.67	°	Mean Aerodynamic Chord	MAC	5.89	m
Quarter chord sweep angle	$\Lambda_{0.25c}$	25	°	Spanwise position of MAC	y_{MAC}	9.31	m
TE sweep angle	Λ_{TE}	16.27	°	Position of front spar		0.15	x/c
Maximum thickness to chord	t/c max	0.12	-	Position of rear spar		0.60	x/c

The dihedral angle was chosen based on values from literature for a subsonic swept wing shown in Table 6.3. The 7° dihedral angle was verified by the lateral placement of the landing gear and the spanwise placement of the engines, as shown in Figure 7.11.

[1] https://booksite.elsevier.com/9780340741528/appendices/data-a/table-1/table.htm

Table 6.3: Guidelines for preliminary dihedral design. Values are in degrees.

Wing position	Low	Mid	High
Unswept wing	5 to 7	2 to 4	0 to 2
Subsonic swept wing	3 to 7	-2 to 2	-5 to -2
Supersonic swept wing	0 to 5	-5 to 0	-5 to 0

6.3. Winglet Design

Sustainability is a critical component in the design of AirEco's aircraft, as already discussed in Chapter 4. To improve environmental sustainability, care is taken to minimise drag and therefore fuel consumption. Winglets are an important addition to reduce aerodynamic drag caused by tip vortices. The aim is to minimise the lift over drag ratio, especially during cruise conditions, where data is used from different studies based on wind tunnel tests and numerical simulations. Based on the data seen in Figure 6.3 and Table 6.4, the choice is made to go for split scimitar winglets (which can be seen in Figure 6.4) due to these having the best performance at cruise conditions.

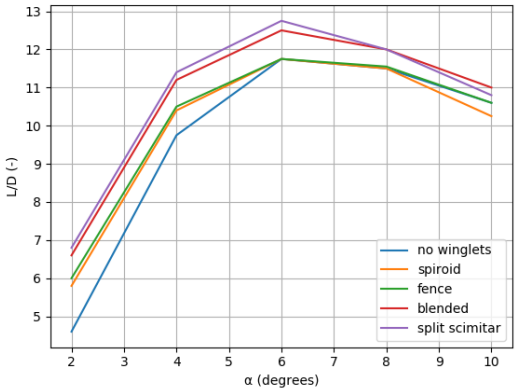

Figure 6.3: Comparison of lift over drag for different winglet designs based on [41].

Table 6.4: Comparison of lift over drag for different winglet designs based on [42].

Winglet Type	CL/CD	Range [km]	% increase
No winglet	37.39	7790.3	-
Blended	38.86	8096.6	3.78
Wing fence	39.07	8140.4	4.30
Spiroid	38.77	8077.9	3.56
Split Scimitar	39.38	8205.0	5.05
Square Spiroid	38.31	7982.0	2.40

To investigate the effect of the split scimitar winglets being added to the wing of AirEco's aircraft, both the wing with and without the winglets was modelled in XLFR5. A comparison between the spanwise local drag coefficient is shown in Figure 6.5. A decrease in local drag coefficient of up to 16.67% is achieved at the wingtips, which leads to an approximate drag reduction of 6% as compared to a wing without winglets and a 3% drag reduction as compared to conventional blended winglets[2]. Detailed structural design of the winglets will be performed in a later design stage. However, it is estimated that the winglet plus the supporting structure add around 212 [kg] to the weight, around 1.1 [m] to the halfspan and have a height of approximately 2.62 [m][3].

[2] http://www.b737.org.uk/winglets.htm#splitscimitar
[3] http://www.b737.org.uk/winglets.html

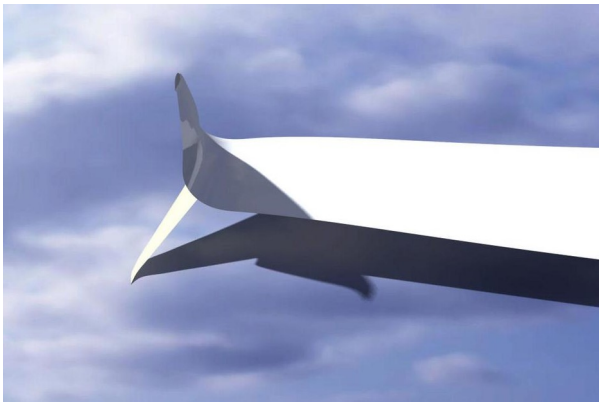

Figure 6.4: AirEco split scimitar winglet.

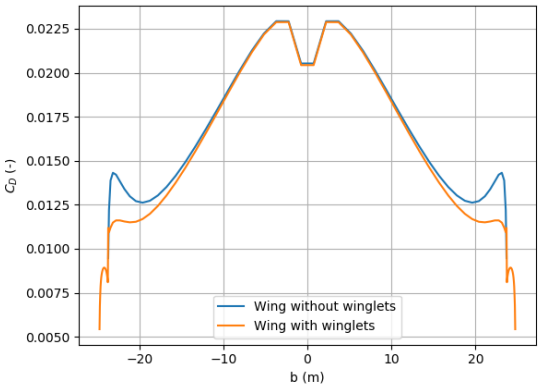

Figure 6.5: Spanwise local drag coefficient for AirEco's wing with and without winglets.

6.4. Aerodynamic Performance

After the airfoil selection and the final wing design, the aerodynamic performance of the aircraft was evaluated. Use was made of the XFOIL[4] and XFLR5[5] software as well as analytical models based on literature.

Lift performance

The lift performance was evaluated with an analytical model based on formulas from the DATCOM and Raymer method. The lift gradient of the airfoil was found to be 6.57 [rad] through XFOIL. Validation of the XFOIL software was already done in the Midterm Report [5]. The lift gradient of the entire wing can then be calculated using Equation 6.3. The airfoil efficiency factor is assumed to be 0.95 here [39].

$$C_{L_\alpha} = \frac{2\pi A}{2 + \sqrt{\frac{A^2(1-\mathrm{M}^2)}{k^2}\left[1 + \frac{\tan^2 \Lambda_{c/2}}{(1-\mathrm{M}^2)}\right] + 4}} \tag{6.3}$$

$$A > \frac{4}{(C_1+1)\cos(\Lambda_{\mathrm{L\,E}})} \tag{6.4}$$

Two important values to calculate are the aircraft maximum lift coefficient and the aircraft stall angle. The maximum lift coefficient is used in the iterative sizing of the wing area and determines if high lift devices are required, and if so, which type. AirEco's aircraft has a high aspect ratio wing, since Equation 6.4 is satisfied (in which C1 is a taper ratio correction factor found in literature [39]), and thus the values are calculated using Equation 6.5 and Equation 6.6. The parameters in these equations are all based on historical data from literature [39], for which trend lines are created in Python to include these calculations in the iterative design process. The values for the maximum lift coefficient and the stall angle, along with the lift curves of the airfoil and the wing, can be seen in Figure 6.6. The maximum lift coefficient is too low to meet the landing and take-off conditions as set by the Performance department. Therefore, high lift devices are required, which are presented in Section 7.2.

$$C_{L_{\max}} = C_{\ell_{\max}} \left(\frac{C_{L_{\max}}}{C_{\ell_{\max}}}\right) + \Delta C_{L_{\max}} \tag{6.5}$$

$$\alpha_{C_{L_{\max}}} = \frac{C_{L_{\max}}}{C_{L_\alpha}} + \alpha_{0L} + \Delta\alpha_{C_{L_{\max}}} \tag{6.6}$$

[4] https://web.mit.edu/drela/Public/web/xfoil/
[5] http://www.xflr5.tech/xflr5.htm

Drag performance

The zero-lift drag calculations are based on the component drag method shown in Equation 6.7, where the subsonic drag of each component of the aircraft is taken into account based on the wetted area, S_{wet}. The local skin friction coefficient, C_f, is either laminar or turbulent depending on the location on the aircraft and the streamwise location. The form factor, FF, for the wing is calculated using Equation 6.8, and for the fuselage and the nacelles of the engine are given by Equation 6.9 and Equation 6.10, respectively. The parameter, f, is defined as the length divided by the diameter for the fuselage and the nacelle. The miscellaneous drag consists of wave drag, leakage drag and protuberance drag caused by antennas, lights and manufacturing defects.

$$(C_{D,0})\,\text{subsonic} = \frac{\Sigma\left(CfFFQS_{\text{wet}}\right)}{S_{ref}} + C_{D_{\text{misc}}} + C_{D_{\text{L\&P}}} \tag{6.7}$$

$$FF = \left[1 + \frac{0.6}{(x/c)m}\left(\frac{t}{c}\right) + 100\left(\frac{t}{c}\right)^4\right]\left[1.34M^{0.18}\left(\cos\Lambda m\right)^{0.28}\right] \tag{6.8}$$

$$FF = \left(1 + \frac{60}{f^3} + \frac{f}{400}\right) \tag{6.9}$$

$$FF = 1 + (0.35/f) \tag{6.10}$$

$$C_D = C_{D_0} + \frac{C_L^2}{\pi \cdot A \cdot e} \tag{6.11}$$

The miscellaneous drag is estimated based on historical data. The total drag of the aircraft can be calculated using Equation 6.11. For AirEco's aircraft, this value is then multiplied with correcting factors for the effects of the sharkskin (2%) and the split scimitar winglets (3%) as described before. The final aerodynamic properties for cruise, landing and take-off are given in Table 6.5. Note that the increase in drag during take-off and landing is caused by the deflection of the high lift devices, which is 20° and 50°, respectively, and the deployment of the landing gear. Additionally, the airfoil and wing lift curve is given in Figure 6.6 and the aircraft drag polar is given in Figure 6.7.

Table 6.5: Aerodynamic properties for cruise, landing and take-off.

	$C_{L,max}$	C_D	$C_{D,0}$	**L/D**	**Re**
Cruise	1.650	0.0325	0.0178	18.97	$30.09 \cdot 10^6$
Take-off	2.035	0.195	0.136	10.43	$10.02 \cdot 10^6$
Landing	2.422	0.399	0.269	6.0704	$9.35 \cdot 10^6$

Looking at the values from Table 6.5, AirEco's aircraft achieves excellent lift over drag performance during cruise thanks to its low zero-lift drag and induced drag. The drag coefficient of AirEco's aircraft during cruise is 1.5% lower than the simulated drag coefficient of the A321 [43], partially credited to the effect of the sharkskin and split scimitar winglets.

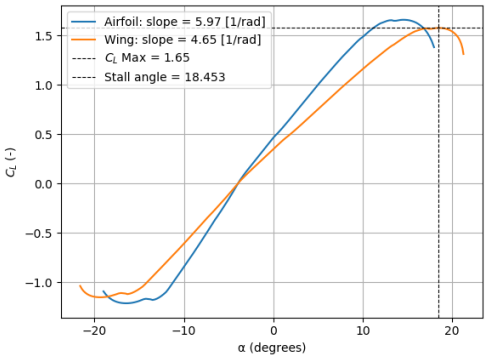

Figure 6.6: Airfoil and wing lift curve at M = 0.78 and Re = 31.2 · 10^6.

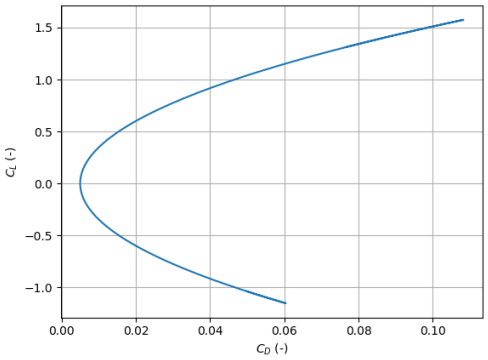

Figure 6.7: Drag polar of the aircraft at M = 0.78 and Re = 31.2 · 10^6.

Moment performance

Another important aspect to consider is the moment coefficient of the aircraft. To ensure static longitudinal stability, a negative change in the pitching moment is required when a positive change in the angle of attack occurs. This means that the moment coefficient gradient has to be less than zero such that the aircraft returns to a stable state when disturbed. Additionally, the moment coefficient at zero lift (which happens at an angle of attack of -4°) has to be positive. The moment curve of the aircraft, created using the XFLR5 software, is given in Figure 6.8 and fulfills all of these criteria. A summary of the aerodynamic properties that have been discussed in this section is given in Table 6.6.

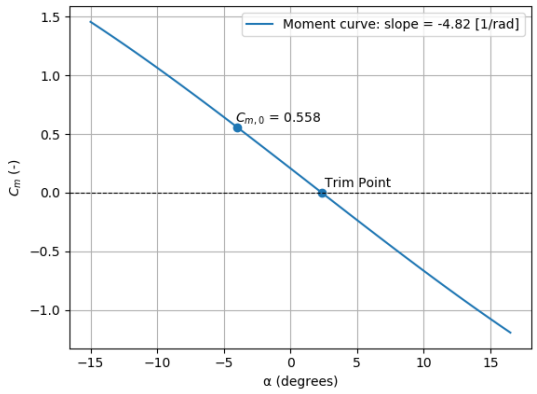

Figure 6.8: Aircraft moment curve at M = 0.78 and Re = 31.2 · 10^6.

Table 6.6: Summary of aerodynamic properties.

Parameter	Value	Unit
$C_{L,des}$	0.617	-
$C_{l,des}$	0.628	-
$C_{L,\alpha}$	4.65	1/rad
$C_{l,\alpha}$	5.97	1/rad
$C_{m,\alpha}$	-4.82	1/rad
$C_{m,zerolift}$	0.558	-
α_{stall}	18.45	°
$\alpha_{zerolift}$	-4	°

6.5. Verification and Validation

Verification of the calculations is done using several unit and system tests. Properties that are calculated by the analytical model are verified using hand calculations, where it is ensured that the maximum absolute error is in range of round-off errors (1 · 10^{-4}). Sanity checks are performed on the calculated values and plots created based on literature. For example, for Figure 6.6, the gradient of the airfoil lift curve slope (5.97 [1/rad]) must be below the theoretical slope of an airfoil of 2π, as derived from thin airfoil theory. Visual checks were also performed on the lift curve and drag polar, ensuring that the lift curve has a positive slope up to the stall

angle and then decreases. It was also ensured that the drag polar has a drag bucket and that the drag coefficient first decreases with increasing lift and afterwards increases.

The wing planform calculations are validated by redoing the calculations with input data from the A321 and comparing the results with literature. The results along with the error calculations are shown in Table 6.7. The input parameters are the aspect ratio and quarter chord sweep of the A321-200, along with an estimated wing loading based on literature. All values are taken from the elsevier database of civil jet aircraft[6]. Considering the differences are all below 1%, the calculations of the wing planform parameters are considered validated.

Table 6.7: Wing planform validation with A321 Data.

Parameter	Literature	Program	Unit	Difference
Surface area	122.40	122.39	m^2	0.0016%
Wing span	33.91	33.90	m	0.029 %
Taper ratio	0.240	0.240	-	0.0 %
Root chord	6.149	6.147	m	0.033 %
Tip chord	1.476	1.475	m	0.067 %
MAC	4.29	4.288	m	0.047 %

To validate the analytical model, which calculated the lift and drag characteristics of AirEco's aircraft, numerical data from the XFLR5 software was used. Since XFLR5 is a commercially available software that has been validated in the past[7], it is not deemed necessary to repeat the validation of this software. The wing with the NASA-SC(2)-0612 airfoil was modelled and simulated under cruise, landing and take-off conditions. A comparison of the numerical and analytical results of the lift curve and drag curve is given in Figure 6.9 and Figure 6.10, respectively. The difference in the maximum lift coefficient and lift coefficient at zero angle of attack is 3.60% and 4.11%, respectively. Additionally, the error in minimum drag value is 2.31%. With both curves matching up well and with the differences being below 5%, the calculations are considered validated.

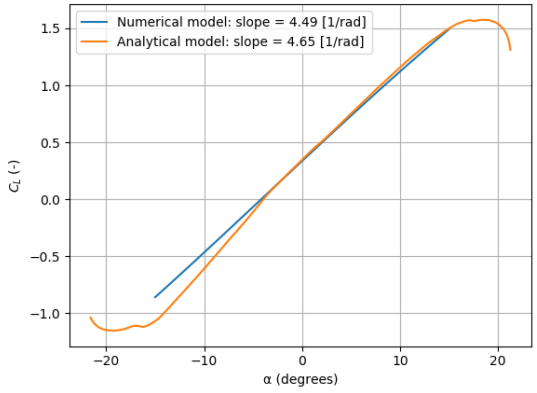

Figure 6.9: Lift curve comparison between the numerical and analytical model at M = 0.78 and Re = $31.2 \cdot 10^6$.

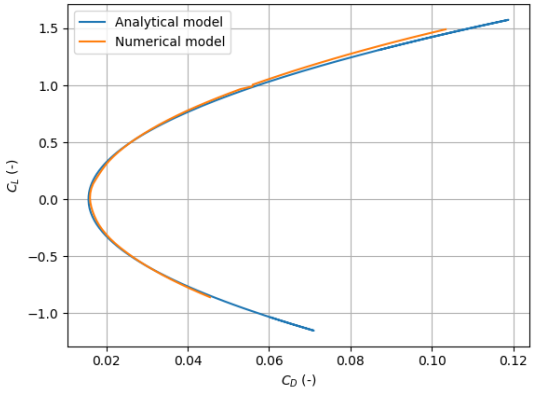

Figure 6.10: Drag curve comparison between the numerical and analytical model at M = 0.78 and Re = $31.2 \cdot 10^6$.

[6] https://booksite.elsevier.com/9780340741528/appendices/data-a/table-1/table.html
[7] https://www.mh-aerotools.de/airfoils/jf_validation.htm

6.6. Sensitivity Analysis

Several assumptions were taken in the design of the wing, and several parameters, such as the sweep angle, aspect ratio and dihedral angle were assigned a certain value based on literature and historical data. The effect of changing one of these values (within acceptable bounds to be still compatible with the rest of AirEco's design) on the lift distribution and lift over drag ratio is shown in Figure 6.11 and Figure 6.12. The values that change between the different lines are shown in Table 6.8. This table also shows the Root Mean Squared Error (RMSE) for each change for both plots. The RMSE shows the error between the two models, and is calculated using Equation 6.12, where n is the amount of data points, y_i is the values for the normal AirEco wing and $\hat{y}_i$ is the values for the modified wing. The low RMSE values indicate that the aerodynamic analysis is not sensitive to changes in assumed values, as long as these values stay within a reasonable bound (completely removing the wing sweep will have a much larger effect on the performance for example, but this is not realistic as AirEco's aircraft would not be able to fly at M = 0.78 with unswept wings).

$$RMSE = \sqrt{\frac{1}{n}\sum (y_i - \hat{y}_i)^2} \tag{6.12}$$

Table 6.8: Results of the aerodynamics sensitivity analysis.

	Leading edge sweep [°]	A [-]	Dihedral angle [°]	RMSE lift distribution	RMSE L/D
Normal	27.7	9	5	-	-
Less sweep	20	9	5	0.019	0.504
Less aspect ratio	27.7	8	5	0.023	1.481
More dihedral	27.7	9	7	0.0	0.0

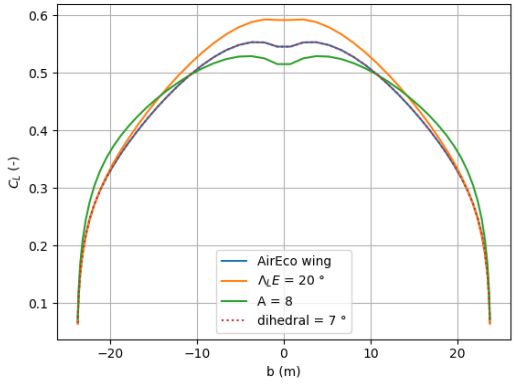

Figure 6.11: Comparison of spanwise lift distribution at M = 0.78 and Re = 31.2 · 10^6.

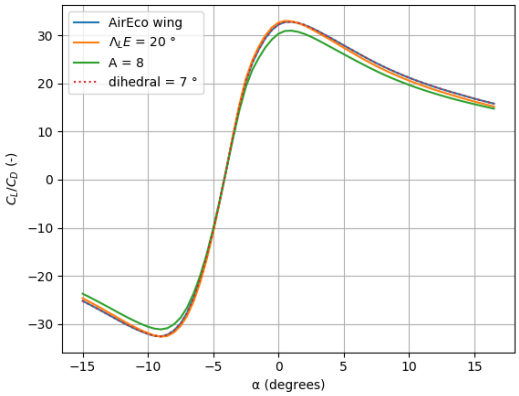

Figure 6.12: Comparison of C_L/C_D at M = 0.78 and Re = 31.2 · 10^6.

While the aerodynamic analysis is not very sensitive to changes in wing planform parameters as long as they are within reasonable bounds, changing certain general aircraft parameters definitely has a large influence on the aerodynamic design and performance. Such parameters include Mach number, cruise altitude, MTOW and wing loading. The effect of changing these values is given in Table 6.9.

Increasing the Mach number while keeping all other values constant leads to a decrease in the design lift coefficient of the airfoil and wing, with no change in wing planform parameters. However, as shown in Equation 6.1, a higher Mach number limits the thickness of the airfoil. For M = 0.85, a thinner airfoil than 12% is required which means the entire airfoil selection process and wing design has to be redone such that the aircraft can fly. Decreasing the cruise

altitude has a similar effect; it leads to lower lift coefficient values which means a different airfoil can be selected that is optimised for those values.

Increasing the MTOW by 50% leads to an increase in wing planform dimensions. The surface area increases by 50%, which is logical considering it is calculated using the wing loading which is kept constant. Because of this constant wing loading, the lift coefficient values also do not change. Increasing the wing loading by 50% decreases the surface area and increases the design lift coefficient of the airfoil and wing. There is a limit as to how much the wing loading can be increased, as this also effects the take-off and landing distance. Furthermore, the obtained values for the lift require a different airfoil selection. To provide this lift coefficient, a thicker airfoil would be needed. However, this leads to issues with the critical Mach number, so the aircraft would have to fly at a lower speed to avoid the formation of shock waves. This massively increases the drag and could stall the wing, making control surfaces ineffective. Another option is to further increase the sweep angle, though this decreases the lift produced by the wing and would require a redesign of the wing (and with that a new structural analysis on the wing box).

Table 6.9: Effect of varying aircraft parameters on aerodynamic design and performance.

	AirEco	**M = 0.85**	**h = 9000 m**	$1.5 \cdot$ **MTOW**	$1.5 \cdot$ **Wing Loading**
S [m^2]	257.6	257.6	257.6	386.40	171.733
b [m]	48.15	48.15	48.15	58.97	39.31
MAC [m]	5.838	5.838	5.838	7.15	4.76
C_L design	0.617	0.516	0.447	0.617	0.938
C_l design	0.628	0.524	0.455	0.628	0.955

7. Stability & Control

The aim of this chapter is to elaborate on the subsystems that ensure the stability and control of the design. Section 7.1 explains the revolutions that were sought after in the department. Section 7.2 is concerned with the mobile surfaces on the wing while Section 7.3 focuses on the loading diagrams and wing placement. Longitudinal and lateral stability are treated in Section 7.4 and Section 7.5 respectively. The placement of the landing gear is presented in Section 7.6. Lastly, Section 7.7 contains the verification and validation and Section 7.8 performs a sensitivity analysis.

7.1. Revolution in Stability and Control

As with all aspects of the design, revolutionary ideas were sought out to improve the sustainability of the aircraft. A literature study was conducted on non-conventional ways of controlling commercial aircraft. A master thesis by Geleyn [44] found that there were no feasible or beneficial alternatives for pitch and yaw control. Roll control could be done with other control surfaces on the wing however the results in fuel savings were ”not revolutionary” and the profitability was deemed ”debatable”.

For the configuration of the empennage, the V-tail was researched further. In theory the combined yaw and pitch control should allow for a smaller total tail surface area [45]. However due the the one engine inoperative requirements and the fact that AirEco's design has wing mounted engines, the V-tail has to be oversized which negates the original benefits of having a smaller tail [46]. The reason for this oversizing is that fact that during one engine inoperative, both of the 'ruddervators'[1] are occupied with providing enough yaw to keep the aircraft flying straight. To still have pitch authority in this case the tail surfaces need to be oversized. Although no actual revolutions were found in stability and control, the Section 7.3 and 7.4 describe how stability and control facilitates revolution in other departments.

7.2. Mobile Surfaces on the Wing

To ensure adequate controllability of an aircraft, the mobile surfaces on the wing must be sized accordingly. The mobile surfaces typically found on a wing are the High Lift Devices (HLDs), ailerons and spoilers. The preliminary design of these three subsystems will be addressed in this section.

The HLDs ensure that the wings of the aircraft are able to generate enough lift during low speed manoeuvres such as take-off and landing. They provide an enhancement to the lift curve that was discussed in Section 6.4, allowing for greater C_L values and flight at higher angles of attack. Designing the HLDs is an iterative process ensuring on the one hand that the take-off and landing requirements are met, while on the other hand leaving enough space for the ailerons.

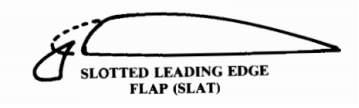

Figure 7.1: Leading Edge HLD [47].

Figure 7.2: Trailing Edge HLD [47].

[1] Combination of rudder and elevator, the control surface on a V-tail

This process converged to a solution where slotted flaps (slats) are used on the Leading Edge (LE) and double slotted flaps along the Trailing Edge (TE). To quantify their effect on the lift curve, three aspects are considered; an increase in $C_{L_{max}}$, a shift in zero lift angle of attack and an increase in C_{L_α}. The first two are defined in Equation 7.1 - 7.2 respectively [47].

$$\Delta C_{L_{max}} = 0.9 \Delta C_{l_{max}} \frac{S_{wf}}{S} \cos \Lambda_{hinge\_line} \tag{7.1}$$

$$\Delta \alpha_{0_L} = 0.9 \Delta \alpha_{0_l} \frac{S_{wf}}{S} \cos \Lambda_{hinge\_line} \tag{7.2}$$

$$C_{L_{\alpha_{flapped}}} = \frac{S'}{S} C_{L_{\alpha_{clean}}} \tag{7.3}$$

Where S_{wf} is the flapped wing area and Λ_{hinge_line} is the sweep angle at the hinge line of the HLD. Both $\Delta C_{l_{max}}$ and $\Delta \alpha_{0_l}$ are specific to the chosen type of HLD and follow from literature [47]. The increase in C_{L_α} follows from Equation 7.3, where S' is the increased wing surface area with flaps extended.

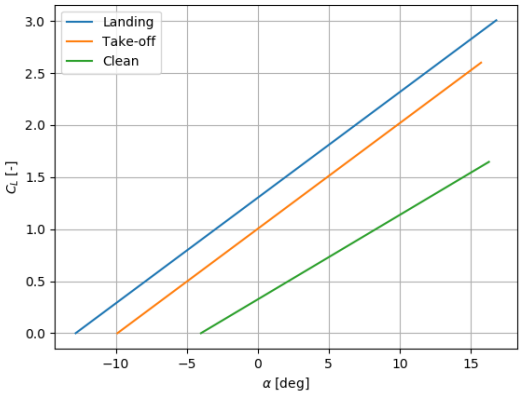

Figure 7.3: Linearised lift curves for landing, take-off and cruise.

With the parameters in Table 7.1, the linearised flapped lift curves can be constructed and are shown in Figure 7.3. Combining the lift curves and the required C_L values for take-off and landing (discussed in Section 6.4), it becomes clear that the angles of attack required are 10.1 [deg] (take-off) and 11.1 [deg] (landing). This puts the aircraft within the typical range of 10-12 [deg][2] and ensures that there will be no tail strike during these operations (Figure 7.4).

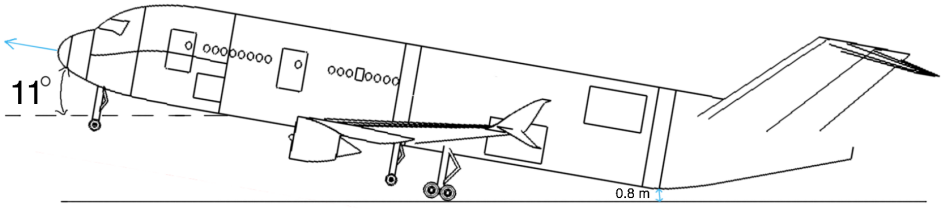

Figure 7.4: Aircraft at critical angle of attack, main landing gear touching down. Sufficient tail clearance is demonstrated.

Concurrently, the ailerons were designed. It is important to define the HLDs and ailerons in such a way that both provide the required performance, while also both fitting on the wing. The required performance for ailerons follows from regulations. For this analysis, the steady state roll requirement specific to the aircraft's class was considered which is equal to banking 30 [deg] in 1.5 [s] [48]. To analyse steady state roll, one must first define the rolling moment coefficient (Equation 7.4) and roll damping coefficient (Equation 7.5).

$$C_{l_{\delta a}} = \frac{2 c_{l\alpha} \tau}{S_{ref} b} \int_{b_1}^{b_2} c(y) y dy \tag{7.4}$$

$$C_{l_P} = -\frac{4 \left(c_{l\alpha} + c_{d_0} \right)}{S_{ref} b^2} \int_0^{b/2} y^2 c(y) dy \tag{7.5}$$

[2] https://simpleflying.com/concorde-angle-of-attack/

Table 7.1: Parameters defining the HLDs for the LE and TE.

Parameter	Symbol	Value	Unit
LE type	-	Slat	-
LE flapped area	S_{wf}	183.7	m^2
LE hinge line sweep	Λ_{hinge_line}	26.6	deg
LE lift coefficient shift	$\Delta C_{l_{max}}$	1.6*c'/c	-
LE chord extension	c'/c	1.07	-
TE type	-	Double slotted	-
TE flapped area	S_{wf}	165.3	m^2
TE hinge line sweep	Λ_{hinge_line}	21.1	deg
TE lift coefficient shift	$\Delta C_{l_{max}}$	1.6*c'/c	-
TE chord extension	c'/c	1.32	-
Take-off α zero shift	$\Delta\alpha_{0_l}$	-10	deg
Landing α zero shift	$\Delta\alpha_{0_l}$	-15	deg
Increased surface area	$S^{'}$	328.1	m^2

Where b_1 and b_2 are the inboard and outboard location of the ailerons and $c(y)$ is the length of the chord at spanwise location y. Both c_{l_α} and c_{d_0} are airfoil parameters discussed in Section 6.1. τ is the aileron effectiveness which is a function of the aileron chord length (c_a) and follows from literature [48]. The steady state roll rate is then defined as Equation 7.6, with δ_a as the maximum aileron deflection. Using the aileron parameters in Table 7.2 and Table 7.3, the roll rate requirement is satisfied.

$$P = -\frac{C_{l_{\delta a}}}{C_{l_P}}\delta_a\frac{2V}{b} \tag{7.6}$$

Table 7.2: Parameters defining the ailerons.

Symbol	Value	Unit
$\delta_{a_{max}}$ up	25	deg
$\delta_{a_{max}}$ down	20	deg
c_a / c	0.25	-
τ	0.53	rad^{-1}

To limit the effects of aileron reversal at high speeds, part of the LE flaps will be replaced by a flaperon. A flaperon is an inboard flap that can operate as an aileron, which has the benefit of being located on a more rigid part of the wing and therefor causing less wing twist when operated. As is typical for large commercial aircraft, it will be located behind the engine [49]. To limit the effects of adverse yaw, the ailerons will be deflected in a differential manner, having more deflection up than down. This means the lift increase in the up going wing is reduced which in turn reduces the induced drag that causes the adverse yaw.

Spoilers are mobile surfaces that sit on top of the wing which can be deployed after landing to induce drag and reduce lift, enabling the wheels to exert more braking force. They can also be used in flight for roll control, but due to their non linear behavior this is not preferred by pilots [47]. Because a conceptual method was missing and a more detailed analysis of landing performance is necessary, the

Table 7.3: Spanwise locations of the mobile surfaces on the wing.

Mobile surface	Start [b/2]	Stop [b/2]
LE Slats	0.18	0.92
TE Double slotted flaps	0.14	0.72
Ailerons	0.74	0.97
Flaperon	0.30	0.40

actual sizing of the spoilers will have to be done in a later stage of the design. In conclusion, Table 7.3 presents the spanwise locations of the other aforementioned subsystems.

7.3. Loading Diagrams and Wing Placement

Before longitudinal stability can be analysed, the range of the center of gravity (c.g.) must be known. To find the c.g. range, use is made of loading diagrams. AirEco's unique challenge was the fact that it had to take into account two radically different operational configurations; both hybrid and full hydrogen. The two configurations inherently come with a significantly different c.g. range because of the locations of both the tank and fuel mass.

Furthermore, AirEco had to consider two loading cases per configuration. Because the hydrogen tanks are fixed during the flight phase, the mass of the tanks can actually be included in the Operational Empty Weight (OEW) [50]. The c.g. range that stems from this assumption will therefore be used for the analysis of longitudinal stability in flight (Section 7.4). During ground operations however, the tanks will be removed and are thus not part of the OEW but part of the fuel mass. For this reason, the c.g. range that stems from this assumption will be used in the sizing of the landing gear (Section 7.6). To find the c.g. of the OEW, use is made of Equation 7.7 in conjunction with Table 7.4, which contain the weights of the subsystems that follow from the Class II weight estimation (Section 5.2).

Table 7.4: Weights and c.g. locations of subsystems making up the OEW weight of the aircraft.

Component	W [kN]	X_{cg} [m]
Fuselage	237.4	22.7
Empenage	29.04	51.7
Fixed systems	91.62	22.7
Wing	124.2	23.7**
Engine	54.81	18.7**
Nacelles	19.26	18.7**
Hydrogen Tank*	101.1/201.1	31.8

*Only if included in OEW, weights noted for hybrid and full hydrogen configuration respectively.
**Found after optimisation described in Section 7.4.

$$x_{CG_{\text{OEW}}} = \frac{\sum_i x_{CGi} \cdot W_i}{\sum_i W_i} \tag{7.7}$$

From these OEWs and their c.g. locations, the loading diagrams are constructed. The loading diagram shows from bottom to top how the c.g. shifts (x-axis) along the MAC with increasing weight (y-axis) by loading different components onto the aircraft. The maximum c.g. range that follows from these diagrams is then taken with a margin of 2% and used for the respective analysis. The loading diagram where the hydrogen tanks are included in the OEW is shown in Figure 7.5, while Figure 7.6 shows the loading diagram for when the tanks are part of the fuel weight. Figure 7.6 presents the critical loading case during ground operations, where tanks are loaded before the passengers and cargo (further elaborated upon in Chapter 10).

It must be noted that the placement of the wing has a profound influence on the shape and range of the loading diagrams. This is mainly due to the fact that moving the wing will result in a different x_{CG} for the wing group, resulting in a different $x_{CG_{OEW}}$. Also because the c.g. range is expressed in MAC from the Leading Edge of the MAC (LEMAC), shifting the wing will essentially move the x-axis. This dependency will be further elaborated upon in Section 7.4.

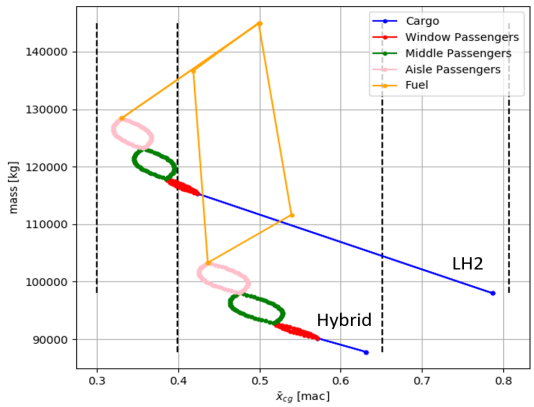

Figure 7.5: Loading diagram for in flight case.

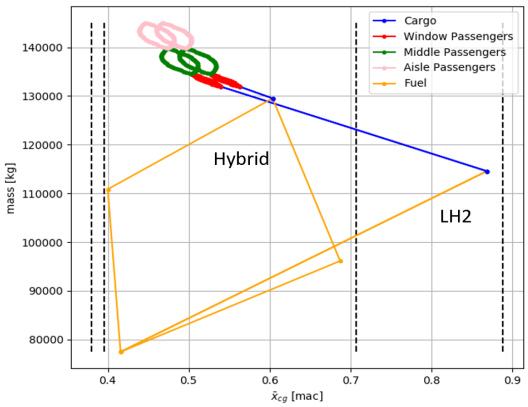

Figure 7.6: Loading diagram for ground operations.

7.4. Longitudinal Stability in Flight

With the c.g. ranges known from Section 7.3, the critical one for flight will be used to do an analysis on the longitudinal stability of the aircraft and perform the sizing of the horizontal tail. The sizing of the horizontal tail is done by means of a scissor plot [45], which combines the c.g. limits set by controllability and stability requirements with the c.g. ranges that follow from the loading diagrams.

During flight, the horizontal tail must allow for stability and controllability. Stability follows from is guaranteeing enough lift so that the neutral point (n.p.) is aft of the center of gravity. The n.p. is the point through which the total lift increase in the case of an increase of angle of attack acts. If the n.p. is in front of the c.g. an increase in angle of attack would lead to a pitch up moment in turn causing an increase in angle of attack which would make the aircraft statically unstable. Secondly the tail should allow for enough authority to trim the aircraft during cruise and rotate the aircraft during take-off and landing. This is the controllability requirement. The stability requirement limits the most aft position of the c.g. while the controllability requirement limits the c.g.'s most forward position.

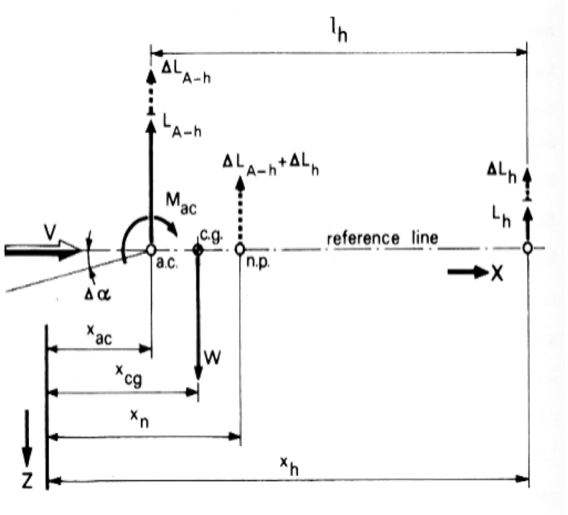

Figure 7.7: Illustration of the neutral point. [45]

The actual location of these limits follows from a derivation solving the moment equation in Figure 7.7 and can be found in Oliviero [45]. Equation 7.8 presents the location of the neutral point as a function of the horizontal tail size fraction (S_h/S). In Equation 7.9 a stability margin (S.M.) is included which is equal to 0.05MAC. Equation 7.10 presents the location of the $\bar{x}_{cg}$ limit for controllability, also as a function of S_h/S.

$$\bar{x}_{np} = \bar{x}_{ac} + \frac{C_{L\alpha_h}}{C_{L\alpha_{A-h}}}\left(1 - \frac{d\varepsilon}{d\alpha}\right)\frac{S_h l_h}{S\bar{c}}\left(\frac{V_h}{V}\right)^2 \qquad (7.8)$$

$$\bar{x}_{cg} = \bar{x}_{np} - \text{S.M.} \qquad (7.9)$$

$$\bar{x}_{cg} = \bar{x}_{ac} - \frac{C_{m_{ac}}}{C_{L_{A-h}}} + \frac{C_{L_h}}{C_{L_{A-h}}} \frac{S_h l_h}{S\bar{c}} \left(\frac{V_h}{V}\right)^2 \tag{7.10}$$

Here, $\bar{x}_{ac}$ is the location of the aerodynamic center, $C_{L_{\alpha_h}}$ is the lift curve slope of the horizontal tail, $C_{L_{\alpha_{A-h}}}$ is the lift curve slope of the aircraft without tail, $\frac{d\varepsilon}{d\alpha}$ is the downwash gradient and l_h is the tail arm. Furthermore $C_{m_{ac}}$ is the moment coefficient in the aerodynamic center, $C_{L_{A-h}}$ is the lift coefficient of the aircraft without tail, C_{L_h} is the lift coefficient of the horizontal tail and $\left(\frac{V_h}{V}\right)$ is the tail speed ratio. Elaborate semi-empirical methods to estimate all of these parameters during conceptual design exist in literature [45] and were applied accordingly.

Several of the aforementioned parameters depend on wing positioning. These are l_h, $\bar{x}_{ac}$, $\frac{d\varepsilon}{d\alpha}$. Hence (as discussed in Section 7.3) it can be noted that shifting the wing has an influence on both the c.g. range as well as the c.g. limits set by the stability and controllability requirements. Through an iterative design process, the wing position X_{LEMAC} was optimised to allow for a minimum horizontal tail size. A small horizontal tail is desirable as it will provide a reduction in drag. Figure 7.8 shows the scissor plot and c.g. range that follow from the optimal wing position. Having obtained reference values for the aspect ratio (A_h), taper ratio (λ_h) and LE sweep (Λ_{LE_h}) of the horizontal tail from literature [51], combined with the surface area (S_h) the horizontal tail is sized and defined in Table 7.5.

Table 7.5: Parameters defining the horizontal tail and wing position.

Symbol	Value	Unit
Configuration	T-Tail	-
S_h	56.17	m^2
A_h	4.5	-
λ_h	0.4	-
b_h	15.90	m
Λ_{LE_h}	35	deg
MAC_h	3.75	m
X_{LEMAC}	21.6	m

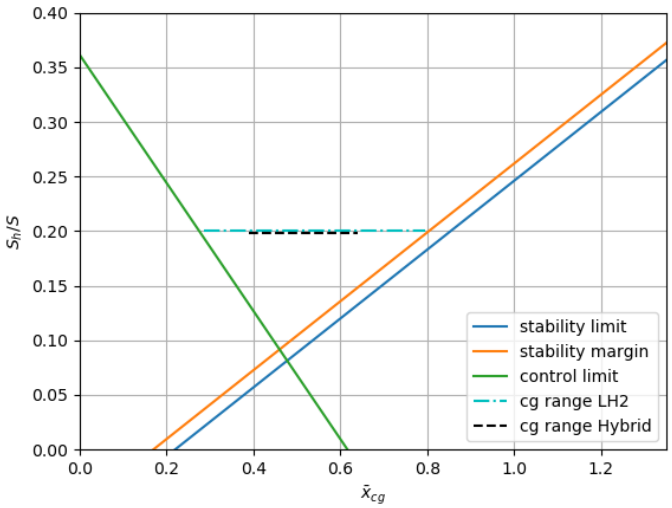

Figure 7.8: Scissor plot for optimal wing positioning showing the c.g. range for minimum tail size.

A remarkable feature of the empennage is the T-tail configuration. The reason for this design choice is that because of the large c.g. range (explained in Section 7.3), a very effective tail is needed to guarantee stability and controllability. The T-tail has the added benefits of having cleaner air (larger V_h/V and smaller $\frac{d\varepsilon}{d\alpha}$) and a larger l_h. From Equation 7.8 and 7.10 it can be observed that these changes allow for a larger c.g. range and thus a smaller tail. The T-tail does come with a weight penalty due to the structure needed to hold the horizontal tail in place. However, this must be taken as necessary drawback as it was found during the design that a conventional tail would simply have to be too large ($S_h/S = 0.4$). A risk inherent to the T-tail configuration is that of deep stall. Early mitigation methods consist of adding 15% to

the horizontal tail size [45], and employing the use of a stick pusher[3]. During the later design stages and aerodynamic analysis of the aircraft, this risk should definitely be addressed further.

7.5. Lateral Stability

When sizing the vertical tail, it is important to understand which flight case will be critical for lateral stability. In the case of wing mounted engines, this is when flying with one engine inoperative [52]. In the one engine inoperative case, the vertical tail in conjunction with the rudder should have enough authority to overcome the moment generated by the thrust differential and keep the aircraft in a straight (side-slipping) flight. The vertical tail size follows from the fast sizing method presented by Roskam [40] which consists of finding the design point in Figure 7.9 and sizing the vertical tail and rudder accordingly. Taking some reference values from Raymer [47] the vertical tail geometry was completed and presented in Table 7.6.

Table 7.6: Parameters defining the vertical tail.

Symbol	Value	Unit
S_v	49.3	m^2
A_v	1	-
λ_v	0.8	-
b_v	6.81	m
Λ_{LE_v}	45	deg
MAC_v	6.84	m

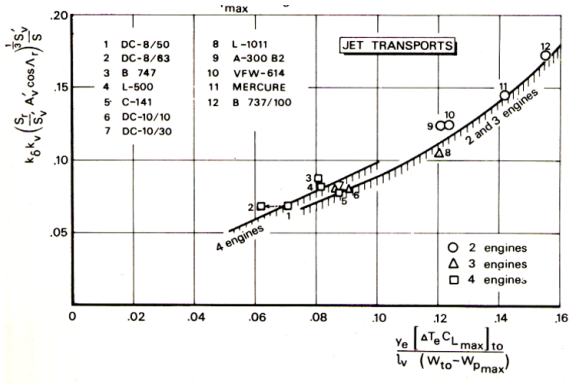

Figure 7.9: Fast sizing method for aircraft with wing mounted jet engines from Roskam [40].

7.6. Landing Gear

To ensure longitudinal and lateral stability on ground, the landing gear has to be designed to meet three requirements. These are as follows:

- The angle between the aft center of gravity and main landing gear should be larger than the tip-back angle. The tip-back angle is 15° [53].
- The arrangement of the landing gear should guarantee that the center of gravity is located inside the triangle formed by the landing gears. This means that the turnover angle should be less than 55° [53].
- The landing gear should allow for at least a 5° clearance angle for the engines [53].

Furthermore, the nose landing gear (NLG) must always carry at least 8% of the weight to ensure on-ground manoeuvrability. Due to the length of the fuselage and the forward location of the aft center of gravity, it was decided to design two sets of main landing gears (MLG): one to satisfy the tip-back angle requirement and one to satisfy the turnover angle and clearance angle requirement. The latter landing gear is placed on the wing (Table 7.7), at the location of the rear spar. The other landing gear is placed on the belly of the fuselage (Table 7.7). Finding the actual locations of the landing gears is an iterative procedure with many constraints as mentioned above. It consists of finding an initial position, then checking if the angle requirements are met and lastly summing the moments around the c.g. to ensure the NLG carries the correct load. The process converged to the landing gear configuration that is presented in

[3] https://www.skybrary.aero/index.php/Stick_Pusher

Table 7.7: Landing gear dimensions.

# NLG wheels	2	# NLG struts	1
# MLG wheels wing	4	# MLG wing struts	2
# MLG wheels fuselage	8	# MLG fuselage struts	2
NGL tire load [kg]	5798.29	NLG/MLG wing wheel outer diameter [m]	0.74
MLG wing tire load [kg]	6160.68	NLG/MLG wing wheel width [m]	0.20
MLG fuselage tire load [kg]	13589.74	MLG fuselage wheel outer diameter [m]	1.02
Wheel pressures [kg/cm2]	11.92	MLG fuselage wheel width [m]	0.30
MLG fuselage strut length [m]	3.54	NLG longitudinal position [m]	3.20
NLG/MLG wing strut length [m]	3.70	MLG wing longitudinal position [m]	23.27
MLG wing lateral position [m]	5.29	MLG fuselage longitudinal position [m]	26.59
Tip-over angle [°]	25	Turnover angle [°]	45.23

Table 7.7.

7.7. Verification and Validation

The conceptual design of the HLDs and ailerons was done using a validated method [49]. To ensure the method was applied properly, unit tests and hand calculations verified all subsystems of the code. In the end, a sanity check was performed by comparing to the mobile surfaces found on the wing of an A320 [4]. Indeed, the spanwise locations of the mobile surfaces were deemed reasonable and comparable to the reference aircraft.

The code for the loading diagrams and scissor plots were adapted from another program which was verified and validated by Pescio [54]. To verify correct implementation of the code, results were compared when putting in the parameters for the Avro RJ85, the aircraft that was used for validation of the original program. One piece of code that still had to be verified was the convergence to a minimum tail size in the optimisation program. This was done by means of inspection of Figure 7.10, which shows the horizontal tail size as a function of X_{LEMAC}. The minimum is indeed at the optimum wing position and the graph has the expected shape. To verify the implementation of the loading diagrams in the scissor plot the loading diagrams were re run with the optimum wing position and the c.g. ranges in both programs were compared.

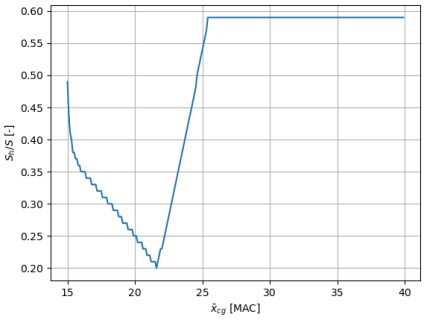

Figure 7.10: Convergence of horizontal tail size to minimum.

The vertical tail sizing followed from the implementation of a validated method (Roskam [40]) and the code was verified using hand calculations. The landing gear design was verified with unit tests and validated by visually checking the results (Figure 7.11 - 7.12) to see if all requirements were met. Furthermore, a sanity check was performed to see if the program would respond the expected way to certain input changes.

7.8. Sensitivity Analysis

Designing for stability and control is a prime example of the iterative nature of aircraft design. For example during the design iterations it became clear that the slightest design alteration in any other department would lead to a resizing of the tail surface areas. This interdependency

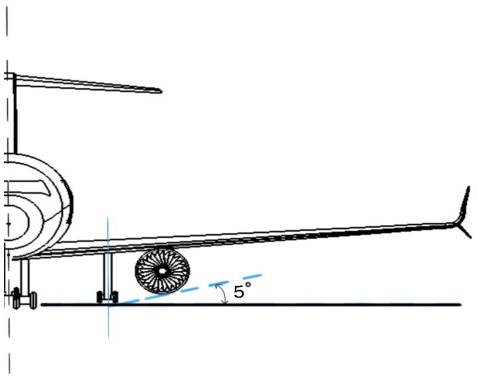

Figure 7.11: Lateral position of the landing gear, clearance angles indicate that the requirements have been met.

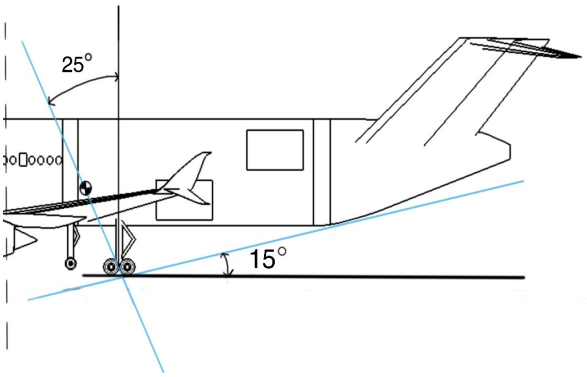

Figure 7.12: Longitudinal position of the landing gear, clearance angles indicate that the requirements have been met.

mainly stems from the fact that all stability and control is closely related to the c.g. location, which changes with virtually any design decision that is made elsewhere. Within the stability and control department, it became clear during the design that wing position had the most profound influence on the sizing of both the horizontal and vertical tail. Because shifting the wing group also leads to a significant shift in c.g. range, the sizing and placement of the landing gear was directly affected by this as well. The design of the fuel bay and fuselage are important processes; as they both influence the tail arm of the horizontal and vertical tail. In Section 7.4, it is also shown that choosing a different tail type has a profound influence on the horizontal tail size. Switching from a T-tail to a conventional tail would lead to a surface area increase of 74%. Lastly, the sizing of the HLDs and ailerons are mainly dependent on the required take-off and landing performance, as well as the available surface area on the wing.

8. Propulsion

Propulsion is a key part of AirEco's revolutionary solution to achieve sustainable aviation. To ensure that the adaptability concept is feasible, it is crucial to have an engine that can run on a hydrogen-biofuel mix as well as on 100% hydrogen without any major modifications to the engine. This chapter deals with the engine design. Instead of designing an engine from scratch, which is costly and too complicated at this stage of the design, an existing engine is chosen. Modifications required to to meet the adaptability goal will be also discussed. Section 8.1 discusses several reference engines, of which one is selected. The required modifications to that engine are discussed in Section 8.2. Lastly, the modified engine model is presented in Section 8.3.

8.1. Engine selection

The engine selection is based on the sea level thrust requirement of 419 [kN]. This follows from the thrust and wing loading diagram presented in the Midterm report [5].

The first engine that was considered is the Kuznetsov NK-88 jet engine that was used by the Tupolev TU-155, the first hydrogen aircraft. With a total take-off thrust of 103 [kN] [55], this engine does not meet the thrust requirements of AirEco's design. However, it does showcase that it is possible to fly on liquid hydrogen.

Two other engines were considered: the Trent 7000 and the General Electric GEnx engine. The Trent 7000 is used on the A330neo, has an 11% better fuel consumption than its predecessor and is 6 [dB] quieter[1]. However, this is a three spool engine, and for AirEco's aircraft, a twin spool engine is preferred, as it is lighter, simpler in design and cheaper to manufacture and maintain[57]. The General electric GEnx engine is the successor of the CF6 engine with GE90 technology. It is used on Boeing 787 Dreamliner, has a 15% better fuel compustion and uses 30% fewer parts than its predecessor, [2]. It has as an additional benefit that in case of damage, the engine core or the fan can be replaced separately instead of having to replace the entire engine[3]. Based on these properties, and being a twin spool engine, the GEnx engine was chosen. In Table 8.1, the GEnx engine parameters are presented.

Table 8.1: General Electric GEnx engine parameters and dimensions [56].

Parameter	Value	Unit
Bypass ratio	8	-
Thrust (TO/Cruise)	296/260.2	kN
Fan diameter	2.66	m
Length	4.70	m
Engine diameter	3.2	m
Dry weight	55.07	kN

8.2. Engine modifications

With the engine selection done, several modifications have to be made to the engine to ensure that it can run on both a hydrogen-biofuel mix and on 100% hydrogen with the highest possible efficiency. This section describes these modifications, as well as their effect on performance and their feasibility.

[1] https://www.rolls-royce.com/products-and-services/civil-aerospace/airlines/trent-7000.aspx#/

[2] https://www.geaviation.com/commercial/engines/genx-engine

[3] https://youtu.be/S1ahHWXGx5Y

It is believed to be possible to have an engine in 2035 that can burn hydrogen and biofuel simultaneously and separately [21]. This view is also supported by the Enable H2 project[4]. However, burning hydrogen increases the flame temperature which leads to higher NO_x emissions. The increased flame speed and temperature due to hydrogen might also lead to unstable combustion and excessive temperatures in the engine, respectively. It is therefore needed to increase the cold airflow and decrease the fuel injection speed when switching from the hybrid-biofuel mix of 80/20 to full hydrogen combustion.

A second modification to reduce NO_x emissions is to ensure lean premixed (LP) combustion. However, this might cause issues regarding flashback. This is the phenomenon in which a flame travels back into the burner, resulting in catastrophic thermal damage to the combustor components[5]. Flashback is more likely to occur when using hydrogen due to its combustion velocity being 4 times as high as (bio)kerosene [58]. Flashbacks can occur in many ways, and there are several modifications to the GEnx engine needed for its mitigation [59]:

- Flashback due to the flame getting too close to the boundary layer: this can be avoided by increasing the air that is injected in the boundary layer.
- Flashback due to the flame travelling too fast: this can be solved by setting the combustor to a low swirl number which leads to a more stable combustion .
- Flashback due to all hydrogen upstream igniting: this is solved by increasing the mass flow rate of hydrogen.

These modifications are all applied to the GEnx engine. Per the advice of Langella [21], the engine is designed for 100% hydrogen with a safety margin applied to the properties of the engine, such that it can be safely operated on a biofuel-hydrogen mix.

The thrust an engine can produce is limited by the amount of heat the turbine can withstand. Hence, in order to push the limits of the engine, advanced cooling methods are considered. The heat exchanger technology used to cool down the engine turbines is inspired from the AHEAD hybrid engine cooling system. The AHEAD engine uses cryogenic liquefied natural gas to cool down the high pressure turbine blades, which has a positive effect on the turbine efficiency (10% increase when compared to bleed air cooling) [60, 61, 62]. As shown in Figure 8.1, liquid hydrogen is heated up to a gaseous state by the exit bleed air of the high pressure compressor where it is used to cool down the bleed air entry of the high pressure turbine.

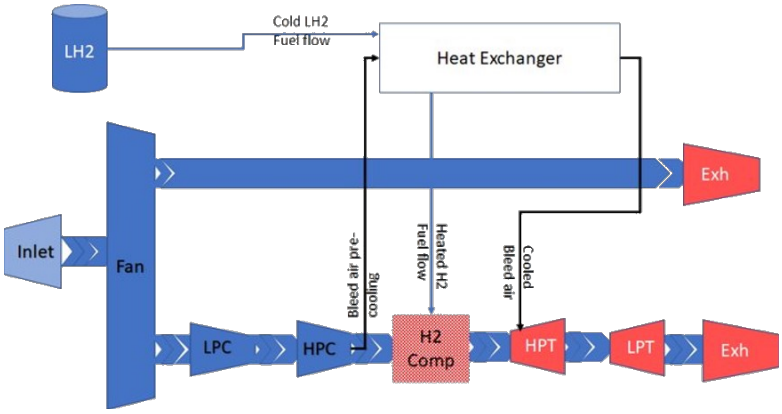

Figure 8.1: Integration of Engine cryogenic bleed air cooling system CBACS.

.

[4] https://www.enableh2.eu/technologies/
[5] https://youtu.be/S1ahHWXGx5Y

8.3. Engine Model

To calculate the engine performance when using a biofuel-hydrogen mix and full hydrogen combustion, a gas turbine model is made.

8.3.1. Assumptions

The calculations are based on the Joule-Brayton cycle in which atmospheric air is compressed, heated through the combustion chamber, expanded and ejected into the atmosphere [57]. For the gas turbine, the cycle is assumed to be ideal. The following simplifications are made:

- Compression and expansion processes are isentropic.
- The gasses are considered to be ideal, and the composition and specific heat values C_p and C_v are taken at atmospheric conditions.
- The kinetic and potential energy between the various component inlets and exits is ignored.
- The engine cycle model is treated as an open cycle, where the atmosphere is assumed to cool down the exhaust gases at the inlet.
- Any pressure losses that can occur in the connections between the engine components, the combustion chamber, the inlet and the exit of the engine are ignored.
- A constant mass flow is assumed.
- The mechanical losses that can occur during the power transmission between the expansion and compression processes are ignored.

With these simplifications, a preliminary gas turbine evaluation was done on both the hybrid and the full hydrogen option.

8.3.2. Preliminary Engine Model Calculations

Table 8.2 and Table 8.3 contain all the inputs used to start the calculations for the model.

Table 8.2: Gas and atmosphere parameters for engine model [57].

Parameter	Symbol	Value	Unit
Altitude	h_0	0	m
Ambient pressure	P_0	101325	Pa
Ambient density	ρ_0	1.225	kg/m^3
Ambient temperature	T_0	288.15	K
Gas constant	R	287	J/kgK
Hydrogen calorific value	LHV_{H_2}	120	MJ/kg
Biofuel calorific value [63]	LHV_{bio}	38	MJ/kg
Air specific heat at constant pressure	$c_{p_{air}}$	1000	J/kgK
Gas specific heat at constant pressure	$c_{p_{gas}}$	1150	J/kgK
Ratio of specific heat for air	κ_{air}	1.4	-
Ratio of specific heat for gas	κ_{gas}	1.33	-

Table 8.3: Final engine characteristics input parameters [60].

Parameter	Symbol	Value	unit
Air mass flow rate	$\dot{m}_{total}$	1471	kg/s
Intake isentropic efficiency	η_{inlet}	0.97	-
Mach number	M	0.78	-
Inlet velocity	v_0	265.4	m/s
Fan pressure ratio	Π_{fan}	1.65	-
Fan isentropic efficiency	η_{fan}	0.93	-
Bypass ratio	BPR	9.4	-
LPC isentropic efficiency	η_{LPC}	0.9	-
HPC isentropic efficiency	η_{HPC}	0.9	-
LPT isentropic efficiency	η_{LPT}	0.91	-
HPT isentropic efficiency	η_{HPT}	0.91	-
High and low speed shaft mechanical efficiency	η_{mech}	0.99	-
Combuster efficiency	η_{cc}	0.99	-
LPC pressure ratio	Π_{LPC}	5	-
HPC pressure ratio	Π_{HPC}	12	-
Nozzle efficiency	η_{nozzle}	0.98	-
Combuster pressure ratio	Π_{cc}	0.96	-
Hydrogen combuster exit	T_{04}	1720	K
Biokerosene combuster exit	T_{046}	1600	K

In Table 8.2, the ambient pressure, density and temperature are given at sea level since the engine is modelled at 0 [m] altitude. Air mass flow rate and inlet velocity in Table 8.3 was calculated using Equation 8.1 and Equation 8.2, respectively.

$$\dot{m}_{\text{total}} = \rho(\pi \frac{D_{\text{fan}}^2}{4}) v_0 \quad (8.1) \qquad v_0 = M \cdot \sqrt{\kappa_{\text{air}} R T_0} \quad (8.2)$$

For the hybrid engine, the calculations were made using an engine with two combustion chambers instead of one for the sake of simplicity. However, AirEco's engine uses only one combustion chamber. It has already been discussed that one combustion chamber works with both fuel options. By using the air-breathing propulsion formulas and the input values in Table 8.2 and Table 8.3, it is possible to calculate the fuel mass flow from the two combustion chambers, the total p ure 8.2.

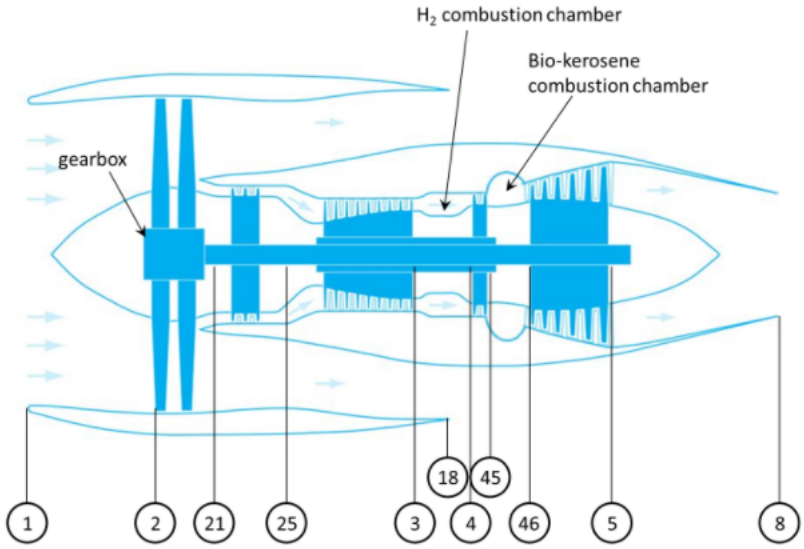

Figure 8.2: AHEAD hybrid engine model [60].

The bypass and core mass flow are calculated using Equation 8.3 and Equation 8.4, respectively. The total thrust depends on whether the fan and core exit nozzles are chocked or not. This is checked by using the critical ratio formula. The fan nozzle exit is choked, hence Equation 8.6 is used. However, the core nozzle exit is not choked, meaning Equation 8.7 is used. Finally, the specific fuel consumption was calculated by using Equation 8.5.

$$\dot{m}_{\text{bypass}} = \text{BPR} \cdot \dot{m}_{\text{core}} \quad (8.3) \qquad \dot{m}_{\text{core}} = \frac{\dot{m}_{\text{total}}}{1 + \text{BPR}} \quad (8.4) \qquad \text{SFC} = \frac{\dot{m}_{LH_2} + \dot{m}_{\text{Biofuel}}}{F_{\text{core}} + F_{\text{fan}}} \quad (8.5)$$

$$F_{\text{fan}} = \dot{m}_{\text{bypass}} \cdot (v_{18} - v_0) + A_{18}(p_{18} - p_0) \quad (8.6)$$

$$F_{\text{core}} = (\dot{m}_{\text{core}} + \dot{m}_{\text{LH}_2} + \dot{m}_{\text{Biofuel}}) \cdot (v_8 + v_0) \quad (8.7)$$

The same calculations are performed on the full hydrogen engine design, which is done with using only one combustion chamber. The output values from the hybrid and the full hydrogen engines are illustrated in Table 8.4 and Table 8.5, respectively.

Table 8.4: Hybrid engine calculations output.

Parameter	Value	Unit
$\dot{m}_{\text{core}}$	141.42	kg/s
$\dot{m}_{\text{bypass}}$	1329.39	kg/s
$\dot{m}_{\text{hydrogen}}$	0.528	kg/s
$\dot{m}_{\text{biofuel}}$	2.19	kg/s
Fuel ratio	4.1	-
F_{Fan}	199998.63	N
F_{Core}	18716	N
F_{Total}	218.72	kN
SFC	12.42	g/kNs

Table 8.5: Full hydrogen engine calculations output.

Parameter	Value	Unit
$\dot{m}_{\text{core}}$	141.42	kg/s
$\dot{m}_{\text{bypass}}$	1329.39	kg/s
$\dot{m}_{\text{hydrogen}}$	0.528	kg/s
F_{Fan}	199998.63	N
F_{Core}	55577.05	N
F_{Total}	255.58	kN
SFC	2.09	g/kNs

8.4. Verification and Validation

The engine model calculations were verified by inspecting and testing the model stage calculations. Unit tests were performed on the engine model stages where inputs were varied and the output results were analysed and checked if they met expectations as found in literature. The verifications that were performed on the output are:

- Core flow pressure is expected to increase after the compression stages and decrease after the expansion stages.
- Core flow temperature is expected to increase after the compression stages and decrease in the expansion stages.
- The exhaust core flow is expected to be more than the inlet due to the addition of the fuel mass flows, which also means fuel mass flows can not be lower or equal to zero.
- The chamber exhaust temperature is expected to always be higher than the high pressure compressor exit temperature.
- The bypass flow is expected to always be larger than the core flow.
- The thrust the engine will provide can not be negative, which also implies to the specific fuel consumption.
- It is expected that by increasing altitude, air mass flow would decrease due to the lower density and temperature and thus thrust and specific fuel consumption.
- It is expected that by increasing the low heating value of a fuel, the fuel mass flow would decrease and thus the thrust and the specif fuel consumption.

Validating the engine model was not an easy job, since data for an existing hydrogen engine was not available. The NK-88 engine used on the TU155 was the only found engine that burned hydrogen, but some parameters about that engine were missing and not enough were found for validation. The model was checked by using the GEnx engine parameters and kerosene LHV of 43 [MJ/kg] to see if it is giving output values close to that of the hydrogen engine. The model resulted in a thrust of 327 [kN] when using the GEnx fan diameter of 2.66 [m] and kerosene LHV of 43 [MJ/kg]. By comparison with the thrust value in Table 8.1, the results are quite similar and the model can be validated. However, the model will need to be further developed to accurately estimate the thrust and the specific fuel consumption when using hydrogen as a fuel.

8.5. Sensitivity analysis

The engine model thrust and specific fuel consumption were the main required outputs and a sensitivity analysis was done to see how they are affected with different design input parameters.

For the full hydrogen configuration, starting the calculations with the GEnx fan diameter, bypass ratio and a lower combustor exit temperature resulted in higher thrust and lower specific fuel consumption. That was also the case with the hybrid configuration. However, it should be noted that the combustor temperature exit for both hydrogen and biofuel remained unchanged. This is because it will affect the fuel flow ratio, which should be kept constant with a ratio of 4:1.

From Table 8.6 and Table 8.7, it can be seen that the thrust is most affected output and the specific fuel consumption did not decrease by a large margin.

Table 8.6: Input and output values for hybrid engine.

	Parameter	Original GEnx	Modified GEnx
Input	BPR	8	9.4
	Fan Diameter [m]	2.66	2.4
Output	Thrust [kN]	305	218.72
	SFC [g/kNs]	12.81	12.42

Table 8.7: Input and output values for hydrogen engine.

	Parameter	Original GEnx	Modified GEnx
Input	BPR	8	9.4
	Fan Diameter [m]	2.66	2.4
	Combuster Temperature Exit [K]	1600	1720
Output	Thrust [kN]	319.9	255.6
	SFC [g/kNs]	1.75	2.088

Further study on the modifications to the injection system for using hydrogen is under progress. By 2035, it is predicted that the technology will be more developed and mature enough for the usage of hydrogen in turbofan engines.

9. Hydrogen Tank

A lot of design parameters are dependent on the concept of the hydrogen tank design because of the non-conventional integration and low density of hydrogen. For preliminary design the first choices that are made on the concept of the tanks mainly takes into account the way of refueling, fitting of the tanks and the placement of the tanks and corresponding systems. The choice between integral and non-integral tanks that is made previously in Section 4.3 is dominant because of the different design philosophies and will be justified first in Section 9.1. When the concept is determined the sizing can begin resulting in the dimensions and weight of the system, this is done in Section 9.3. Afterwards the design of subsystems begins, containing the fuel system (Section 9.4) and the shell design (Section 9.5). All calculations have to be verified, which is done in Section 9.6.

9.1. Concept Design

In the Midterm report [5] a preliminary estimate was made for the amount of tanks and their effect on the length of the fuel-bay section. After some further research now a choice between integral and non-integral tank has to be made and justified. In this case integral tanks mean that the tanks stay in the fuselage for the entire lifespan and are not designed to be taken out and thus refueled on site. Non-integral tanks are replaced, inspected and refilled every flight.

Integral tanks have the benefits of optimising the space that is needed for the hydrogen. Although there is more stress on the tank wall because of a bigger diameter it is lighter as there is less area through which heat can leak, meaning the tank can be kept at a lower temperature. Also there is need for fewer fuel systems, venting connections and piping than for the non-integral tanks. However, a big driving requirement is that the tanks have to be vented in case of a thermal or structural leak. This means the design has to incorporate multiple tanks for redundancy, meaning a deviation from the optimal design. Because the tanks are not designed for replacement the fatigue loading drives the tank wall thickness as the difference in temperature and pressure with every flight is large [7]. Another important aspect to consider is the need for a total new infrastructure for refuelling hydrogen at every airport the aircraft flies to. This includes the piping, storage, refueling and above all safety. Because of the requirement

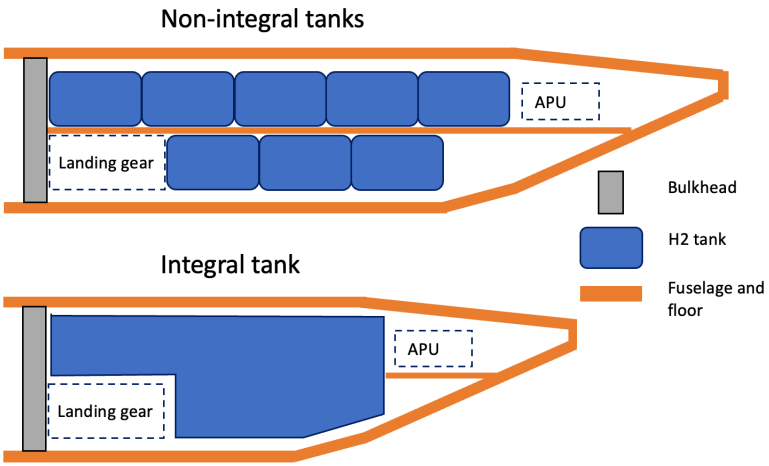

Figure 9.1: Fitting concepts

that the aircraft will be in service by 2035 it will be difficult to certify flying with integral tanks before that time [64].

Integral tanks are replaced every flight like replacing battery packs. Although this takes away the worries about fatigue loading and a new elaborate infrastructure, the fuel bay length increases by a factor of 1.6 as the packing density gets much worse.

The insulation of tanks requires a vacuum [65]. For integral tanks a vacuum pump would be needed to regulate this pressure, which takes up space and adds weight. The vacuum for non-integral tanks can be done in the factory where they are filled. By properly sealing the tanks in the factory there is no need for a vacuum pump system on the aircraft, which saves a lot of weight because it would be needed for every tank.

9.2. Tank Fitting

The tanks can be fitted in the fuselage in different ways. Key aspects are the number of tanks, the alignment of tanks, the implementation of structural integration with the fuselage and the tank door that accommodates for loading. The concepts that are analysed can be found in Figure 9.2. The columns represent a different way of packaging.

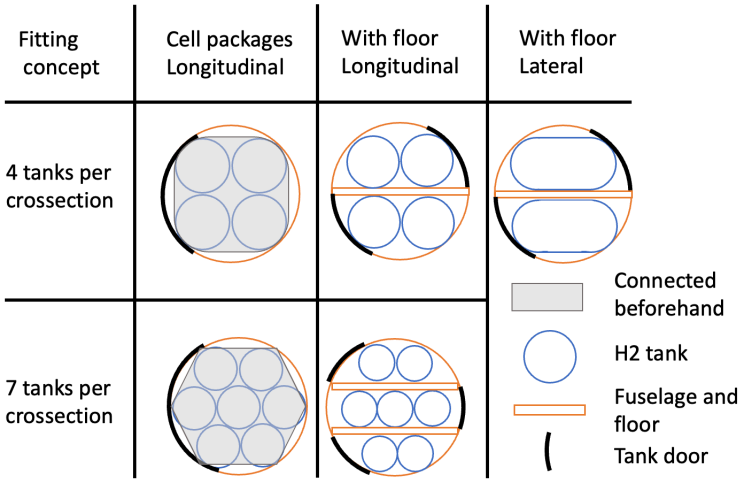

Figure 9.2: Fitting concepts

Cell packages organised in longitudinal direction make up for the first concept, using a structural connection between the tanks in one cross-section before loading it in the aircraft. The benefit of this concept is that the loading time is decreased as all tanks will be connected to the same system, which results in less connections that have to be made. The drawback of this concept is that the loading door has to be larger, which means that the fuselage requires more reinforcement and becomes heavier.

The second way of packing, shown in the second column, comprises loading the tanks longitudinally on an upper or lower floor inside the fuselage. Compared to the first concept, this concept benefits the fuselage structure as the doors can be smaller. In addition, there are no problems with conventional loading vehicles on the airports, as presented in Section 10.3.

The final column of Figure 9.2 presents the concept of packaging tanks that are oriented in lateral direction. This concept benefits the packaging density in the lateral direction. This

concept also provides a benefit with respect to loading the tanks, as the tanks do not have to be turned in the fuselage. This will be further explained in Section 10.3.

The rows in Figure 9.2 present the number of tanks that are packaged inside the fuselage. An analysis is done for four and seven tanks, because these numbers are optimal for the packing density. Using one big tank is omitted, as the loading door would have to be the size of half the fuselage.

Based on the requirement analysis, the cell packaging in longitudinal direction is eliminated because of three reasons. First of all, the dimensions due to this packaging exceed the maximum dimensions for conventional aircraft transporters[1]. Secondly, every airport where the aircraft is operated would require a new type of loading vehicle. Finally, the loading door would have to be very large, resulting in a heavier fuselage structure, as well as a complicated system that has to be designed for spaces in the fuel bay where there are only tanks on the upper side of the fuselage. A full trade-off on fitting of the tanks is shown in Table 9.1.

Table 9.1: Concept trade-off the tank design

Fitting concept	Cell packages Longitudinal	With floor Longitudinal	With floor Lateral
4 tanks per cross section	(-) door size (-) non conventional loading vehicle (-) putting package together in advance (+) packing density (+) loading time	(-) packing density (-) added loading time (+) door size (+) loading simplicity	(–) packing density (+) loading symplicty (+) door size
7 tanks per cross section	(–) door size (-) non conventional transport vehicle (-) putting package together in advance (+) packing (+) loading time	(–) packing (–) added loading time (+) door size (+) loading simplicity	n.a.

As the the packing density and thus the resulting fuselage length is driving estimations are made on the fuel bay length when using these concepts. Based on the trade-off and this table 9.2, the concept is chosen that fits four tanks longitudinally on an upper and lower floor. The main reason for this is that conventional cargo doors can be used, which requires less fuselage reinforcement. In addition, this means that conventional loading vehicles can be used. As the simplicity of the lateral packaging concept did not outweigh the packing density of longitudinal concept, this concept has not been chosen.

Table 9.2: Comparable concept fuel bay lengths.

Concept	4 tanks per crossection			7 tanks per crossection	
	Cell packages	Longitudinal with floor	Lateral with floor	Cell packages	Longitudinal with floor
Number of tanks [m]	16	16	13	28	28
Single tank length [m]	3.57	4.04	4.78	4.34	4.43
Fuel bay length [m]	14.9	16.8	17.9	13.15	18.0

[1] https://www.aeroexpo.online/aeronautic-manufacturer/cargo-high-loader-347.html

9.3. Tank Sizing

To calculate the length and weight of the tanks, a simple program is made. The sizing starts with the fuselage diameter and the size of the floor, which leaves space for the tanks to be fitted as determined before in Section 9.2. The tanks are constrained by the fuselage wall, the floor in the middle and each other making for an optimal tank diameter while leaving space for structural integration. Before calculating the length of the tanks the amount of tanks, mass of hydrogen and wall thickness are determined, shown in Table 9.3. The mass of hydrogen is given by earlier estimation. The amount of 16 tanks is chosen because of a few reasons. First of all, it is chosen to make the cargo doors as small as they can be without sacrificing much on packing density (see Section 10.3). The length over diameter has to be low such that the tanks can be loaded laterally and then turned inside the fuselage. This process is described in more detail in Section 10.3.

The diameter of the tanks is obtained by fitting the tanks in the fuselage with a 30 [cm] floor. The gravimetric potential of the whole system is discussed [64] and researched upon [65] to come to an average shown in Table 9.3. Elliptical caps at the sides of tanks are used with an optimal elliptical ratio of a/b of 1.66 saving 5 percent on fuel bay length as compared to spherical end caps [66].

Table 9.3: Tank sizing inputs and outputs.

Inputs		Outputs	
Hydrogen weight [kN]	133	Tank diameter [m]	2.38
Gravimetric efficiency [-]	0.35	Single tank length [m]	3.84
Hydrogen vented before take-off [%]	10	Top tanks total length [m]	20.17
Hydrogen average density take-off [kg/m^3]	65	Bottom tanks total length [m]	12.10
Amount of tanks [-]	16	Total weight [kg]	38736
Inner diameter [m]	6.3		
Tank cap elliptical ratio a/b [-]	1.66		
Tank wall [mm]	43		
Longitudinal structural margin [-]	0.05		

9.4. Fuel system design

Once the tanks were designed and the engines were selected and modified accordingly, the fuel system was designed to ensure successful fuel delivery from the tanks to the engines. At this stage of the conceptual design, only the most important elements have been considered. These are the location of the fuel delivery lines and connection between all tanks and engines, the insulation of the pipes and the venting system of the tanks as well as pipes accounting for both controlled and uncontrolled venting. First, the pipe arrangement between the tanks and engines will be discussed.

Figure 9.3 shows how the tanks will be connected and the how fuel delivery will take place along the pipes. Each line of tanks on both the top and bottom floor of the tank compartment is connected in series, and separate parallel pipelines are implemented for each line of tanks in series, thus adding redundancy to the pipes in case of a leak or pipe failure. If a tank fails, it can be shut off separately while still enabling the rest of the tanks to deliver fuel to the engines and having sufficient fuel to complete the mission. Furthermore, two cross-feed valves connect the two sets of parallel pipelines in each floor to ensure that every tank is able to deliver fuel to every engine in case of an emergency or failure of a tank or pipe [67].

The pipes from the bottom floor have been connected with the pipes from the top floor via the yellow dots shown in Figure 9.3. This will happen inside the wing box. Right at the connection points between the pipes, small heaters will increase boil-off to help with the extraction of gaseous hydrogen from the tanks and together with valves will enable easy fuel delivery through the pipes to the engines. This avoids the need for using fuel pumps since the use of heaters and valves will serve as a means of controlling the flow through the pipes.

Due to the tank and pipe locations along the fuselage with respect to the cabin, it is assumed that in the case of a leak, it is unlikely that the hydrogen reaches the passengers. In the event of a pipe leak or failure where a significant amount of fuel is spilled, hydrogen will not spread as far as other fuels as it evaporates in a significantly shorter time, and it will rapidly exit the fuselage through the designated vents. If the spilled fuel is ignited, which has a high chance of happening, the duration will be so short such that it does not burn the fuselage to the point of collapse as would for example be the case for kerosene [7]. Therefore, at this stage this is not considered to pose significant threats and is not investigated further. Nevertheless, in more detailed design stages, experimental testing should be performed to validate that the results are indeed correct and fuel spills are correctly vented.

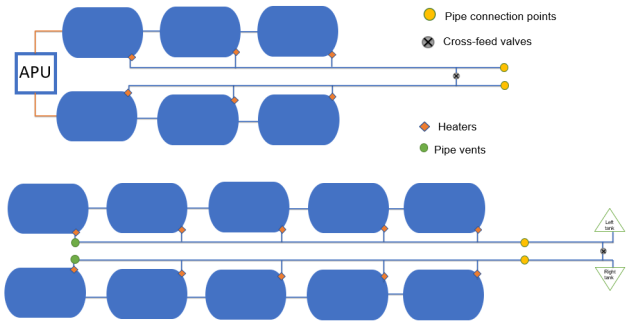

Figure 9.3: Top view of the tank compartment.

The green dots located in the pipes of the upper floor tanks indicate the locations of the venting system for the pipes. This consists of two pipes connected to the top of the fuselage, which enables venting of the pipes in case of pressure regulation or a leak. According to Brewer [7], the volume vent rate that should be aimed for is 0.155 [kg/s] in case of an emergency. Since the pipe design is taken from Brewer, it is assumed that this vent rate will be met without any further modifications. The connection of these pipes to the outside through the top skin of the fuselage is also shown in Figure 9.4.

The external vents shown in Figure 9.4 consist of lightning-protected vents with a flame arrestor which permits overboard discharge of gaseous boil-off without the hazard of flame propagation to the fuel tanks. These vents are located at the top of the vertical tail, and at two different locations along the fuel compartment. One of them is directly connected to the pipe venting system, enabling pipe venting, and the other one is there to account for any uncontrolled venting required due to for example unexpected leaks. The vent located at the top of the vertical tail is directly connected to the tanks through a pipe as shown in Figure 9.4.

The auxiliary power unit (APU) runs on gaseous hydrogen [67]. It is placed at the end of the tail cone and connected to the end of the two tanks on the bottom floor of the tank compartment.

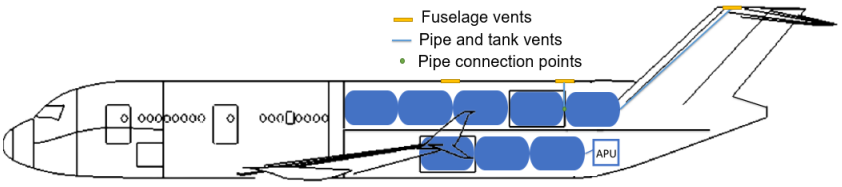

Figure 9.4: Side view of the tank compartment.

Figure 9.5 shows the front view of the tank compartment. The tanks have a connection to the outside of the fuselage that will enable additional means of pressure regulation and venting. This is done through rupture discs. Each tank has two rupture discs for redundancy. The three vent holes located in the tank compartment floor ensure that any uncontrolled venting or leaks of the tanks on the lower floor can take place and escape through the venting holes on the upper surface of the fuselage [67].

The fuel pipes are placed on top of the tanks due to the fact that the hydrogen will be extracted as a gas from the tanks. To enable easy loading and connecting of the tanks, the connection of the pipes with the tanks is made on the elliptical part of the tank such that that it is at a slightly lower height and can be connected from the sides of the tank compartment. This can be seen in Figure 9.6. Tanks placed on the left and right hand sides of the tank compartment as well as upper and bottom floor decks will have to be designed accordingly to have the pipe connection points and rupture discs on the correct orientation.

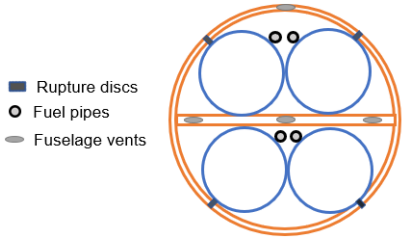

Figure 9.5: Front view of the tank compartment.

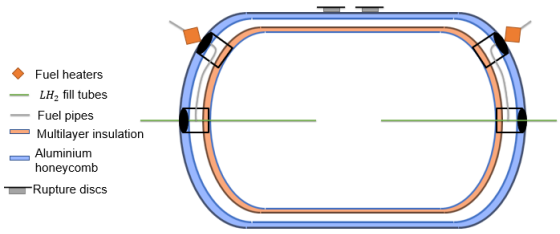

Figure 9.6: Tank wall structure.

Another important aspect to consider is the pipe insulation. Even though gaseous hydrogen will be transported through the pipes, it is still cryogenic thus running the risk of potentially liquefying oxygen around it. Two types of insulation systems were considered initially: vacuum-jacketed and rigid, closed cell foam insulation. A closed cell foam insulation system will be used mainly due to its lower manufacturing costs, easier installation and higher reliability despite being slightly less efficient in terms of insulation than the vacuum-jacketed insulation system [7]. The selected insulation system consists of an inner tube of Type 321 stainless steel due to its compatibility with hydrogen and low thermal expansion coefficient, a closed cell polyurethane foam, and an outer jacket made of AA 6061 aluminium alloy to minimise weight. The pipes will be welded together to minimise the risk of leaks. The design follows from Brewer [7], and the inner and outer pipe diameters were obtained by re-scaling the ones used in Brewer [7] to feed the required fuel flow of 0.53 [m/s].

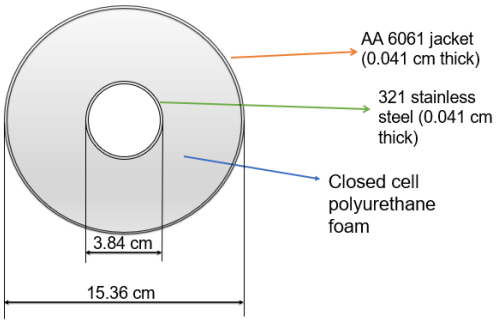

Figure 9.7: Pipe insulation material and dimensions.

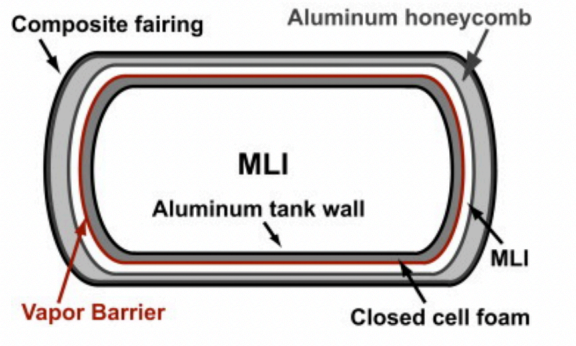

Figure 9.8: Tank wall.

9.5. Shell and Insulation

The tank shell design uses multi layer insulation (MLI)[65] instead of Rohacell, which is more conventional. MLI is more difficult to realise because a vacuum is required. This makes a design using MLI heavier. However, from personal communication with Universal Hydrogen [68] it became clear that the lower volume that can be achieved with MLI outweighs the disadvantages.

The wall of the tank will be made from AA 7085-T6, which should withstand the pressure inside the tank. This aluminium alloy is chosen for its great fatigue strength of 344 [MPa] (obtained using GRANTA EduPack 2020). To compute the required wall thickness for the tank, Equation 9.1 is used. The maximum stress will be in the cylindrical part of the tank. Using the fatigue strength, a maximum tank pressure of 1.2 [MPa] (12 bar), a tank diameter of 2380 [mm] (see Table 9.3) and a safety factor of 2, the required wall thickness is equal to 8.3 [mm] (see Equation 9.2). All additional layers of the tank wall can be found in Table 9.4 [65]. The closed foam is in place to make sure that no hydrogen passes through the aluminium wall.

$$t_{tank} = \frac{p_{tank} \cdot r_{tank}}{\sigma_h} \tag{9.1}$$

$$t_{tank} = \frac{2 \cdot 1.2 \cdot 2380/2}{344} = 8.3 \tag{9.2}$$

Table 9.4: Tank layer thickness.

Inner pressure wall	8 [mm]
Closed foam	5 [mm]
Vaper vacuum layer	5 [mm]
MLI isolation	10 [mm]
Honeycomb structure	10 [mm]
Outside wall	5 [mm]
Total wall thickness	43 [mm]

9.6. Verification and Validation

To verify the program used to calculate the tank dimensions, hand calculations are performed to check if the program works correctly. For simplicity, that hand calculation assumes that the tanks will have spherical end caps instead of elliptical end caps, and the skin thickness is neglected. As discussed in Section 9.3, the program is verified if the difference in tank length is below 5%. The inputs for the hand calculation will be the same as the inputs for the program (with a wall thickness of 0) Section 9.6.

$$V_{tankSingle} = \frac{4}{3}\pi(\frac{D_{tankSingle}}{2})^3 + (L_{tankSingle} - D_{tankSingle})\pi(\frac{D_{tankSingle}}{2})^3 \tag{9.3}$$

$$L_{tankSingle} = \frac{V_{tankSingle} - \frac{4}{3}\pi(\frac{D_{tankSingle}}{2})^3 + D_{tankSingle}\pi(\frac{D_{tankSingle}}{2})^2}{\pi(\frac{D_{tankSingle}}{2})^2} \tag{9.4}$$

Equation 9.3 shows the formula that is used to calculate the volume of a cylinder with spherical ends. The formula is rewritten in Equation 9.4 to calculate the length from a single tank from the volume and diameter. As can be seen in Section 9.6, the hand calculations differ from the design tool with 4.98 %, which means that the tool has been verified.

To validate the design outcome, reference material is used to check the implementation in actual aircraft. Important to validate are the tank loading, the tank size and the wall thicknesses. The design has been presented to Universal Hydrogen to judge the size of the tanks, the fuel system and venting system [68].

Table 9.5: Tool verification.

Inputs		Result	Program	Verification	Difference
Hydrogen Weight [kN]	133	Single tank length [m]	3.538	3.724	4.98%
Hydrogen average density take-off [kg/m^3]	65				
Tank Diameter [m]	2.38				
Tank cap elliptical ratio a/b [-]	1.66				
Amount of tanks	16				

10. Operations

This chapter describes the operations of the AirEco aircraft. First of all the effect of the two different configurations for airlines is described in Section 10.1. The turnaround time of AirEco is presented in Section 10.2, which is an important indicator for airlines. The usage of removable hydrogen tanks differentiates AirEco from other aircraft, the loading and logistics of these are described in Section 10.3 and Section 10.4. Lastly, the compatibility of the AirEco aircraft with ground vehicles and existing airport infrastructure is described in Section 10.6.

10.1. Airline Operations

Airlines can opt to fly AirEco in two configurations. Either 100% hydrogen, or hybrid with 80% of the fuel mass biofuel and remaining 20% hydrogen. Airlines can fly with other fuel mixtures as well, however they must realise that these are less sustainable, as was shown in Section 5.1, and that every time you change the fuel fraction you require engine modifications. Each configuration has different advantages, other than the fuel costs and emissions levels. When range is a priority, the hybrid configuration can provide as much as 8192 [km] of range. When operated from Amsterdam Schiphol Airport the extent of flight is visible in Figure 10.1. However, with this configuration payload is limited to just 150 passengers. If an airline instead needs to carry a lot of payload, then they should opt for the 100% hydrogen configuration. They can fly for a maximum of 5623 [km], shown in Figure 10.2, and carry 150 passengers plus 10.87 [tons] of cargo.

Figure 10.1: Extent of range of AirEco in the hybrid configuration (centre is Amsterdam Schiphol Airport).

Figure 10.2: Extent of range of AirEco in the 100% hydrogen configuration (centre is Amsterdam Schiphol Airport).

10.2. Turnaround Time

The turnaround time is important to consider, especially for airlines. The quicker the turnaround time, the faster airlines can get the aircraft into the air again, allowing them to have more flights per day. The turnaround time is mainly affected by loading of the aircraft, but also cleaning. The following average times for each process completed during turnaround have been identified:

- Loading bags: 140 [kg/min] [69]
- Unloading bags: 190 [kg/min] [69]
- Boarding passengers: 15 [pax/min] per door [69]
- Deboarding passengers: 25 [pax/min] per door [69]
- Fueling: 8 [min] [69]
- Catering: 10 [min] [69]
- Cleaning: 7 [min] [69]

- Unloading cargo containers: 1.2 [min/container][1]
- Loading cargo containers: 1.4 [min/container][1]

The hydrogen tanks will be loaded in a similar fashion as to the cargo containers. However, since they need to be connected to the fuel system, approximately 15% more time is required to load and unload the tanks compared to cargo containers. Moreover, for this analysis it is assumed airlines are using 6 LD-8 containers, which will take less time than loading 12 LD-3 containers[2].

Both the hybrid version and 100% hydrogen aircraft have two possible turnaround times depending on the safety of loading and unloading the hydrogen tanks at the same time as the passengers. First, assuming that the hydrogen tanks and passengers can be loaded and unloaded at the same time. A schematic of this turnaround for the 100% hydrogen aircraft is shown in Figure 10.3. This results in a turnaround time of 47.9 [min]. When using LD-3 containers instead, the turnaround time increases to 61 [min]. If passengers and hydrogen tanks cannot be loaded at the same time, the turnaround time would be 63.9 [min]. This turnaround time diagram is shown in Figure 10.4. The turnaround time for this loading will not change if airlines decide to use LD-3 containers. The hybrid aircraft has a turnaround time of 33 [min] if hydrogen tanks can be unloaded and loaded at the same time as passengers, as can be seen in Figure 10.5. If the hydrogen tanks cannot be unloaded/loaded at the same as passengers, the turnaround time is 39.9 [min].

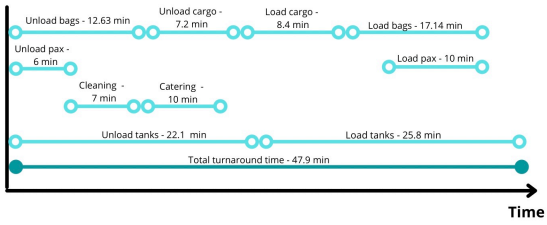

Figure 10.3: Turnaround time for full hydrogen aircraft assuming tanks can be loaded same time as passengers.

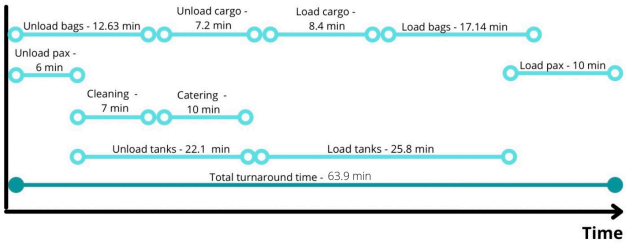

Figure 10.4: Turnaround time for full hydrogen aircraft assuming tanks cannot be loaded same time as passengers.

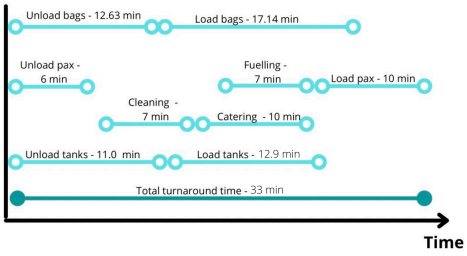

Figure 10.5: Turnaround time for hybrid aircraft assuming tanks can be loaded same time as passengers.

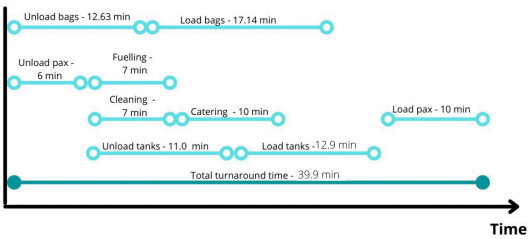

Figure 10.6: Turnaround time for hybrid aircraft assuming tanks cannot be loaded same time as passengers.

[1] https://aviation.stackexchange.com/questions/17564/what-is-the-average-time-taken-to-load-and-unload-the-luggage

[2] https://incodocs.com/blog/unit-load-device-uld-air-container-specifications/

10.3. Hydrogen Tanks Loading and Unloading

Loading and subsequent storing of the tanks is a crucial element of operations, to which a great deal of time and effort was dedicated. The loading and storage of the tanks greatly effect each other, and therefore were designed hand in hand following a set of objectives. These goals are: optimum storage inside the fuel bay to decrease the length of the aircraft; a small door to decrease the complexity and weight of the system; the use of airport current cargo loaders; and ensuring a rapid loading and unloading time.

To best comply with all the goals multiple revolutionary door concepts were thought of. These are the following:

- Large tail cone swing door like that of the 747 Dreamlifter. Tanks are stored longitudinally in the fuselage in groups of 4. This option is excluded as opening and closing the door is slow making loading time to extensive, tanks cannot be stored in the tail cone making the aircraft longer, and a larger heavier structure is required.
- Rear loading ramp like that of a Lockheed C-5 Galaxy. This option is excluded as it is ideal for rolling objects (objects that can drive in the fuselage) and not for loading traditional cargo like tanks.
- Loading the tanks and storing the tanks transversely in the fuselage. This option is compatible with current cargo loaders and requires a smaller door. However, it is excluded as the packing of the tanks is not optimal, making the fuselage roughly 4-5 [m] longer.
- Loading and storing the tanks longitudinally through a large side door in the fuselage. Packing of the tanks is optimal, but it is not compatible with current cargo loaders and it would require a large door, at least as wide as the length of a tank.
- Loading the tanks transversely, and then rotating them inside the fuselage to store them longitudinally. This is the selected option as it results in optimal packing, it is compatible with current vehicles, loading time is not extensive, and a medium sized door in the fuselage is required.

The chosen loading and storing configuration is now further detailed. The fuel bays are accessed from two side doors in the fuselage, both 3.85 [m] wide and 2.5 [m] tall. These doors are situated on opposite sides of the fuselage, such that both fuel bays can be loaded simultaneously, as visible in Figure 10.7. The tanks are then loaded one-by-one transversely using a cargo loader with a bay at least 2.7 [m] wide and 4 [m] long. When the tanks are inside the fuselage, they are rotated and pushed into their correct position by the ground crew. Pushing is facilitated by a set of wheels and motors positioned in the floor, as commonly used in cargo aircraft. The ground grew then connects the tanks to the main fuel system, and walks out to get the next tank. This is because these is no space in the fuel bays for the ground crew to walk once the tanks are in. Although it increases the loading time slightly, it greatly reduces the length of the fuel bays. The loading of the last tank is most critical. This tank is partially rotated outside the fuselage and later pushed into position. A full schematic of the process is shown in Figure 10.8.

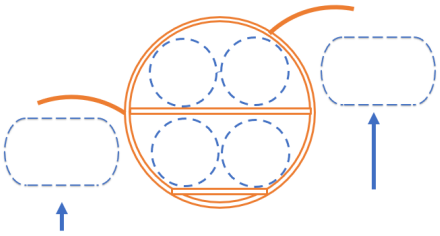

Figure 10.7: Front view of the fuel bays.

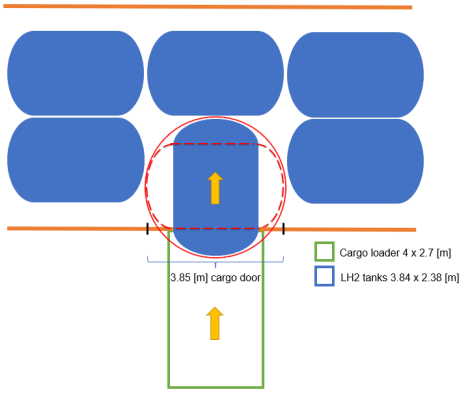

Figure 10.8: Top view of the fuel bay showing the loading of the final tank inside the fuselage.

10.4. Hydrogen Tanks Logistics

The biggest impediment to hydrogen aviation will be the lack of infrastructure. AirEco's solution accommodates to this problem, however introducing more complicated logistic. Therefore, for the success of this proposal, a detailed plan of the logistics behind the revolutionary hydrogen refueling is necessary.

In the first years of the project, where airlines will mostly fly with the hybrid configuration, the tanks will be filled at hydrogen plants. The tanks will then be loaded into conventional shipping containers to be transported to the airport by truck. In the future these can be electric trucks, eliminating any possible emissions from the transportation of the tanks. The tanks have been designed to fit inside a traditional 40-foot container, which is 2.44 [m] wide, 2.59 [m] high and 12.19 [m] long[3]. The goal is to use the existing global freight network. Later on, when airlines will shift their fleet towards 100% hydrogen, the process will change. Until demand for hydrogen is low, using trucks to ship the tanks to the airport is feasible, even today. However, when demand increases using trucks will create conjurations around airports, which is not sustainable. Therefore, with time, hydrogen pipelines will be built from the hydrogen plant to the airport, where the tanks would be filled.

Another solution that would circumvent the building of completely new hydrogen pipeline systems, is using ammonia as a hydrogen carrier [70]. Ammonia can be used as a cheap and efficient one-way carrier of hydrogen. One-way carriers are decomposed at the distribution site to yield hydrogen and a byproduct that is environmentally benign, but has no value. Ammonia has the advantage that it is already mass produced, and thus pipelines already exist. Furthermore, ammonia can be easily transported by rail, truck and oceangoing tankers. This allows production of hydrogen/ammonia to take place far from airports, and in countries with a sustainable advantage for its production, such as Saudi Arabia who will be building the largest green ammonia plant powered by renewable solar energy[4]. The ammonia would then be decomposed into hydrogen nearby an airport, requiring a significantly shorter pipelines. The setbacks of ammonia is that it is toxic, but nonetheless it is commonly used chemical that can be handled safely. Urea has also been considered as a one-way hydrogen carrier. Although not toxic, its hydrogen content is half of that of ammonia.

[3] https://www.icontainers.com/help/40-foot-container/

[4] https://energy-utilities.com/saudi-arabia-s-5bn-green-hydrogenbased-ammonia-news111872.html

At the airport the process will not change with time. Once the tanks arrive or are filled at the airport, they can be stored off site, away from the congested area. When needed cargo transporters will carry them to the stand for them to be loaded by cargo loaders into the aircraft. At arrival tanks are unloaded off the aircraft and inspected. In the hybrid era these tanks would be placed into containers, and shipped back to the hydrogen plant, for the cycle to restart. While in the fully hydrogen future the tanks would be stored at the airport, waiting to be refilled. A visual representation of the process is shown in Figure 10.9.

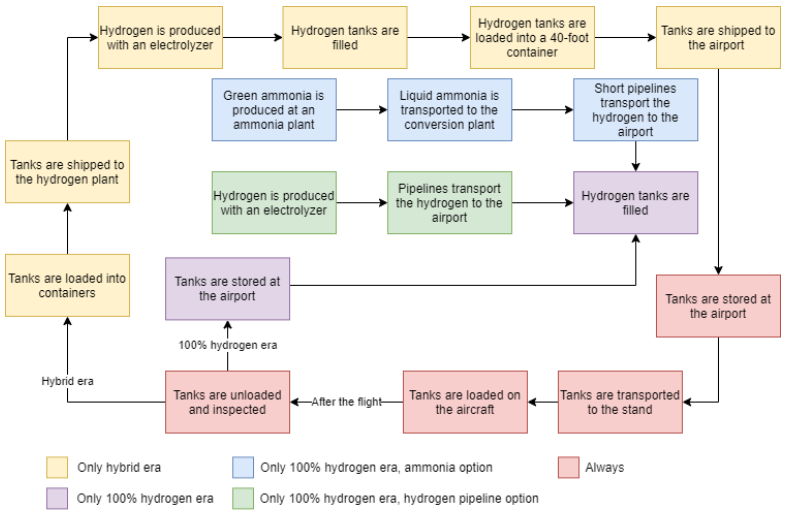

Figure 10.9: Flow diagram of the hydrogen tanks logistics.

Another element of logistics is tank ownership. Inspiration is taken from ULDs, which are often leased or sold to airlines, and not manufactured by aircraft manufactures, such as Boeing and Airbus. The intention of AirEco is not to be a manufacturer nor a supplier of hydrogen tanks. Tanks would thus be provided by an external company, specialised in the manufacturing of pressurised vessels. This limits AirEco's risk, as they will not enter a sector where they lack essential expertise. Furthermore, this will reduce labour and manufacturing costs for AirEco. Nonetheless, in the long run special contracts and partnerships with manufacturers of hydrogen tanks should be made to ensure compatibility of the tanks, as well as reduced prices for customers. The tanks could then be sold or leased to airports and airlines, or even to hydrogen producers.

10.5. Aircraft Logistics

It is also important to consider all of the operational activities required for AirEco's aircraft. For this, an operational and logistics flow diagram has been created for the operational phase of the aircraft, as seen in Figure 10.10. It has been accounted for that the aircraft may need to have maintenance checks in case of damage or a hydrant refuelling system is necessary if airlines choose to fly with 80% biofuel.

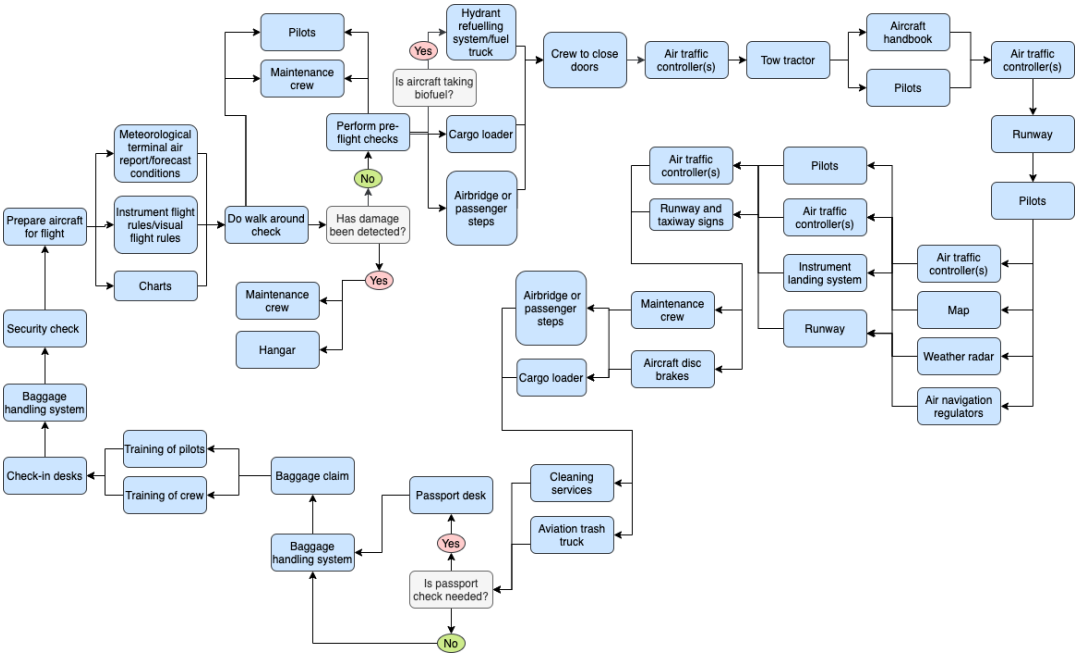

Figure 10.10: Operation and logistics flow diagram.

10.6. Compatibility with Airport Infrastructure and Support Vehicles

AirEco's aircraft is compatible with all ground support vehicles. Most importantly, it requires no additional infrastructure, nor any change to currently available main deck cargo loaders. Airports only need to provide enough space to store the hydrogen tanks. Making an appropriate estimate of how much space is required is too difficult now in this premature phase of the design, as traffic at an airport cannot be approximated. An overview of the ground operations and compatibility of AirEco with all ground support vehicles is shown in Figure 10.11.

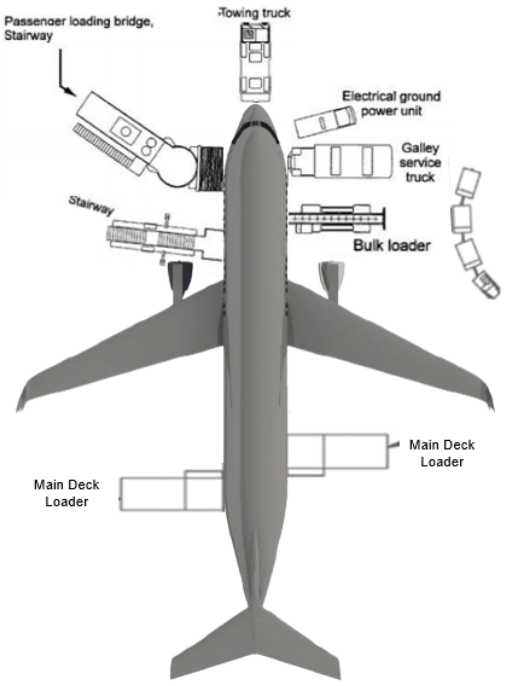

Figure 10.11: Ground operations and compatibility of AirEco with all ground support vehicles.

11. Structures & Materials

This chapter will focus primarily on deriving the structural geometry of the fuselage and wing box, as well as selecting material for both subsystems. Therefore, a structural analysis of the fuselage is performed in Section 11.2 and one for the wing box in Section 11.3. However, first the considered materials are described in Section 11.1.

11.1. Materials

Following from the conceptual design, together with the previous literature study conducted on materials regarding their characteristics and typical uses within aircraft parts, a more specific material selection was conducted for the main structural parts of the design, namely the fuselage and the wing box.

Initially a wide variety of materials were considered including different type of aluminium alloys, aluminium-lithium alloys, titanium alloys, carbon fibre reinforced composites, fibre metal laminates and sandwich panels. For the main structural parts of the aircraft, wing box and fuselage, these were narrowed down to the ones shown in Table 11.1.

Table 11.1: Materials considered for the selection.

Metal alloys	Composites	Fibre Metal Laminates
AA 7075-T6	T300 carbon fiber/epoxy	GLARE 2A
AA 7475-T761	T700G carbon fiber/epoxy	GLARE 2B
AA 7085-T6	T800S carbon fiber/epoxy	GLARE 3
AA 2024-T3		GLARE 4B
Airware® 2198-T8		GLARE 5
Airware® 2098-T8		
Airware® 2050-T84		

A detailed investigation was carried out to produce a database with all the required material properties for each of the selected materials. The main source of information used for the aluminium alloys was Matweb[1], an online materials information resource. For the third generation aluminium-lithium alloys, material data sheets from Constellium [2] were used. Similarly, for carbon fibre composites, material data sheets from Toray[3] were used. And lastly, the material properties for GLARE laminates were obtained from the Journal of Materials [71].

These properties namely include densities, stiffness, ultimate and yield strengths in tension, shear and compression, fracture toughness and poisson's ratios as well as cost.

For composites a more detailed analysis was conducted to investigate how fibre direction affected the properties. A quasi-isotropic lay-up was assumed with 20% of the fibres at 0 degrees, 70% of the fibres at $\pm$ 45 degrees and 10% at 90 degrees since this is a common lay-up used for aircraft structural parts such as fuselage and wing box skins [72] and was considered appropriate for the initial material analysis and selection. The plots shown in Figure 11.1 show the variation in stiffness and strength with fiber direction for composite T300. The constant brown line shown in each plot shows the average properties when computed at 0 degrees with the specified percentages of fibers in each direction. Whilst the purple line shows the average properties computed at at each different fiber direction with the specified

[1] http://www.matweb.com/index.aspx

[2] https://www.constellium.com/markets-applications/aerospace

[3] https://compositesnl.nl/en/members/toray-advanced-composites/

percentages.

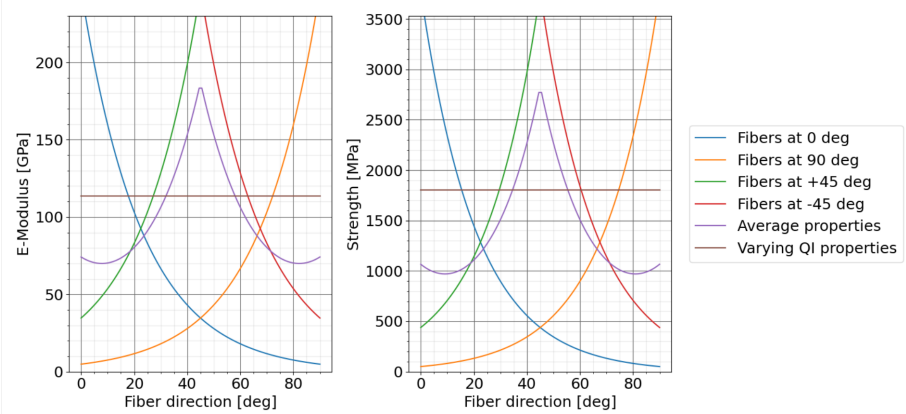

Figure 11.1: Stiffness and strength properties varying with fiber direction for T300 composite.

With this analysis, it was then possible to estimate more accurate properties for the selected composites depending on the type of loading considered. Furthermore, a 60% fiber volume percentage was assumed for all composites as it is fiber volume content applied in the composites produced by Toray [4] and was found to give a good balance between strength and stiffness as well as weight.

For the fatigue analysis of the materials, S-N curves were constructed. This enabled the determination of fatigue limits at the required number of cycles. Based on requirement AE-OPER-06, the aircraft shall be able to withstand a total of 60,000 flight cycles. For fatigue calculations at this early stage of the design process, this was multiplied by a factor of 16, meaning that at this point the fatigue limits obtained are for a total of 960,000 flight cycles. A large factor was selected to ensure that the structure is not under-designed initially, since fatigue can be a critical mode of failure for many aluminium alloys.

Due to the lack of experimental fatigue data available, the approximations shown in Table 11.2 were used to plot the graphs of metal alloys and GLARE. An α value of 0.3 was used for aluminium alloys, and 0.5 for GLARE laminates. A stress concentration factor K_t was used to account for holes in the structure by dividing the endurance limit by 3. The final plots can be seen in Figure 11.2 and Figure 11.4.

For composites, a slightly different approach was used. Under cyclic loading their strength can be assumed to reduce linearly as the number of cycles increases. Again, due to the lack of experimental data available, a constant slope of 0.83 was estimated from Kassapoglou's work [73]. The stresses were then divided by K_t = 3 to account for any stress concentrations due to small holes in the structure. The final plot is shown in Figure 11.3.

Table 11.2: Approximations used for S-N plots of metal alloys and GLARE.

N	S
0	S_{ult}
1000	$0.9 * S_{ult}$
1000000	$\alpha * S_{ult}$

[4] `https://compositesnl.nl/en/members/toray-advanced-composites/`

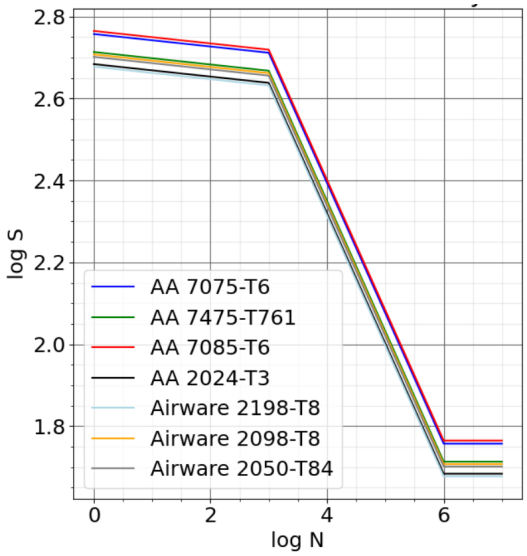

Figure 11.2: S-N curves for aluminium alloys.

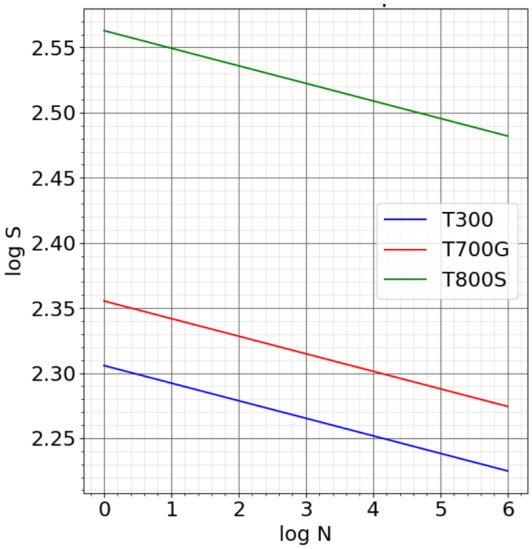

Figure 11.3: S-N curves for composites.

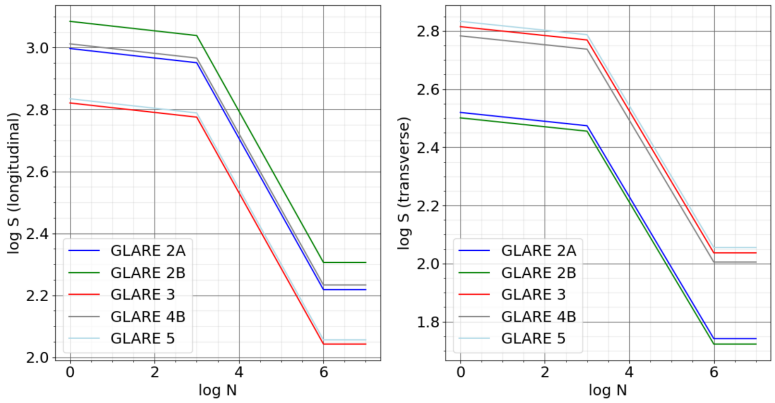

Figure 11.4: S-N curves for different GLARE types.

11.2. Fuselage Structural Analysis

This section deals with the structural analysis of the fuselage. First load cases are identified, followed by the structural analysis, then the material selection, and lastly verification and validation, as well as a sensitivity analysis are performed. Important to note is that the fuselage is designed for the 100% hydrogen configuration as it is more critical.

11.2.1. Fuselage Load Cases

Several load cases are considered for the design of the fuselage. Unit load cases (ULC) are derived from the flight envelope shown in Figure 11.5, to ensure that the entire load envelope is considered. This method is in line with what suggested in Megson's book [74]. For ULC.1 and ULC.4, C_L corresponds to $C_{L_{max}}$, while for all other ULC $C_{L_{clean}}$ is taken. ULC.1 and ULC.2 are repeated with zero-thrust, respectively representing an engine failure at take-off and thrust in the idle position during a nose dive. Lastly, the load factors n are multiplied by a 1.5 FoS, as these are ultimate load cases. A complete summary of all considered ULC is provided in Table 11.3.

Superposition of loads, yielding combined load cases (CLC), is necessary to find the fuselage design load cases. ULC.2 and ULC.5 are superimposed with a vertical tail side gust load, through a non-zero yaw-angle of ± 20. These ULC are selected as their higher velocity makes the vertical tail load larger, and hence more critical. The yaw angle will be subject of a sensitivity analysis later on. Finally, all ULC are superimposed with cabin pressurisation, ULC.7. The pressure differential is obtained from requirements. For damage tolerance and static loading the pressure differential is $2\Delta p$, while for fatigue it is Δp. A complete summary of all considered CLC is provided in Table 11.4.

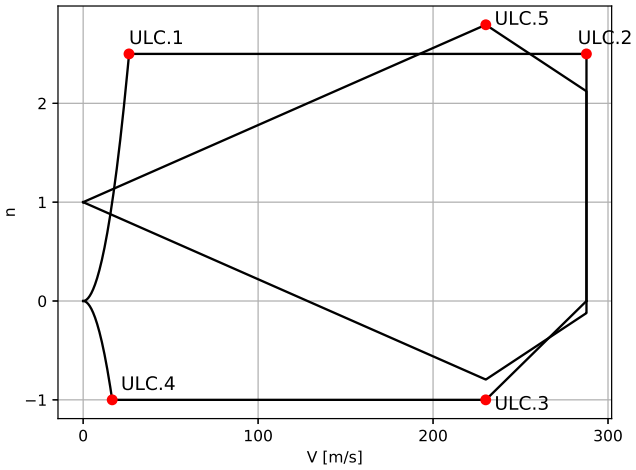

Figure 11.5: Flight envelope used to determine the fuselage ULC.

Table 11.3: ULC for the fuselage

Load Case	Description
ULC.1.a	$n = 2.5$, $C_L = 1.65$, $V = 25$ [m/s], and $T = 511$ [kN]
ULC.1.b	$n = 2.5$, $C_L = 1.65$, $V = 25$ [m/s], and $T = 0$ [kN]
ULC.2.a	$n = 2.5$, $C_L = 0.64$, $V = 288$ [m/s], and $T = 511$ [kN]
ULC.2.b	$n = 2.5$, $C_L = 0.64$, $V = 288$ [m/s], and $T = 0$ [kN]
ULC.3	$n = -1$, $C_L = 0.64$, $V = 230$ [m/s], and $T = 511$ [kN]
ULC.4	$n = -1$, $C_L = 1.65$, $V = 16$ [m/s], and $T = 511$ [kN]
ULC.5	$n = 2.8$, $C_L = 0.64$, $V = 230$ [m/s], and $T = 511$ [kN]
ULC.6	Vertical tail side load with $\psi = \pm 20$
ULC.7	Cabin pressurisation with $2\Delta p = 104100.8$ [Pa]

Table 11.4: CLC for the fuselage

Load Case	Description
CLC.1.a	ULC.1.a+ULC.7
CLC.1.b	ULC.1.b+ULC.7
CLC.2.a	ULC.2.a+ULC.7
CLC.2.b	ULC.2.b+ULC.7
CLC.3	ULC.3+ULC.7
CLC.4	ULC.4+ULC.7
CLC.5	ULC.5+ULC.7
CLC.6	ULC.2.a+ULC.6+ULC.7
CLC.7	ULC.5+ULC.6+ULC.7

11.2.2. Static Loading

Static loading of the fuselage is comprised of bending, shear, and buckling. The moment (M_x, M_y and M_z), and shear force (S_y and S_z) distributions along the fuselage have to be determined. The first step is to find the wing lift. To do so, Equation 11.1 is used, where α is the angle of attack, which will vary depending on the C_L of each load case, and W is the MTOW, as this is most critical. Using the MTOW for the weight is in line with Şen's work [75]. To find the lift of the tail plane, a sum of moments about the c.g. is performed. The pitching moment is first determined using Equation 11.2, where C_m, the pitching moment coefficient, which also depends on α, and $\bar{c}$ is the MAC. Furthermore, drag and thrust are assumed to act through the c.g., and hence were ignored. Using Equation 11.3, where l_w and l_h are respectively the

wing and tail moment arms, the tail lift is found. The tail's lift was then subtracted from the total lift, L, to find the wing's lift, which was then used to iterate by redoing the sum of moment until both L_h and L_w would converge [74].

$$Lcos(\alpha) = nW - Tsin(\alpha) \quad (11.1) \qquad M = C_m \frac{1}{2}\rho V^2 S\bar{c} \quad (11.2) \qquad L_h = \frac{L_w l_w + M}{l_h} \quad (11.3)$$

The next step is making a free body diagram (FBD). The weight of the fuselage is assumed to be uniformly distributed along its whole length, while the empennage weight is considered a point load. Tank, fuel, and payload weight are also assumed to be uniformly distributed. Lastly, the weight and lift forces are balanced by reaction forces at the front and rear spar. The FBD for cruise flight is shown in Figure 11.6. Throughout the static analysis, the weights shown in the FBD are multiplied by the load factor n [75].

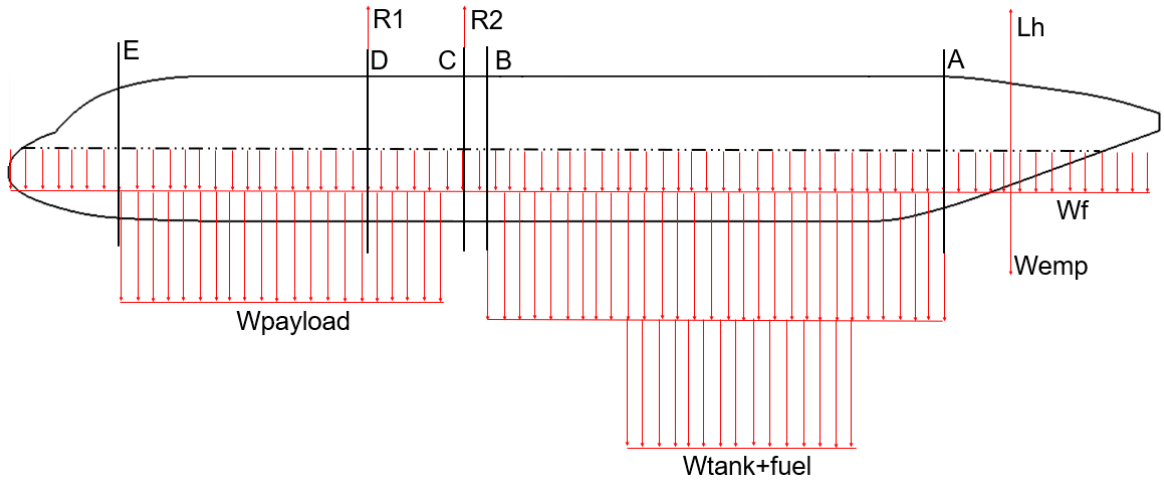

Figure 11.6: FBD of the fuselage during cruise flight without any side gust load from the vertical tail.

The fuselage is analysed at multiple locations along its length. These correspond to either the introduction of new loads (points D and C), or to clear geometrical and layout transitions (point B). Geometrical dimensions, such as stiffener area and skin thickness, will be constant between two consecutive locations, creating a fuselage segment. With this determined, the moment and shear forces distributions can be derived, and the static loading analysis is performed.

Bending, Shear and pressurisation

Bending, shear and pressurisation are analysed simultaneously, to determine an optimal skin thickness and stiffener area for minimum mass. Bending moments M_y and M_z cause the fuselage to bend, while shear forces S_y and S_z, and torque T cause shear stress in the fuselage. The pressure differential Δp will cause tension in the fuselage.

Before bending and shear are analysed, assumptions and key geometrical characteristics are defined, as well as a coordinate system. The coordinate system is given in Figure 11.7, while assumption and characteristics are the following:

- The fuselage is a perfect circle, with symmetry about both the y and z axis, thus $I_{zz} = I_{yy}$.
- The fuselage is assumed to be cylindrical.

- The fuselage is assumed to be a thin walled structure.
- The axial stress, σ_x, is carried by the stiffeners and by the skin.
- It is assumed that the stiffeners carry no shear.
- It is assumed that the stiffeners are point masses.
- The stiffeners are spaced evenly along the circumference of the fuselage.
- 80 stiffeners are used based on comparison with similar aircraft and an optimisation code.
- All loads act through the center line of the fuselage.

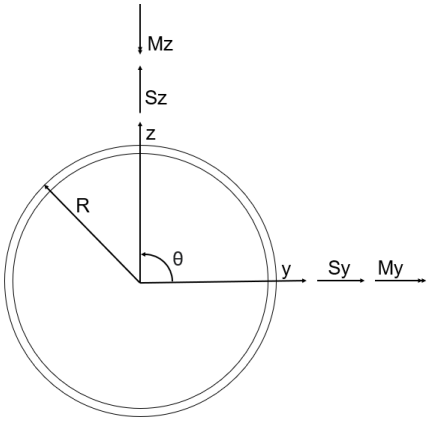

Figure 11.7: Cross section of the fuselage, showing the used coordinate system.

Bending causes an axial stress σ_x in the fuselage's cross section. Moreover, the pressurisation has a contribution to the axial stress. Therefore, the longitudinal pressurisation stress, which is a tensile stress, is superimposed with the bending stress, yielding Equation 11.4 for σ_x [5]. In the equation Δp is the pressure differential, R the fuselage radius, and t the skin thickness. To reduce computational time, the axial stress is evaluated only at two points in the cross section. These points correspond to the locations of maximum compression and tensile stress in the cross section, and are identified by differentiating Equation 11.4 and setting the derivative equal to zero. The two points are found at $\theta = arctan(M_y/M_z)$. This is in line with Heerens' work [76]. Pressurisation has another stress contribution in the circumferential direction, σ_y, given by Equation 11.5.

$$\sigma_x = \frac{M_z y}{I_{zz}} + \frac{M_y z}{I_{yy}} + \frac{2\Delta p R}{2t} \qquad (11.4)$$

$$\sigma_y = \frac{2\Delta p R}{t} \qquad (11.5)$$

Shear forces and torques will cause a shear stress τ. Unlike axial stress, pressurisation has no contribution to shear, and therefore τ is given by Equation 11.6. Here $Q_z = \int_A y dA$ and $Q_y = \int_A z dA$ are the first moment of area, t is the skin thickness, and J is the polar moment of inertia, or $2I$. Furthermore, the moments of inertia, I_{yy} and I_{zz} only consider the skin, as the stiffeners are assumed to carry no shear. Similar to bending, the the shear stress is evaluated only at two points, corresponding to maximum and minimum shear. The points are located at $\theta = arctan(S_y/S_z)$.

$$\tau = -\frac{S_y Q_z}{I_{zz} t} - \frac{S_z Q_y}{I_{yy} t} + \frac{TR}{J} \qquad (11.6)$$

[5] http://www.ase.uc.edu/~pnagy/ClassNotes/AEEM438%20Solids%20Lab/8th%20lab.pdf

Since the fuselage is subject to multiple loads and stress simultaneously, the stresses have to be combined. This is done with Mohr's circle. The radius of the circle, which corresponds to the maximum in plane shear stress, is obtained with Equation 11.7, while the two principle stresses, $\sigma_{1,2}$ are given by Equation 11.8. These, together with τ_{max}, are the design stresses. The principle stresses should be less than the yield stress, while τ_{max} should be less than the shear strength. With these constraints, an optimisation code is ran to minimise the area of the cross section by changing the stiffeners areas and the skin thickness.

$$\tau_{max} = \sqrt{\left(\frac{\sigma_x - \sigma_y}{2}\right)^2 + \tau^2} \qquad (11.7)$$

$$\sigma_{1,2} = \frac{\sigma_x + \sigma_y}{2} \pm \tau_{max} \qquad (11.8)$$

Buckling Analysis

Buckling is the fourth element of static loading. For buckling the fuselage is divided in four panels: top, bottom, right, and left (see Figure 11.8). Then, a buckling analysis is conducted for each panel using the maximum compression stress in that panel derived from the load cases. For this analysis, it is optimised to find the optimal skin thickness and optimal stiffener thickness for minimum cross sectional area.

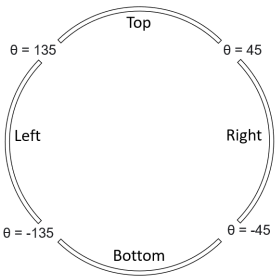

Figure 11.8: Division of the fuselage cross section for the buckling analysis.

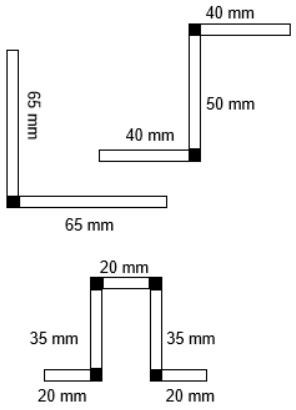

Figure 11.9: Technical drawing of the three considered stiffeners all with $A = 130t$ [mm].

Three types of stiffeners are considered for buckling: hat-shaped, Z-shaped, and L-shaped. These stiffener types were selected as they are most common, and offer a wide design range, from simple geometry to high buckling resistance. All these stiffeners are designed to have the same cross sectional length of 130 [mm] when unfolded, such that the thickness is the only design variable. Figure 11.9 shows the dimensions of the three stiffeners.

The buckling analysis begins by calculating the critical buckling stress of the stiffened panels. This has two components: the crippling stress of the stiffeners and the buckling stress of the skin, both given by Equation 11.9, where E is the material modulus of elasticity, v the Poisson Ratio, C is the buckling constant, and t and b the thickness and width of the element respectively. The buckling constant varies depending on the considered boundary condition. Furthermore, it depends on the aspect ratio of the panels (ratio between frame and stiffener spacing). The frame spacing is 550 [mm], the same as the A320, and is constrained by the window width [75]. With 80 stiffeners the stiffener pitch is 260 [mm], and thus the aspect ratio is 2.1. For the skin, two boundary conditions are possible: clamped on all sides, which $C = 8$,

or simply supported on all sides, which yields $C = 4$. The later is chosen as it is more critical, but this will be part of a sensitivity analysis later on. In the end, the stiffener of choice is the hat-shaped one, due to its higher stiffness, and hence higher crippling load. Mounting it upside down will not impair inspection and maintenance. The critical buckling stress is then found using Equation 11.10, where the A_i's are the areas of the respective elements.

$$\sigma_{cc} = \frac{C\pi^2 E}{12(1-v^2)}\left(\frac{t}{b}\right)^2 \qquad (11.9)$$

$$\sigma_{cr} = \frac{\sum \sigma_{cc_i} A_i}{\sum A_i} \qquad (11.10)$$

11.2.3. Fatigue Loading

Fatigue in the fuselage is characterised by the pressurisation cycle. Stress fluctuates from a maximum at cruise to zero on ground. Therefore, the mean stress is non-zero and the amplitude stress is half the maximum stress. Furthermore, fatigue will be analysed only in the cabin and cockpit section of the fuselage, or from point B to E, as the rest of the fuselage is not pressurised.

The maximum stress is determined using the Mohr's circle. For pressurisation, σ_x is the pressurisation longitudinal stress or $\sigma_x = \frac{\Delta p R}{2t}$, while σ_y is the pressurisation circumferential stress or $\sigma_y = \frac{\Delta p R}{t}$. Note that here for fatigue Δp is considered. Furthermore, here t is not just the skin thickness, but it considers that the stiffeners are smeared over the fuselage cross section, yielding a larger t. Simplifying the equations reveals that the maximum stress is equal to σ_y, and thus the stress amplitude is equal to $\sigma_y/2$. However, since the mean stress is non-zero, but equal to the amplitude stress, and the constructed S-N curves work only for zero mean stress, the stress amplitude has to be converted. This is done through Equation 11.11, where σ_{amp} and σ_{ult} are respectively the amplitude stress at non-zero mean stress and the material's ultimate strength [77].

$$\sigma_{amp_0} = \frac{2\sigma_{amp}}{1 - \frac{\sigma_{amp}}{\sigma_{ult}}} \qquad (11.11)$$

11.2.4. Damage Tolerance

Designing for damage tolerance is a very important aspect of aircraft structural design. As explained in CS25 regulations [78], the aircraft shall be capable of successfully completing a flight in which damage has occurred to the structure. For the fuselage, a crack size of 0.55 [m] is assumed [79]. This is a reasonable crack size resulting from an uncontained engine failure where a turbine blades strikes the fuselage. The same crack size will be assumed for the damage tolerance analysis of the fuselage.

To calculate the limit load the structure can withstand with a crack size of 0.55 [m], Equation 11.12 was used.

$$K_c = \sigma_{limit} \cdot \sqrt{\pi \cdot a_{crit}} \qquad (11.12)$$

Where a_{crit} is half the critical crack size and K_c is the critical stress intensity factor for which unstable cracking will start to occur for a given material.

To relax the damage tolerance criterion the concept of crack arrest is applied [80]. Since the

frame spacing in the fuselage is 0.55 [m], the same as the established critical crack size, it can be assumed that when the crack size is close to the assumed critical length it reaches a frame, which adds strength to the skin. Thus, this increases the critical limit load the skin can withstand. A factor of 1.6 was selected to increase the critical limit load [81]. This effect is quantified in Figure 11.10 for the aluminium alloys AA 7075-T6 and AA7085-T671, as well as for the carbon fibre composite T800S. For AA 7085-T6, a critical crack size of 0.5 [m], since this was considered to be the approximate rib spacing at the locations where damage is likely to occur. And therefore, for the wing box, crack arrest is assumed to occur at an earlier stage.

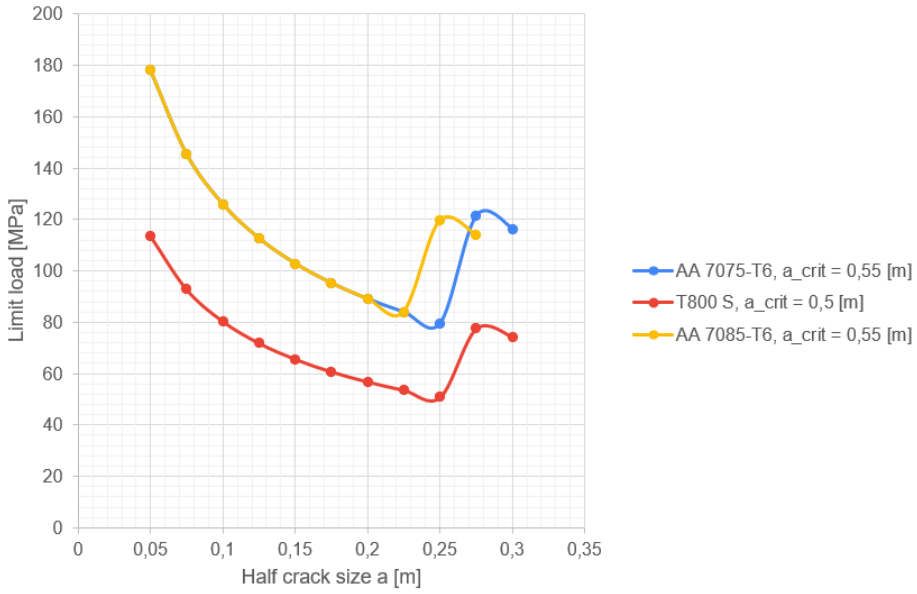

Figure 11.10: Crack arrest in AA 7075-T6, T800S and AA 7085-T6.

11.2.5. Material Selection and Final Geometry

After performing the fuselage structural analysis, the properties of the selected materials listed in Table 11.1 were inputted into the optimisation code to obtain the fuselage geometry. The main objective of the code was to optimise the cross-sectional area of the fuselage for a given material such that it is able to withstand all loads during flight. For the final material selection, the following aspects were considered:

- Performance
- Weight
- Cost
- Availability
- Maintenance, repair and inspectability
- Manufacturing
- Durability
- Environmental impact

Taking the above listed items into consideration, all GLARE types were discarded. The main reasons are performance and cost. Regarding the cost of GLARE, there are differing perspectives. According to Vasiliev's work [82], fiber metal laminates are typically an order of magnitude more expensive than aluminium alloys, however this does not mention GLARE in particular, other studies as confirmed by Dr.ir. R.C. Alderliesten, have proven the cost of GLARE to be around six times the cost of monolithic aluminium, thus similar to composites. Furthermore, the transverse properties of GLARE obtained from literature [71] were not better than those for composites or aluminium alloys, and this resulting in large required thicknesses, combined with high material costs led to the exclusion of GLARE in the more detailed material analysis.

This left the aluminium alloys, including the aluminium lithium alloys, and the carbon fibre reinforced composites. For each material type the best material was selected based on weight and cost, as these are very important and they are the only clear difference within a material family. Table 11.5 summarises the weights obtained for each material for the fuselage structure, as well as an estimate of the cost of each material [83] and relevant properties for the comparison and selection. The information as well as the values shown in Table 11.5 were obtained from the GRANTA EduPack 2020[6] software.

Table 11.5: Comparison between fuselage materials for final selection.

	AA 7075-T6	AA 7085 T761	Airware® 2198-T8	Airware® 2050-T84	T300	T700 G	T800S
Performance	DT, buckling, fatigue	DT, buckling, fatigue	DT, buckling, fatigue	DT, buckling, fatigue	DT, buckling	DT, buckling	DT, buckling
Weight [kg]	12,008.4	12,095.6	12,145.3	11,782.5	9964.3	9863.4	8633.4
Cost [EUR/kg]	5.03	5.03	10	10	33.5	33.5	33.5
Total cost [EUR]	60,402.3	60,840.9	121,453	117,825	333,804.05	330,423.9	289,218.9
Availability	Yes	Yes	Yes	Yes	Yes	Yes	Yes
Maintenance & Manufacturing	More experience with current practices, cheaper manufacturing, less processing energy required	More experience with current practices, cheaper manufacturing, less processing energy required	More experience with current practices, cheaper manufacturing, less processing energy required	More experience with current practices, cheaper manufacturing, less processing energy required	Fewer part count, less maintenance required, expensive manufacturing	Fewer part count, less maintenance required, expensive manufacturing	Fewer part count, less maintenance required, expensive manufacturing
Durability	Susceptible to corrosion, excellent against UV radiation, non-flammable	Susceptible to corrosion, excellent against UV radiation, non-flammable	Susceptible to corrosion, excellent against UV radiation, non-flammable	Susceptible to corrosion, excellent against UV radiation, non-flammable	Good against UV radiation, slow-burning	Good against UV radiation, slow-burning	Good against UV radiation, slow-burning
Primary production embodied energy [MJ/kg]	184-203	184-203	184-203	184-203	655 - 723	655 - 723	655 - 723
End of life	Recycle, downcycle	Recycle, downcycle	Recycle, downcycle	Recycle, downcycle	Downcycle, combust for energy recovery	Downcycle, combust for energy recovery	Downcycle, combust for energy recovery

[1] https://www.ansys.com/products/materials/granta-edupack

Within the aluminium alloys, Airware® 2050-T84 is the lightest, however, when compared to AA 7075-T6, the second lightest alloy, the structure is only 225 [kg] lighter. This sums up to roughly 25 [kg] of fuel saved per flight. Nevertheless, third generation aluminum lithium alloys are considered to be at least two times as expensive as traditional aluminium lithium alloys [84], thus making them unsuitable to meet the strict cost requirement. Hence the two materials that made it to the final round were AA 7075-T6 and the carbon composite T800S. Out of the composites considered, T800S was selected as it provided the lightest structure.

Although T800S is significantly more expensive than AA 7075-T6, it was decided to perform a detailed comparison of the two materials, such to see if T800S advantages over AA 7075-T6 outweigh its significant cost disadvantage by looking at the properties listed in Table 11.5 for each material.

The weight reduction achieved with T800S results in a fuel reduction of 378 [kg] per 5000 [km] flight. On a conventional aircraft operating on kerosene this fuel reduction could potentially result in a significant decrease in emissions for an airline. Nevertheless, it is important to note that AirEco will mostly be operating on liquid hydrogen, which by 2050 is expected to be produced in a green way. Therefore, although more fuel means higher operational cost, there is no negative environmental impact of using more fuel. In reality, the primary production of aluminium alloys is substantially greener, as illustrated in Figure 11.11, thus making T800S less environmentally sustainable than AA 7075-T6. Data was obtained from GRANTA WebEdu

[6] https://www.ansys.com/products/materials/granta-edupack

pack 2020. Furthermore, when considering end-of-life, aluminium alloys are significantly better in terms of both, recyclability and downcyclability.

Apart from weight reduction, composites score better for maintenance and durability. Less maintenance is required for composites due to lower part count, but there is also less experience with regards to failure and inspection intervals of composite structures[7]. In terms of durability, aluminum alloys are susceptible to corrosion, and thus require additional surface treatments.

With regards to cost, an important point should be noted. The comparison between costs for the selected material was done purely based on material costs, where a clear difference was observed. However, an important aspect that should be carefully evaluated is panel cost, where the manufacturing methods as well as thickness steps between adjacent panels is also considered.

At this stage it can be done on a qualitative level. For aluminium alloys thickness steps are carefully incorporated in the structure by chemical milling. This is done once the panels are produced through stretch forming or roll bending. For composites on the other hand, one is able to implement different thicknesses along a panel in a single manufacturing method such as automated fibre placement or automated tape laying [85]. Furthermore, stringers in aluminium structures are usually riveted, resulting in additional stress concentrations to be generated in the fuselage as well as the additional weight for the rivets. In the case of composites, stringers are usually bonded using an adhesive, and this can be cured together with the skins in one single step. These manufacturing discrepancies between both group of materials lead to fewer part count as well as less manufacturing steps for composites when compared to aluminium alloys [86]. Nevertheless, the main benefit of aluminium alloys in this respect is still the experience of workers as well as the infrastructure an machinery required to produce these parts and based on the data obtained from GRANTA EduPack materials software, the individual manufacturing methods are significantly cheaper and can benefit to a greater extent of the learning curve effect when considering larger batch sizes. Therefore it can be assumed that at this stage of the design, the cost analysis still yields better results for aluminium alloys, however, a suggestion would be to look at this aspect more closely once more material data is available from a manufacturer.

With all aspects considered, a final decision was made. Although, composites provide great benefits with respect to weight reduction, the fuselage will be made out of AA 7075-T6 alloy. The main reason for this is cost once again. With the strict requirement on cost of not more than 120% the cost of the A321XLR it is not affordable for AirEco's aircraft to be made out of composites, which cost about six times as much as aluminium alloys. As manufacturing costs cannot be quantitatively introduced in the analysis, the final decision is made mainly based on material costs which are also a significant part of the total cost [87]. Nevertheless, it is still assumed that when considering manufacturing costs and the relevant cost reductions due to fewer part count and less manufacturing steps, the cost per panel for composites will still be higher than for aluminium.

Figure 11.12 shows the parts of the A321XLR that are made with composite materials. The fuselage is made primarily out of aluminium alloys, except for the nose cone, meaning that a full composite fuselage structure will not allow the cost requirement to be met, specially considering the fact that AirEco is a significantly larger aircraft.

[7] http://compositeslab.com/composites-compared/composites-vs-aluminum/

Nevertheless, the selected material meets AirEco's sustainability goals. On the environmental aspect, from an aircraft producer perspective, primary production of aluminium has a smaller environmental impact than for composites. Additionally, recyclability at end-of-life is possible. With regards to the economical pillar, aluminium is significantly cheaper than composites, and similarly manufacturing of AA 7075-T6 is substantially less expensive, both due to lower raw material cost and lower tooling cost. And lastly on a social aspect, manufacturing of aluminium is less labour intensive, and maintenance techniques and inspection intervals are fully developed.

The skin thickness and stringer dimensions for each of the four panels along the length of the fuselage for the final material are shown in Table 11.6.

Table 11.6: Required skin thicknesses and stringer dimensions per panel for AA 7075-T6.

	MATERIAL: AA 7075-T6					
Section	**Skin thickness [mm]**	**Number of stringers**	**Stringer area [mm^2]**	**Stringer thickness [mm]**	**Failure mode**	**Total mass [kg]**
A-B Bottom	1.5	20	558.26	4.3	Buckling	1001.80
A-B Top	3.3	20	130.00	1.0	DT	1041.13
A-B Sides	1.9	20	545.86	4.2	Buckling	1091.65
B-C Bottom	4.5	20	500.00	3.8	Fatigue	242.69
B-C Top	4.5	20	500.00	3.8	Fatigue	242.69
B-C Sides	4.5	20	500.00	3.8	Fatigue	242.69
C-D Bottom	5.8	20	262.15	2.0	Buckling	372.76
C-D Top	5.9	20	174.52	1.3	DT, Buckling	363.47
C-D Sides	7.2	20	130.00	1.0	DT	421.91
D-E Bottom	5.8	20	262.15	2.0	Buckling	1234.15
D-E Top	5.9	20	174.52	1.3	DT, Buckling	1203.41
D-E Sides	7.2	20	130.00	1.0	DT	1396.89

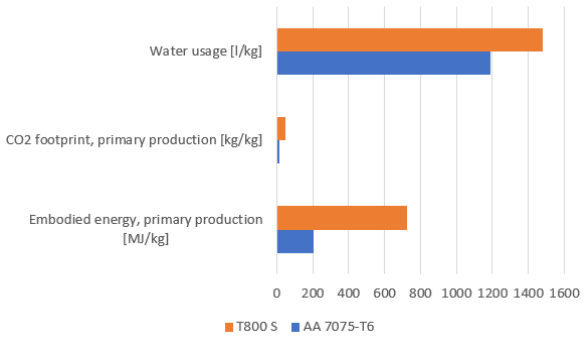

Figure 11.11: Difference in energy, CO_2 and water required to produce composites and aluminium.

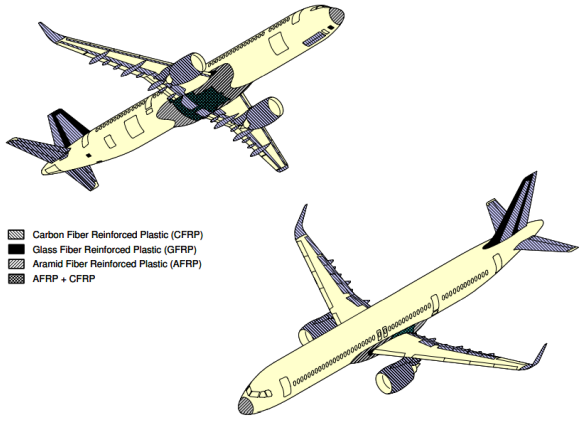

Figure 11.12: Composites used in the A321XLR aircraft.[8]

[8] https://www.airbus.com/content/dam/corporate-topics/publications/backgrounders/techdata/aircraft_characteristics/Airbus-Commercial-Aircraft-AC-A321.pdf

11.2.6. Geometry Corrections

In the fuselage design the pressurization load for static and fatigue loading were inverted, and hence the results shown in Table 11.6 are partially incorrect. Therefore, this section will reflect on the changes that would occur in the geometry if the correct pressurization loads would be used. The results in the aft section of the fuselage (A-B) would not change, as this segment is not pressurized. That differs in the middle part of the fuselage, which was critical in fatigue. With the correct pressurization load the fatigue load is halved, and fatigue is no longer critical. Here buckling and damage tolerance are expected to become critical. Nonetheless, the required skin and stringer thickness would be less than the current. In the forward section of the fuselage, bending and shear are expected to become more critical. However, it is difficult to say if they will replace damage tolerance and buckling as the critical failure mode. On one side, damage tolerance would not change, as the correct pressurization load of Δp was used, and buckling would decrease, as the larger pressurization load of $2\Delta p$ would induce more tension in the fuselage, reducing the maximum compressive stress. On the other hand, shear and bending were never close to being the critical failure mode. Therefore, the failure mode is expected not to change. Additionally, this suggest that again in the forward fuselage section, were buckling is critical, the skin and stringer thickness could be reduced slightly. However, more analysis is required to make a proper estimation.

Regarding composites, which were mostly critical in damage tolerance, little variation would be expected. Firstly, all composites have a very high fatigue resistance, meaning that if the pressurization load is halved, fatigue becomes even less critical. Secondly, as damage tolerance dominates and its results are correct, only minor changes to the fuselage geometry are expected. Again, these changes would occur were bending or shear become critical, or were buckling was critical.

11.2.7. Tank Door

The access door to load the tanks is of a reasonable size, at a width of 3.85 [m] and an altitude of 2.5 [m]. Although, it is not larger than a main deck cargo door on the 777 freighter[8], it is interesting to perform an analysis. To carry out the analysis a framed cut-out is assumed, where the door section is non-load bearing. Furthermore, it is assumed that the shear flow on either side of the door is the same, as well as the shear flow above and below the door.

The frame cut-out process can be visualised in Figure 11.13. Panels 1, 3, 7 and 9 have a width equal to the frame spacing and a height equal to the Panel 5 is the door. The resulting shear flows, q_H, q_S and q_C are then found with Equation 11.13 through Equation 11.15. The analysis revealed that reinforcement is required. A smeared skin thickness (skin + stiffening elements) of 15 [mm] is need in panels 1, 3, 7, and 9.

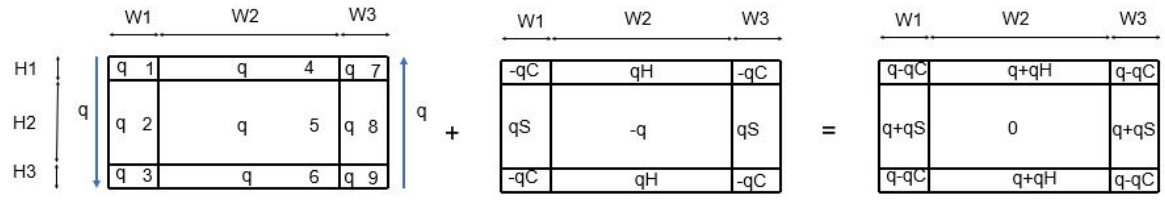

Figure 11.13: Frame cut-out process used to find the shear flows induced by the tank door.

[8] http://brinkley.cc/AC/b777f.htm

$$q_H = \frac{qH_2}{H_1 + H_3} \quad (11.13) \qquad q_S = \frac{qL_2}{L_1 + L_3} \quad (11.14) \qquad q_C = \frac{q_H L_2}{L_1 + L_3} \quad (11.15)$$

11.2.8. Verification & Validation

Verification and validation are necessary to asses the validity of the results given in the previous section. A first stage verification is done through inspection. This meant plotting the moment and shear forces distribution, as well as the stresses distributions. Using the moments and shear forces distributions, one should check that moments and shear forces are zero at the end points, as well as that S_y is the derivative of M_z and S_z the derivative of M_y. Both of these are true, as visible in Figure 11.14. Furthermore, this plot is used to verify the load cases, by checking that the moments and shear forces correspond to the load case in question and that their values are reasonable when compared to other load cases. Plots like Figure 11.16 and Figure 11.15 are used to verify the normal stress. Firstly, it is checked that the normal stress is continuous in each panel. Then, it is verified that for CLC.5, which has a positive load factors, the fuselage experiences tension in the upper panel and compression in the lower panel. The opposite is true for CLC with a negative load factor. Lastly, shear is visually verified using Figure 11.17 and it is checked that it is continuous in each panel. To conclude, the stresses, moments and shear forces distributions are visually verified.

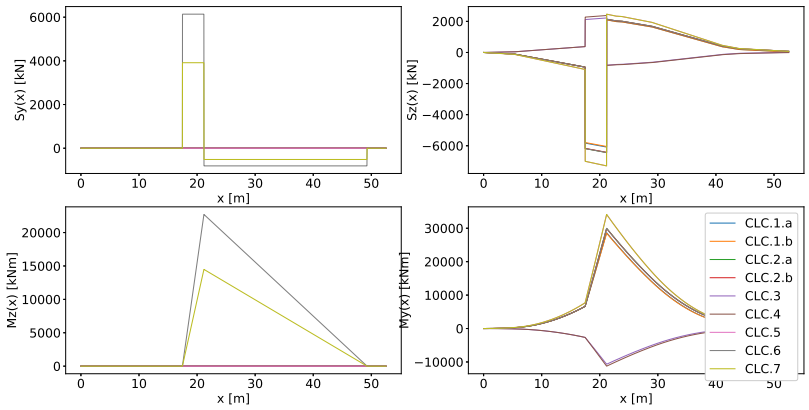

Figure 11.14: Moment and shear forces distributions over the length of the fuselage for all CLC shown in Table 11.4.

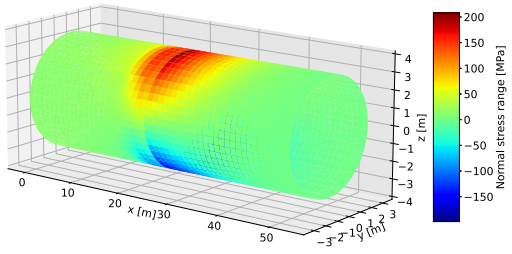

Figure 11.15: Normal stress distribution over the fuselage from CLC.5.

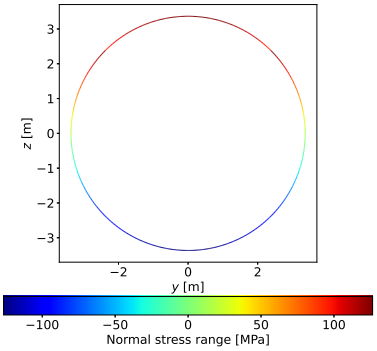

Figure 11.16: Distribution of the normal stress in the fuselage cross section for CLC.5 at location C.

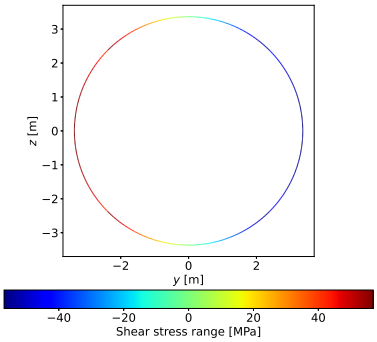

Figure 11.17: Distribution of the shear stress in the fuselage cross section for CLC.5 at location C.

The bending, shear and pressurisation analysis is verified by constructing different models to calculate the same thing. In Section 11.2.2, bending, shear and pressurisation are evaluated at just a few critical points in the cross section. The first model used for comparison and verification checks that the theory and formulas are implemented correctly by conducting the same analysis, but at all points in the cross section. Nonetheless, the results do not differ. The second verification model had the objective of checking the coding itself. It made use of a different coding structure and optimisation function, but again the results were the same. This suggests that the original model is verified.

The buckling model is verified using stress plots and a problem for which the solution is known. Using a stress plots at each load case, it was verified that the maximum compression stress in the panel was indeed the one chosen for the design. Furthermore, as a simple unit test, it was checked that the maximum compression stress in the right panel and the left panel were the same, as the CLC are symmetrical. This means that also the skin thickness and stiffener thickness should be the same in the left and right panels. These were all indeed the case. Additionally, the buckling model was checked by inserting input values from a stiffened panel problem, and verified that the models results corresponded with the problem's answers. Again, there was no deviation. All in all, the buckling model is verified.

Validation of the obtained skin thicknesses and stringer areas was done by comparing the results with the A320 geometry, obtained from Şen's thesis [75]. Even though the actual thicknesses cannot be validated because they're significantly larger due to bigger aircraft dimensions, the change in thickness for the panels along the circumference, as well as along the fuselage length are validated. Throughout the pressurised part of the fuselage close to the front and rear spar of the wing box, the panels get thicker. This increase in thickness is more significant for the side panels. The same increase in thickness is observed for the skin thickness of the fuselage of the A320, thus validating the thickness variation.

11.2.9. Sensitivity Analysis

The sensitivity analysis is performed to assess how sensible the material selection and fuselage geometry are to certain assumptions that were made previously. Part of the sensitivity analysis will focus on changing the load cases by altering the thrust and the yaw angle. CLC.1 and CLC.2 are both evaluated for cruise thrust and for zero thrust. As visible in Figure 11.18,

there is practically no difference in the shear distribution, and therefore also in the moment distribution, between CLC.1.a with cruise thrust and CLC.1.b with zero thrust. Thus, one can say that assessing a load case with and without thrust will have no impact on the final geometry, and therefore defeating the point of assessing more load cases without thrust.

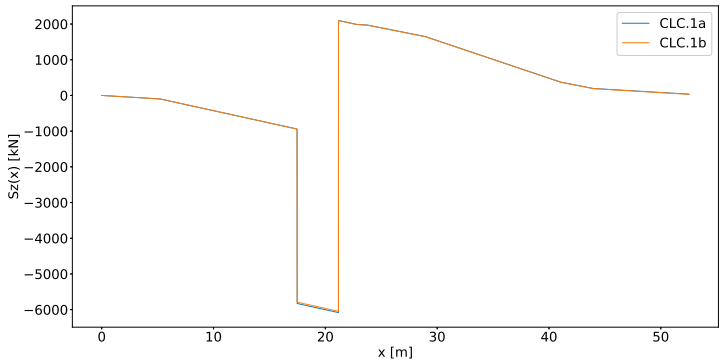

Figure 11.18: S_z distribution for CLC.1.a and CLC.1.b showing that there is practically no difference for zero and non-zero thrust.

Yaw has a significantly larger effect on the results. CLC.6 and CLC.7 include a side load from the vertical tail induced by a ± 20 [deg] yaw. Due to this rather large yaw angle, a large bending moment about the z-axis is induced, which causes the normal stress to rotate, resulting in a maximum compressive and tensile stresses in the side panels. Thus, buckling and damage tolerance tend to be more critical in the side panels, which is unusual. Therefore, in the sensitivity analysis the yaw angle is decreased to ± 10 and ± 5 [deg]. The new results are shown for an aluminium, AA 7075-T6, and for a composite, T800S, in Table 11.7. As expected, reducing the yaw angle mostly effects the fuselage side and bottom panels. However, the only area reductions occur where buckling was critical, as the yaw angle mostly affects buckling and only meagerly damage tolerance. Therefore, composites, which are less critical in buckling, are less sensitive to the yaw angle compared to metals, which suffer more from buckling. Additionally, because of this damage tolerance becomes a more frequent failure mode at lower ψ.

Table 11.7: Result from the sensitivity analysis conducted by changing the yaw angle, ψ.

	AA 7075-T6				T800 S			
Panel	**Original failure mode**	**%ΔA with $\psi = 10$**	**%ΔA with $\psi = 5$**	**New failure mode**	**Original failure mode**	**%ΔA with $\psi = 10$**	**%ΔA with $\psi = 5$**	**New failure mode**
A-B Bottom	Buckling	-1%	-1%	Buckling	DT, Buckling	-2%	-3%	DT, Buckling
A-B Top	DT	0%	0%	DT	DT	0%	-4%	DT
A-B Sides	Buckling	-4%	-6%	Buckling	DT, Buckling	-6%	-9%	DT, Buckling
B-C Bottom	Fatigue	0%	0%	Fatigue	DT, Buckling	-3%	-5%	DT, Buckling
B-C Top	Fatigue	0%	0%	Fatigue	DT	0%	0%	DT
B-C Sides	Fatigue	0%	0%	Fatigue	DT, Buckling	0%	0%	DT
C-E Bottom	Buckling	-13%	-14%	DT	DT	0%	0%	DT
C-E Top	DT, Buckling	-2%	-2%	DT	DT	0%	0%	DT
C-E Sides	DT	0%	0%	DT	DT	0%	0%	DT
Total		**-2.9%**	**-3.4%**			**-0.9%**	**-1.8%**	

Buckling, together with damage tolerance, is the most common failure mode for metals and composites. Therefore, as part of this sensitivity analysis, the assumptions made for buckling and damage tolerance are re-evaluated to access their effect on the structural geometry of the

fuselage. For buckling it was assumed that the skin was simply supported on all sides, thus yielding a buckling constant, C of 4. Now, the skin is assumed clamped on all sides increasing C to 8. For damage tolerance the critical crack size is decreased to 0.3 [m] and crack arrest is ignored. The sensitivity analysis for buckling is conducted with AA 7075-T6, as buckling is more critical in metals, while the damage tolerance sensitivity analysis is performed for T800S for the same reason.

Table 11.8: Result from the sensitivity analysis conducted by changing the critical crack size.

	T800 S			
Panel	**Original failure mode**	Δt **with** $a_{crit} = 0.3$ **m**	ΔA **with** $a_{crit} = 0.3$ **m**	**New failure mode**
A-B Bottom	DT, Buckling	13.29%	-7.48%	DT, Buckling
A-B Top	DT	19.78%	0.00%	DT
A-B Sides	DT, Buckling	15.74%	-27.64%	DT, Buckling
B-C Bottom	DT, Buckling	16.50%	0.98%	DT
B-C Top	DT	19.15%	0.00%	DT, Buckling
B-C Sides	DT, Buckling	17.96%	0.00%	DT
C-E Bottom	DT	18.12%	0.00%	DT
C-E Top	DT	18.24%	0.00%	DT
C-E Sides	DT	18.17%	0.00%	DT
Total		**17.60%**	**-3.86%**	

The buckling sensitivity analysis revealed essentially no change in the geometry, as the buckling constant C, although double, only affects the skin, which provides only a small contribution to buckling resistance. On the other hand, the damage tolerance sensitivity has better results, shown in Table 11.8. A thicker skin is required, which is logical as, even though the critical crack size is now smaller, there is no stiffening element to provide reinforcement to the skin. Therefore, having a thicker skin will stop the crack from rapidly propagating. This analysis shows how sensitive composites are to damage tolerance, thus potentially requiring further iterations to come up with an optimal skin thickness that will withstand the assumed critical crack size. For aluminium alloys this is less the case since other failure modes, such as fatigue and buckling, are more critical.

11.3. Wing Box Structural Analysis

The wing box is an essential component that carries all the loads of the wing during the operational life of the aircraft. These loads result in shear stresses due to shear forces and normal stresses due to bending, which the wing box should be able to withstand. Additionally, the wing box structure must not fail in buckling and fatigue, nor due to external damages (i.e. damage tolerance). To design the wing box structure, the front spar, the rear spar, the upper skin and the lower skin have been optimised for minimum thickness, while ensuring that sheet buckling is prevented. This is done at five locations along the wing span, such to achieve a lighter wing box structure. In addition, the analysis is performed for the materials presented in Section 11.1.

The following sections provide an explanation of the numerical model that has been created to design the wing box. First of all, the load cases that have been considered in the analysis will be discussed. After that, the reader is introduced to the wing box geometry that is used to calculate the centroid, the areas, and the moments of inertia of the cross-section. Afterwards, the

approach to compute shear and bending stresses is described. Thereafter, a material is selected that is optimal within the constraints set by requirements, and the final skin thicknesses and numbers of stringers are presented. Subsequently, it is checked whether the stresses in the wing box do not exceed the stresses for fatigue and damage tolerance. Finally, the entire program will be verified and validated, and a sensitivity analysis is performed.

11.3.1. Wing Box Load Cases

When modelling the wing box structure, six load cases have been considered. The load cases are summarised in Table 11.9.

Table 11.9: Load cases considered for wing box design.

	Description	Altitude	Velocity	Configuration	Thrust setting	Load factor
LC.1	Taxi	h_{sea}	0	CL_{clean}	0	1
LC.2	Take-off	h_{sea}	V_{to}	CL_{to}	T_{to}	n_{max}
LC.3	Cruise	h_{cruise}	V_{cr}	CL_{clean}	T_{cr}	n_{max}
LC.4	Loiter	h_{loiter}	V_{loiter}	CL_{clean}	T_{cr}	n_{max}
LC.5	Approach	h_{sea}	V_{app}	CL_{max}	0	n_{max}
LC.6	Landing impact	h_{sea}	0	CL_{max}	0	-2.6

The loads that are introduced on the wing box are influenced by the load case that is considered. For loiter (LC.4), the loiter altitude (h_{loiter} = 2133 [m]) has been based on the aircraft hold altitude of London Heathrow Airport[9], and the loiter velocity (V_{loiter} = 110.42 [m/s]) is optimised for maximum endurance (Section 13.3).

Upon runway impact during landing (LC.6), the maximum load factor of the impact is set equal to the Airbus A320 vertical G-force hard landing threshold, which equals 2.6G ([88]). In addition, to obtain an extreme load case, it is assumed that all lift has been dumped from the wings, such that the entire impact load is taken up by the landing gear. This means that there is a maximum downward bending moment outboard of the landing gear due to the wing, the engine weight and, the fuel weight (in case of the hybrid configuration only). Regarding downward bending, the most extreme load case is obtained when the entire wing is filled with biofuel. Zero lift is obtained at an effective velocity of 0 [m/s].

Computation of the V-n diagram

The V-n diagram shows the different load factors achieved at different velocities. It consists of a manoeuvre diagram and a gust diagram, which are superimposed in order to find the maximum load factor. The computation of the manoeuvre diagram will not be explained in detail but the key arguments will be elaborated upon. The maximum positive load factor follows from CS 25.337(b) [78]. This requirement describes that the positive manoeuvring load factor for any speed up to the dive speed V_D may not be less than n_{max} and is described by Equation 11.16,

$$n_{max} = 2 + \left(\frac{24000}{W + 10000} \right) \tag{11.16}$$

where W is the design maximum take-off weight in [lb]. The negative limit manoeuvring load factor follows from 25.337(c) [78], which describes that the negative limit manoeuvring load factor may not be less than -1 and must linearly decrease from the value at cruise velocity V_c to zero at V_D.

[9] http://news.bbc.co.uk/2/hi/uk_news/7196158.stm

The gust diagram has been constructed as described by CS 25.341 [78]. The gust design velocity follows from Equation 11.17,

$$U_{ds} = U_{ref} F_g \left(\frac{H}{107} \right)^{1/6} \tag{11.17}$$

where U_{ref} is the reference gust velocity, F_g is the flight alleviation factor and H is the gust gradient distance. The gust reference velocity linearly decreases from 17.07 [m/s] EAS at sea-level to 13.41 [m/s] EAS at 4572 [m] and then linearly decreases to 6.36 [m/s] EAS at an altitude of 18288 [m], as described by CS 25.341(a)(5) [78]. The flight alleviation factor is a function of the maximum landing weight, maximum take-off weight, maximum zero fuel weight and maximum operating altitude. The corresponding equations can be found in CS 25.341(a)(6).

Assuming quasi-steady aerodynamics, the load factor variation with time can be described by Equation 11.18 [89],

$$\Delta n_s(t) = \pm \frac{U_{ds}}{2g} \cdot \left[\omega \sin(\omega t) + \frac{1}{1 + (\omega\lambda)^{-2}} \left(\frac{1}{\lambda} e^{-t/\lambda} - \frac{1}{\lambda} \cos(\omega t) - \omega \sin(\omega t) \right) \right], \quad 0 \leq t \leq 2\pi/\omega \tag{11.18}$$

where the radial frequency is given by ω, and the time constant by λ. The corresponding formulas to calculate these parameters can be found in Equation 11.19 and 11.20. The minimum and maximum gust load factor are then equal to $1 - \Delta n_s$ and $1 + \Delta n_s$.

$$\omega = \frac{\pi V}{H} \tag{11.19}$$

$$\lambda = \frac{W/S}{C_{L_\alpha}} \cdot \frac{2}{\rho V g} \tag{11.20}$$

Critical loading case

The maximum load factor (n_{max} = 2.8 [-]) has been found by generating multiple V-n diagrams, and then selecting the critical diagram that shows the largest load factor. This diagram is presented in Figure 11.5. It can be seen that the maximum load factor has been obtained at cruise velocity.

11.3.2. Shear, Moment and Free Body Diagrams

The free-body-diagrams of the wing box in flight and during ground operation can be found in Figure 11.19 and Figure 11.20, respectively. These figures show the different forces acting on the wing box structure. The shear forces that have been included in the wing box model are lift, wing weight, engine weight, engine thrust, the weight of biofuel stored in the wings and the resultant force on the landing gear. The latter two forces are optional, as the aircraft has no biofuel stored in its wings when it runs on hydrogen only, and the resultant force from the landing gear is only present when the aircraft is in contact with the ground.

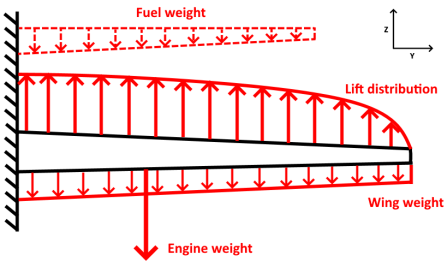

Figure 11.19: Free body diagram of the wing structure in flight

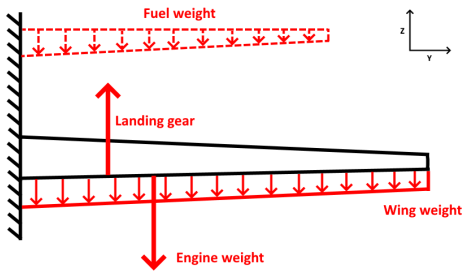

Figure 11.20: Free body diagram of the wing structure on ground

The shear force distribution along the half span for the clean and landing configuration can be found in Figure 11.21 and Figure 11.22 respectively. These graphs show the shear flow distribution for a full hydrogen aircraft, so there is no shear force due to fuel weight present. It should be noted that the wing shear force for the cruise configuration has been computed with the MTOW in a full hydrogen configuration. The shear force diagram along the X-axis has been omitted since drag is neglected in this analysis. This only leaves the engine thrust, which introduces a constant shear force along the span between the root and the engine mounting position. The moment diagram along the Z-axis will also be omitted following the same reasoning.

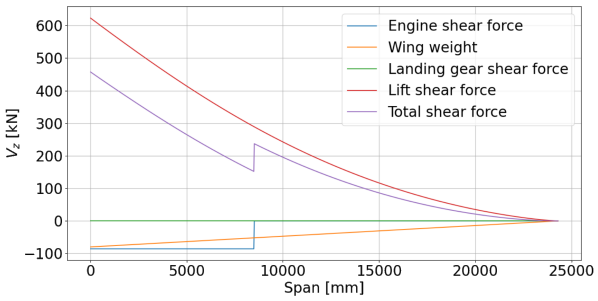

Figure 11.21: Shear force in Z-direction along the span in cruise conditions, subjected to n $=$ n_{max}. 100% hydrogen propulsion.

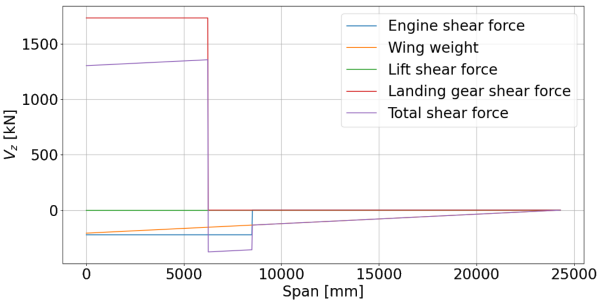

Figure 11.22: Shear force in Z-direction along the span at landing impact, subjected to n $= 2.6$. 100% hydrogen propulsion.

For comparison, the shear force diagrams including biofuel weight are shown in Figure 11.23 and Figure 11.24. These graphs show the shear force distribution in the wing for an aircraft that has 100% biofuel propulsion. It is clearly shown that the fuel weight decreases the shear force at the root.

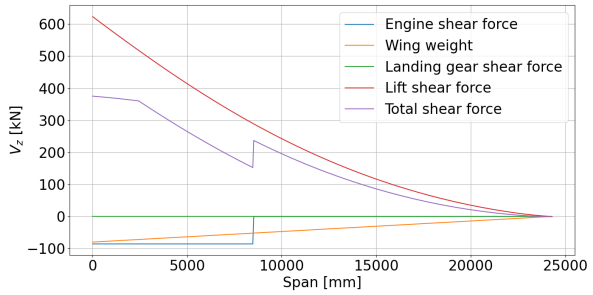

Figure 11.23: Shear force in Z-direction along the span in cruise conditions, subjected to n $=$ n_{max}. 100% biofuel propulsion.

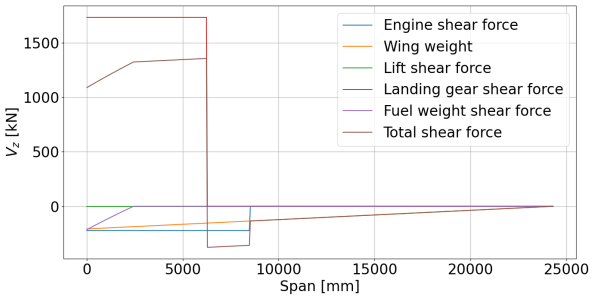

Figure 11.24: Shear force in Z-direction along the span at landing impact, subjected to n $= 2.6$. 100% biofuel propulsion.

The moment diagrams around the X-axis are presented in Figure 11.25 and 11.26. The bending moment along the span due to lift has been obtained from XFLR5 and has been corrected for the flight velocity. Furthermore, in both cases, the tank moment along the span is zero, since the maximum bending moment at the root is achieved when no bending relief is provided by the biofuel stored in the wings.

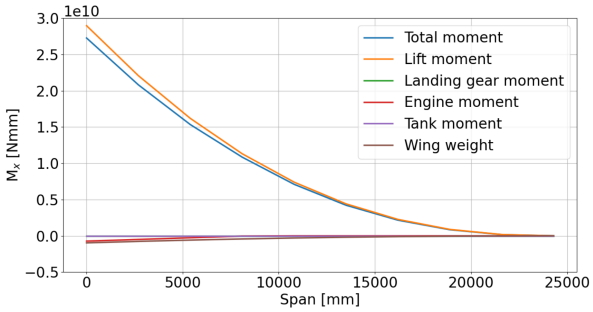

Figure 11.25: Moment around the X-axis in cruise conditions, subjected to n = n_{max}

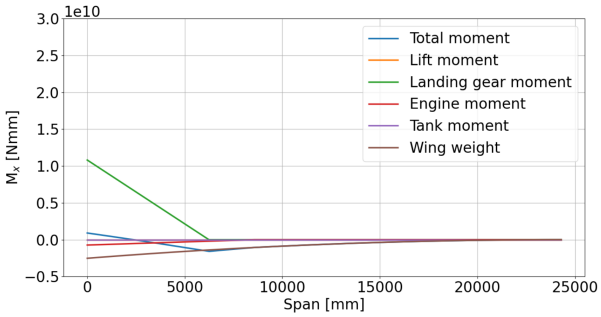

Figure 11.26: Moment around the X-axis at touchdown, subjected to an impact load of n = 2.6.

11.3.3. Wing Box Geometry

Before the load analysis is performed, the geometry and a coordinate system have to be defined. The coordinate system that is used has its origin on the leading edge, where the X-axis points towards the trailing edge and the Z-axis points upwards. As the coordinate system should be right-handed, the Y-axis points in the spanwise direction from the root to the tip of the wing.

The wing box consists of four skin panels: a front spar, a rear spar, an upper sheet and a lower sheet. In the analysis, these panels have to be fitted inside the airfoil, which is a NASA-SC(2)-0612 (Section 6.1). In reference aircraft, for example the A320, the wing box upper sheet is part of the wings skin. However, in this analysis the wing box will be modelled as a unsymmetrical rectangular box. The front and rear spar are fitted inside the airfoil at 15% and 60% of the local wing chord length respectively, as obtained from literature [90]. The wing box geometry that has been used as a basis for the wing box design is shown in Figure 11.27. Note that the wing box is not symmetric: the upper and lower skin have a different angle with respect to the horizontal.

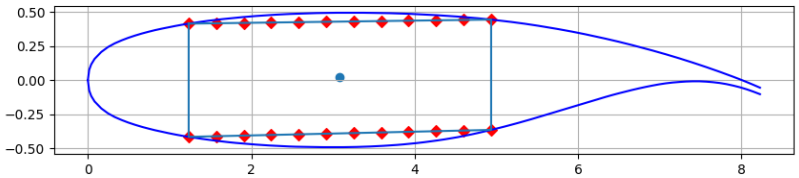

Figure 11.27: Basis for the geometry of the wing box inside the airfoil. Note that the number of stringers and skin thicknesses are not equal to the final wing box design.

11.3.4. Shear Stresses

Due to the shear forces that the wing box experiences, as explained in Section 11.3.2, there will be shear stresses introduced in the wing box. The shear stress is related to the shear flow in each skin section via the skin thicknesses (see Equation 11.21).

$$\tau = \frac{q}{t} \tag{11.21}$$

For each load case, which determines the shear force on the wing box, the shear flows have been computed using Equation 11.22 and Equation 11.23 [74]. In analysing shear flow, an

imaginary 'cut' was made in the front spar of the wing box, where, by definition, the shear flow then equals zero. Starting at the 'cut', the base shear flows are calculated using the first part of Equation 11.22. Using Equation 11.23, the redundant shear flow is calculated to close the 'cut'.

$$q_s = -\left(\frac{V_x I_{xx} - V_z I_{xz}}{I_{xx} I_{zz} - I_{xz}^2}\right) \int_0^s t x ds - \left(\frac{V_z I_{zz} - V_x I_{xz}}{I_{xx} I_{zz} - I_{xz}^2}\right) \int_0^s t z ds + q_{s,0} \tag{11.22}$$

$$q_{s,0} = -\frac{\oint q_b / G t ds}{\oint ds / G t} \tag{11.23}$$

$$q_t = \frac{T}{2A_m} \tag{11.24}$$

As the thicknesses of the four wing box panels are variable and not necessarily equal to one another, and the wing box is asymmetric (see Figure 11.27), the location of the shear centre is unknown. However, it is known that for a rectangular section, made from one material, the shear centre is located at the centroid of the section, as a shear force acting through the centroid of a rectangular section will not introduce a torque on the section.

As the wing box is almost a rectangular section (see Figure 11.27), it is therefore assumed that the shear centre is located at the centroid of the wing box when it has equal skin thicknesses in the front and rear spar and equal skin thicknesses in the top and bottom panel.

In addition, it is assumed that all shear forces act through the shear centre of the wing box, except for the lift force, which acts through the aerodynamic centre of the wing. The aerodynamic centre is located at 31% of the chord length for a clean configuration and at 37% of the chord length for landing configuration (all HLD deployed). As a result, the lift force is replaced by a pure shear force, acting through the shear centre in positive Z-direction, and a torque about the Y-axis using superposition. This aerodynamic torque introduces shear stresses in the wing box, and the corresponding shear flow q_t is computed using Equation 11.24. In this equation, T is equal to the aerodynamic torque in [Nmm] and A_m is the enclosed area of the wing box cross-section in [mm^2].

In computing the skin thicknesses of the wing box, a constraint is set on the maximum shear stress that may be experienced by the wing box. This is equal to the yield stress of the material, divided by a safety factor of 1.5.

11.3.5. Bending Moment

The wing box is subjected to moments about its X-axis and its Z-axis. During flight, the moment about the X-axis is mainly dominated by the lift distribution over the wing, whereas the moment about the Z-axis is mainly dominated by the engine thrust. In case hardly any lift is produced by the wing (i.e during taxi or landing), the bending moment about the X-axis is mainly dominated by the wing weight and the resultant force on the landing gear.

The bending stress at a location (X, Z) can be obtained from Equation 11.25, where I_{xx} [mm^2] and I_{zz} [mm^2] denote the second moment of area around the X- and Z-axis respectively, I_{xz} denotes the product moment of inertia [mm^2] and (X, Z) denotes the coordinates with respect to the centroid of the wing box cross-section. Stringers increase the moment of inertia along the respective axes. For this analysis, the HAT-stringer is selected following the same reasoning as described in Section 11.2.2. The dimensions of this stiffening element can be found in Figure 11.28 and are constant along the span. The shape and cross-sectional area will be

constant for both the upper and lower skin, unlike the A320 reference aircraft which features I-shaped stringers on the top panel and T-shaped stringers on the bottom panel[10].

$$\sigma_y = -\frac{(M_z I_{xx} - M_x I_{xz})\, x - (M_x I_{zz} - M_z I_{xz})\, z}{I_{xx} I_{zz} - I_{xz}^2} \quad (11.25) \qquad \sigma_{cr} = K_c E \left(\frac{t}{b}\right)^2 \quad (11.26)$$

The dominant contribution of the lift distribution over the span creates tension in the lower part and compression upper part of the wing box. Due to compression in the upper skin, buckling may occur. This reduces the load bearing capability of the sheet, and therefore should be accounted for. The critical buckling stress at which the sheet starts buckling, is described by Equation 11.26 [91], where K_c denotes the flat plate buckling coefficient [-], t the thickness of the sheet and b the stringer pitch [mm]. In order to mitigate this is to sufficiently strengthen the wing box to keep the σ_y below σ_{cr}.

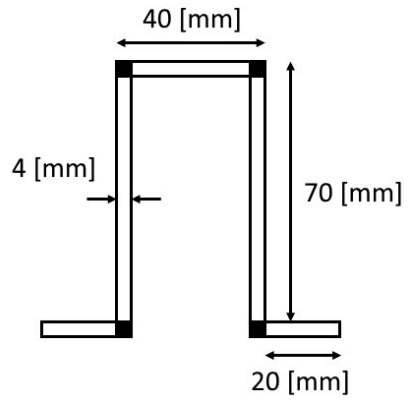

Figure 11.28: Hat stringer for wing box upper and lower skin panels. Area equals 880 [mm^2].

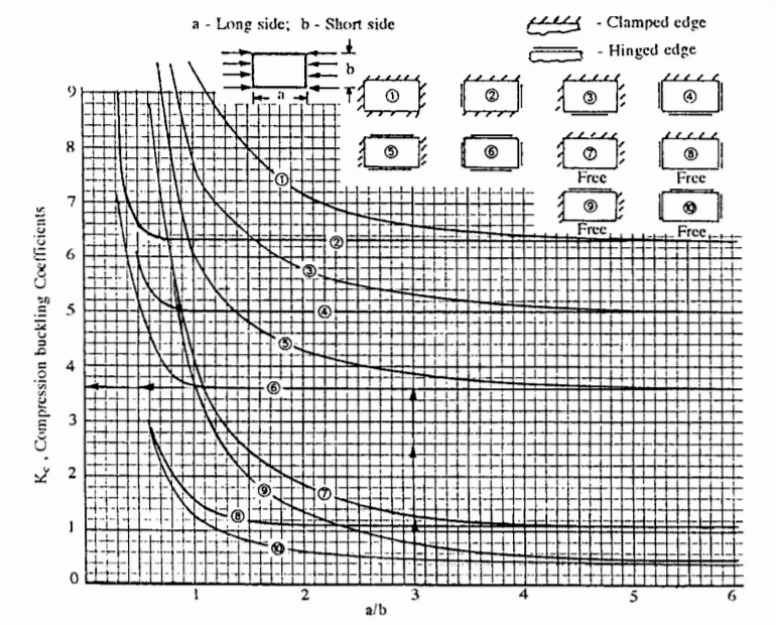

Figure 11.29: K_c coefficients for compression [91].

In the wing box analysis, Figure 11.29 is used to determine K_c. In this graph, a denotes the distance between two ribs and b the stringer pitch. Between two ribs, the wing box can be modelled as (6) (as defined in Figure 11.29), with 4 hinged edges. For large a»b, K_c converges to 3.6 in graph (6).

11.3.6. Material Selection and Final Geometry

For the wing box material selection, a similar reasoning as the one used for the fuselage applies. The material properties and characteristics stated in Table 11.5 also apply to the wing box materials. For GLARE, the material properties in transverse direction are used, because the properties of GLARE are less good in transverse direction compared to longitudinal direction. In an early stage of the optimisation, it was found that GLARE resulted in skin thicknesses and numbers of stringers that were almost double the numbers that were found for aluminium

[10] https://www.gettyimages.nl/detail/nieuwsfoto%27s/employees-work-on-a-section-of-airbus-a320-wing-inside-nieuwsfotos/981030088

alloys and carbon fibre laminates. Therefore, the analysis for GLARE has been omitted to speed up the optimisation process.

In the end, using carbon fibre laminates as wing box material resulted in a significantly lighter wing box structure. The properties of the carbon fibre laminates for the wing box are equal to the properties for the fuselage structure, as only one lay-up is assumed. However due to the strict cost requirement, they were not selected. After carbon fibre laminates, the best performing aluminium alloy in terms of structural weight was AA 7085-T6. The weight of half the wing box span equals 6800 [kg]. The results of the other materials together with a total cost estimation can be found in Table 11.10.

Table 11.10: Wing box weights and cost for the different materials.

Material	AA 7075-T6	AA 7475-T761	AA 7085-T6	AA 2024-T3	Airware® 2050-T84	T300 carbon	T700G carbon	T800S carbon
Wing weight [kg]	7009.46	7635.33	6799.09	9493.62	6924.87	5698.18	5780.93	4977.25
Cost [EUR/kg]	5.03	5.03	5.03	5.03	10	33.5	33.5	33.5
Total cost [EUR]	35,257.57	38,405.70	34,199.44	47,752.91	62,948.72	190,889.16	193,661.25	166,737.79

The final geometry is presented in Table 11.11. To make the design lightweight and more sustainable by using less material, it was decided to change the thickness and stringer layout at five rib locations along the span. One notable place where the layout changes is at the first rib outboard of the landing gear (at y = 6300 [mm]). During a hard landing, this is the point where most tension will be experienced in the upper skin panel, due to large vertical G-forces (2.6G max.) and downward bending.

Table 11.11: Final geometry of the wing box.

Material: AA7085-T6 | Stringer area: 880 [mm^2] (hat stringer)							
Spanwise location: 0 $\leq$ y < 2400 [mm]							
$t_{front\ spar}$ [mm]	$t_{rear\ spar}$ [mm]	$t_{top\ skin}$ [mm]	$t_{bottom\ skin}$ [mm]	$n_{stringers\ top}$ [-]	$n_{stringers\ bottom}$ [-]	$\sigma_{max,\ upper}$ [MPa]	$\sigma_{max,\ lower}$ [MPa]
11.55	11.67	19.42	20.37	22	18	353.20	350.15
Spanwise location: 2400 $\leq$ y < 6300 [mm]							
$t_{front\ spar}$ [mm]	$t_{rear\ spar}$ [mm]	$t_{top\ skin}$ [mm]	$t_{bottom\ skin}$ [mm]	$n_{stringers\ top}$ [-]	$n_{stringers\ bottom}$ [-]	$\sigma_{max,\ upper}$ [MPa]	$\sigma_{max,\ lower}$ [MPa]
11.31	10.82	16.66	17.29	22	18	353.16	349.55
Spanwise location: 6300 $\leq$ y < 10900 [mm]							
$t_{front\ spar}$ [mm]	$t_{rear\ spar}$ [mm]	$t_{top\ skin}$ [mm]	$t_{bottom\ skin}$ [mm]	$n_{stringers\ top}$ [-]	$n_{stringers\ bottom}$ [-]	$\sigma_{max,\ upper}$ [MPa]	$\sigma_{max,\ lower}$ [MPa]
11.00	11.72	12.51	13.77	20	15	348.11	349.47
Spanwise location: 10900 $\leq$ y < 14000 [mm]							
$t_{front\ spar}$ [mm]	$t_{rear\ spar}$ [mm]	$t_{top\ skin}$ [mm]	$t_{bottom\ skin}$ [mm]	$n_{stringers\ top}$ [-]	$n_{stringers\ bottom}$ [-]	$\sigma_{max,\ upper}$ [MPa]	$\sigma_{max,\ lower}$ [MPa]
9.78	10.02	6.17	8.11	20	15	343.85	338.46
Spanwise location: 14000 $\leq$ y $\leq$ 24298 [mm]							
$t_{front\ spar}$ [mm]	$t_{rear\ spar}$ [mm]	$t_{top\ skin}$ [mm]	$t_{bottom\ skin}$ [mm]	$n_{stringers\ top}$ [-]	$n_{stringers\ bottom}$ [-]	$\sigma_{max,\ upper}$ [MPa]	$\sigma_{max,\ lower}$ [MPa]
9.82	8.64	5.86	4.92	18	11	252.20	331.40

The most critical load case that determined the skin thicknesses and the number of stringers is bending during cruise flight with a load factor of 2.8 (LC.6). The stresses maximum stresses that are encountered in the upper and lower skin panels are provided in the last two columns of Table 11.11. These stresses should not exceed the yield stress of AA 7085-T6, including a safety factor of 1.5. In addition to Table 11.11, Table 11.12 shows the maximum stresses for a load factor of 1.0 in cruise flight, as this will be used to asses whether the aircraft complies with constraints on fatigue and damage tolerance.

Table 11.12: Maximum stresses encountered in the wing box for cruise flight, n = 1.0.

Material: AA7085-T6 | σ_y = 530 [MPa] | n = 1.0		
	$\sigma_{max,\ upper}$ [MPa]	$\sigma_{max,\ lower}$ [MPa]
$0 \leq y < 2400$	111.66	110.74
$2400 \leq y < 6300$	111.46	110.39
$6300 \leq y < 10900$	109.94	109.50
$10900 \leq y < 14000$	108.75	107.05
$14000 \leq y \leq 24298$	79.10	103.94

11.3.7. Wing Box Fatigue

In every flight cycle, the wing box will be loaded in two extreme load cases, which will result in a minimum and a maximum stress in each wing box component. The load cases that are considered as extreme are cruise flight (LC.3) and (hard) landing (LC.6). During cruise flight, the wing box is exposed to a maximum upward bending moment, which results in compression in the upper sheet and tension in the lower sheet. During hard landing, the wing box outboard of the landing gear will bend downwards, and the top panel will be loaded in tension and the bottom panel will be loaded in compression.

Hence, the entire wing box section will encounter a maximum and a minimum stress due to the two extreme load cases during every flight cycle. These stresses are calculated as explained in Section 11.3.5. Adding the absolute values of the maximum and minimum stress and dividing by a factor two results in the stress amplitude σ_{amp}. It must be verified that the stress amplitude in the wing box does not exceed the fatigue stress of the materials as explained in Section 11.1. For AA7085-T6, the fatigue stress equals 58.96 [MPa]. Note that for the fatigue stress analysis, a load factor (n) equal to 1.0 is used for cruise, as the the maximum load factor of 2.8 will only rarely occur during the operational life of the aircraft. In addition, it should be noted that the landing impact load factor (2.6G) leads to a conservative approach to fatigue, because the aircraft structure will not be exposed to a hard landing during every flight in reality.

With the wing box geometry presented in Table 11.11, the stress amplitude is calculated in the four corners of the wing box, as these points lie most far away from the neutral axis of the wing box cross-section, independent of the orientation of the neutral axis. The calculated stress amplitudes are presented in Table 11.13. It can be concluded that stress amplitudes in the wing box do not exceed the fatigue stress of AA7085-T6.

Table 11.13: Stress amplitudes in the wing box corners. TL = top left corner, TR = top right corner, BR = bottom right corner, BL = bottom left corner.

Material: AA7085-T6				
Spanwise location [mm]	$\sigma_{amp,\ TL}$ [MPa]	$\sigma_{amp,\ TR}$ [MPa]	$\sigma_{amp,\ BR}$ [MPa]	$\sigma_{amp,\ BL}$ [MPa]
$0 \leq y < 2400$	42.637	48.108	42.227	50.083
$2400 \leq y < 6300$	27.240	32.447	26.901	33.675
$6300 \leq y < 10900$	27.091	23.255	26.983	24.474
$10900 \leq y < 14000$	26.231	25.558	25.155	25.821
$14000 \leq y \leq 24298$	20.091	19.386	25.911	26.401

11.3.8. Wing Box Damage Tolerance

Similarly to what is explained in Section 11.2.4, the wing box should remain operational when damage has occurred in the structure. Similar to the analysis for the fuselage, damage can occur due to an uncontained engine failure, where one of the turbine blades perforates the wing box. It is assumed that this will create a crack size of 0.50 [m]. Using Equation 11.12, the stress for damage tolerance that may not be exceeded equals 79.66 [MPa] for AA7085-T6. The maximum stresses that occur in the wing box exceed this value, which means that the damage tolerance requirement is not met. However, this analysis did not include the principle of crack arrest. As the crack size approaches the rib pitch, the effective damage tolerance stress increases (see Figure 11.10). As explained in Section 11.3.8, the rib pitch around the engine, which is located at 35% of the wing span (b), equals 65 [cm], and the effective stress for damage tolerance is multiplied by 1.5. This factor is lower than the 1.6 taken for the fuselage because the rib pitch is larger than the crack size, while the crack size of the fuselage is the same as the frame spacing. As a result, the stress for damage tolerance becomes 119.50 [MPa]. In this case, the maximum stresses that are experienced during cruise flight (n = 1.0) will not exceed the stress for damage tolerance.

Rib pitch

From literature, a rib pitch of 20 to 100 cm was obtained[11]. However, in comparison with modern reference aircraft, no rib pitch between 20 to 40 [cm] was found. Therefore, the minimum rib pitch will be set to 40 [cm] along locations close to the root. The rib pitch in these aircraft also increases along the span, since the load on the wing decreases along the span. Following this reasoning, the rib pitch can be defined as presented in Table 11.14. To get a better view of the spanwise locations of the ribs, a 3D has been provided in Figure 11.30. As this preliminary rib pitch is purely based on literature, a more detailed analysis should be carried out in the future on the rib pitch and rib design.

Table 11.14: Rib pitch along the wing span.

Start	End	Rib Pitch [cm]
0	$0.1 \cdot b/2$	40
$0.1 \cdot b/2$	$0.3 \cdot b/2$	50
$0.3 \cdot b/2$	$0.5 \cdot b/2$	60
$0.5 \cdot b/2$	$0.7 \cdot b/2$	65
$0.7 \cdot b/2$	$0.8 \cdot b/2$	0.75
$0.8 \cdot b/2$	$b/2$	0.85

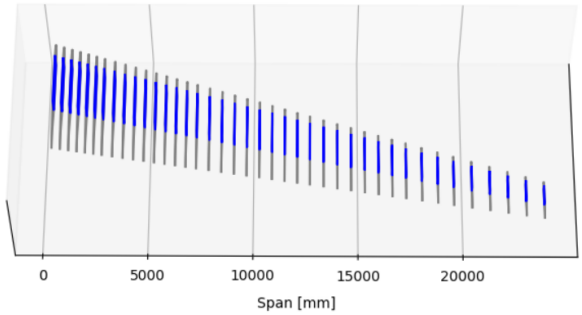

Figure 11.30: Rib locations along the span, visualised.

11.3.9. Aileron reversal

Aileron reversal, also called control reversal, occurs when the wing is insufficient torsionally stiff along the lateral axis when a control input is given[12]. In order to verify the compliance with AE-STR-03, i.e. no aileron reversal shall be present in the mission profile, it is verified that the torsional stiffness at the aileron is sufficient to prevent aileron reversal. For this analysis, two dimensional flow is assumed. Therefore, one can make use of Section 28.3.2 from Megson [92]. The speed at which aileron reversal occurs may not be lower than the manoeuvre speed

[11] https://ocw.tudelft.nl/wp-content/uploads/AE1102_Structures_Slides_4.pdf
[12] https://aviation.stackexchange.com/questions/2405/how-does-aileron-reversal-work

V_A [m/s], as prescribed by CS 25.1583(a)(3)(i) and can be calculated using Equation 11.27 [92, 78],

$$V_r = \sqrt{\frac{-K\left(\partial C_L/\partial \xi\right)}{\frac{1}{2}\rho S c\left(\partial C_{M,0}/\partial \xi\right)\left(\partial C_L/\partial \alpha\right)}} \quad (11.27) \qquad J = \frac{4A^2}{\oint \frac{ds}{t}} \quad (11.28)$$

where K is the torsional stiffness ($K = G \cdot J$) in [N/m^2], $\partial C_L/\partial \xi$ is the rate of change of the lift coefficient with aileron deflection ξ in [rad^{-1}], $\partial C_{M,0}/\partial \xi$ is the rate of change of the wing pitching moment coefficient with aileron deflection in [rad^{-1}] and $\partial C_L/\partial \alpha$ is the wing lift gradient in [rad^{-1}]. The torsional constant is calculated using Equation 11.28, where A is equal to the enclosed area.

From the analysis it follows that the aileron reversal speed at sea-level and cruise are equal to 263 [m/s] and 483 [m/s], respectively. This is below the manoeuvre speed V_A. Therefore, it has been verified that our aircraft structure is compliant with CS 25.1583(a)(3)(i).

11.3.10. Verification and Validation of Wing Box programs

As a complicated model is used to design the wing box, it is necessary to ensure that all calculations are verified and the outcomes are validated. Alongside code verification, which includes looking for programming mistakes, the analysis of the shear stresses and the bending stresses have to be verified.

Shear stress analysis verification

In order to verify that the shear stresses in the wing box are realistic, the shear flows that have been found in the wing box cross-section are compared to a section in which the shear flow distribution is known: a rectangle. To see whether the shear flows are calculated correctly and have the correct sign, the program is used to compute the shear flow in a rectangular wing box cross-section with an equal thickness in all skin panels, when it is subjected to a load of 10 [kN] in either positive X- or Z-direction. The results are shown in Figure 11.31 and Figure 11.32. The results match with what is expected from theory and intuition: for a shear force in positive X-direction, the shear flow is zero at Z=0 and the shear flow is maximum at X=0. For a shear force in positive Z-direction, the shear flow is zero at X=0 and the shear flow is maximum at Z=0.

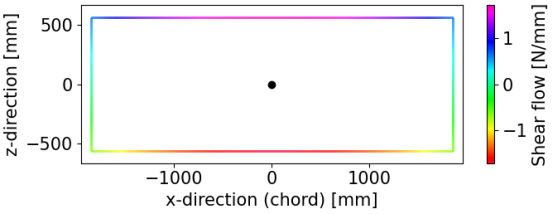

Figure 11.31: Shear flow distribution in rectangular cross-section. V_X = 10 [kN] (positive X-direction), t = 10 [mm]. Clockwise direction of shear flow is positive.

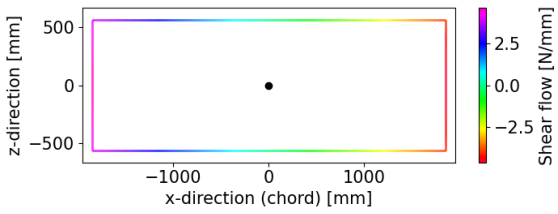

Figure 11.32: Shear flow distribution in rectangular cross-section. V_Z = 10 [kN] (positive Z-direction), t = 10 [mm]. Clockwise direction of shear flow is positive.

In addition to using a known shear flow distribution for verification, the assumptions made in Section 11.3.4 have to be verified. These assumptions are listed below.

- **SF-1** - The shear centre of the wing box is located at the centroid of the wing box.
- **SF-2** - Drag is neglected in the analysis of shear flows.
- **SF-3** - The stringers do not carry any shear stress.

Figure 11.33 and Figure 11.34 show the shear flow distribution in the wing box cross-section and the rectangular section at the wing root, respectively. Both sections are modelled with equal skin thicknesses, i.e. the front spar thickness of the actual wing box equals the front spar thickness of the rectangular section. The shear forces are considered for cruise flight, with a maximum engine thrust setting (V_x = 128 [kN]) and a maximum lift force (V_z = 457 [kN]) at the root. These loads are obtained from the shear forces presented in Section 11.3.2. The aerodynamic torque has also been included, which results in a positive clockwise shear flow, as the aerodynamic centre lies in front of the centroid of the wing box. Using Equation 11.24, the constant shear flow due to the torque equals 228 [N/mm]. Hence, the absolute values of the minimum and maximum shear flow are not equal in the cross-section, as the the shear flow due to the torque is positively added in clockwise direction of the shear flow. As the shear force in Z-direction is the largest, one would expect this shear flow to be most dominant. This is the case, as the maximum and minimum shear flows are found in the front and rear spar, respectively. Again, the shear flow in the rear spar is lower, as the shear flow is defined positive in clockwise direction, which means that a pure shear force in positive Z-direction produces a negative shear flow in the rear spar (see also Figure 11.32).

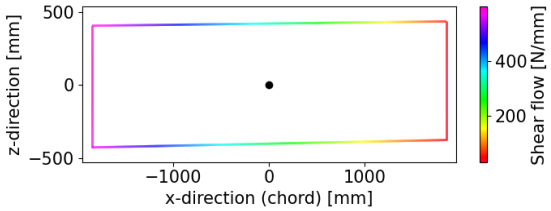

Figure 11.33: Shear flow distribution in wing box cross-section. V_z = 457 [kN] (positive z-direction), V_x = 128 [kN] (positive x-direction). Clockwise direction of shear flow is positive.

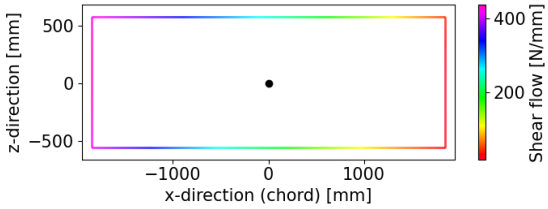

Figure 11.34: Shear flow distribution in rectangular cross-section. V_z = 457 [kN] (positive z-direction), V_x = 128 [kN] (positive x-direction). Clockwise direction of shear flow is positive.

From comparison between the rectangular section (Figure 11.34 and the wing box section (Figure 11.33), one observes that the shear flow distribution in the actual wing box cross-section is similar to the shear flow distribution in the rectangular section. As the actual wing box is nearly rectangular, this outcome lives up to expectations. In addition, it can be seen that the shear flow is not distributed symmetrically around the X- and Z-axis. This has to do with the fact that two forces (V_x and V_z) cause shear in the cross-sections. Due to V_x, the shear flow in the bottom skin is negative and the shear flow in the upper skin is positive. Due to V_z, the shear flow in the front spar is positive and the shear flow in the rear spar is negative. As a result, the magnitude of the shear flow is the lowest in the bottom right corner of the wing box, whereas it is the highest in the top left corner. Note that there are no negative shear flows in the wing box due to the positive aerodynamic torque in the wing box. This verifies that the program superimposes the shear flows due to V_x and V_z correctly. Hence, the assumption to set the shear centre equal to the centroid of the wing box cross-section (**SF-1**) result in a shear flow distribution that makes sense.

Assumptions **SF-2** and **SF-3** also result in a conservative load analysis. As the drag is neglected, the only shear force acting in x-direction is the engine thrust. The aerodynamic drag of the wing is directed opposite of the engine thrust, which means that the total shear force V_x on the wing would decrease. Hence, if drag is neglected, the shear force in X-direction is overestimated, resulting in a more conservative design. Assumption **SF-3** omits the effect of stringers in carrying shear in the wing box. In designing the wing box, this means that all shear is carried by the wing box skins. Essentially, this would mean that the wing box skins

are slightly over-designed, as the stringers could take up part of the shear stresses in reality.

Bending stress verification
The following assumptions are made within the bending moment program:

- **BND-1** - The bending moment along the span can be accurately modelled by aerodynamic analysis programs, e.g. XFLR5.
- **BND-2** - The cross-section of the wing box is assumed to be thin-walled.
- **BND-3** - Stringers are assumed to be point areas located on the skin.
- **BND-4** - Wing drag is assumed to be zero.

The first assumption, **BND-1**, states that the bending moment can be accurately modelled by aerodynamic analysis programs. In the bending analysis, use was made of XFLR5 in order to compute the bending moment due to lift along the span. Validation of this program was already touched upon in Section 6.5 and will therefore not be repeated. Furthermore, the wing drag is assumed to be zero following **BND-2**. This overestimates the shear force in X-direction and moment around the Z-axis, since drag acts in the opposite direction of the thrust providing some relief. Hence, this assumption overestimates the bending moment around the Z-axis and the therefore the load that the structure is subjected to.

BND-3 and **BND-4** both introduce errors in the moment of inertia. **BND-3** entails among other things that higher order terms of the skin thickness are neglected, omitting their contribution. However, the effect of this is assumed to be small due to the large h»t. **BND-4** neglects the contribution of the moment of inertia around the stringers' own axis, therefore underestimating their contribution. Furthermore, the centroid is also assumed to be located on the skin. This overestimates the moment of inertia slightly, due to the increased distance from the centroid of the wing box. Due to the large area of the stringers at a large distance from the centroid, this is assumed to be reasonable.

In order to verify if the program provides an output that follows intuition, use was made of a 3D plot. In cruise, due to the spanwise lift distribution, it is expected that this will create tension in the lower panel and compression in the upper panel. Figure 11.35 shows the bending stress along the upper panel and front spar. The figure shows that the upper panel is in compression, close to the yield stress corrected by the factor of safety at the root. Therefore, the yield requirement is limiting the wing box close to the root.

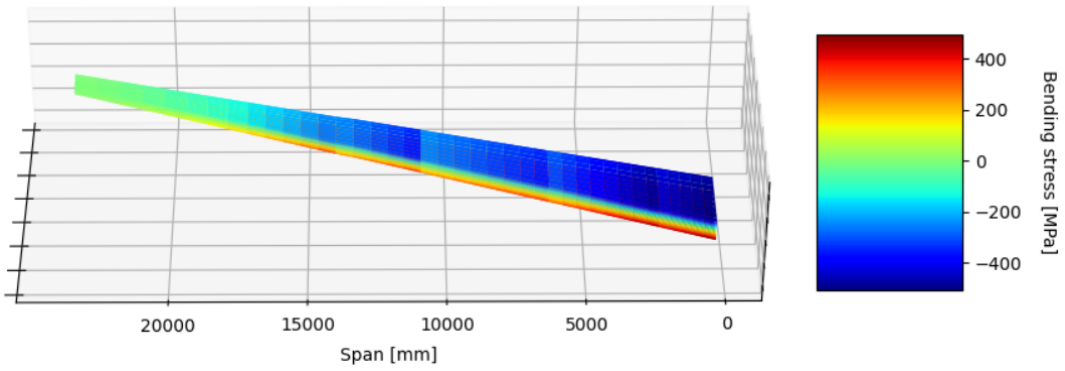

Figure 11.35: 3D plot showing the compressive bending stress along the upper panel of the wing box in cruise conditions, subjected to $n = n_{max}$.

Figure 11.36 shows the tension in the lower panel of the wing box, as expected. The figures also show the increase in stress at the locations where the wing box changes geometry, as can be found in Table 11.11, to create a more optimal design.

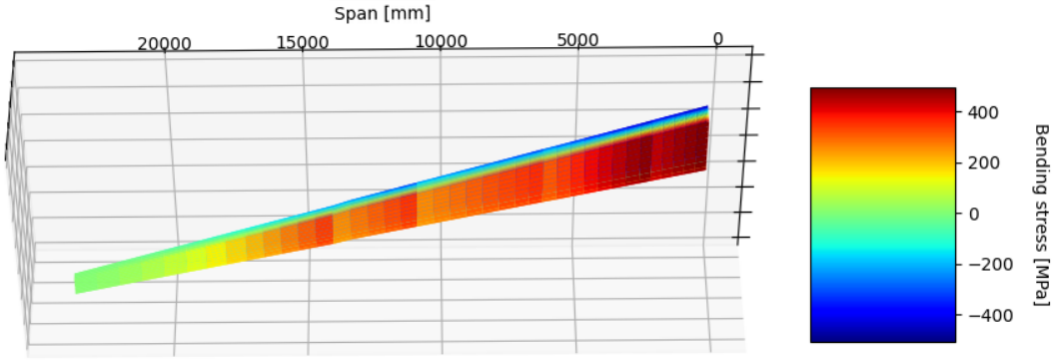

Figure 11.36: 3D plot showing the tension along the lower panel of the wing box in cruise conditions, subjected to $n = n_{max}$.

Increasing the engine thrust by a factor thousand yields the result as shown in Figure 11.37. In this case, the bending moment along the span due to lift is negligible with respect to the engine thrust ($M_z >> M_x$). Hence, tension is expected in the rear spar between and compression in the front spar. Figure 11.37 confirms this. Note that the engine thrust does not provide a bending moment for locations $y > y_{eng}$, due to the fact that it does not introduce a shear force in regions outboard of the engine. It should also be noted that the load and resulting stresses in Figure 11.37 are not representative for the wing box structure.

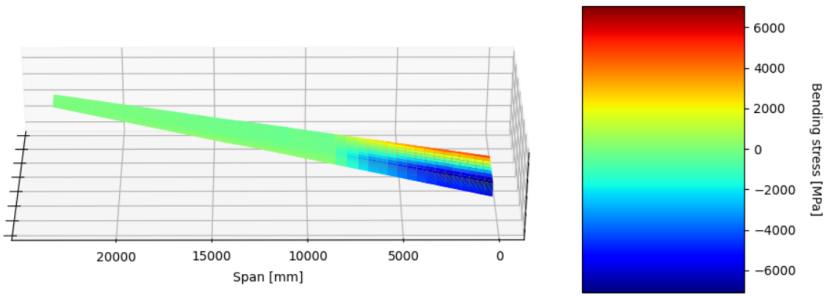

Figure 11.37: 3D plot showing compression and tension in the front and rear spar, subjected to a thrust load of $1000 \cdot T$.

11.3.11. Wing Box Sensitivity Analysis

In order to see how input parameters of the wing box design program change the output for the wing box geometry and the material selection. In this sensitivity analysis, two parameters are changed: the maximum load factor n_{max} and the stringer area. The maximum load factor is increased from 2.8 to 3.8, and the stringer area is increased from 880 to 1100 [mm^2] (equivalent to increasing the stringer thickness by 1 [mm]).

The results of increasing the load factor on the wing weight can be found in Table 11.15. The table shows that the wing weight increases when the aircraft is subjected to a higher load. In terms of an increase in structural wing weight the T700G and T800S carbon material achieve the lowest relative structural mass increase. This is due to the fact that in both cases damage

tolerance is limiting, rather than the yield strength corrected by the FoS for the other materials. The maximum compressive stress in the top sheet of T700G and is 273.6 [MPa]. Corrected by the FoS, the yield stresses of T700G is 419 [MPa]. Therefore, the structure does not yield under the subjected load and has a large margin until the yield limit is achieved. The damage tolerance stress of T700G is 65.841 [MPa]. The highest achieved damage tolerance stress in the upper or lower panel for T700G is 65.582 [MPa], therefore meeting the damage tolerance requirement. The same reasoning holds for T800G, albeit with different calculation results. Moreover, the critical buckling stress, as prescribed by Equation 11.26, is also significantly higher due to the modulus of elasticity of these materials. However, when comparing costs, AA 7085-T6 still comes out on top showing a wing weight increase of roughly 134 [kg]. The wing box geometry along the span for n $= 3.8$ can be found in Table 11.16.

Table 11.15: Structural wing box weights for n = 2.8 and n = 3.8.

Material	AA 7075-T6	AA 7475-T761	AA 7085-T6	AA 2024-T3	Airware® 2050-T84	T300 carbon	T700G carbon	T800S carbon
Wing weight (n = 2.8) [kg]	7009.46	7635.33	6799.096	9493.62	6924.87	5698.18	5780.93	4977.25
Wing weight (n = 3.8) [kg]	8747.27	9790.24	8478.50	12364.26	8865.20	7181.69	5781.95	5029.29

Table 11.16: Wing box geometry for n = 3.8.

Material: AA7085-T6 | Stringer area: 880 [mm^2] (hat stringer)							
Spanwise location: 0 $\leq$ y < 2400 [mm]							
$t_{front\ spar}$ [mm]	$t_{rear\ spar}$ [mm]	$t_{top\ skin}$ [mm]	$t_{bottom\ skin}$ [mm]	$n_{stringers\ top}$ [-]	$n_{stringers\ bottom}$ [-]	$\sigma_{max,\ upper}$ [MPa]	$\sigma_{max,\ lower}$ [MPa]
11.27	11.45	27.47	28.11	24	17	350.92	351.83
Spanwise location: 2400 $\leq$ y < 6300 [mm]							
$t_{front\ spar}$ [mm]	$t_{rear\ spar}$ [mm]	$t_{top\ skin}$ [mm]	$t_{bottom\ skin}$ [mm]	$n_{stringers\ top}$ [-]	$n_{stringers\ bottom}$ [-]	$\sigma_{max,\ upper}$ [MPa]	$\sigma_{max,\ lower}$ [MPa]
10.02	10.73	23.86	25.13	24	16	351.38	350.40
Spanwise location: 6300 $\leq$ y < 10900 [mm]							
$t_{front\ spar}$ [mm]	$t_{rear\ spar}$ [mm]	$t_{top\ skin}$ [mm]	$t_{bottom\ skin}$ [mm]	$n_{stringers\ top}$ [-]	$n_{stringers\ bottom}$ [-]	$\sigma_{max,\ upper}$ [MPa]	$\sigma_{max,\ lower}$ [MPa]
10.91	11.34	17.76	19.60	23	15	349.35	350.11
Spanwise location: 10900 $\leq$ y < 14000 [mm]							
$t_{front\ spar}$ [mm]	$t_{rear\ spar}$ [mm]	$t_{top\ skin}$ [mm]	$t_{bottom\ skin}$ [mm]	$n_{stringers\ top}$ [-]	$n_{stringers\ bottom}$ [-]	$\sigma_{max,\ upper}$ [MPa]	$\sigma_{max,\ lower}$ [MPa]
9.02	10.15	11.18	12.88	19	14	352.91	340.66
Spanwise location: 14000 $\leq$ y $\leq$ 24298 [mm]							
$t_{front\ spar}$ [mm]	$t_{rear\ spar}$ [mm]	$t_{top\ skin}$ [mm]	$t_{bottom\ skin}$ [mm]	$n_{stringers\ top}$ [-]	$n_{stringers\ bottom}$ [-]	$\sigma_{max,\ upper}$ [MPa]	$\sigma_{max,\ lower}$ [MPa]
7.72	6.90	5.66	8.47	19	10	326.74	342.74

The wing box weights for the different materials when the stringer thickness is increased by 1 [mm] are presented in Table 11.17. In addition, Table 11.18 shows the wing box geometry for the increased stringer area. From comparison with Table 11.11, the figure shows that the skin thicknesses in the wing box decrease as the stringer area increases. Although the skin thicknesses decrease, the total weight of the wing box increases, which is shown in Table 11.17. One could expect that this effect also hold vice verse. However, continuously decreasing the stringer area may lead to crippling of the stringer before the wing box skin buckles. Future research on the relationship may be beneficial with respect to performance and sustainability of the wing box design.

Table 11.17: Structural wing box weights for A = 880 [mm^2] and A = 1100 [mm^2]

Material	AA 7075-T6	AA 7475-T761	AA 7085-T6	AA 2024-T3	Airware® 2050-T84	T300 carbon	T700G carbon	T800S carbon
Wing weight A = 880 [mm^2]	7009.46	7635.33	6799.09	9493.62	6924.87	5698.18	5780.939	4977.25
Wing weight A = 1100 [mm^2]	7101.75	7784.86	6932.78	9603.95	7111.20	5758.99	5811.96	5040.11

Table 11.18: Wing box geometry for $A_{stringer}$ = 1100 [mm^2].

Material: AA7085-T6 | Stringer area: 1100 [mm^2] (hat stringer)							
Spanwise location: 0 $\leq$ y < 2400 [mm]							
$t_{front\ spar}$ [mm]	$t_{rear\ spar}$ [mm]	$t_{top\ skin}$ [mm]	$t_{bottom\ skin}$ [mm]	$n_{stringers\ top}$ [-]	$n_{stringers\ bottom}$ [-]	$\sigma_{max,\ upper}$ [MPa]	$\sigma_{max,\ lower}$ [MPa]
12.11	10.17	18.09	20.08	23	16	349.47	353.23
Spanwise location: 2400 $\leq$ y < 6300 [mm]							
$t_{front\ spar}$ [mm]	$t_{rear\ spar}$ [mm]	$t_{top\ skin}$ [mm]	$t_{bottom\ skin}$ [mm]	$n_{stringers\ top}$ [-]	$n_{stringers\ bottom}$ [-]	$\sigma_{max,\ upper}$ [MPa]	$\sigma_{max,\ lower}$ [MPa]
10.55	11.41	15.45	16.72	22	16	349.51	349.54
Spanwise location: 6300 $\leq$ y < 10900 [mm]							
$t_{front\ spar}$ [mm]	$t_{rear\ spar}$ [mm]	$t_{top\ skin}$ [mm]	$t_{bottom\ skin}$ [mm]	$n_{stringers\ top}$ [-]	$n_{stringers\ bottom}$ [-]	$\sigma_{max,\ upper}$ [MPa]	$\sigma_{max,\ lower}$ [MPa]
11.44	11.74	11.06	13.13	20	13	346.74	348.06
Spanwise location: 10900 $\leq$ y < 14000 [mm]							
$t_{front\ spar}$ [mm]	$t_{rear\ spar}$ [mm]	$t_{top\ skin}$ [mm]	$t_{bottom\ skin}$ [mm]	$n_{stringers\ top}$ [-]	$n_{stringers\ bottom}$ [-]	$\sigma_{max,\ upper}$ [MPa]	$\sigma_{max,\ lower}$ [MPa]
6.60	8.42	6.96	9.26	17	10	318.55	333.87
Spanwise location: 14000 $\leq$ y $\leq$ 24298 [mm]							
$t_{front\ spar}$ [mm]	$t_{rear\ spar}$ [mm]	$t_{top\ skin}$ [mm]	$t_{bottom\ skin}$ [mm]	$n_{stringers\ top}$ [-]	$n_{stringers\ bottom}$ [-]	$\sigma_{max,\ upper}$ [MPa]	$\sigma_{max,\ lower}$ [MPa]
8.82	8.39	6.33	4.65	17	9	223.71	336.11

12. Manufacturing

This chapter will focus on the manufacturing process of the aircraft. It is divided into three parts: wing manufacturing, fuselage manufacturing and final assembly.

12.1. Wing Manufacturing

The wing is made out of an aluminium alloy, allowing the use of exiting and proven manufacturing technique. First the ribs and stringers are produced. The ribs will be produced with either press forming or machining. Press forming is a rather inexpensive method to manufacture parts with average levels of complexity, and will be used for most ribs. However, ribs placed at highly loaded points, such as at the engines and MLG, will be machined. Although higher costs and waste, machining ensures manufacturing of integral, high load resistant parts. The stringers will be extruded, as with press forming the size of piece is limited, as well as its thickness (thickness cannot exceed 3 [mm]) [93]. The wing's skin panels, which have a different thickness from root to tip, will be machined from a single block of material[1].

The wing assembly follows the part manufacturing. The wings will be assembled using semi-automated technology. Wing manufacturing will make use of the robotic Panel Assembly Line (PAL)[2] (see Figure 12.1). Workers position the wing panels, stringers and ribs, and then PAL will glide back and forth on tracks riveting all parts together. These machines have been proven to increase production rates by 33%, reliving workers from physically strenuous and repetitive jobs. The wing will be constructed from two integral panels, one for the lower skin and one for the upper skin. The manufacturing plan of the wing subsystem is shown in Figure 12.2.

Figure 12.1: Robotic Panel Assembly Line (PAL) used for the wing's assembly[3].

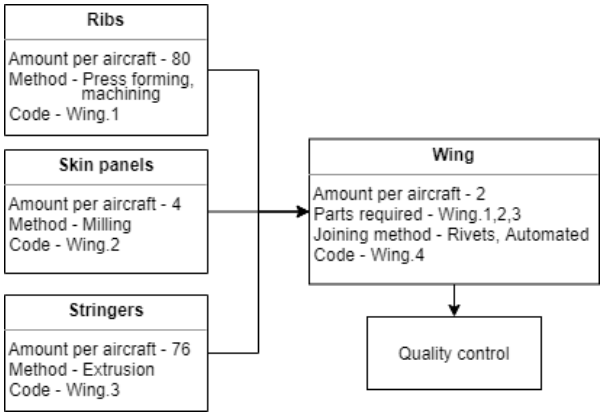

Figure 12.2: Manufacturing plan of the wing subsystem.

12.2. Fuselage Manufacturing

Similar to the wing, the fuselage will be built using an aluminium alloy. Like the wing stringers, the stiffeners are produced with extrusion. The frames are produced with press forming. However, like the ribs, heavily loaded frames, like the ones at the front and rear spar, are machined.

[1] https://www.airbus.com/aircraft/how-is-an-aircraft-built/production.html

[2] https://www.wired.com/2016/10/meet-giant-robot-builds-boeings-wings/

[3] https://eu.usatoday.com/story/todayinthesky/2015/06/02/boeing-says-wing-production-has-started-for-737-max-jets/28372587/

Single curved skin panels are produced with conventional roll bending, an inexpensive method widely implemented to manufacture metal fuselage skin panels. Fuselage double curved panels, needed for the tail and cockpit sections of the fuselage, are manufactured using stretch forming [93].

The fuselage has to be assembled, as it is divided into panels and into segments, as it was preluded in Section 11.2. The fuselage is divided into five cylindrical segments (segment B to A from Figure 11.6 is divided in two due to its long length), and two conical shapes. Each fuselage segment is also divided into four panels: top, bottom and sides. These panels are constructed using a semi-automated method similar to Boeing's Fuselage Automated Upright Build used to manufacture 777s[4] (see Figure 12.3). Teams of workers are tasked to load and set stiffeners and frames on top of skin panels, after which robot pairs drill and fasten each part. The same technology will then be used to join four panels to make a fuselage section. This level of automation relieves stress from the workers, making working conditions less physically strenuous and more safe. Additionally, this technology will improve quality and increase production speed. The fuselage floor and the interior piping for the hydrogen is then added to complete a fuselage segment. The manufacturing plan of the fuselage subsystem is shown in Figure 12.4

Figure 12.3: Boeing's Fuselage Automated Upright Build used to assemble the fuselage[5].

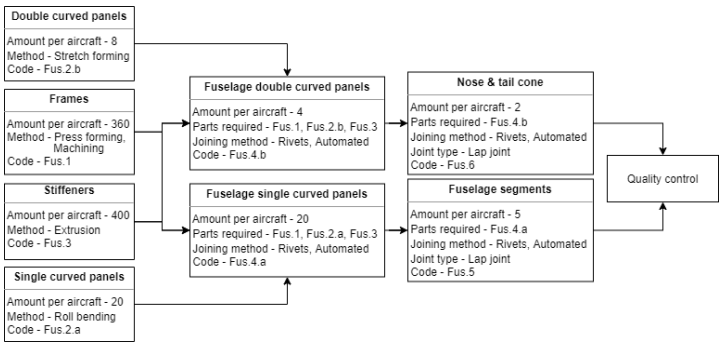

Figure 12.4: Manufacturing plan of the fuselage subsystem.

12.3. Final Assembly

The final assembly is best described with a production plan provided in Figure 12.5, which shows the flow of the activities.

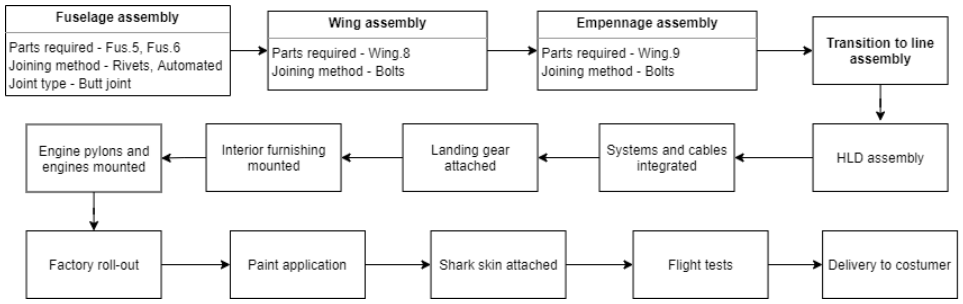

Figure 12.5: Manufacturing plan of the final assembly.

[4] https://www.boeing.com/features/2017/02/faub-777-assembly-02-17.page
[5] https://www.wired.com/2017/03/boeing-faub-assembly-robot-777/

13. Performance Analysis

This chapter contains an in depth analysis of the aircraft's performance, which is key to investigate whether the aircraft will comply with regulations and requirements. First, in Section 13.1, a mission profile will be determined, showing the different phases of the mission. Partly based on this mission profile, a payload-range diagram is constructed in Section 13.2. The performance diagram is generated in Section 13.3, which serves as a basis for many important performance parameters. The climb characteristics and flight envelope that follow from the performance diagram are discussed in Section 13.4 and Section 13.5 respectively. Section 13.6 covers the take-off and landing distances of the aircraft. Section 13.7 and Section 13.8 contain the sustainability aspects of performance, analysing the aircraft noise and its emissions respectively. Afterwards, the complete performance analysis is verified and validated in Section 13.9. Finally, a sensitivity analysis is conducted in Section 13.10 to investigate how parameters changed when inputs/assumptions are altered.

13.1. Mission Profile

The mission profile of the aircraft shows the different phases of flight. It is based upon the typical mission of commercial aircraft, in which a second cruise phase is included. This is included in case of emergencies. It is assumed that 45 minutes of flight is needed for diversion cruise and 15 minutes for loiter 2, in comparison to the 30 minutes needed for loiter 1 [94]. The AirEco aircraft is designed such that it carries enough fuel for the whole mission, which is 5000 [km].

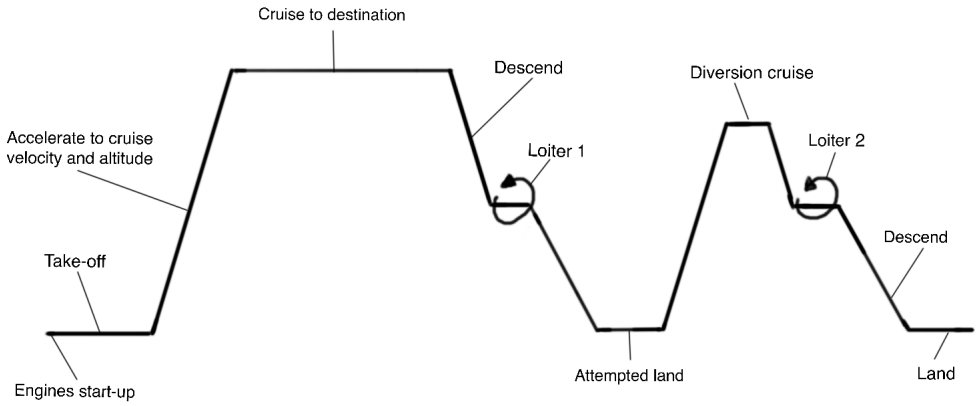

Figure 13.1: Mission profile for AirEco.

13.2. Payload-Range Diagram

The payload-range diagram is indirectly based upon the mission profile. Certain fuel fractions have been estimated through literature for all phases of flight in the mission profile, excluding cruise and loiter phases.These have to be calculated to determine the range for different amounts of payload and fuel.

However, before the fuel fractions and the range can be calculated, three distinct points have to be identified. These are: zero range and maximum payload, maximum payload and MTOW, and maximum fuel weight with no payload. For the second point, the fuel weight has to be

calculated based on the given conditions and for the third point, the MTOW has to be calculated. Thereafter, for these two points, the product of all fuel fractions, M_{ff}, can be found using Equation 13.1. The fuel fraction for loiter, W_7/W_6 can be determined through Equation 13.2. The fuel fraction for cruise, W_5/W_4, can be then be found by dividing M_{ff} by all other known fuel fractions.

$$M_{ff} = 1 - \frac{W_f}{\text{MTOW}} \tag{13.1}$$

$$\frac{W_6}{W_7} = e^{\frac{L_{\text{loiter}} \cdot 60 \cdot g \cdot c_{j,\text{loiter}}}{LD_{\text{loiter}}}} \tag{13.2}$$

However, before it is possible to calculate the range, W_5/W_4 has to be multiplied by a fraction as the original method for constructing the payload-range diagram assumes normal jet fuel. The use of hybrid fuel or only liquid hydrogen changes the fuel fraction. If only liquid hydrogen is used, W_5/W_4 is determined by: $W_5/W_4 = 1 - (1 - W_5/W_4) \cdot 120/46.2$, where 120/46.2 is the specific energy of liquid hydrogen divided by that of jet fuel. When hyrbid fuel is used, the fuel fraction is determined as follows: $W_5/W_4 = 1 - (1 - W_5/W_4) \cdot 60/46.2$, where 60 is the average specific energy for 20% liquid hydrogen and 80% biofuel.

The range is then found using:

$$R = \left(\frac{V_{\text{cruise}}}{g \cdot c_j}\right)_{\text{cruise}} \cdot \left(\frac{L}{D}\right)_{\text{cruise}} \ln\left(\frac{W_4}{W_5}\right) \tag{13.3}$$

Calculating the range for each of the three different points for the liquid hydrogen version of the aircraft and the hybrid results in the payload-range diagrams depicted in Figure 13.2 and Figure 13.3. As can be seen, both models have a maximum range higher than 5000 [km], however the hybrid aircraft can go much farther. To be exact, the 100% hydrogen aircraft has a maximum range of 5623 [km] and the hybrid has one of 8192 [km]. With 100% hydrogen, airliners can also take 30.4 [ton] of payload and with 20% hydrogen and 80% biofuel, 15.4 [ton] of payload can be taken on board the aircraft. This allows the airlines with flexibility as when liquid hydrogen becomes more common in the future, they can pick whether they want to go farther with less payload or not as far, but with double the payload.

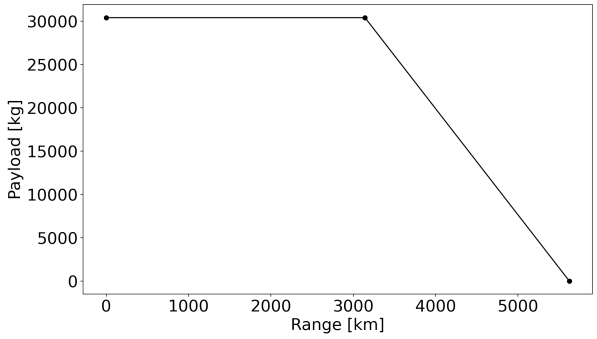

Figure 13.2: Payload-range for 100% liquid hydrogen aircraft.

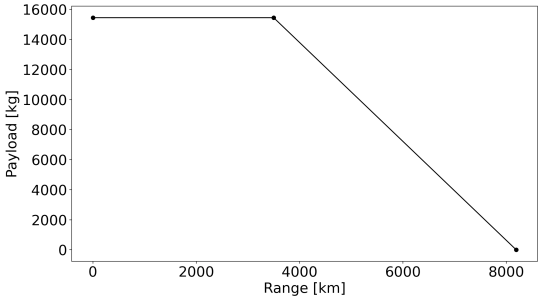

Figure 13.3: Payload-range for 20% liquid hydrogen and 80% biofuel aircraft.

13.3. Performance Diagram

The performance diagram is fundamental to a wide array of performance characteristics. The diagram is straightforwardly obtained by plotting the total drag force and constant thrust against the velocity. The altitude is kept as a variable input, so the diagrams can be made for different altitudes. The drag curve can also be referred to as the thrust required, while the constant thrust is also the thrust available of the aircraft. The total drag force is obtained from the drag equation, and is plotted from the stall to dive speed. The first is calculated using the

lift equation and $C_{L_{max}}$, while the latter is calculated by taking the cruise speed and dividing this by 0.8, which follows from CS-25 regulations (CS-25.335b, [78]). The constant thrust is simply obtained by multiplying the thrust loading by the MTOW. Then, by also further adjusting for altitude changes where needed the performance diagram can be calculated for multiple heights, examples of which are shown in Figure 13.4 and 13.5.

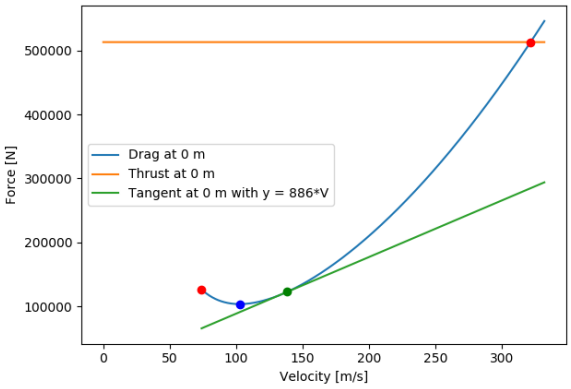

Figure 13.4: Performance diagram at sea level.

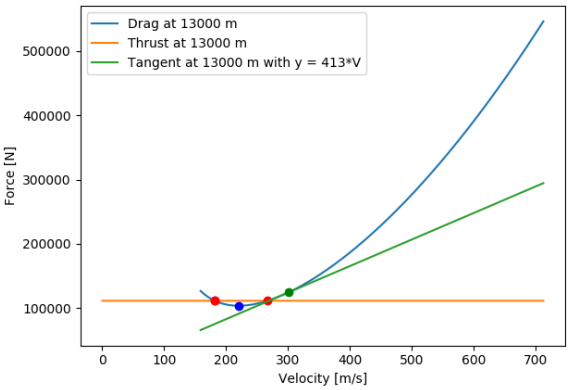

Figure 13.5: Performance diagram at h = 13000m.

Here, the red points indicate the minimum and maximum velocity. Note from Figure 13.4 that the maximum speed is immediately limited by the thrust limit and is therefore lower than the dive speed. While the minimum speed is usually the same as the stall speed (65 m/s at sea level from Figure 13.4), this too is ultimately limited by the thrust as can be seen in Figure 13.5. The blue point indicates the speed at minimum drag, which is the optimal speed for maximum endurance. Finally, the green point denotes the optimal flight velocity for maximum range. As can be seen from the figure, this point is found by plotting a tangent from the origin that touches the drag curve.

The performance parameters at cruise are shown in Table 13.1. The cruise altitude, for which all of the parameters are calculated, is defined to be 10000 [m] as can be seen in the table. This altitude is determined using the performance diagram and by inspection; it was found that this altitude gives an optimal speed for maximum range of 0.79 Mach, which is perfectly in line with the set requirements (AE-PERF-CRU-03, [1]). Conversely, this is also defined to be the recommended cruise speed V_{cruise}.

Table 13.1: Performance parameters of AirEco at cruise.

Parameter	Value	Unit
Cruise altitude h_{cruise}	10000	m
Minimum speed V_{min}	127.39 (0.43)	m/s (M)
Maximum speed V_{max}	306.58 (1.02)	m/s (M)
Optimal speed for max. range V_{opt}	236.64 (0.79)	m/s (M)
Speed at minimum drag $V_{\text{D,min}}$	176.71 (0.59)	m/s (M)

13.4. Climb Characteristics

To obtain the climb characteristics of the aircraft, first the take-off (or lift-off) speed V_{TO} must be determined. This is determined using: $V_{\text{TO}} = 1.05 \cdot V_{\text{min}}$ [95]. Now, the following equations can be used to calculate the climb angle γ and rate of climb (ROC) of the aircraft:

$$\sin(\gamma) = \frac{T - D}{W} \qquad (13.4)$$

$$\text{ROC} = V_{\text{TO}} * \sin(\gamma) \qquad (13.5)$$

For the climb angle, the maximum excess thrust $T - D$ can be obtained by from Figure 13.4 by subtracting the minimum drag denoted in blue by the thrust available. Finally, the climb gradient can be calculated by dividing ROC by V_{TO} and multiplying this by a hundred. The results are shown in Table 13.2.

Table 13.2: Climb characteristics of AirEco.

Parameter	Value	Unit
Climb angle γ	16.5	°
Take-off speed V_{TO}	77.63	m/s
Rate of climb ROC	21.94	m/s
Climb gradient	28.27	%

The climb gradient is also a part of the one engine inoperative CS-25 regulations (CS-25.121 [78]). These boil down to having a minimum climb gradient of around 0-5 % in different situations. Halving the total thrust available, subsequently recalculating the climb angle and ROC gives a new climb gradient of 10.56 %. When also halving the take-off speed and considering the other outlined situations in CS25, it was found that the aircraft meets all the requirements quite comfortably due to its higher than average excess thrust.

13.5. Flight Envelope

The performance diagram can also be used to construct the flight envelope. The flight envelope is a useful diagram that depicts various performance limits of the aircraft: the minimum & maximum speed (V_{min} & V_{max}); theoretical ceiling and maximum speed for maximum rate of climb ($V_{\text{ROC}_{\text{max}}}$). The flight envelope is shown in Figure 13.6.

As explained in Section 13.3, the minimum speed is usually the stall speed, until it is limited by the thrust, whereas the maximum speed is always limited by the thrust. The theoretical ceiling is obtained by examining the aforementioned performance diagram and finding the altitude at which there is no excess thrust anymore: the aircraft is physically unable to climb at this point. Finally, $V_{\text{ROC}_{\text{max}}}$ coincides with the speed for maximum endurance, as one has to fly at minimum drag to achieve the highest excess thrust; and conversely, the highest ROC.

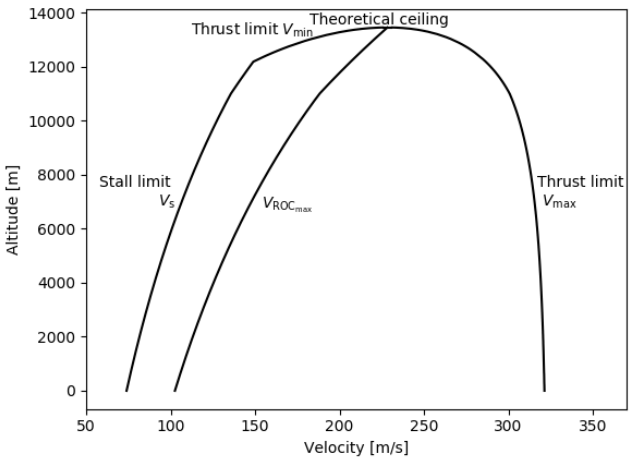

Figure 13.6: Flight Envelope AirEco with performance limits.

13.6. Take-off and Landing Characteristics

Take-off and landing characteristics are important to consider for any aircraft. Not being able to take-off and land at airports means that the aircraft cannot get into the air and airlines cannot operate the it. In terms of take-off characteristics, the aircraft has to comply with a take-off distance of 2200 [m]. Landing distances will be calculated as per CS-25 regulations, although there are no specific requirements on how much landing distance is required.

The take-off and landing distances were calculated using Equation 13.6 and Equation 13.7, obtained from Roling [95].

$$\text{Take-off distance} = \frac{V_{lof}^2}{2\bar{a}} = \frac{(1.05V_{min})^2}{2\frac{g}{W}(\bar{T} - \bar{D} - \bar{D}_g)} \qquad \text{where } \bar{D}_g = \mu_{rolling}(W - \bar{L}). \tag{13.6}$$

$$\text{Landing distance} = x_{tr} + x_{brake} = 2.6V_{min} + \frac{W^2}{2gS}\frac{2}{\rho}\frac{1.3^2}{C_{L_{max}}}\frac{1}{\bar{T}_{\text{ref}} + \bar{D} + \mu_{\text{brakes on}}(W - \bar{L})} \quad (13.7)$$

A discharge angle of 45 [°] is usually chosen for thrust reversers[1], hence $\bar{T}_{ref} = \sqrt{2}/2 \cdot \bar{T}$. It is also assumed that for take-off, $\bar{T}$ is equal to 0.8 of the maximum thrust as aircraft usually do not apply maximum thrust at take-off[2].

The take-off will be calculated for two different conditions: dry and wet runway. The landing distance will be calculated on a dry runway with no thrust reversers, wet runway with thrust reversers and for one-engine inoperative on a wet runway. For a dry runway, $\mu_{\text{rolling}} = 0.04$ and $\mu_{\text{brakes on}} = 0.4$. For a wet runway, $\mu_{\text{rolling}} = 0.05$ and $\mu_{\text{brakes on}} = 0.225$[3]. The results are shown in Table 13.3.

Table 13.3: Take-off and landing distances of AirEco aircraft.

Situation	**Take-off** [m]	**Landing** [m]
Dry runway	1813	1828
Wet runway	1779	1841
Engine inoperative	-	6836

13.7. Noise

Besides the more obvious performance parameters, one should not underestimate the importance of noise. Especially in the context of this project, where sustainability is key, it is important to correctly identify aircraft noise. In literature, two main sources of noise are identified that contribute to an aircraft's total noise: the airframe and the engine [96].

13.7.1. Measurement points

According to the International Civil Aviation Organisation (ICAO), the noise of an aircraft has to be calculated/measured at three distinct points. These points are: lateral, flyover and approach. The ICAO defined these points as follows:

- Lateral: a point 450 [m] from the runway center line and parallel to it, where maximum noise level occurs[4]. According to Airbus, this occurs at an altidude of 304.8 [m][5]
- Flyover: a point which is 6500 [m] from the start of the take-off roll and after power cutback of the engines[4]. Power cutback occurs at a height of 650 [m], and afters the aircraft decreases the climb gradient to 4%[5].
- Approach: a point that is 120 [m] below the aircraft and 2300 [m] from the point of touchdown. A descent angle of 3 ° is assumed[4].

Airframe and engine noise are dependent on the distance to the measurement point, d, and two angles to the measurement point. There are two angles which influence noise, namely the directivity angle, α^*, and the lateral emission angle, β^*. α^* is the angle between the aircraft-fixed axis and the axis from the aircraft to the observer. β^* is defined as the angle between the aircraft symmetry plane and observer plane [96]. Based on these definitions and the ones for the measurements, the values can be identified for d, α^* and β^*. These are shown in Table 13.4.

Table 13.4: Values for observer distance, directivity angle and lateral emission angle.

Reference	d [m]	α^* [°]	β^* [°]
Lateral	543.51	90	55.89
Flyover	343.70	94	0
Approach	120.00	87	0

[1] https://engineering.purdue.edu/~propulsi/propulsion/jets/basics/reverse.html

[2] https://www.skybrary.aero/index.php/Reduced_Thrust_Takeoff

[3] https://skill-lync.com/projects/project-1-powertrain-for-aircraft-in-runways-90

[4] https://www.icao.int/Meetings/EnvironmentalWorkshops/Documents/Noise-Certification-Workshop-2006/Boettcher_3.pdf

[5] https://www.slideshare.net/FernandoNobre1/aircraft-noise-27755949

13.7.2. Airframe Noise

The airframe noise of the aircraft is computed using a model developed by Dobrzynski, which is explained in the PhD thesis from Bertsch [96]. According to Dobrzynski, the airframe noise is produced by the trailing edge devices, leading edge devices, spoilers and landing gear. However, all these components are not in use at every single measurement point seen in Section 13.7.1. These components used for each point are as follows:

- Lateral: Trailing edge devices, leading edge devices, and landing gear
- Flyover: Trailing edge devices and leading edge devices
- Trailing edge devices, leading edge devices, spoilers and landing gear

The noise from the trailing edge devices are calculated using Equation 13.8. $L_{norm/vel/geo}$ is the reference noise level, ΔL_{dir} is the emission directivity correlation and $\Delta L_{spec}(Str)$ is the spectral shape function expressed in terms of the Strouhal number. The Strouhal number is dependent on the frequency the noise occurs at. Typical values in aircraft noise studies are between 500 [Hz] and 5000 [Hz] [97]. Moving on, for the trailing edge devices, $L_{norm/vel/geo}$ is a function of d and ΔL_{dir} is a function of β^*.

$$L_{c_l>0.5} = L_{norm/vel/geo} + \Delta L_{dir} + \Delta L_{spec}(Str) \tag{13.8}$$

For leading edge devices, the total sum of the noise is given by Equation 13.8. Here, $L_{norm/spec}(Str)$ is the normalised reference level as a function of the Strouhal number, Str. ΔL_{geo} is the geometry dependent adjustment factor and is dependent on the distance to the measurement point. ΔL_{vel} is the velocity dependence noise level. Lastly, ΔL_{dir} is a function of both α^* and β^* for leading edge devices.

$$L_{slat} = L_{norm/spec}(Str) + \Delta L_{geo} + \Delta L_{vel} + \Delta L_{dir} \tag{13.9}$$

The total noise produced by the spoilers is given by Equation 13.10. L_{geo} in case of spoilers are a function of the distance to the measurement point in question. $L_{dir/spec}(Str)$ is the combination of directivity and spectral shape function effects, which is a function of α^*.

$$L_{spoiler} = L_{norm} + \Delta L_{geo} + \Delta L_{vel} + \Delta L_{dir/spec}(Str) \tag{13.10}$$

Lastly, the landing gear noise is determined by Equation 13.11. Here, the spectral shape function is different for the front landing gear (fg) and main landing gear (mg). Moreover, only ΔL_{geo} is a function of the distance to the measurement point.

$$L_{gear} = L_{norm} + \Delta L_{geo} + \Delta L_{vel} + \begin{cases} \Delta L_{spec,mg}(Str) & maingear \\ \Delta L_{spec,fg}(Str) & frontgear \end{cases} \tag{13.11}$$

13.7.3. Engine Noise

As the engine used in the design is a turbofan, the engine noise should be further divided into jet noise and fan noise. Jet noise will be predicted using the noise estimation method developed by Stone [98], whereas fan noise will predicted using Heidmann's method [99]. Both are outlined in the PhD thesis of Bertsch [96], which is the primary source used for all the relations in this engine noise prediction. The engine parameters subscripts will follow the stations depicted in Figure 13.7.

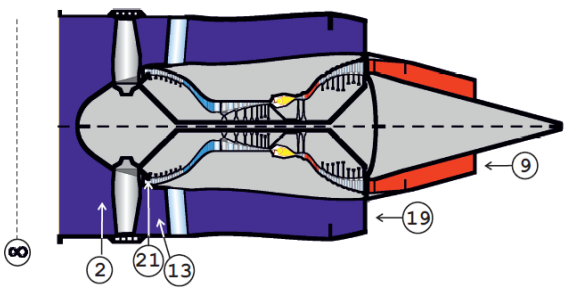

Figure 13.7: Schematic for engine noise prediction [96].

Jet Noise
In Stone's model, a distinction is made between single jets and coaxial jets. As the engine used has a bypass, the engine is defined to be a coaxial jet. For a coaxial jet the following equation is used to calculate jet noise level [96]:

$$L_{jet} = L_{norm} + \Delta L_{dir/spec}\left(Str_{c-jet}, \alpha^*_{cor}\right) + \Delta L_{c-jet} \tag{13.12}$$

Here L_{norm} is the normalised reference level. $\Delta L_{dir/spec}$ is a combined term for spectral shape and directivity, based on an empirical database as a function of the Strouhal number Str and the corrected directivity angle α^*_{cor}. Finally, ΔL_{c-jet} is added to account for the secondary jet.

Fan Noise
Fan noise can be further separated into fan inlet and fan exhaust noise contribution. Both are modeled separately and consist of a normalised noise level which is the same and (a) broadband, (b) discrete-tone and (c) combination-tone noise contributions [96]:

$$L_{fan,in} = L_{norm} + \underbrace{L_{bbn,in}}_{(a)} + \underbrace{L_{dtn,in}}_{(b)} + \underbrace{L_{ctn,in}}_{(c)} \qquad L_{fan,ex} = L_{norm} + \underbrace{L_{bbn,ex}}_{(a)} + \underbrace{L_{dtn,ex}}_{(b)} \tag{13.13}$$

Note that additional correctional factors like c_i and c_j from Bertsch [96] are neglected.

As can be seen from Equation 13.13, the noise contributions (a-c) are separately evaluated at both the inlet and exhaust. However, the way these noise level are determined are all rather similar. There are three underlying functions for each of these noise components: a directivity function ΔL_{dir}, a spectral shape function $\Delta L_{\text{spec}}(f)$ and the ΔL_{vel} velocity term. Again, all relations, tables and equations that are used to determine the noise contributions are documented by Bertsch and in Heidmann's model [96, 99].

For each noise contribution, the outcomes of the underlying functions are added to L_{norm}, an example for the exhaust broadband noise contribution $L_{bbn,\,\text{ex}}$ is shown below:

$$L_{bbn,\,\text{ex}} = L_{\text{norm}} + \Delta L_{\text{dir}} + \Delta L_{\text{spec}}\,(f) + \Delta L_{\text{vel}} \tag{13.14}$$

The directivity function is determined semi-empirically from Heidmann tables [99], which is only dependent on the directivity angle α^*. Every directivity function is different with specific tables for every noise contribution, with a further distinction between fan inlet and exhaust noise.

ΔL_{vel} is dependent on the flow velocity at the fan tip. According to Bertsch, this was modified by Guérin to fit new engine configurations [96, 100]. Here, specific values and relations are given for relative mach number ranges at operating condition Ma_{rel} and design point Ma^d_{rel}. Again, for every term in Equation 13.13 these values and the ranges are defined differently.

Finally, there is the spectral shape function $\Delta L_{\text{spec}}(f)$. Contrary to the other underlying functions, this relation is the same for every term (a-c) in Equation 13.13. This relation is a function of frequency f and blade passing frequency f_b (engine rotation speed times blade count).

Once all the terms are known, they can be substituted into Equation 13.13 and the total fan noise can then be calculated:

$$L_{fan} = L_{fan,in} + L_{fan,ex} \tag{13.15}$$

13.7.4. Results

Using the parameters defined for the aircraft and the methods explained in Section 13.7.2 and Section 13.7.3, the maximum noise level of the aircraft can be calculated for each measurement. Note that noise levels have been added by means of energetic summation, to account

for the logarithmic nature of the calculations. The noise levels with all the reduction measures, presented in Section 4.4.2, are also considered. The cabin noise is calculated by determining the sound transmission loss through the fuselage and with the sound absorption material presented in Section 4.4.3. The overall results, including noise reduction, are shown in Table 13.5. When noise reduction measures have been considered, the noise of AirEco's aircraft for each measurement point is similar to that of current aircraft. However, the total noise at the lateral and approach points are actually lower than some current aircraft thanks to the noise reduction technologies applied on the landing gear. It also makes sense that cabin noise can reach up to around 83 [dB] since the tea leaf fibre waste material only has a sound absorption coefficient of approximately 0.12 at a frequency of 500 [Hz]. This is however, still below the harmful noise level.

Table 13.5: Overall noise of the AirEco aircraft.

	Max. airframe noise [dB]	Max. jet noise [dB]	Max. fan noise [dB]	Max. noise [dB]	Noise with reduction measures [dB]	Cabin noise [dB]
Lateral	113.22	101.16	91.78	113.51	93.51	32.73 - 82.28
Flyover	96.53	101.16	97.32	103.46	95.46	33.40 - 84.04
Approach	115.14	103.81	101.16	115.60	95.60	33.5 - 84.13

13.8. Emissions

The emissions model for the AirEco aircraft considers the GHG from both combustion of the fuel and the production. The combustion GHG are determined using the NASA CEA program[6]. The GHG from production were determined from literature and are presented in Section 4.2.2.

The NASA CEA program was run for different fuel fractions. The assumption that biokerosene had the same chemical composition as Jet-A fuel was made and since the LH2 is burned as a gas, hydrogen gas was chosen. These fuels were combusted in air. The mass fractions of the different products of the chemical reactions were then computed by the program at the same temperature and pressure that the combustion chamber will operate at. The mass fractions were then multiplied by the fuel weight to get the total mass of the GHG. To calculate the overall GHG emissions due to production of biofuel and liquid hydrogen, the values from literature, as seen in Section 4.2.2, were multiplied by the fuel weight of each of the fuels for different fuel fractions. The assumption was also made that in 2035, 3.4% of the liquid hydrogen will come from green hydrogen production, which slightly decreases the CO_2 emissions.

For a fuel fraction of 0.2, the total GHG emissions, in CO_2 equivalent, is 124802.17 [kg] and for a fuel fraction of 1, the total is 147447.95 [kg]. This is lower than the emissions for a flight with an A321. This makes sense as the combustion of hydrogen does not release any CO_2 or CH_4. The main cause of emissions for liquid hydrogen comes from its production. Moreover, it is also expected that the emissions of hybrid fuel, where 20% is liquid hydrogen are lower. Due to this small amount of LH2, there are not a lot of hydrogen molecules able to react with the carbon in the biofuel, decreasing the amount of CH_4 released into the air. This is also the worst form of GHG emissions and would increase the total emissions a lot more compared to the CO_2.

13.9. Verification & Validation

Verification and validation were completed for all programs used to calculate parameters in this performance chapter. However, the noise and emissions model were not validated. This

[6] https://cearun.grc.nasa.gov/

is because the noise calculations are based upon another model, which has already been validated and the emissions are based on real life data. The performance diagram, climb characteristics and flight envelope are all highly interconnected, therefore these are taken together in the verification and validation process.

All programs were first verified by checking for syntax, runtime and semantic errors. If IF-statements were utilised in a program, a code coverage test was conducted. Thereafter, specific values were changed to see if it would yield the desired result. In the payload-range program, this meant seeing if, i.e, an increased lift-to-drag ratio increased would increase maximum range. For the performance diagram, one check was seeing if increasing the height would cause the thrust available to shift downwards and the drag curve would shift to the right. In terms of take-off and landing distance, it was verified if decreasing the thrust loading caused the take-off and landing distances to increase. For noise, if, for example, the trailing edge devices or landing gear became bigger, then noise would also increase. Lastly, in the emissions program, it was verified if lists were added together in the correct way.

After verification, the above programs were validated by using a reference aircraft: the A320. The program was supplied with the aircraft's input parameters from literature, the results of the program were then compared to the actual values. A summary of the validation results is shown in Table 13.6.

Table 13.6: Validation Performance Parameters with A320 Data.

Parameter	Literature	Program	Unit	Difference
Maximum range	5000.4 [1]	5109	km	2.17%
Minimum speed (V_s, at sea level)	63.79[1]	61.28	m/s	4.1 %
Maximum cruise speed (28000 ft)	0.82[2]	0.84	Mach	2.8 %
Optimal speed (37000 ft)	0.79[2]	0.77	Mach	2.9 %
Take off speed	77.2[3]	76.7	m/s	0.6 %
Rate of climb	17.8[4]	17.4	m/s	2.5 %
Service ceiling	11917.68[5]	11920	m	0.02 %
Take-off distance (dry runway)	2210	2136.88	m	3.42%
Landing distance (dry runway)	1600	1697.24	m	5.73%

[1] (124 kts) https://www.aerofly.com/dokuwiki/doku.php/aircraft:airbus_a320
[2] (max. and economical cruise (optimal) 487kt and 454 kt respectively) https://www.airliners.net/aircraft-data/airbus-a320/23
[3] (155 kts) http://www.aerospaceweb.org/question/performance/q0088.shtml
[4] (Max. ROD of 3500 ft/min) https://contentzone.eurocontrol.int/aircraftperformance/details.aspx?ICAO=A320
[5] (39100 ft) https://simpleflying.com/how-high-do-planes-fly/

13.10. Sensitivity Analysis

A sensitivity analysis is conducted to investigate the extent to which performance results will differ when the input parameters are altered. Here, some of the most important parameters are increased and decreased by 10 %, followed by an analysis of the new results. Noise will not undergo a sensitivity analysis because it was seen in the verification process that the program was quite insensitive to changes in parameters. However, this insensitivity is to be expected due to the logarithmic addition. A sensitivity analysis will also not be presented for the emissions model. The calculation of emissions for different fuel fractions is already a sensitivity analysis in itself.

For the payload-range, it was chosen to increase and decrease $c_{j\text{cruise}}$, LD_{cruise} and V_{cruise}. The result of this is shown in Table 13.7. The maximum range of the aircraft changes at most by 17%, which occurs when V_{cruise} is increased by 10%.

Table 13.7: Sensitivity analysis for payload-range diagram.

Parameter	Original	Change $c_{j\text{cruise}}$	Change LD_{cruise}	Change V_{cruise}	Unit
Maximum range	5623	5112 - 6248	5061 - 6185	5567 - 6804	km

For the performance diagram (and by extension the climb characteristics and flight envelope), the MTOW, C_{D_0} and the thrust loading is chosen. The MTOW is chosen because it was one of the most frequently changed parameters throughout the design, C_{D_0} because it has a big impact on the drag curve in the diagram, and the thrust loading because it is the main driver behind the thrust available. The results are shown in Section 13.10. Note that all parameters are evaluated at cruise, except for the climb characteristics. Also, some parameters are omitted because they directly follow from the parameters listed below.

Table 13.8: Sensitivity analysis for performance diagram

Parameter	Orginal	MTOW change	C_{D_0} change	T/W change	Unit
Minimum speed	0.43	0.40-0.45	0.43-0.43	0.43-0.43	Mach
Maximum speed	1.02	0.97-1.07	1.09-0.97	0.96-1.08	Mach
Optimal speed	0.79	0.76-0.83	0.81-0.77	0.79-0,79	Mach
Speed at D_{min}	0.59	0.56-0.62	0.61-0.58	0.59-0.59	Mach
Climb angle	16.4	16.4-16.4	16.6-16.6	14.3-18.54	◦
Rate of climb	21.94	20.82-23.01	22.22-21.67	19.19-24.69	m/s

As can be seen from the table, all parameters behave exactly as expected. For example, the minimum speed does not change with a changing C_{D_0}, nor does it change due to the thrust loading as it is only depended on the weight and $C_{L_{\text{max}}}$. Furthermore, while every parameter changes at a different magnitude, all parameters change with approximately 15% at most. The aircraft still retains its performance characteristics. Although, it should be noted that C_{D_0} has a big effect on the max. speed and speed at minimum drag, and that T/W has a big effect on the max. speed and climb characteristics especially.

For the sensitivity analysis of the take-off and landing distances, it was decided to change MTOW, T/W and V_{min} as they are utilised for both take-off and landing calculations. The results are depicted in Table 13.9. The take-off distance is least sensitive to a change in MTOW and most sensitive to a change in V_{min}. For V_{min}, the take-off distance changes by more than 30%. The landing distance is very sensitive for a change in V_{min} as well, changing by about 90%. This is not ideal, however V_{min} is used to calculate several values used in the landing distance calculations.

Table 13.9: Sensitivity analysis for take-off and landing distances.

Parameter	Original	Change MTOW	Change T/W	Change V_{min}	Unit
Take-off distance (dry runway)	1860	1790 - 1954	1595 - 2232	1393 - 2475	m
Landing distance (dry runway)	1703	869- 2948	1410 - 2123	670 - 3292	m

14. RAMS

Part of evaluating the operational phase of the AirEco aircraft is considering the Reliability, Availability, Maintainability and Safety (RAMS). The chapter describes these criteria in Section 14.1, Section 14.2, Section 14.3 and Section 14.4 respectively. The new technologies that the aircraft contains (most notably the propulsion and fuel system) are described in detail here. The aircraft subsystems that are the same as conventional aircraft and that are already flight proven are not discussed here.

14.1. Reliability

Since a conventional configuration has been chosen for the aircraft design, it is assumed that most parts are reliable. This is because the same design methods have been used for years and certain measures have been put into place to ensure the reliability of current aircraft. However, the hydrogen tank and fuel system are two new technologies on the aircraft, which may affect reliability.

The biggest problem for the reliability of hydrogen tanks is the possibility of thermal leaks. When the insulation fails the temperature in the tanks will increase, consequently also increasing the pressure. With active venting, the hydrogen can be vented which reduces this pressure. If the increasing pressure is too high, passive venting is implemented as well. This is done by using two rupture disks installed in the tank shell (the second one is for redundancy). In case the maximum design pressure is reached, they break, venting all hydrogen directly through the wall of the fuselage. The fuel system for the hydrogen tanks has been designed with redundancy in mind. One tank is always connected to two other tanks and all tanks are able to deliver fuel to both engines. Hence, if a tank or a pipe fails, fuel will always reach the engines.

14.2. Availability

Availability is defined as the amount of time the aircraft is actually available for use. Time is lost after each operational cycle by refuelling, boarding and deboarding of passengers and maintenance checks. The availability is also highly dependent on whether the aircraft flies on 100 % hydrogen or the biofuel-hydrogen mix.

Refuelling and loading

The refuelling and loading time depends on the fuel source and the procedure of refueling and loading. The critical case is the 100% hydrogen option, as already described in Section 10.2. The turnaround time is 64.4 [min] when the hydrogen tanks and passengers are not loaded simultaneously, and 48 [min] when loaded simultaneously. Refuelling and loading passengers together is not allowed for wide cut gasoline fuels (such as JET B), while it is allowed for kerosene if fire fighting crew is on standby[1]. It must be noted that fire fighting practice for hydrogen fire is different than for kerosene, as explained in Section 14.4. Currently no rules exist yet for refueling with hydrogen while passengers are boarding. According to the engineers at Universal Hydrogen[2], there are no safety concerns for loading passengers and non-integral hydrogen tanks. However, at this point of the design the 64 [min] is taken since no official rules for this exist. During the certification phase of the aircraft and the fuel system, safety tests will be done to see if loading tanks and hydrogen can be done in a safe manner and if it can be

[1] https://www.skybrary.aero/index.php/Refuelling_with_Passengers_on_Board

[2] https://www.hydrogen.aero/#contact-us

certified in future regulations. The turnaround time of the AirEco aircraft is lower when flying on the hydrogen-biofuel mix, being 40 [min] if it cannot be loaded simultaneously and 34 [min] if that is possible.

Maintenance
The aircraft is not available for use during maintenance checks and repairing of the aircraft. This is further discussed in Section 14.3. Since the AirEco aircraft uses removable hydrogen tanks, maintenance checks are expected to take less time than conventional aircraft.

Engine modifications
The downtime of the AirEco aircraft due to engine modifications when switching from the hydrogen-biofuel mix to 100% hydrogen is negligible. An engine that works on a mix of hydrogen and biofuel can also fly on 100% hydrogen [21]. The only adjustments that have to be made are changing the injection speed of the fuel and increasing the amount of cold airflow to avoid excessive temperatures in the engine.

14.3. Maintainability

Maintenance is extremely important for aircraft. It ensures that the aircraft is safe to fly. If a crack is present and is not identified or if an on-board sensor is faulty, catastrophic damage may occur. Therefore, it is import to check all aircraft components. Moreover, new technologies are implemented on the aircraft. Hence, it is important to define the maintenance procedures for these technologies to ensure that the aircraft is always safe to fly.

14.3.1. Engine Maintenance

General electric has developed the GE's Analytics Based Maintenance software (ABM) where it gathers data such as temperature and vibrations from thousands of sensors installed across its fleet. The ABM helps in predicting the failure modes and optimises the flying hours of the engines. Moreover, ABM allows engine smart operation to optimise the fuel burn and reduce the jet fuel cost[3]. The engine core can be separated from the fan and replaced by a new core. This will reduce the maintenance time. New materials are introduced to the chosen engine such as T-aluminide for the Low Pressure Turbine (LPT) and composite carbon fibers for the fan. These new materials will require new repair schemes and new technologies. For General Electric, this means that they have to set up more GEnx shops. In 2014, there were not enough of these shops[4]. However, it is assumed that by 2035, General Electric will have set up more shops as the engine used for the AirEco aircraft is also currently being used on the Dreamliner. Hence, the number of GEnx shops for engine repairs in 2035 and further should not be an issue for the airport, airlines or the AirEco aircraft.

14.3.2. Tank Maintenance

Tank maintenance will mainly be taken care of by a third party as they are produced on an external location. When the tanks are used they are shipped back to the factory for inspection and refueling. Before loading the tanks on the aircraft they have to be inspected such that they make it throughout the complete flight. This will mainly be done by using pressure and temperature sensors within the tank. If the temperature and pressure graphs are linear it means that there is no leak and that they only increase due to slight heat loss through the

[3] https://www.ge.com/news/reports/getting-air-time-software-helps-emirates-keep-planes-running

[4] https://www.aviationpros.com/aircraft/maintenance-providers/mro/article/11486426/maintaining-the-genx-what-you-need-to-know-now

insulation. If pressure or temperature rises exponentially a thermal leak could be present, which necessitates the venting of hydrogen. The tank should later be sent back and repaired.

14.3.3. Sharkskin Maintenance

The sharkskin is an unconventional addition to the aircraft. As described in Section 4.2.1, the AeroSHARK adhesive film is used. This adhesive foil is resistant against temperature, corrosion and UV but it will degrade over time. The expected lifetime is about 5-8 years, meaning that adhesive film will be replaced during D checks. The adhesive film is coated to increase longevity, making it dirt repellent and weather resistant[5], which avoids maintenance and cleaning after every flight.

14.3.4. Maintenance Activities

In aviation, there are five types of maintenance checks. These are as follows:

- Line maintenance (LM): This type of maintenance check covers the most basic inspections. Typically, this check is completed every 24 to 60 flight hours. It is usually completed before or after flight[6].
- A checks: This check is performed every two to three months [101] and takes approximately 10 hours to complete[6].
- B checks: This type of check is usually completed during the same time as an A check. However, it is only completed every 6 to 8 months. It may take between 160 and 180 labour hours to complete[6].
- C checks: The check is usually completed every 20 to 24 months. It may take 1 to 2 weeks to complete[6].
- D checks: This maintenance check usually takes place every 6 to 10 years. The whole check may take between 30,000 and 50,000 labour hours and can be spread over a period of 4 to 6 weeks[6]. Airlines typically merge D checks with C checks [101].

Since A checks and B checks are typically combined by airlines, B checks will not be considered for the maintenance schedule. Moreover, D checks will not be considered in the schedule either as it is usually combined with C checks. The maintenance schedule for each aircraft component, based on these maintenance checks and based upon the typical maintenance procedures, is shown in Table 14.1. As is shown here, the fuselage exterior, hydraulics, engines and landing gear are inspected during almost every check. However, since the hydrogen tanks are not integrated, it is assumed that they will only be inspected when they arrive to the airport. They will not be on board of the aircraft during A, B, C and D checks. Hence, the hydrogen tanks only go through line maintenance.

Table 14.1: Maintenance check for different aircraft components[6789].

Aircraft component	Maintenance check
Wing	C
Fuselage exterior	LM, A, C
Hydrogen tanks	LM
Aircraft hull	A, C
Hydraulics	LM, A, C
Fuselage interior	A, C
On-board sensors	A, C
Emergency equipment	LM, A, C
Empennage	C
Fuel tank	C
Engines	LM, A, C
Landing gear	LM, A, C

[5] https://airwaysmag.com/airlines/lufthansa-basf-roll-out-sharkskin-tech/

[6] https://www.naa.edu/types-of-aviation-maintenance-checks/

[7] https://www.aircraftengineer.info/aircraft-maintenance-checks/#gsc.tab=0

[8] https://www.aviationpros.com/aircraft/article/10388655/whats-this-a-check-c-check-stuff

[9] https://www.qantasnewsroom.com.au/roo-tales/the-a-c-and-d-of-aircraft-maintenance/

14.4. Safety

Safety is a critical aspect to consider in the design of the AirEco aircraft. The driving factor behind this is the propulsion and fuel system, which is a new and unconventional technology that leads to some safety risks.

Hydrogen Hazards

Hydrogen is still perceived as a dangerous fuel source. It has several properties that have to be dealt with to allow for safe operation of the aircraft. Hydrogen has a boiling point of -252 [$^{\circ}$ C]. Storing it as a liquid in the hydrogen tanks leads to a hazard of the infrastructure being frozen, which in turn poses as a risk for personnel doing the maintenance [20]. All tanks and pipes thus have to be properly insulated and materials have to be selected that do not become brittle at such a low temperature.

The low boiling temperature also leads to a risk of the hydrogen boiling and evaporating when the temperature increases, which leads to a pressure increase and can lead to possible leakages. To prevent this, the fuel system includes a venting system as described in Section 9.4. These vents are lightning-protected and contain a flame arrestor to avoid flame propagation.

Hydrogen has a much larger flammability limit and has a lower ignition energy than kerosene which makes the likelihood of a fire much higher. Thus any sparks or flames should be kept away from hydrogen, however this practice is not much different than dealing with jet fuels. Due to the high diffusivity of hydrogen, the risk of fire is reduced in an open space, however any hydrogen build-up in the fuel bay is dangerous especially because of the high burn rate of hydrogen. The high burn rate can have a positive or negative effect depending on the situation, as a faster burn rate means the fire has less time to spread and might not be as destructive [102]. However, the risk of explosions in a confided space is high. To deal with these risks, it is important to review and adapt the rescue and firefighting procedures to deal with hydrogen hazards. For example, it is advised not to extinguish the fire but to let the hydrogen burn up to prevent explosions while keeping the surroundings of the fire cooled by spraying water on them. Carbon dioxide or dry chemicals can also be used. Although it should be noted dry chemicals are better as they make the fire more visible[10].

Hydrogen Tank Failure

The tanks can fail in two ways. A normal leak and a thermal leak. With a normal leak the hydrogen leaks through the tank wall inside the fuselage. This can be dangerous as the hydrogen is very flammable, especially when the air gets so cold the oxygen around it liquidises. To deal with this, rupture disks are used. These are safety devices that respond to pressure differences and allow for quick venting of gasses. Even when the slightest leak is detected, the rupture disks will break so all hydrogen will vent through the fuselage wall within seconds, keeping the passengers inside the aircraft safe.

The second kind of leak is a thermal leak. In this case the hydrogen in the tank will slowly warm up thus increasing the pressure. When this happens hydrogen will be vented in an active way making sure the pressure stays between nominal margins. When the pressure gets to high the rupture disks are broken passively because of pressure and all hydrogen is vented away to avoid any safety issues.

[10] https://h2tools.org/bestpractices/liquid-hydrogen-fires

15. Financial Analysis

This chapter deals with the financial analysis of the AirEco aircraft. The first thing to do is to predict the number of aircraft sold, which is done in Section 15.1. To get to the break-even point and estimate the return on investment, first the development & manufacturing costs and the direct operational costs are estimated in Section 15.2 and Section 15.3 respectively. With that, a profit analysis can be done in Section 15.4.

15.1. Number of Aircraft Sold

As discussed in Section 3.5, AirEco's best scenario would be to partner with Boeing and use their channels and resources to bring AirEco's solution to the market. Between 2020 and 2039 Boeing projects to sell 32,270 single aisle aircraft[1]. To adjust for a prediction in 2035 the assumption is made that the number of aircraft sold will be proportional to the fleet size, which Boeing predicts to grow 3.2% annually over the next 20 years[1]. Applying a 3.2% growth to the 32,270 [a/c] deliveries over the course of 15 years yields an estimate of 51,760 [a/c] delivered between 2035 and 2055.

To figure out which percentage of this could be delivered by AirEco, Boeing's current backlog is considered. The 737MAX-7 is the most similar to AirEco's design in terms of range and passenger capacities (Table 3.2) and as of right now it makes up 5.8% of Boeing's total outstanding orders. Assuming AirEco's aircraft will replace the 737MAX-7 entirely puts the predicted total number of aircraft sold over the course of 20 years at 3,036 [a/c] or 152 [a/c] on average annually. On the one hand this might seem too ambitious taking into account the added premium and size penalty that AirEco's solution entails while offering the same capacities in terms of range and passengers. On the other hand one might argue that these downsides are offset by the added sustainability also inherent to the AirEco aircraft. Because these effects are difficult to quantify, the 737MAX-7 replacement scenario shall be taken as a baseline for the further cost and profit analysis.

A project lifetime of 20 years is taken as an estimate, considering that the goal is to switch over to full hydrogen flight by 2050. By this time AirEco can still sell the modified version of the original aircraft for another five years, while also rolling out a second model that is optimised as a hydrogen only design. The project lifetime assumption of 20 years puts to total number of aircraft sold at 3,036 [a/c].

15.2. Development and Manufacturing Costs

Before presenting an estimation of the development and manufacturing costs, an overview of the cost breakdown structure of the AirEco mission is presented in Figure 15.1.

[1] https://www.boeing.com/commercial/market/commercial-market-outlook/

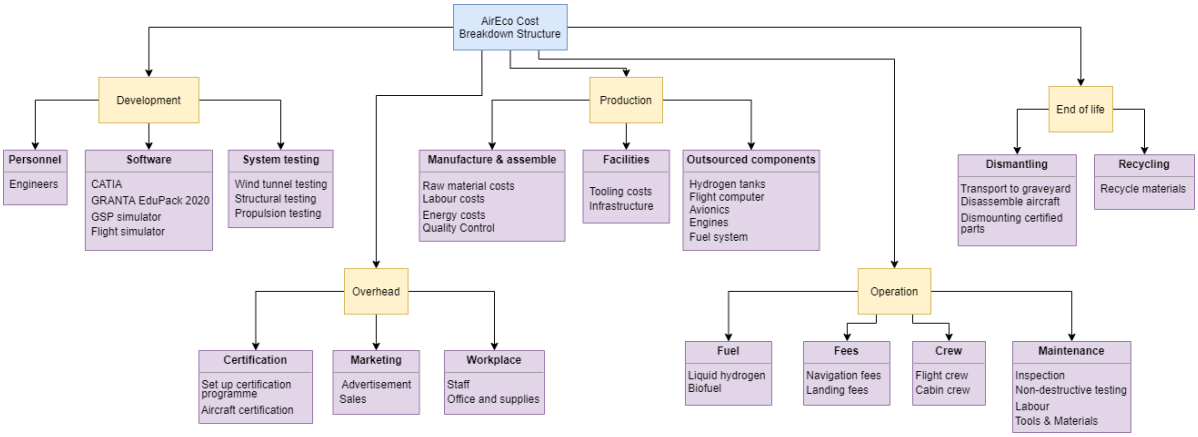

Figure 15.1: Cost breakdown structure of AirEco.

Development and manufacturing costs are estimated using the Markish method [103]. Development costs are non-recurring costs required to bring an aircraft into production. It includes preliminary and detailed design, tooling, testing, and certification. Manufacturing cost is subdivided into labour, materials and other costs. The per pound costs from Markish are also adjusted for inflation: development costs to 2021, and manufacturing costs to 2035. Note that the cost associated with the development of the hydrogen tanks and the engines are not considered, as these are outsourced to an external party. Furthermore, the tanks' manufacturing cost is not considered, as the tanks are build by a separate company and then leased to airlines. The cost of the engine are considered as part of manufacturing. The AirEco GENX engine costs $25 millions[2], while the A321XLR CFM LEAP-1A costs $14 millions[3].

The development costs of AirEco and of the A321XLR are displayed in Table 15.1. At $6.80 billions the total development costs of AirEco are substantially higher than those of the A321XLR. However, this is expected as the cost model is based on weight and AirEco is substantially heavier. Most likely the development cost of the A321XLR are actually overestimated, as it is a modified version of the already existing A321.

Table 15.1: Development cost breakdown for AirEco and for the A321XLR expressed in millions of USD.

	Engineering	ME	Tool Design	Tool Fabrication	Support	Total
AirEco	2719	680	714	2366	319	6798
A321XLR	1590	397	417	1383	187	3974

$$C_Q = C_{unit} Q^{\frac{ln(s)}{ln(2)}} \tag{15.1}$$

The manufacturing costs for both aircraft, displayed in Table 15.2, are very high. This is because the learning effect is not taken into account. Considering the learning curve effect, using Equation 15.1, where Q is the quantity of aircraft produced, C_{unit} the cost of producing one aircraft, and s the effect of the learning curve, results in substantially lower manufacturing costs. For labor costs the learning curve effect is 0.85, while for material and other costs it is 0.95 [103]. The resulting learning curves are displayed in Figure 15.2. To find the average cost per aircraft the learning curves are integrated from 1 to Q, and then the integral is divided by Q. The updated manufacturing costs are displayed in Table 15.3

[2] https://www.aerospacemanufacturinganddesign.com/article/cit-aerospace-genx-engines-dreamliners-073115/

[3] https://www.geaviation.com/press-release/jv-archive/smbc-aviation-capital-orders-additional-cfm-leap-1a-engines

Table 15.2: Manufacturing cost breakdown for AirEco and for the A321XLR expressed in millions of USD per aircraft. Note that a discount of 20% is considered for the engines as they are purchased in bulk.

	Labor	Materials	Other	Engine	Total
AirEco	240	64	50	40	354
A321XLR	132	39	29	28	200

Table 15.3: Manufacturing cost breakdown for AirEco and for the A321XLR with the learning curve effect expressed in millions of USD per aircraft. Note that a discount of 20% is considered for the engines as they are purchased in bulk.

	Labor	Materials	Other	Engine	Total
AirEco	48	38	30	40	156
A321XLR	26	23	17	22	88

The total cost of producing AirEco's aircraft are shown in Table 15.4. At a cost of $158 millions (122% of the A321XLR cost), AirEco's aircraft does not meet its cost requirement set at 120% the cost of the A321XLR. However, this value constitutes an upper bound on the cost. As Boeing will continue with the project, AirEco will gain from their experience and economies of scale, thus lowering costs. Therefore, a lower bound on costs that considers the effect of a partnership with Boeing is also evaluated.

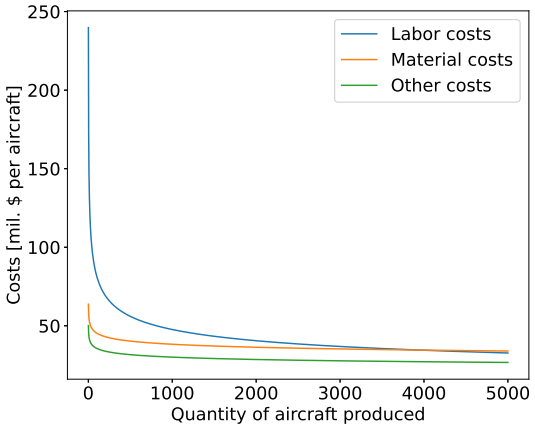

Figure 15.2: Learning curves of the three costs which make up the manufacturing cost of AirEco.

The lower bound on the development cost is found by implementing the commonality effect for the system, the payload, the wing and the fuselage subsystems. In these subsystems, AirEco is likely to share many components with other Boeing aircraft. The reduction factors for the commonality effect are obtained from Zhang et al. article [104]. For manufacturing costs, Zhang et al. suggests to increase the learning curve effect, but it should never be less than 0.75. The learning curve effect s for labor costs is now 0.8, while that of material and other costs is 0.9. The lower bound results on costs are shown in Table 15.4.

Table 15.4: Upper bound of AirEco and the A321XLR total production cost expressed in millions of USD per aircraft.

	Development	Manufacturing	Total
AirEco	2.2	155.7	157.9
A321XLR	1.1	88.1	89.2

Table 15.5: Lower bound of AirEco's total production cost expressed in millions of USD per aircraft.

	Development	Manufacturing	Total
AirEco	1.9	106.3	108.2

15.3. Direct Operating Costs

The direct operating costs (DOC) of an aircraft can be subdivided into four main components: fuel, maintenance, crew and fees. This section will give an explanation on how each is estimated. In the following analysis one flight for both AirEco and the A321 XLR is assumed to be 2 hours long. Furthermore, it is assumed that the aircraft fly at their max fuel weight.

15.3.1. Fuel Costs

Fuel cots will differ depending on the configuration. The price of hydrogen is expected to be $1.22 per kg [105], while that of biofuel $1.5 per kg [106]. On the other hand kerosene is substantial cheaper at $0.5 per liter or $0.61 per kg [106]. The fuel costs are shown in Table 15.6.

Table 15.6: Fuel costs of AirEco and of the A321 XLR.

	AirEco 100% hydrogen	AirEco hybrid	A321 XLR
Fuel cost [$/flight]	20269	60248	20000

15.3.2. Maintenance Costs

Maintenance costs makes up a substantial part of an aircraft operating costs, roughly 10% [107], thus it is important to evaluate them. For hydrogen aircraft, maintenance costs are expected to differ compared to traditional kerosene aircraft. According to a study conducted on hydrogen powered aviation, maintenance costs for a fully hydrogen aircraft are expected to grow by 6%, and constitute as much as 24% of a hydrogen aircraft cost increase [19]. This rise in cost is attributed to a larger airframe, but mostly to more frequent checks to the LH_2 tanks. Nonetheless, maintenance costs related to the propulsion system are expected to decrease in the long run [19].

To estimate the maintenance cost a CER found in literature was used [107]. The model is a regression model, which uses many regression parameters as inputs, such as the MTOW, fuselage length and the number of engines. The outputs of the model are the four main components of maintenance costs: base maintenance, line maintenance, components, and engine overhaul. However, this model should not be trusted blindly, as it is build on most frequently used aircraft and is validated using an aircraft in the same family as one used to develop the CER. Nonetheless, it will serve the propose for a rough estimate of maintenance costs. Also, no existing model will ever be perfect for an hydrogen aircraft, as these are simply not considered yet.

The maintenance costs results obtained from the CER are shown in Table 15.7. The tables shows costs for AirEco, as well as for the its main competitor the A321XLR. When compared to the A321XLR maintenance costs are 15.6% higher, mostly driven by more expensive engine overhaul due to higher thrust engines, and more expensive line maintenance, due to a higher starting cost. Nonetheless, as predicted in the long run extra expenditures resulting from hydrogen tanks inspection will decrease, resulting in just a 8.2% increase in maintenance cost simply due to the larger size of the aircraft.

Table 15.7: Maintenance costs from the CER for both AirEco (including 6% increment for hydrogen) and for the A321XLR.

	AirEco [$/FH]	A321-XLR [$/FH]
Line Maintenance	220.8	175.7
Base maintenance	165.6	131.7
Engine overhaul	479.9	366.5
Components	440.7	458.0
Total maintenance cost	**1307.0**	**1131.9**

15.3.3. Crew Cost

Crew cost can be divided into flight crew cost and cabin crew cost. Cabin crew cost assumed one flight attendant per 50 passengers[4]. Flight attendants were assumed to have a salary of 60 USD/hr for domestic flights and 78 USD/hr for international flights. Furthermore, a block time of 3 hours was assumed which consists of a 2 hour flight and one hour for on-ground operations. For the flight crew cost estimation, a total amount of 493 USD/block hour was assumed and two crew members [108]. Values for AirEco and A321XLR vary because the formulas used for the estimation were a function of the MTOW of the aircraft, they were taken from Al-Shamma et al.'s work [108]. At a further stage when more details are known about the exact flight hours and salaries, these will be re-evaluated. The cost estimates can be found in Table 15.8.

Table 15.8: Crew cost estimation for AirEco and A321XLR aircraft.

	AirEco	A321XLR
Cabin crew (domestic) [$/flight]	540	900
Cabin crew (international) [$/flight]	702	1170
Flight crew [$/flight]	2278	2177

15.3.4. Fees and Other Costs

Fees include landing fees and navigation fees. A distinction was made between the fees for international and domestic flights. The relations used to estimate these costs where a function of the maximum landing weight as maximum take off weight and were estimated using Al-Shamma et al.'s work [108]. Although these can vary per airport, an estimation is provided that accounts for these types of cost. At a later stage, when the exact departure and arrival airports are known, they will be updated. Additionally, navigation fees are only required for international flights [108]. The cost estimates can be found in Table 15.9.

Table 15.9: Landing and navigation fee estimation for AirEco and A321XLR aircraft.

	AirEco	A321XLR
Landing fee (domestic) [$/flight]	624	426
Landing fee (international) [$/flight]	2037	1392
Navigation fee [$/flight]	1805	1492

15.3.5. Total Direct Operating Costs

A summary of the total DOC can be found in Table 15.10. When AirEco's aircraft is flown with 100% hydrogen the domestic and international DOC are respectively 109% and 104% of the A321 XLR. Therefore the requirement stating that DOC shall be less than or equal to 130% of those of the A321 XLR is met. On the other hand, when AirEco's aircraft is flown in its hybrid configuration domestic and international DOC are respectively 264% and 244% those of the A321 XLR. From a DOC there is no real incentive to fly hybrid.

Table 15.10: Total DOC for AirEco and for the A321 XLR.

DOC [$/flight]	AirEco 100% hydrogen	AirEco hybrid	A321 XLR
Domestic	28130	68109	25767
International	29705	69684	28494

[4] https://simpleflying.com/aircraft-flight-crew-requirements

15.4. Program Profitability Analysis

Now that an estimation is made of the cost and number of aircraft sold an analysis can be performed on the profitability of AirEco's program. If the net profit is known, the Return on Investment (ROI) follows from Equation 15.2. Table 15.11 presents a summarised analysis of the costs and revenues that follow from the previous sections. The price of the aircraft follows directly from the cost requirement set in the Baseline Report [1].

$$\text{ROI} = \frac{\text{Value of Investment} - \text{Cost of Investment}}{\text{Cost of Investment}} \tag{15.2}$$

Table 15.11: AirEco's profitability analysis, combining the revenues and cost to arrive at a profit and ROI.

	[%]	Value	[%]	Lower Cost Bound
Revenues				
# of aircraft		3,036		3,036
Price [m USD]		155.4		155.4
Total [m USD]		471,794		471,794
Cost				
Development [m USD]		6,798		5,801
Engineering [m USD]	40.0%	2,719	39.1%	2,266
Manufacturing Engineering [m USD]	10.0%	680	6.8%	397
Tool Design [m USD]	10.5%	714	11.8%	684
Tool Fabrication [m USD]	34.8%	2,366	39.1%	2,267
Support [m USD]	4.7%	319	3.2%	186
Manufacturing [m USD]		472,767		322,669
Labour [m USD]	30.7%	145,121	25.1%	80,897
Material [m USD]	24.4%	115,368	20.9%	67,393
Engines [m USD]	25.7%	121,440	37.6%	121,440
Other [m USD]	19.2%	90,776	16.4%	52,939
Per aircraft		156		106
Profit				
Profit [m USD]		-7,771		143,324
ROI [-]		-1.6%		43.6%

As can be observed from Table 15.11, when using the baseline cost scenario for development and production, the AirEco program actually has a negative ROI. However when considering the economies of scale and commonality benefits that a partnership with Boeing will introduce, the program turns out to be profitable. The two bounds presented in Table 15.11 give a range in which this preliminary analysis predicts the profit of AirEco to fall. This range will of course be subjected to change when a more detailed financial analysis is carried out. A further recommendation for this analysis would be to include a scenario for different market shares, so that the revenues and number of aircraft sold are also put within a range. Because the number of aircraft sold has a direct influence on the learning curve and therefore the manufacturing cost, the cost analysis would have to be reiterated as well.

16. Final Design

This chapter presents the final design of the AirEco aircraft. An overview of the properties of the aircraft compared with the A321neo is given in Section 16.1. The final model of AirEco's aircraft is shown in Section 16.2. The resource allocation of the project is presented in Section 16.3. Thereafter, a risk assessment is performed in Section 16.4, and Lastly, to check if the design meets all the requirements, a compliance matrix is shown in Section 16.5.

16.1. Design Overview

The main features and parameters of AirEco are provided in Table 16.1, and can be compared to the ones of the A321neo. The A321neo provides a better comparison to AirEco than the A321XLR. Additionally, many features of the A321XLR are unavailable. The cost parameters are compared with the A321XLR due to specific cost requirements related to the A321XLR. In Figure 16.1 the two aircraft can be compared side by side.

Table 16.1: Main features and characteristic of AirEco compared to the A321neo. *the first value is for the hybrid version while the second value is for the full hydrogen version. Both times consider that it is not possible to load hydrogen tanks and passengers simultaneously.

Parameters	AirEco	A321neo
MTOW [kg]	147815	97000
OEW [kg]	107237	50100
Max biofuel mass [kg]	33369	-
Max hydrogen mass [kg]	16585	-
Max hydrogen tanks [-]	16	-
Pax [-]	150	240
Max payload hybrid [kg]	15450	-
Max payload 100% hydrogen [kg]	30439	-
Max payload [kg]	30439	25500
Max thrust [kN]	511.2	294.6
Wing span [m]	48.6	35.8
Fuselage length [m]	52.5	44.5

Parameters	AirEco	A321neo
Fuselage diameter [m]	6.73	3.95
Max range hybrid [km]	8192	-
Max range 100% hydrogen [km]	5623	-
Max range [km]	8192	7410
Cruise Mach [-]	0.79	0.78
Number of engines [-]	2	2
Max ROC [m/s]	16.5	12.7
Landing distance [m]	1841	1400
Takeoff distance [m]	1813	1828
List price [mil. $] (A321 XLR)	161	129.5
Operating cost [$/flight]	29705	28494
Turn around time [min]	52/57.6*	45

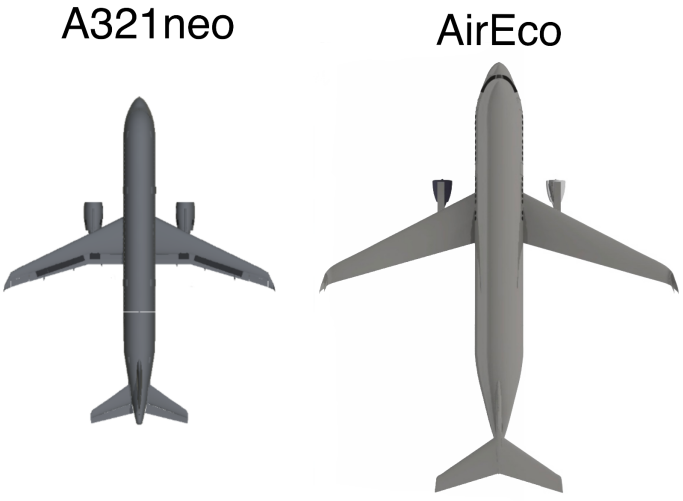

Figure 16.1: A321neo size versus AirEco size.

16.2. Final Model

The final model of the aircraft is depicted from the top in Figure 16.2 and from the side in Figure 16.3. The emergency exits, cargo door and the door for the hydrogen tanks are also shown in this picture.

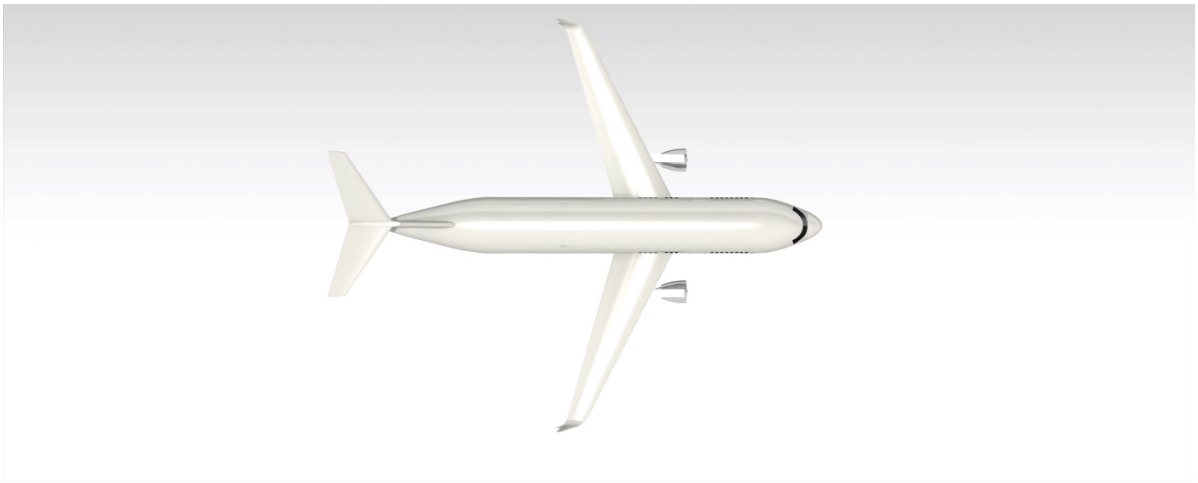

Figure 16.2: Top view of aircraft model.

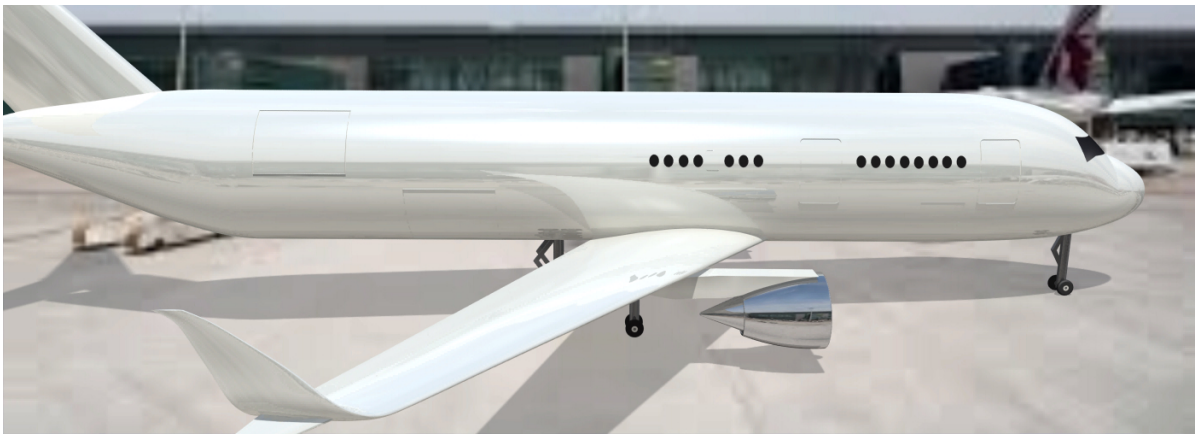

Figure 16.3: Aircraft model at airport.

16.3. Resource Allocation and Technical Budget Breakdown

Resource allocation and technical budget breakdown is an important part of any design project. It helps define how certain parameters should change in each part of the design phase. Moreover, it also aids in calculating the technical performance measurement, which is a way one can measure the risks inherent in a project[1].

In order to define the contingencies used for the technical performance parameter, a resource allocation has to be completed. This is done by selecting a few parameters that are important to the design. In this case, these parameters are: MTOW, OEW/MTOW, range, maximum thrust, passengers, T/W and the wing loading. A database of reference aircraft, similar in either maximum take-off weight or range and number of passengers to AirEco's aircraft, were

[1] https://project-management-knowledge.com/definitions/t/technical-performance-measurement/#:~:text=Technical%20Performance%20Measurement%20is%20a,design%20elements%20of%20the%20system.

used to select a target value and a specification value. Based on these values, contingencies were calculated for each of the parameters. The contingencies are then designed to decrease as the design moves further along in the design process. For the preliminary design, the contingencies are two-thirds of ones defined for the conceptual phase and the ones for detailed design are a third of the conceptual phase. If at the detailed design, the contingency is larger than 5%, they are further reduced by a half (compared to the previous phase), until the contingency is 5% or less, though in the production phase the contingencies for each parameter have to be 0%. The contingency management is shown in Table 16.2. The contingency for the current values of the aircraft are also included. It can be seen that from the conceptual phase to the current phase, some of the contingency percentages increased. These parameters are: maximum thrust, T/W and wing loading. This is partly due to the fact that these values were only iterated in order for the class I and class II methods to converge. It was not attempted to decrease them any further.

Table 16.2: Contingency management for all phases of design.

	MTOW	OEW/MTOW	Range	Max Thrust	Passengers	T/W	Wing Loading
Conceptual	25%	25%	15%	15%	25%	15%	20%
Current	11%	25%	11%	43%	0%	28%	26%
Preliminary Design	17%	17%	10%	10%	17%	10%	15%
Detailed Design	8%	8%	5%	5%	8%	5%	7%
Manufacturing	4%	4%	0%	0%	4%	0%	3%
Flight test	0%	0%	0%	0%	0%	0%	2%
Production	0%	0%	0%	0%	0%	0%	0%
Relative importance	15%	5%	25%	10%	25%	5%	5%

To calculate the technical performance measurement for each design phase, Equation 16.1 is utilised. The relative performance of each performance parameter can be found in Table 16.2. Range and passengers are the most important as they are stakeholder requirements. MTOW and maximum thrust are the next most important as they can increase fuel required and hereby costs and emissions. To get the target value and the current value, the value calculated is subtracted from 1, which is the specified value. The result is shown in Figure 16.4.

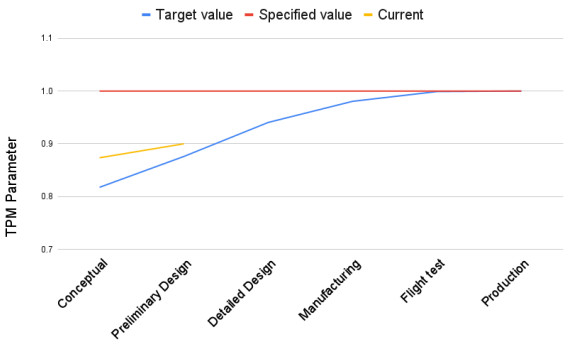

Figure 16.4: Technical performance measurement for each design phase.

$$\text{TPM}_{\text{phase}} = \sum (\text{contingency} \cdot \text{relative importance}) \tag{16.1}$$

16.4. Risk Analysis

Over the course of the project, both technical and organisational risks were identified [109, 1, 5]. Based on these previous risk assessments, a more specific risk assessment is performed, which includes the technical risks that are relevant for the conceptual design. The risks are identified and assessed in terms of consequence and probability in Section 16.4.1. Both probability and consequence are given a score between 1 (improbable/minor) and 5 (frequent/catastrophic). The risk policy that proposes preventive and mitigating measures is outlined in Section 16.4.2, after which a new risk matrix is constructed.

16.4.1. Risk Identification & Assessment

In Table 16.3 the risks are identified and assessed. These risks are summarised in Table 16.4. The risk assessment mainly focuses on risks related to the conceptual design of AirEco, rather than general risks. One important general risk that should be mentioned, as a follow up to the financial analysis in Chapter 15, is that the costs may exceed the cost requirement of 120% of the Airbus A321XLR. This risk has already been dealt in the financial analysis.

Table 16.3: Subsystem risk identification and assessment

Risk	Code	Cause	Consequence	P	C
Performance					
Performance parameters from analysis deviate significantly from actual aircraft performance	PERF-AN-01	Assumptions made for revolutionary energy source inaccurate; new engine not optimal	The aircraft performance worse then expected, potentially endangering AE-PERF requirements	3	3
Performance of the aircraft is not competitive with in 2035	PERF-CO-01	New aircraft are released that outperform the design, due to it being adaptable	The aircraft will not perform as expected in the market during its launch.	3	3
Performance of aircraft does not entirely comply with all the CS-25 regulations	PERF-CS-01	CS-25 regulations which are not explicitly quantified end up being hard to comply with	Not all regulations are satisfied and aircraft is not certified: AE-USER-REG-01 not satisfied	3	5
Structures					
Load cases in reality are more extreme then what is assumed in the design	STR-LC-01	Aircraft ends up in a rare/dangerous situation	Loads exceed the ones assumed in the design, AE-STR requirements potentially compromised	2	3
Fatigue characteristics deviate from reality	STR-FT-01	Preliminary fatigue model yields a too low stress altitude	Aircraft's operational lifetime less then intended AE-OPER-05 not satisfied	3	3
Structural properties defined deviate from the actual required properties in reality	STR-AN-01	Accuracy of conducted structural analysis is insufficient	The structure performs inadequately: AE-STR requirements not satisfied	4	4
Stability and Control					
Aircraft tips over during loading of payload and tanks	SC-LD-01	Incorrect loading procedures of the airliners	Aircraft gets damaged and will not be able to perform flight. CS-25 regulations in danger	3	4
Aircraft gets into deep stall	SC-DS-01	Use of T-tail leads to possibility of deep stall	Normal stall recovery actions become ineffective, potentially leading to a crash.	4	4
Control surfaces get stuck	SC-CO-01	Control mechanism and actuator fails	Controllability for pilot (partially) jeopardised	2	3
Aerodynamics					
Aerodynamic parameters from analysis do not sufficiently reflect actual parameters from reality	AER-AN-01	Assumptions from preliminary aerodynamic analysis leads to insufficient accuracy	Worse than expected aerodynamic performance or an over-designed aircraft	4	3
Shock waves occur at a lower Mach number	AER-SH-01	Airfoil model is inaccurate	Aircraft performs sub-optimally in transsonic conditions, leading to a very high drag	3	3
	AER-SH-02	Mach drag divergence number is estimated to be too high		2	3
Power and Propulsion					
The required hybrid engine is not optimally developed yet by 2035	PP-ENG-01	Combustion flashback effect	Inadequate performance of the engines	3	4
	PP-ENG-02	Use of hydrogen based fuel		3	4
Tank leakage in walls occurs during operation	PP-LE-01	High fatigue loads decreasing the strength of tank walls	Hydrogen gets into the fuselage, leading to liquefied oxygen, severely compromising safety	2	5
Thermal leakage of the tank	PP-TH-01	Problems in insulation (material, outside temperature, compromised vacuum, etc.)	Hydrogen can not be stored at the desired temperature, leading to excess of max. pressure breaking the rupture disks.	3	2
Problems with delivery hydrogen tanks	PP-DE-01	Logistical issues due to third party	Tanks cannot be delivered to the aircraft leading to a compromised mission	3	4
	PP-DE-02	Technical issues like a (thermal) leakage		2	4
Materials and Manufacturing					
Price aluminium increases significantly	MM-PR-01	High demand of aluminium by 2035	Too high production cost. AE-USER-COST-01 not satisfied	2	4
Delivery interval of 27 aircraft per month is not met	MM-DI-01	Batch deliveries come in to late, or are of insufficient quality	Production of aircraft cannot meet client demand, negatively affecting AirEco's reliability	2	3

Table 16.4: Risk matrix for all subsystem risks

	Probability of hazard				
Severity of consequences	**Improbable (1)**	**Remote (2)**	**Occasional (3)**	**Probable (4)**	**Frequent (5)**
Minor (1)					
Moderate (2)			PP-TH-01		
High (3)		STR-LC-01, SC-CO-01 AER-SH-02, MM-DI-01	PERF-AN-01, STR-FT-01 PERF-CO-01, AER-SH-01	AER-AN-01	
Critical (4)		PP-DE-02, MM-PR-01	PERF-CS-01, SC-LD-01 PP-ENG-01, PP-ENG-02	SC-DS-01	
Catastrophic (5)		PP-LE-01			

As can be seen from the the risk identification table and the risk matrix, most hazardous risks stem from Stability & Control and Power & Propulsion. Stability and Control is precarious due to the inclusion of hydrogen tanks at the back of the aircraft, resulting in a large surface area of the T-tail. Power and Propulsion is naturally risky due to the revolutionary propulsion system that requires liquid hydrogen.

16.4.2. Risk Policy

As can be seen from Table 16.4, there are no risks located in the green acceptable region. Therefore, all risks require mitigating or preventive measures, which are shown in Table 16.5. Table 16.6 summarises the risk assessment after the proposed measures have been implemented.

Table 16.5: Risk policy for subsystem risks

	Measures	**P**	**C**
PERF-AN-01 PERF-CS-01	Reducing probability by also performing actual flight tests and by using flight simulator software, so that the aircraft will perform well and according to CS-25	1 3	1 5
PERF-CO-01	Carefully monitoring the market, ensuring that the marketing strategy emphasizes the adaptability for the energy transition and revolutionary aspects to decrease probability	2	3
STR-LC-01	Using flight simulator and investigating the loads on the aircraft, ensuring that all load cases are considered, while adding cases to analysis if necessary to reduce probability	2	3
STR-FT-01	Doing actual fatigue testing, rather than only modelling to reduce probability	1	3
STR-AN-01	Conducting FEM analysis for a more accurate estimation, reducing probability	2	4
SC-LD-01	Making an extensive and clear flight manual for the airliners to reduce probability	2	4
SC-DS-01	Using stick pushers and allowing the use of HLD to significantly reduce probability	1	4
SC-CO-01	Ensuring redundancy so pilot can use other control surfaces, mitigating consequence	2	2
AER-AN-01	Conducting CFD analysis for a more accurate estimation, reducing probability	3	3
AER-SH-01 AER-SH-02	Conducting tests in a transsonic wind tunnel with either the airfoil or the whole wing to investigate the drag divergence Mach number and improve airfoil model.	2 1	3 3
PP-ENG-01 PP-ENG-02	Putting more research in these kind of engines, investigating flashback and the hybrid engines more. This decreases the probability of occurrence ultimately	2 2	4 4
PP-LE-01	Doing regular maintenance checks, making repairs where cracks occur and using the tanks efficiently to avoid putting them under unnecessary stress. Manually breaking rupture disk to vent everything from the tank quickly, reducing probability and severity	1	3
PP-TH-01	Employing extra measures to monitor outside temperature and vacuum within tank. First actively venting the tank in case insulation is compromised and temperature rises, if pressure gets too high passively venting the tank, reducing probability and severity	2	1
PP-DE-01 PP-DE-02	Proper training of personnel, having clear manuals. Even having redundant tanks in case it is really necessary so the flight will not get cancelled.	2 1	4 4
MM-PR-01	Monitoring the production and demand of aluminium, adapting and e.g. forming partnerships with aluminium production companies if necessary, reducing probability.	1	4
MM-DI-01	Establishing insurances and contracts with third parties, so AirEco gets well compensated in case this happens, decreasing severity of consequence.	2	2

Table 16.6: Risk matrix after applying risk policy

	Probability of hazard				
Severity of consequences	**Improbable (1)**	**Remote (2)**	**Occasional (3)**	**Probable (4)**	**Frequent (5)**
Minor (1)		PP-TH-01			
Moderate (2)		SC-CO-01, MM-DI-01			
High (3)	PERF-AN-01, STR-FT-01 AER-SH-02, PP-LE-01	PERF-CO-01 STR-LC-01, AER-SH-01	AER-AN-01		
Critical (4)	SC-DS-01, PP-DE-02 MM-PR-01	STR-AN-01, SC-LD-01 PP-ENG-01, PP-ENG-02 PP-DE-01, PERF-CS-01			
Catastrophic (5)	PERF-CS-01				

The risk matrix shows that there are no risks in the unacceptable (red) or undesirable (orange) region anymore, and for every risk in the yellow region (acceptable risks requiring a mitigation/prevention measure) there is a measure in place. Also note that that Stability & Control risks are not as detrimental anymore, except the risk related to loading which remains important to consider.

However, the Power & Propulsion risks related to the engine and the tanks are still very notable and should be properly taken into account in the future. Other risks in the yellow region are related to structural or aerodynamic analyses (AN), which are mitigated by performing more detailed analyses and physical tests. Another important risk is the performance risk related to CS-25 regulations. As stated in Table 16.5, this should be mitigated by performing flight tests. Furthermore, a close collaboration with flight authorities is required to fully certify the use of hydrogen propulsion.

16.5. Compliance with Requirements

The compliance matrix is shown in Table 16.7. A green color means the requirement is met, yellow means it is partially met, orange means that it is yet to be determined (TBD) and red means it is not met. In case the requirement is either not met, partially met or cannot be verified at this stage, further research should be done in order to meet the requirement in the detailed design phase.

Table 16.7: Compliance Matrix of AirEco's Design.

User Requirements			
Requirement Identifier	**Requirement**	**Met**	**Comment**
AE-USER-PERF-01:	The aircraft shall have a range of 5000 [km] including fuel reserves.		100% hydrogen: 5623 [km], 20% hydrogen & 80% biofuel: 8192 [km]. Compliance shown in Section 13.2.
AE-USER-PERF-02:	The aircraft shall have a capacity of 150 passengers.		Designed for 150 passengers, compliance shown in Section 16.1.
AE-USER-PERF-03:	The aircraft shall have a cargo capability for passenger belongings of at least 3750 [kg].		Designed for cargo capability of at least 3750 [kg]. Compliance shown in Section 16.1.
AE-USER-STR-01:	The aircraft's structure shall be able to withstand all loads experienced during its operational phase.		Designed for maximum load case, while Factor of Safety of 1.5 has been included. Compliance shown in Chapter 11.
AE-USER-STR-02:	The aircraft shall have a structure that accommodates the chosen propulsion system.		Aircraft has a fuel bay at the back that is designed to accommodate the hydrogen tanks. Compliance shown in Section 11.2.
AE-USER-REG-01:	The aircraft shall comply with the current CS-25 safety and reliability regulations.		Not all CS-25 regulations are possible to check at this stage of the design. Therefore, TBD.
AE-USER-OPER-01:	The aircraft dimensions shall enable safe operation at airports.		Aircraft does not have a larger span or length than current aircraft. Compliance shown in Section 16.1.
AE-USER-SUS-01:	The aircraft shall have a propulsion system based on renewable energy principles.		Biofuel and liquid hydrogen are based on renewable energy. Compliance shown in Section 8.2 and Section 4.1.

Table 16.7 continued from previous page

AE-USER-SUS-02:	The aircraft's noise levels shall be compatible with airworthiness regulations both inside and outside the cabin.		Noise is calculated in terms of ICAO definitions, airworthiness regulations in terms of noise could not be found. However, noise levels are somewhat similar to current aircraft.
AE-USER-COST-01:	The aircraft shall cost no more then 120% of the actual price of the A321XLR.		Cost requirement is partially met. It is only met with Boeing's economies of scale. Without this, the requirement is not met. Compliance is shown in Section 15.2.
Performance Requirements			
Requirement Identifier	**Requirement**	**Met**	**Comment**
AE-PERF-CRU-01:	The stall speed shall not be higher than 155 [kts]		Stall speed: 65 [m/s] which is equal to 126.35 [kts]. Compliance is shown in Section 13.3.
AE-PERF-CRU-02:	The cruise altitude of the aircraft shall be between FL230 and FL390		Optimal altitude: 10000 [m], which is approximately FL330. Compliance shown in Section 13.3.
AE-PERF-CRU-03:	The aircraft shall have a cruise speed of Mach 0.75-0.85.		Designed for cruise speed of Mach 0.78, optimal cruise speed is Mach 0.79 at FL330. Compliance shown in Section 13.3.
AE-PERF-TL-01:	The aircraft shall be able to maintain a glide slope of 3 [deg]		Maximum glide slope 16.5 [deg]. Compliance shown in Section 13.4.
AE-PERF-TL-02:	The aircraft shall have a climb speed of at least 15 [m/s]		Maximum climb speed (i.e. ROC) is 21.94 [m/s]. Compliance shown in Section 13.4.
AE-PERF-TL-03:	The aircraft shall have a take-off length of 2220 [m]		Take-off distance on dry runway: 1812.84 [m]. Compliance shown in Section 13.6.
Stability and Control Requirements			
Requirement Identifier	**Requirement**	**Met**	**Comment**
AE-STAB-01:	The aircraft shall be longitudinally, laterally and directionally stable for its most forward and most aft cg position		Empennage is designed for this requirement. Compliance shown in Section 7.4.
AE-STAB-02:	The landing gear shall provide longitudinal, lateral, and directional stability on ground		Landing gear designed for these requirements. Compliance shown in Section 7.6.
AE-CONT-01:	The aircraft shall be longitudinally, laterally and directionally controllable for the most forward and most aft cg position during operation		Empennage is designed for this requirement. Compliance shown in Section 7.4.
AE-CONT-02:	The nose gear shall carry at least 8% of the MTOW to ensure on-ground manoeuvrability		Nose landing gear designed to carry 8% of MTOW. Compliance shown in Section 7.6.
Operational Requirements			
Requirement Identifier	**Requirement**	**Met**	**Comment**
AE-OPER-01:	The aircraft shall fit the current airport class D stand size		Stand size D fits a wing span of 52 [m], span of aircraft is 48.6 [m]. Compliance shown in Section 3.3.
AE-OPER-02:	The aircraft shall be accessible by airbridge		Airbridges can typically reach the height of the A380 second deck (24.1m), and AirEco has a height of 10.43 [m]. Compliance is shown in Chapter 16.
AE-OPER-03:	The aircraft shall have a turnaround time of no more than 45 minutes		Assuming it is safe to load/unload tanks and passengers at the same time: 100% hydrogen: 47.9 [min], 20% hydrogen & 80% biofuel: 33 [min]. Assuming it is not safe: 100% hydrogen: 63.9 [min], 20% hydrogen & 80% biofuel: 39.9 [min]. Compliance shown in Section 10.2.
AE-OPER-04:	The aircraft shall be accessible by existing ground support vehicles		Conventional aircraft configuration selected. Airports are compatible with such a configuration. Aircraft is also not bigger than current aircraft. Compliance shown in Section 3.3.
AE-OPER-05:	The aircraft shall have a lifetime of at least 60000 flight cycles or 120,000 flight hours		Design fatigue life. Compliance shown in Chapter 11.
AE-OPER-06:	The aircraft shall have passenger seats of at least 0.46 [m] width without including armrests		Fuselage cross-section designed for this passenger seat width. Compliance shown in Section 5.3.
AE-OPER-07:	The aircraft shall have a cabin height of at least 2.38 [m]		Fuselage cross-section designed for this cabin height. Compliance shown in Section 5.3.
Material & Manufacturing Requirements			
Requirement Identifier	**Requirement**	**Met**	**Comment**
AE-MAT-01:	The materials used for the structure shall be able to operate safely in all weather conditions.		Aluminium is typically used in aircraft applications, so it can be assumed to be safe to operate. Susceptible to corrosion but a protective layer will be applied to prevent it. Compliance shown in Chapter 11.
AE-MAT-02:	Manufacturing techniques selected shall have a minimum technology readiness level of 7 by 2025.		Manufacturing techniques are already in use. Compliance shown in Chapter 12.
AE-MAT-03	The materials used for structures shall have material design values that minimise probability of structural failure due to material variability.		Safety factors were applied and all material dimensions meet requirements. Compliance shown in Chapter 11.
AE-MAN-01:	The aircraft shall be produced at a delivery interval of 27 aircraft/month		Cannot verify this requirement at this moment in time.
AE-MAN-02:	The manufacturing environment shall be safe for all workers		New technology is used to improve the safety of the workers. Compliance shown in Chapter 12.
Constraints Requirements			
Requirement Identifier	**Requirement**	**Met**	**Comment**

Table 16.7 continued from previous page

AE-COST-01:	The operational cost of the aircraft shall be no more than 130% of the operational cost of the A321XLR		100% hydrogen meets requirement, operational cost is only a maximum 110% of the operational cost of the A321XLR. However, hybrid is between 240% and 260% of the operational cost of the A321XLR. Compliance shown in Table 15.10.
AE-SCHE-01:	The aircraft shall enter service by 2035		Requirement is hard to verify at this moment in time, but selecting a conventional configuration decreases the time for entry into service. However, whether the engine and hydrogen tanks can be developed by that time is uncertain.
AE-NOISE-01:	The aircraft shall have a limit noise footprint level of less than 100.7 [dB] at take-off and landing		Maximum noise level at take-off is 93.5 [dB] and maximum noise level at landing is 95.6 [dB]. Compliance shown in Section 13.7.
AE-NOISE-02:	The aircraft shall have a limit noise footprint level of less than 91.9 [dB] at flyover		Maximum noise level at flyover is 95.5 [dB].
AE-NOISE-03:	The cabin noise level shall be lower than 71.9 [dB]		Maximum noise experienced in cabin 84.3 is [dB] when frequency is 500 [Hz], but can go as low as 33.4 [dB] if frequency of sound is 5000 [Hz]. Compliance shown in Section 13.7.
AE-SUS-01:	The production of the energy source must be sustainable for at least the coming 100 years.		Cannot verify the requirement with current information.
Propulsion Requirements			
Requirement Identifier	**Requirement**	**Met**	**Comment**
AE-PROP-01:	The aircraft shall have sufficient fuel storage to achieve a range of 5000 [km] excluding reserves		100% hydrogen: 5623 [km], 20% hydrogen & 80% biofuel: 8192 [km]. Compliance shown in Section 13.2.
AE-PROP-02:	The aircraft shall have a propulsion subsystem efficiency of TBD, no less than the A321XLR		Hybrid engine has a SFC of 12.4 [g/kNs], and full hydrogen engine after modifcations has a SFC of 2.1 [g/kNs]. Compliance shown in Section 8.3.
AE-PROP-03:	The aircraft shall have sufficient space to store the selected form of propulsion subsystem		Fuselage length designed to house the maximum needed number of hydrogen tanks. Compliance shown in Section 5.3.
AE-PROP-04:	The propulsion system shall be able to perform thrust reversal		Engine is based upon another engine capable of thrust reversal. Compliance shown in Section 8.1.
AE-PROP-06:	The engines shall be easily dismounted for inspection and maintenance purposes		Engine located under the wing, which allows for easy dismounting. Compliance shown in Section 3.3.
AE-PROP-07:	The vibrations induced by the engines shall not be detrimental to the aircraft structure		Cannot be verified at this moment in time.
Structure Requirements			
Requirement Identifier	Requirement	Met	Comment
AE-STR-01:	The aircraft shall be able to withstand an limit load of 2.5 times a factor of safety of 1.5.		Structure is designed for this requirement. Compliance shown in Chapter 11.
AE-STR-02:	All external loads on the structure shall be multiplied by a factor of safety of 1.5.		Compliance shown in Chapter 11.
AE-STR-03:	No aileron reversal shall be present in the mission profile.		Sea level: 263 [m/s], cruise: 483 [m/s]. This is lower than manoeuvre speed V_A. Compliance shown in Section 11.3.
AE-STR-04:	The aircraft shall provide a cabin pressure of 0.812 [bar].		Designed for 0.912 [bar]. Compliance shown in Section 11.2.

17. Systems Integration

In the previous chapters the design of various subsystems of the AirEco has been described. This chapter deals with the integration of the various subsystems, which is done using several diagrams. The hardware diagram, software diagram, electric block diagram and the data handling diagram are discussed in Section 17.1, Section 17.2, Section 17.3 and Section 17.4 respectively.

17.1. Hardware Diagram

The hardware diagram of Figure 17.1 shows the different hardware units of the AirEco aircraft, and where they are located. The different type of connections (electric wiring, data cables and fuel lines) are also indicated in this figure. Note that systems such as the flight instruments and navigation system are not further detailed in this diagram to avoid the diagram being to cluttered and unclear. More details about these systems are shown in Figure 17.2 and Figure 17.4.

17.2. Software Diagram

The software diagram of the AirEco aircraft is shown in Figure 17.2. This diagram shows several subsystems as a large block with their respective software. The interaction of the software within subsystems and between subsystems is shown, as well as the interaction with the environment.

17.3. Electric Block Diagram

The electric block diagram of the AirEco aircraft is shown in Figure 17.3 and shows how the electric power is distributed. Three different power flows are shown. The first one (black normal line) denotes the power distribution in a normal situation. The Auxiliary Power Unit (APU) is powered by batteries and is used to start up the engines. The engines then supply power for the rest of the aircraft, distributed by the power management system. During on-ground operations, the ground power unit powers the APU. In this situation the APU powers the systems that are necessary for ground operations, such as the hydraulics of the landing gear and control surfaces and the environmental control system. In case of failure of the APU, a ram air turbine is used to power the critical systems. The power distribution unit is taken in case the power management system fails.

17.4. Data Handling Diagram

All systems of the AirEco aircraft communicate with each other. This internal communication is shown in the data handling diagram of Figure 17.4. Both the transmitted data to the flight computer, as well as the commands from the flight computer to the subsystems are shown together with the information that is being transmitted and the transmission speed. The ARINC 429 systems will be used for data transmission within the aircraft, which can transmit at data at 12.5 and 100 [kbit/s][1].

[1] https://www.kunbus.com/arinc-429.html

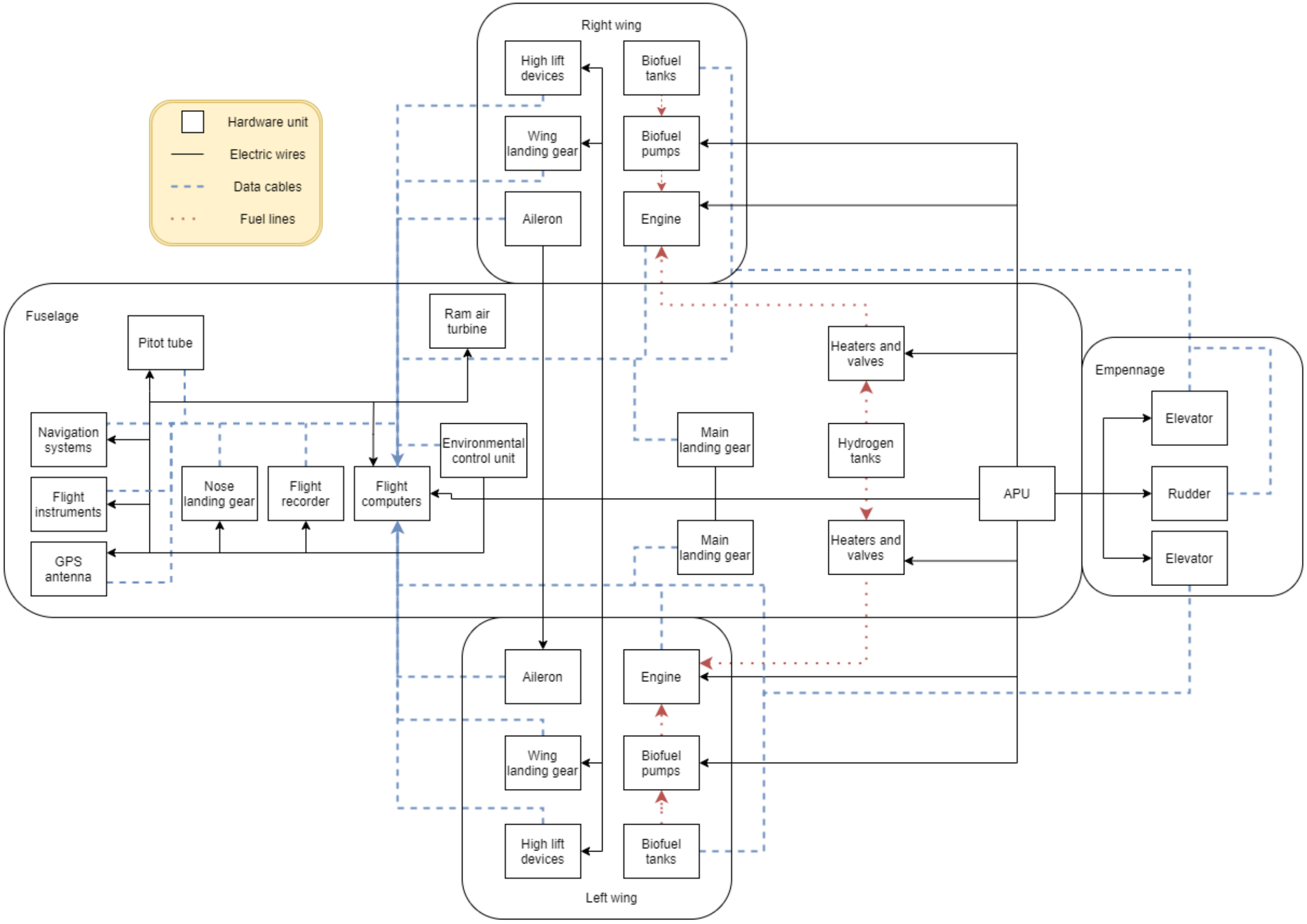

Figure 17.1: Hardware diagram of the AirEco aircraft.

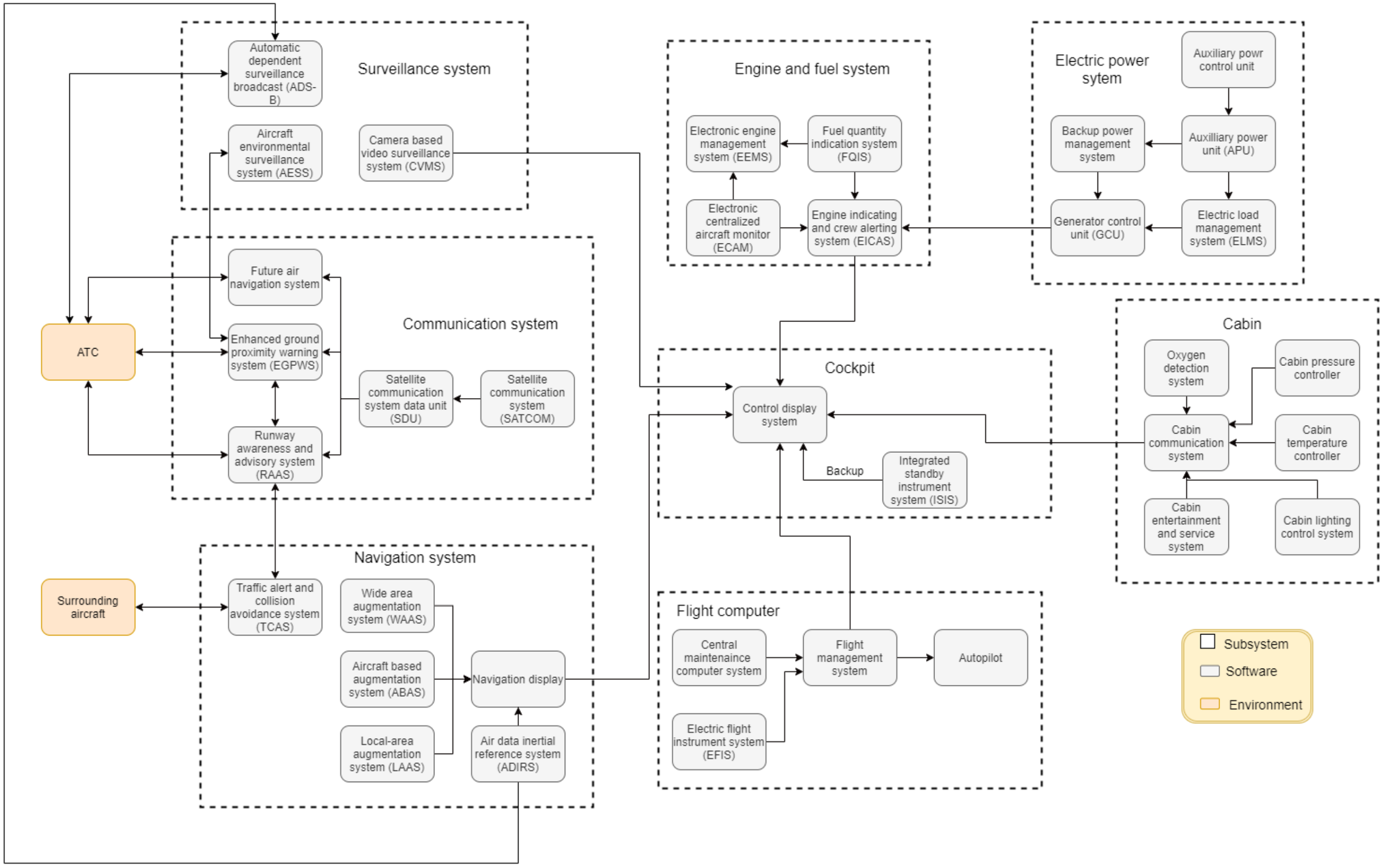

Figure 17.2: Software diagram of the AirEco aircraft.

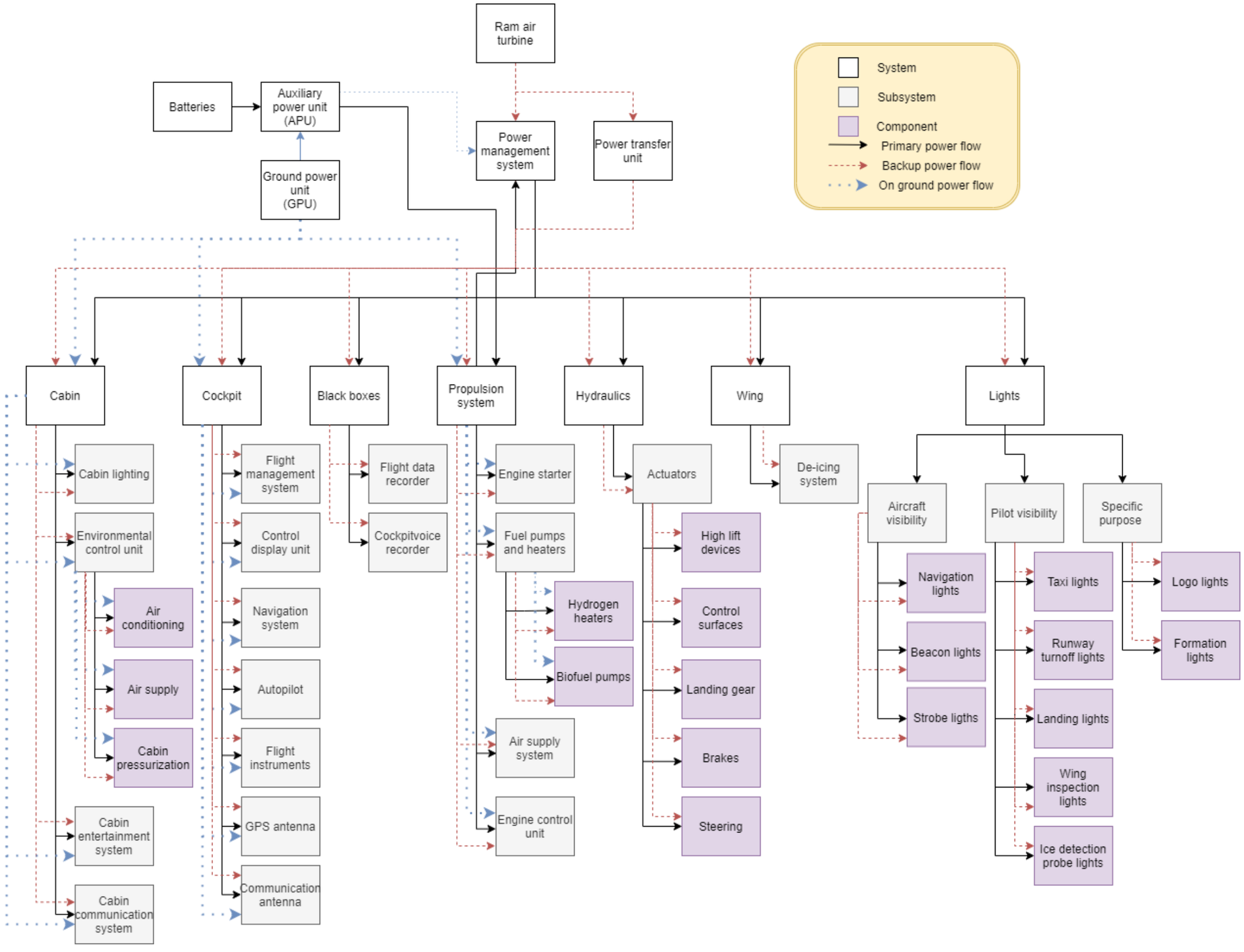

Figure 17.3: Electric block diagram of the AirEco aircraft.

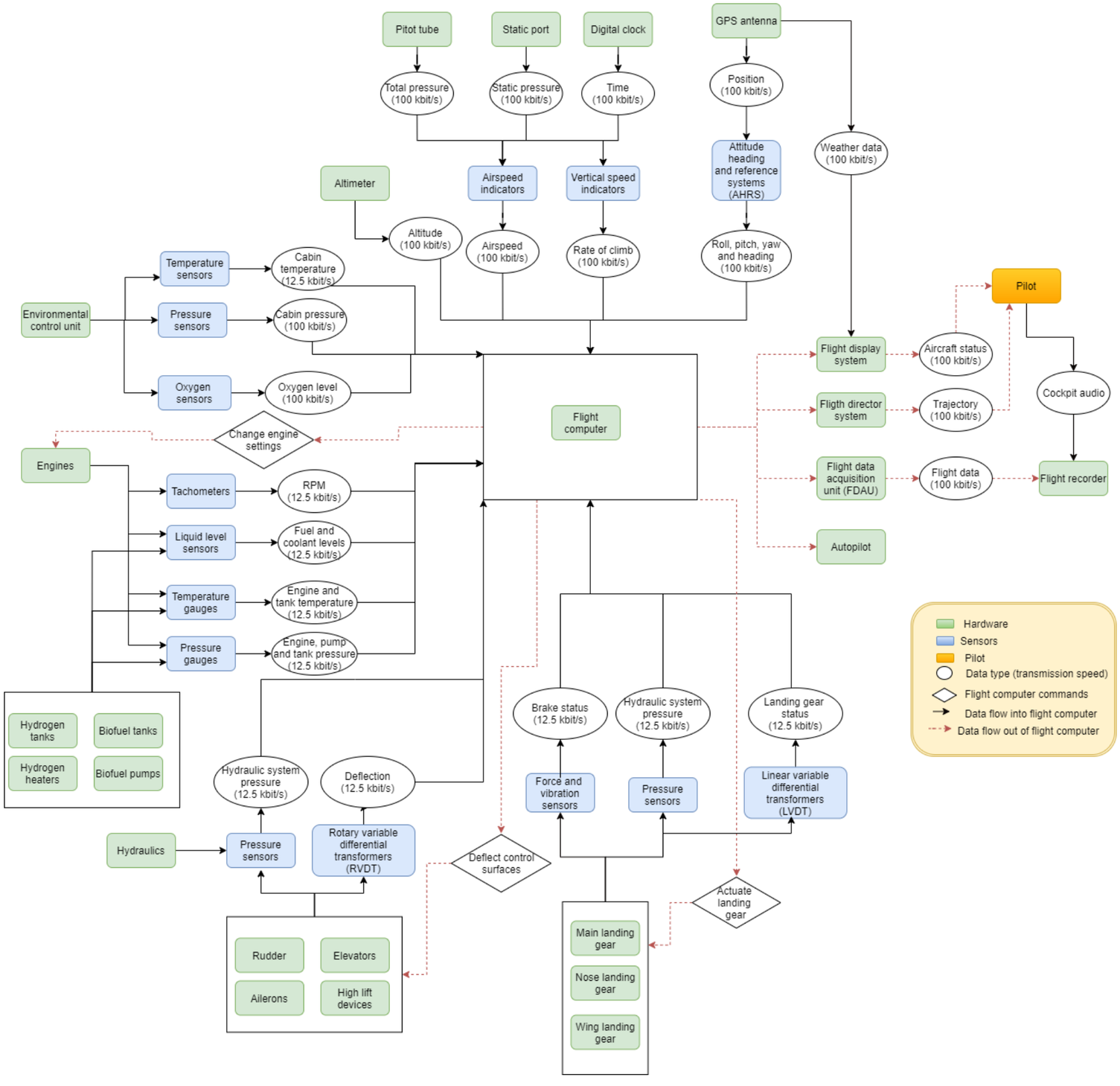

Figure 17.4: Data handling diagram of the AirEco aircraft.

18. Continuation of the AirEco Programme

In this report the complete conceptual design of the AirEco aircraft is presented. Although the conceptual design is concluded with this report, there are still multiple steps to get the AirEco on the market and to have it operate during its lifetime. Section 18.1 describes all the activities to be taken in future phases and Section 18.2 shows the Gantt chart for the next phases of the project.

18.1. Project Development

This section describes the future phases for the AirEco aircraft, as this report only presents the conceptual design. The future consists of detailed design phase, a certification and testing phase, a commercial phase, a production phase, an operational phase and a post-operational phase. These phases, along with the steps in each phase, are shown in Figure 18.1 and Figure 18.2.

Detailed design phase

In the detailed design phase, more in-depth analysis should be done into the different subsystems of the aircraft. This consists of advanced structural analysis using CAD models and finite element models (FEM), advanced aerodynamic design, using wind tunnels testing and computational fluid dynamics (CFD), advanced engine design and dynamic stability analysis. Additionally, certain systems that have only be designed conceptually are designed, such as the hydraulics and electric system. Subsequently, it has to be verified that the design meets all requirements, otherwise design iterations needs to be performed.

If the design meets the requirements, the individual parts are designed. Additionally, the software for the flight control system is designed and tested and the manufacturing process is created. The manufacturing process also already includes the design for the end of life phase of the aircraft, so in this phase companies that can disassemble and recycle the aircraft such as AELS[1] are contacted already. With all this done, the design is validated before the next phase of the process starts. The detailed design phase is expected to take around 9 years.

Certification and testing phase

The certification and testing phase start with the production of multiple prototypes, where each prototype will be used for different tests. The two most important subsystems to verify are the structure of the aircraft and propulsion system, especially with the use of hydrogen and the removable tanks. Afterwards, system and ground tests are performed (which includes vibration and acoustic testing). The last part of this phase is performing a maiden flight. The certification phase is estimated to take around 5 years. The certification of the A380 took around 4 years[2], and with the revolutionary propulsion system it is expected to take a a little longer, although part of the certification of the propulsion system can already be done at the end of the detailed design phase.

[1] https://aels.nl/

[2] https://modernairliners.com/airbus-a380/airbus-a380_history/

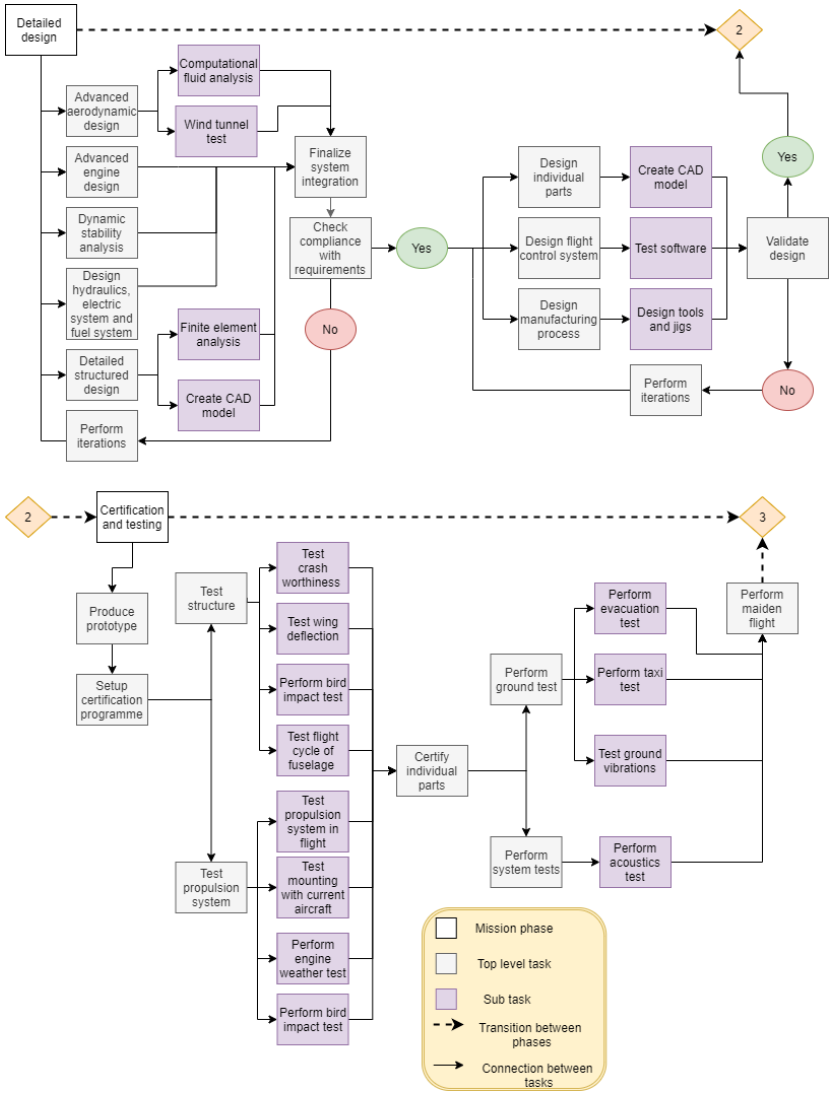

Figure 18.1: Detailed design and certification phase of the AirEco aircraft.

Commercial phase

The commercial phase of the AirEco program will start before production of the aircraft starts and then run in parallel with the production phase. During the commercial phase, an active marketing strategy is pursued and orders are received for the aircraft. Delivering aircraft to airliners is also considered part of the commercial phase.

Production phase

Mostly in parallel with the commercial phase, aircraft production will take place. This phase starts with producing parts that will be produced in-house, which can be turned into subassemblies for the aircraft. Parts that cannot be produced in-house will have to be purchased. These subassemblies can be further assembled to eventually assemble the entire aircraft.

Operational phase

Once aircraft have been built, the operational phase starts, as shown in Figure 18.2. This phase includes crew training, maintenance and the transition to full hydrogen aircraft. All other tasks that make up for the operational phase have already been discussed in Chapter 2. Maintenance is further explained in Section 14.3. Due to the modular design, the AirEco aircraft can be easily updated to stay competitive in the market. To transform from a biofuel-hydrogen

mix to a full hydrogen propulsion system only minor engine modifications are required, as discussed in Section 8.2.

Post-operational phase
The last phase of the aircraft is the end of life phase. From a sustainability point of view, the aim of AirEco is to reuse or recycle as many parts of the aircraft as possible. The first part of this is the removal of parts that can be reused in other aircraft. The engines are a good candidate for this especially since they have likely been modified to be able to work on 100% hydrogen. During this step the aircraft is still certified, so no time and effort is lost in redoing this process[3]. The second phase of this process is the dismantling of the aircraft. Since the aircraft will enter this phase without the hydrogen tanks in place it is assumed that the phase goes quicker than for conventional aircraft.

Certain parts can be reused in different industries than the aviation industry, albeit it with some possible changes to the parts. What is left over of the aircraft can be split in recyclable material which is used to create new parts, and non-recyclable material which is disposed off. The aircraft is mostly made of aluminium which can easily be recycled. It is estimated that a maximum of 10% of the materials of the aircraft cannot be recycled, mostly parts that contain embedded flame retardants which are prohibited from recycling due to regulations, for example insulation blankets, seating cushions, sidewalls and seating panels[3].

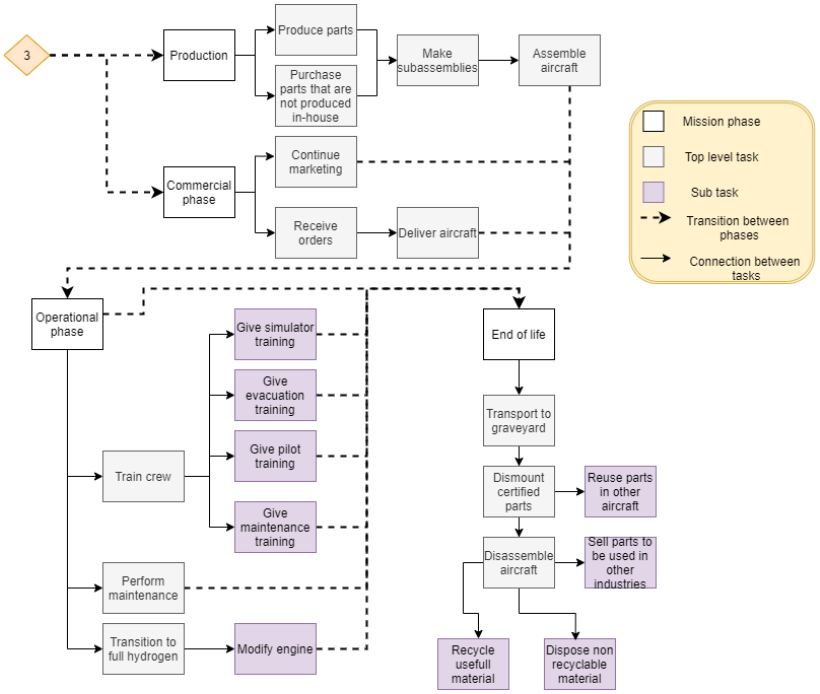

Figure 18.2: Aircraft operation and end of life phase of the AirEco aircraft.

18.2. Project Gantt Chart

A Gantt chart for all activities that have to be executed after the DSE is shown in Figure 18.3. Note that the small green arrow indicates the entry into service year of 2035.

[3] https://www.icao.int/environmental-protection/Documents/EnvironmentalReports/2019/ENVReport2019_pg279-284.pdf

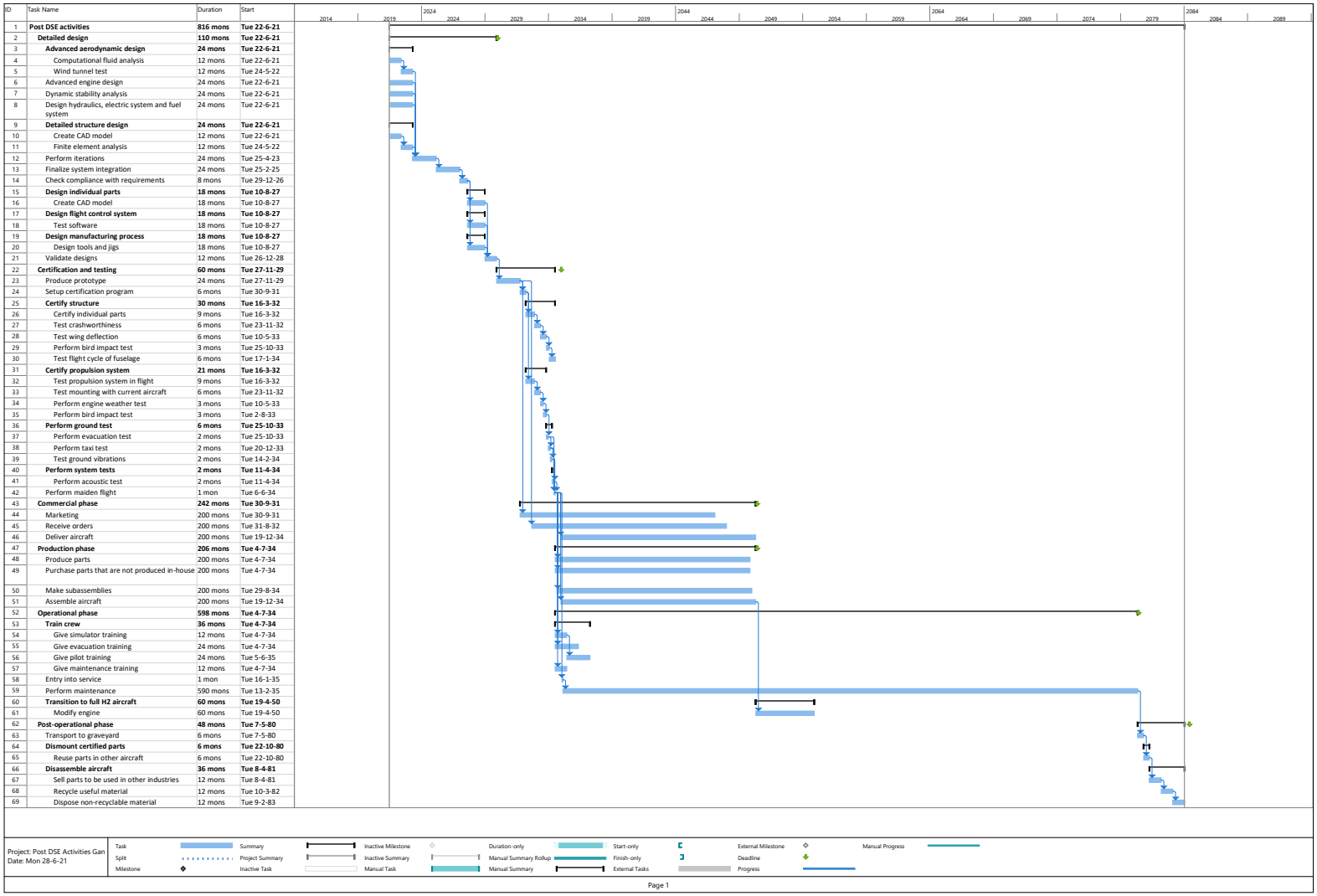

ID	Task Name	Duration	Start
1	**Post DSE activities**	**816 mons**	**Tue 22-6-21**
2	**Detailed design**	**110 mons**	**Tue 22-6-21**
3	**Advanced aerodynamic design**	**24 mons**	**Tue 22-6-21**
4	Computational fluid analysis	12 mons	Tue 22-6-21
5	Wind tunnel test	12 mons	Tue 24-5-22
6	Advanced engine design	24 mons	Tue 22-6-21
7	Dynamic stability analysis	24 mons	Tue 22-6-21
8	Design hydraulics, electric system and fuel system	24 mons	Tue 22-6-21
9	**Detailed structure design**	**24 mons**	**Tue 22-6-21**
10	Create CAD model	12 mons	Tue 22-6-21
11	Finite element analysis	12 mons	Tue 24-5-22
12	Perform iterations	24 mons	Tue 25-4-23
13	Finalize system integration	24 mons	Tue 25-2-25
14	Check compliance with requirements	8 mons	Tue 29-12-26
15	**Design individual parts**	**18 mons**	**Tue 10-8-27**
16	Create CAD model	18 mons	Tue 10-8-27
17	**Design flight control system**	**18 mons**	**Tue 10-8-27**
18	Test software	18 mons	Tue 10-8-27
19	**Design manufacturing process**	**18 mons**	**Tue 10-8-27**
20	Design tools and jigs	18 mons	Tue 10-8-27
21	Validate designs	12 mons	Tue 26-12-28
22	**Certification and testing**	**60 mons**	**Tue 27-11-29**
23	Produce prototype	24 mons	Tue 27-11-29
24	Setup certification program	6 mons	Tue 30-9-31
25	**Certify structure**	**30 mons**	**Tue 16-3-32**
26	Certify individual parts	9 mons	Tue 16-3-32
27	Test crashworthiness	6 mons	Tue 23-11-32
28	Test wing deflection	6 mons	Tue 10-5-33
29	Perform bird impact test	3 mons	Tue 25-10-33
30	Test flight cycle of fuselage	6 mons	Tue 17-1-34
31	**Certify propulsion system**	**21 mons**	**Tue 16-3-32**
32	Test propulsion system in flight	9 mons	Tue 16-3-32
33	Test mounting with current aircraft	6 mons	Tue 23-11-32
34	Perform engine weather test	3 mons	Tue 10-5-33
35	Perform bird impact test	3 mons	Tue 2-8-33
36	**Perform ground test**	**6 mons**	**Tue 25-10-33**
37	Perform evacuation test	2 mons	Tue 25-10-33
38	Perform taxi test	2 mons	Tue 20-12-33
39	Test ground vibrations	2 mons	Tue 14-2-34
40	**Perform system tests**	**2 mons**	**Tue 11-4-34**
41	Perform acoustic test	2 mons	Tue 11-4-34
42	Perform maiden flight	1 mon	Tue 6-6-34
43	**Commercial phase**	**242 mons**	**Tue 30-9-31**
44	Marketing	200 mons	Tue 30-9-31
45	Receive orders	200 mons	Tue 31-8-32
46	Deliver aircraft	200 mons	Tue 19-12-34
47	**Production phase**	**206 mons**	**Tue 4-7-34**
48	Produce parts	200 mons	Tue 4-7-34
49	Purchase parts that are not produced in-house	200 mons	Tue 4-7-34
50	Make subassemblies	200 mons	Tue 29-8-34
51	Assemble aircraft	200 mons	Tue 19-12-34
52	**Operational phase**	**598 mons**	**Tue 4-7-34**
53	**Train crew**	**36 mons**	**Tue 4-7-34**
54	Give simulator training	12 mons	Tue 4-7-34
55	Give evacuation training	24 mons	Tue 4-7-34
56	Give pilot training	24 mons	Tue 5-6-35
57	Give maintenance training	12 mons	Tue 4-7-34
58	Entry into service	1 mon	Tue 16-1-35
59	Perform maintenance	590 mons	Tue 13-2-35
60	**Transition to full H2 aircraft**	**60 mons**	**Tue 19-4-50**
61	Modify engine	60 mons	Tue 19-4-50
62	**Post-operational phase**	**48 mons**	**Tue 7-5-80**
63	Transport to graveyard	6 mons	Tue 7-5-80
64	**Dismount certified parts**	**6 mons**	**Tue 22-10-80**
65	Reuse parts in other aircraft	6 mons	Tue 22-10-80
66	**Disassemble aircraft**	**36 mons**	**Tue 8-4-81**
67	Sell parts to be used in other industries	12 mons	Tue 8-4-81
68	Recycle useful material	12 mons	Tue 10-3-82
69	Dispose non-recyclable material	12 mons	Tue 9-2-83

Figure 18.3: Post Design Synthesis Exercise Gantt chart

19. Conclusion

During the design it has become clear that the level of attainable sustainability is limited by the feasibility with respect to infrastructure and the readiness of technology by 2035. AirEco has presented a solution to this problem, introducing an adaptable concept which will be able to switch configurations during its lifetime and with that become more sustainable. AirEco's aircraft will enter into service by 2035 as a hybrid configuration, running on both hydrogen and biofuel. By 2050, when the production of green hydrogen has become more widespread it will be able to undergo minor modifications, after which it will continue as a fully hydrogen powered aircraft.

With this adaptability, AirEco proposes a unique and revolutionary solution that will exceed any existing aircraft in terms of sustainability. Furthermore AirEco's aircraft will play a key role in facilitating and accelerating commercial aviation's transition to hydrogen powered flight. In that sense one can actually note that the design will be contributing to a sustainable future in two ways. During its own operational lifetime but also acting as a catalyst for the industry. Looking at the bigger picture, one could argue that the latter is what makes this design a revolution.

When looking at the final design, proportionality bias might make it hard for people to believe that a revolution in sustainability has such a familiar shape. However AirEco has shown through rigorous analysis that the solution to true sustainability in the next 15 years does not lie in exotic configurations, but in facilitating a revolutionary propulsion system. Combining this with the other cutting-edge technologies that make the design even more sustainable, the AirEco team is confident that they have proposed a solution which rises to the challenge of creating a revolutionary design.

20. Recommendations

For future continuation of the development and design of AirEco, several recommendations have been made for some of the main departments.

Propulsion:

- The flashback effect should be further researched to have a better understanding of its effect on a mixed injector.
- Conducting further research to better quantify the effect of the swirl number on engine efficiency
- Using the Cantera program is recommended for more accurate emissions results.
- Using simulation tools, such as GSP, is suggested to improve the engine analysis.

Hydrogen tanks:

- Analyse green infrastructure capability for the production of hydrogen.
- Investigate manufacturing of the hydrogen tanks, as well as the airlines' operating cost associated to the tanks.
- More detailed analysis of the tank cargo door.
- Explore the hydrogen tank storage at the airport, from the space required to the facilities needed.
- Develop a standard tank system for all future hydrogen aircraft.

Structures & materials:

- Further iterations should be performed with the new structural weight estimations to converge to a more accurate OEW.
- Investigate the possibility of combining different materials per fuselage section by carrying out a more detailed structural analysis.
- Do research on the relationship between the stringer area and the wing box weight. This includes performing an analysis on stringer crippling.
- Investigate the possibility of talking a current Boeing aircraft, possibly the 777, and retrofitting it with the proposed hydrogen/hybrid propulsion system.
- Investigate the possibility of a family concept by increasing the length of the fuselage.
- Conduct a more detailed analysis on how the production for the selected materials can be optimised to reduce costs.
- Re-evaluate the material selection for the fuselage to obtain more accurate skin thicknesses and stringer areas.

Bibliography

[1] L. Bordas Diaz, et al. “Baseline Report AirEco, AE3200: Design Synthesis Exercise”. In: (Apr. 2021).
[2] Airbus. “Global Market Forecast: Cities, Airports & Aircraft”. In: (2019).
[3] Boeing. “Commercial Market Outlook”. In: (2020).
[4] IHS Markit. *Jane’s All the World’s Aircraft*. Sept. 2019.
[5] L. Bordas Diaz, et al. “Midterm Report AirEco, AE3200: Design Synthesis Exercise”. In: (May 2021).
[6] Strategy&. “The dawn of green hydrogen”. In: (2020).
[7] G.D. Brewer. *Hydrogen aircraft technology*. Routledge, 2017.
[8] B. Dean, et al. “Shark-skin surfaces for fluid-drag reduction in turbulent flow: a review”. In: *Philosophical Transactions of the Royal Society A: Mathematical, Physical and Engineering Sciences* 368.1929 (2010), pp. 4775–4806.
[9] P.R. Viswanath. “Aircraft viscous drag reduction using riblets”. In: *Progress in Aerospace Sciences* 38.6-7 (2002), pp. 571–600.
[10] DW Bechert, et al. “Fluid mechanics of biological surfaces and their technological application”. In: *Naturwissenschaften* 87.4 (2000), pp. 157–171.
[11] S. Martin, et al. “Modeling and optimization of shark-inspired riblet geometries for low drag applications”. In: *Journal of colloid and interface science* 474 (2016), pp. 206–215.
[12] D.W. Bechert, et al. “Drag reduction with riblets in nature and engineering”. In: *WIT Transactions on State-of-the-art in Science and Engineering* 4 (2006).
[13] B. Mele, et al. “Performance Assessment of a Transonic Wing–Body Configuration with Riblets Installed”. In: *Journal of Aircraft* 53.1 (2016), pp. 129–140.
[14] M. Han, et al. “Fabrication of a micro-riblet film and drag reduction effects on curved objects”. In: *TRANSDUCERS’03. 12th International Conference on Solid-State Sensors, Actuators and Microsystems. Digest of Technical Papers (Cat. No. 03TH8664)*. Vol. 1. IEEE. 2003, pp. 396–399.
[15] M. Braun-Unkhoff, et al. “About the Emissions of Alternative Jet Fuels”. In: (2016).
[16] A. Llamas, et al. “Biokerosene from Babassu and Camelina Oils: Production and Properties of Their Blends with Fossil Kerosene”. In: (Aug. 2012).
[17] J. Bosch, et al. “Aviation Biofuels: Strategically Important, Technically Achievable, Tough to Deliver”. In: (Nov. 2017).
[18] A. Zschocke. “High Biofuel Blends in Aviation (HBBA)”. In: (2012).
[19] Fuel Cell and Hydrogen Joint Undertaking. “Hydrogen Powered Aviation: A Fact-based Study of Hydrogen Technology, Economics, and Climate Impact by 2050”. In: (2020).
[20] Council Airports International. “Integration of Hydrogen Aircraft into the Air Transport System”. In: (2121).
[21] I. Langella. personal communication. June 11, 2021.
[22] M.M. Anees, et al. “Physiological and physical impact of noise pollution on environment”. In: *Earth Science Pakistan* 1.1 (2017), pp. 08–11.
[23] M Sadeghian, et al. “Technologies for Aircraft Noise Reduction: Review Paper”. In: *J Aeronaut Aerospace Eng* 9 (2020), p. 218.
[24] H. Batard, et al. “the Zero splice engine intake liner: an efficient way of reducing Aircraft Noise without any weight or aerodynamic penalty”. In: *2004 24th ICAS Congress, Tokyo Japan*. 2004.
[25] S.K.Gupta, et al. “Noise Reduction in Subsonic Jets Using Chevron Nozzles”. In: *Recent Asian Research on Thermal and Fluid Sciences* (2020), pp. 615–625.
[26] S. Martens. “Jet noise reduction technology development at GE aircraft engines”. In: *ICAS Paper* 842 (2002).
[27] X. Han, et al. “Development of acoustic liner in aero engine: a review”. In: *Science China Technological Sciences* (2020), pp. 1–14.
[28] T.A Nguyen, et al. “Effect of hydrogen addition to intake air on combustion noise from a diesel engine”. In: *International journal of hydrogen energy* 38.10 (2013), pp. 4153–4162.
[29] H.H.W Funke, et al. “Experimental Evaluation of the Pollutant and Noise Emissions of the GTCP 36-300 Gas Turbine Operated with Kerosene and a Low NOX Micromix Hydrogen Combustor”. In: (2017).
[30] T.Nguyen, et al. “Effect of hydrogen addition to intake air on combustion noise from a diesel engine”. In: *International Journal of Hydrogen Energy* 38 (Apr. 2013), pp. 4153–4162. DOI: 10.1016/j.ijhydene.2013.01.082.

[31] H.H.W Funke,et al. “Comparison of Numerical Combustion Models for Hydrogen and Hydrogen-Rich Syngas Applied for Dry-Low-Nox-Micromix-Combustion”. In: *Journal of Engineering for Gas Turbines and Power* 140.8 (2018).
[32] L. Burghignoli, et al. “Evaluation of the noise impact of flap-tip fences installed on laminar wings”. In: *CEAS Aeronautical Journal* 11 (2020), pp. 849–872.
[33] J. Sloof, et al. “Aerodynamic and aero-acoustic effects of flap tip fences”. In: *40th AIAA Aerospace Sciences Meeting & Exhibit*. 2002, p. 848.
[34] K. Boorsma, et al. “Landing gear noise control using perforated fairings”. In: *Acta Mechanica Sinica* 26.2 (2010), pp. 159–174.
[35] W. Dobrzynski, et al. “Experimental assessment of low noise landing gear component design”. In: *International Journal of Aeroacoustics* 9.6 (2010), pp. 763–786.
[36] K. Ozcan, et al. “In-Cabin Noise Levels During Commercial Aircraft Flights”. In: (2006).
[37] S. Ersoy, et al. “Investigation of industrial Tea-Leaf-Fibre Waste Material for its Sound Absorption Properties”. In: (Jan. 2009).
[38] J. Roskam. *Airplane design: Part III: Layout design of cockpit, fuselage, wing and empennage: Cutaways and inboard profiles*. University of Kansas, 2002.
[39] D. Raymer. *Aircraft Design: A Conceptual Approach*. Ed. by J. S. Przemieniecki. Second. Sylmar, California: American Institute of Aeronautics and Astronautics, Inc, 1992, pp. 400–407. ISBN: 0930403517.
[40] J. Roskam. *Airplane Design. Part I: Preliminary Sizing of Airplanes*. 3rd ed. Lawrence, Kansas, USA: DARCorporation, 1997.
[41] H. Gongzhang, et al. “Aircraft Winglet Design: Increasing the Aerodynamic Efficiency of a Wing”. In: *Digitala Vetenskapliga Arkivet, KTH Royal Institute of Technology* (2020).
[42] N.N. Gavrilović, et al. “Commercial aircraft performance improvement using winglets”. In: *FME Transactions* 43.1 (2015), pp. 1–8.
[43] J. Sun, et al. “Aircraft drag polar estimation based on a stochastic hierarchical model”. In: *8th International Conference on Research in Air Transportation*. 2018.
[44] D. Geleyn. “Alternative Flight Control in Civil Aviation”. MA thesis. TU Delft, 2016.
[45] F. Oliviero. “Systems Engineering and Aerospace Design - Lectures 3, 4, 5, 9”. In: (2021).
[46] A. Sanchez-Carmona, et al. “Vee-tail conceptual design criteria for commercial transport aeroplanes”. In: *Chinese Journal of Aeronautics* 32.3 (2019), pp. 595–610.
[47] D.P. Raymer. *Aircraft Design: A Conceptual Approach*. 2nd ed. Washington D.C. , USA: AIAA, 1992.
[48] M.H. Sadraey. *Aircraft design: A systems engineering approach*. John Wiley & Sons, 2012.
[49] F. Oliviero. “Aerospace Design and System Engineering Elements II - Lectures 3”. In: (2020).
[50] F. Oliviero. personal communication. June 11, 2021.
[51] P.M. Sforza. *Commercial airplane design principles*. Elsevier, 2014.
[52] F. Oliviero. “Systems Engineering and Aerospace Design - Lecture 9”. In: (2021).
[53] F. Oliviero. “AE3211-I Systems Engineering and Aerospace Design - Design for Lateral-directional aspects, Design for ground operations”. In: (2021).
[54] L. Pescio, et al. “System Engineering and Aerospace Design: Aircraft Tutorial”. In: (Apr. 2021).
[55] K. Fulton. “Cryogenic□Fueled Turbofans: Kuznetsov Bureau’s pioneer work on LH2 and LNG dual□fuel engines”. In: *Aircraft Engineering and Aerospace Technology* 65.11 (1993), pp. 8–11.
[56] *TYPE-CERTIFICATE DATA SHEET for Engine GEnx Series*. EASA. Dec. 2019.
[57] et al. J.P. van Buijtenen. *Gas Turbines Propulsion and Power, AE2203*. The Technical University of Delft. Feb. 2011.
[58] A.C. Benim, et al. *Flashback Mechanisms in Lean Premixed Gas Turbine Combustion*. Elsevier Inc., 2015.
[59] N. Syred, et al. “The effect of hydrogen containing fuel blends upon flashback in swirl burners”. In: *Applied Energy* 89.1 (2012), pp. 106–110.
[60] A.G. Rao, et al. “A hybrid engine concept for multi-fuel blended wing body”. In: *Aircraft Engineering and Aerospace Technology* 86.6 (2014), pp. 483–493. ISSN: 00022667. DOI: 10.1108/AEAT-04-2014-0054.
[61] F. Yin, et al. “Performance assessment of a multi-fuel hybrid engine for future aircraft”. In: *Aerospace Science and Technology* 77 (2018), pp. 217–227.
[62] K.G. Fohmann. “Design of a cooling system for the hybrid engine: Design of a heat exchanger for cooling bleed air with liquefied natural gas”. MA thesis. Delft University of Technology, 2015.
[63] P.S. Mehta, et al. “Estimation of a Lower Heating Value of Vegetable Oil and Biodiesel Fuel”. In: *Energy Fuels* 23.8 (2009), pp. 3893–3898.
[64] L. Gliner. personal communication. May 27, 2013.
[65] D. Verstraete, et al. “Hydrogen fuel tanks for subsonic transport aircraft”. In: *International Journal of Hydrogen Energy* 35.20 (2010). Hyceltec 2009 Conference, pp. 11085–11098. ISSN: 0360-3199.
[66] A. Gomeza, et al. “Liquid hydrogen fuel tanks for commercial aviation: Structural sizing and stress analysis”. In: (2016).
[67] G.D.Brewer, et al. *Tank and Fuel Systems Considerations for Hydrogen Fueled Aircraft*. 1975, pp. 3088–3103.

[68] L. Gliner. personal communication. June 14, 2013.
[69] H. Fricke, et al. “Improving Aircraft Turn Around Reliability”. In: (2008).
[70] U.S. Department of Energy. “Potential Roles of Ammonia in a Hydrogen Economy”. In: *Energy* (2006), pp. 1–23.
[71] G. Wu, et al. *Failure in Structural Materials Overview The Mechanical Behavior of GLARE Laminates for Aircraft Structures*. 2005.
[72] R.C. Alderliesten. *Introduction to Aerospace Engineering - Structures and Materials*. Course AE1102 reader. Delft University of Technology. Faculty of Aerospace Engineering, Oct. 2011.
[73] C. Kassapoglou. *Predicting the Structural Performance of Composite Structures Under Cycling Loading*. Delft University of Technology, 2012, pp. 93–118.
[74] T.H.G. Megson. *Aircraft structures for engineering students*. Ed. by N. McFadden. 6th ed. Vol. 53. Todd Green, 2013. ISBN: 9788578110796. arXiv: arXiv:1011.1669v3.
[75] I. Sen. “Aircraft Fuselage Design Study - Parametric Modeling, Structural Analysis, Material Evaluation and Optimisation for an Aircraft Fuselage (MSc thesis)”. PhD thesis. Delft University of Technology, 2010, p. 180.
[76] N.C. Heerens. “Landing gear design in an automated design environment”. PhD thesis. Delft University of Technology, 2014.
[77] M.F. Ashby,et al. *Materials: Engineering, Science, Processing and Designs*. 3rd ed. Oxford, United Kingdom: Butterworth-Heinemann, 2014.
[78] *Certification Specifications and Acceptable Means of Compliance for Large Aeroplanes CS-25*. European Union Aviation Safety Agency, Dec. 2020.
[79] “ICAF 2011 Structural Integrity: Influence of Efficiency and Green Imperatives”. In: (). DOI: 10.1007/978-94-007-1664-3.
[80] J.A. Volpe National. *Damage Tolerance Atlantic City Airport, Volume I: Introduction Assessment Handbook Fracture Mechanics Fatigue Crack Propagation Research and Special Programs*.
[81] T. Swift. “Damage tolerance capability”. In: *International Journal of Fatigue* 16 (1 Jan. 1994), pp. 75–94. ISSN: 01421123. DOI: 10.1016/0142-1123(94)90446-4.
[82] V.V. Vasiliev. *Mechanics of Laminates*. Jan. 2018. DOI: 10.1016/b978-0-08-102209-2.00003-7.
[83] J.P.C. Pinto. “Economic comparison between materials in the aerospace industry”. Master of Science. Lisbon: Técnico Lisboa, June 2017.
[84] R. J.H. Wanhill. *Aerospace Applications of Aluminum-Lithium Alloys*. Jan. 2013. DOI: 10.1016/B978-0-12-401698-9.00015-X.
[85] A. Hiken. “The Evolution of the Composite Fuselage - A Manufacturing Perspective”. In: *SAE International Journal of Aerospace* 10 (2 Sept. 2017). ISSN: 19463901. DOI: 10.4271/2017-01-2154.
[86] M.F Ashby, et al. *MATERIALS SELECTION MECHANICAL DESIGN IN SECOND EDITION SECOND EDITION British Library Cataloguing in Publication Data Library of Congress Cataloguing in Publication Data*. 1992.
[87] K. Boer. *Development of a cost effective composite wingbox for small aircraft*.
[88] P. Dubois. *Towards an efficient FDA programme*. Oct. 2016.
[89] et al. W.A. Timmer. *AE2111-I Systems Design Project Reader - Aircraft - WP4-5*. Delft University of Technology. Nov. 2020.
[90] F. Oliviero. *AE2111-I Aerospace System Design Lecture Slides*. Delft University of Technology.
[91] M. C. Y. Niu. *Airframe Stress Analysis and Sizing*. second. Hong Kong Conmilit Press LTD., Jan. 1997.
[92] T.H.G. Megson. *Materials: Engineering, Science, Processing and Designs*. 6th ed. Oxford, United Kingdom: Butterworth-Heinemann, 2017.
[93] J. Sinke. *Production of Aerospace Systems*. 2021.
[94] Fuel Requirements for Flight in IFR Conditions. “Legal Information Institute”. In: (2000).
[95] P.C. Roling. “Lecture 04 - Airfield Performance”. In: (2020).
[96] L. Bertsch. “Noise prediction within conceptual aircraft design”. PhD thesis. Technische Universität Braunschweig, 2013.
[97] R.M. Martinez. personal communication. May 31, 2021.
[98] J.R. Stone, et al. “Conventional profile coaxial jet noise prediction”. In: *AIAA journal* 21.3 (1983), pp. 336–342.
[99] M.F. Heidmann. “Interim prediction method for fan and compressor source noise”. In: (1975).
[100] L.Bertsch, et al. “The parametric aircraft noise analysis module-status overview and recent applications”. In: *17th AIAA/CEAS Aeroacoustics Conference (32nd AIAA Aeroacoustics Conference)*. 2011, p. 2855.
[101] Q. Deng. “A practical dynamic programming based methodology for aircraft maintenance check scheduling optimization”. In: *European Journal of Operational Research* 281.2 (2020).
[102] P.G. Holborn, et al. “Modelling hazardous distances for large-scale liquid hydrogen pool releases”. In: *International Journal of Hydrogen Energy* 45.43 (2020), pp. 23851–23871.
[103] J. Markish. “Valuation Techniques for Commercial Aircraft Program Design by”. PhD thesis. Massachusetts Institute of Technology, 2002.

[104] Y. Zhang, et al. “Exploration and implementation of commonality valuation method in commercial aircraft family design”. In: *Chinese Journal of Aeronautics* 32.8 (2019), pp. 1828–1846. ISSN: 1000-9361. DOI: https://doi.org/10.1016/j.cja.2019.05.005.
[105] N .Pavlenko, et al. “The cost of supporting alternative jet fuels in the European Union”. In: *International Council on Clean Transportation* March (2019), p. 20.
[106] Hydrogen Council. “Path to hydrogen competitiveness: a cost perspective”. In: January (2020), p. 88.
[107] M. Fioriti,et al. “Cost-estimating model for aircraft maintenance”. In: *Journal of Aircraft* 55.4 (2018), pp. 1564–1575. ISSN: 15333868. DOI: 10.2514/1.C034664.
[108] R. Ali, et al. “A Comparative Study of Cost Estimation Models used for Preliminary Aircraft Design”. In: (2014). ISSN: 0975-5861.
[109] L. Bordas Diaz, et al. “Project Plan AirEco, AE3200: Design Synthesis Exercise”. In: (Apr. 2021).